

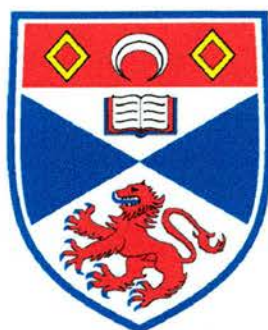
University of St Andrews



Full metadata for this thesis is available in
St Andrews Research Repository
at:

<http://research-repository.st-andrews.ac.uk/>

This thesis is protected by original copyright



University
of
St Andrews

Structural Studies of Layered Perovskites

A thesis presented for the degree of

Doctor of Philosophy

in the Faculty of Science at the University of St Andrews

by Alan Snedden, BSc(Hons), MSc, AMRSC

November 2003



TK
E534

Declarations

I, Alan Snedden, hereby certify that this thesis, which is approximately 40,000 words in length, has been written by me, that it is a work carried out by me and that it has not been submitted in any previous application for a higher degree.

Date: 12/01/04 Signature of candidate:

I was admitted as a research student in September 2000 and as a candidate for the degree of PhD in August 2001; the higher study for which this is a record was carried out in the University of St Andrews between 2000 and 2003.

Date: 12/01/04 Signature of candidate: —

I hereby certify that the candidate has fulfilled the conditions of the Resolution and Regulations appropriate for the degree of PhD in the University of St Andrews and that the candidate is qualified to submit this thesis in application for that degree.

Date: 12/01/04 Signature of supervisor: —

In submitting this thesis to the University of St Andrews I understand that I am giving permission for it to be made available for use in accordance with the regulations of the University Library for the time being in force, subject to any copyright vested in the work not being affected hereby. I also understand that the title and abstract will be published, and that a copy of the work may be made and supplied to any *bona fide* library or research worker.

Date: 12/01/04 Signature of candidate: :

Acknowledgements

Thanks go to the boss, Phil, for guidance and optimism on the project, and for the ever open door, except when he's at the gym.

Thanks also go to staff at Daresbury, ISIS and the ILL for help with neutron diffraction and EXAFS experiments; Fred, Laurie, Ron, Richard, Kevin and Emmanuelle.

For help with the a.c. impedance experiments, thanks to John, John and Angela.

From Guildford, thanks go to Saiful, Jools and Andy for help with the Gulp software. Thanks also to Julian Gale for provision of the software.

The EPSRC and EPSRC perovskite network, for the cash.

Also many thanks to the people in 324 for creating a certain atmosphere, whether they be Lightfoot, Wright or a bit of both; Zoe, Martin, Chris, Chic, Humph, Tim, Phill, Ardak, Mark, Rob, Jorge, Oleg, Nick, Nandini, Peter, Raquel, John, Stewart, Karen, Tim, Thomas

Abstract

In this work studies have been carried out into the structures of three families of layered perovskite using powder neutron diffraction.

It is shown that $\text{Bi}_5\text{Ti}_3\text{FeO}_{15}$ exhibits only one high temperature phase transition, from $A2_1am$ to $I4/mmm$. For another 4-layer Aurivillius phase, $\text{BaBi}_4\text{Ti}_4\text{O}_{15}$, the room temperature structure has been successfully refined in space group $F2mm$. Both of these results are in contradiction to earlier suggestions. La^{3+} doping into 2- and 3-layer structures was investigated in $\text{Bi}_{3-x}\text{La}_x\text{TiNbO}_9$ for $0 \leq x \leq 1$ and $\text{Bi}_{4-x}\text{La}_x\text{Ti}_3\text{O}_{12}$ for $0 \leq x \leq 2$. The transition from polar to centrosymmetric has been examined and is in agreement with documented ferroelectric properties. The series $\text{Bi}_2\text{Sr}_2\text{Ti}_{1-x}\text{Ga}_x\text{Nb}_2\text{O}_{12-x/2}$ and $\text{BaBi}_4\text{Ti}_{4-x}\text{Ga}_x\text{O}_{15-x/2}$ were studied for $x = 0.2, 0.5$ and 1 using powder X-ray diffraction. The presence of a second phase, Bi_2O_3 was identified. The presence of this impurity would suggest that the main phases are unlikely to be oxide ion conductors, as previously suggested.

The structures of the 2-layer Dion-Jacobson phases $\text{CsBiNb}_2\text{O}_7$ and $\text{CsNdNb}_2\text{O}_7$ and the 4-layer $\text{CsBi}_3\text{Ti}_4\text{O}_{13}$ have been determined using space group $P2_1am$. The system of octahedral tilting within the perovskite blocks is analogous to that observed in the ferroelectric Aurivillius phases, though no ferroelectric behaviour has been observed. Contrasting behaviour has been found in the 3-layer phases $\text{CsA}_2\text{Ti}_2\text{NbO}_{10}$ ($A = \text{La}, \text{Nd}, \text{Bi}$), with the Nd and Bi phases adopting an orthorhombically distorted version (space group $I2cm$) of the parent tetragonal structure of the La derivative.

Atomistic calculations have been used to study the possibility of doping Me^{3+} ($\text{Me} = \text{Al}, \text{Ga}, \text{In}$) into $\text{BaBi}_4\text{Ti}_4\text{O}_{15}$ and $\text{Bi}_4\text{Ti}_3\text{O}_{12}$; these suggest the doping of In^{3+} into the $[\text{Bi}_2\text{O}_2]$ layer as the most energetically favoured. The O position in the $[\text{Bi}_2\text{O}_2]$ layer was given as the lowest energy site for oxygen vacancies, however, the possibility of oxygen migration in $\text{Bi}_4\text{Ti}_3\text{O}_{12}$ was found to be unfavourable. At the dilute limit La^{3+} doping was suggested to occur at the $[\text{Bi}_2\text{O}_2]$ layer in $\text{Bi}_4\text{Ti}_3\text{O}_{12}$.

Contents

1	Introduction to Layered Perovskites	1
1.1	Perovskites	1
1.2	Layered Perovskites	2
1.2.1	Aurivillius Phases	3
1.2.2	Ruddlesden-Popper Phases	19
1.2.3	Dion-Jacobson Phases	26
2	Techniques for Materials Analysis	41
2.1	Structural Analysis	41
2.1.1	Crystals, Symmetry and Space Groups	41
2.1.2	X-rays	48
2.1.3	The Neutron	50
2.1.4	Powder Diffraction	52
2.1.5	Rietveld Refinement	53
2.1.6	Glazer Notation	55
2.1.7	Bond Valence Calculations	56
2.2	Physical Property Analysis	56
2.2.1	Ferroelectricity	57

2.2.2	Oxide Ion Conduction	57
2.2.3	a.c. Impedance Spectroscopy	58
3	Aurivillius Phases Containing Trivalent Cations	62
3.1	Ga ³⁺ Containing Aurivillius Structures	62
3.2	Crystallography	64
3.2.1	BaBi ₄ Ti ₄ O ₁₅	64
3.2.2	BaBi ₄ Ti _{4-x} Ga _x O _{15-x/2}	78
3.2.3	Bi ₂ Sr ₂ Nb ₂ Ti _{1-x} Ga _x O _{12-x/2}	85
3.3	Aurivillius Phases Containing Fe ³⁺	89
3.4	Bi ₅ Ti ₃ FeO ₁₅	90
3.4.1	Neutron Data	90
3.4.2	a.c. Impedance	108
3.5	Summary	108
4	Mixed Layer Aurivillius Phases	112
4.1	Bi ₅ TiNbWO ₁₅	112
4.1.1	Electron Microscopy	119
4.2	Bi ₅ Nb ₃ O ₁₅	127
4.2.1	Diffraction Data	128
5	Lanthanides in Aurivillius Phases	133
5.1	Bi _{3-x} La _x TiNbO ₉	133
5.1.1	Bi ₃ TiNbO ₉	134
5.1.2	Bi _{2.8} La _{0.2} TiNbO ₉	136
5.1.3	Bi _{2.6} La _{0.4} TiNbO ₉	137

5.1.4	$\text{Bi}_{2.4}\text{La}_{0.6}\text{TiNbO}_9$	139
5.1.5	$\text{Bi}_{2.2}\text{La}_{0.8}\text{TiNbO}_9$	141
5.1.6	$\text{Bi}_2\text{LaTiNbO}_9$	143
5.1.7	Comparison of La^{3+} Doped Samples	143
5.2	$\text{Bi}_{4-x}\text{La}_x\text{Ti}_3\text{O}_{12}$	157
5.2.1	X-ray and Neutron Diffraction Data	158
5.2.2	Effect of Composition on Structure	164
5.2.3	Discussion	177
6	Other Layered Phases	181
6.1	Dion-Jacobson Phases	181
6.1.1	CsMNb_2O_7	183
6.1.2	$\text{CsM}_2\text{Ti}_2\text{NbO}_{10}$ (M = La, Nd & Bi)	194
6.1.3	$\text{CsBi}_3\text{Ti}_4\text{O}_{13}$	208
6.2	Ruddlesden-Popper Phases	214
6.2.1	$\text{Na}_2\text{La}_2\text{Ti}_{3-x}\text{Ru}_x\text{O}_{10}$	216
6.2.2	$\text{Na}_2\text{Nd}_2\text{Ti}_{3-x}\text{Ru}_x\text{O}_{10}$	222
6.2.3	$\text{Na}_2\text{Nd}_2\text{Ti}_{2.5}\text{Fe}_{0.5}\text{O}_{9.75}$	227
6.2.4	$\text{Na}_2\text{Nd}_2\text{Ti}_2\text{MnO}_{10-x}$	228
7	Atomistic Simulations of Aurivillius Phases	232
7.1	Overview and Prior Work	232
7.2	Introduction to Modelling	233
7.2.1	Intrinsic Atomic Defects and Redox Reactions	238
7.2.2	Dopant Substitution	239
7.2.3	Vacancy Migration	242

7.3	Conclusions	243
8	Concluding Remarks and Further Work	245
A	Space Group Assignments	A-1
B	Synthesis Conditions	B-1
C	Ga ³⁺ Doping Data	C-1
D	Variable Temperature Bi ₅ Ti ₃ FeO ₁₅ Data	D-1
E	Bi _{3-x} La _x TiNbO ₉ Structural Data	E-1
F	Bi _{4-x} La _x Ti ₃ O ₁₂ Structural Data	F-1
G	Publications From This Work	G-1

Chapter 1

Introduction to Layered Perovskites

1.1 Perovskites

The perovskite structure is a very widely known mineral structure-type with the general formula ABX_3 . The ideal 'parent' structure is cubic, with the A-site cations located on the corners of the cube, the B-site cations in the centre of the cube and the anions (usually O^{2-}) in the centre of the faces of the cube, as shown in Figure-1.1. Structures of lower symmetry are commonly reported for ABO_3 perovskites, caused by displacements of the ions away from their special positions.

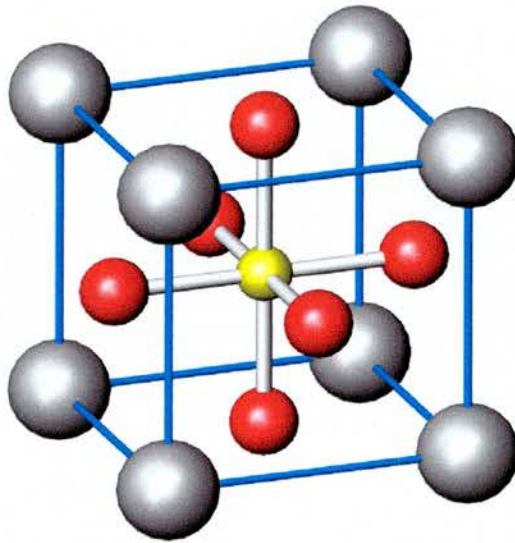


Figure 1.1: Cubic perovskite structure, A-site is grey, B-site is yellow, oxygens are red, unit cell edges shown in blue

1.2 Layered Perovskites

The perovskite structure, which is able to be distorted in a number of ways, is the basis for the various families of layered perovskites. In these structures a block of perovskite, n -layers thick, is separated by an interlayer unit from another perovskite block and so on. There are several different families of layered perovskites, this work focusses upon three; the Aurivillius, Dion-Jacobson and Ruddlesden-Popper phases. Examples of the 2-layer members of these three series are shown as Figure-1.2. Details of the structures are in the following sections.

Commonly the layered structures are present in a 'parent' tetragonal phase at some temperature. Structures which are not tetragonal at room temperature

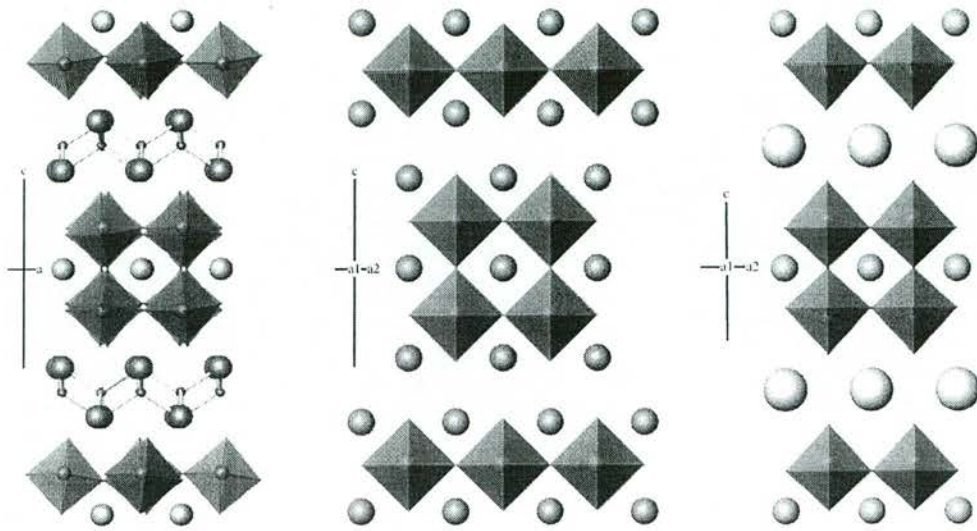


Figure 1.2: Comparison of 2-layer phases. $\text{SrBi}_2\text{Ta}_2\text{O}_9$ (Aurivillius), $\text{Sr}_3\text{Ti}_2\text{O}_7$ (Ruddlesden-Popper) and $\text{CsLaNb}_2\text{O}_7$ (Dion-Jacobson), left to right.

are often pseudotetragonal orthorhombic structures. The requirement for the reduction to orthorhombic symmetry is due to tilting of the perovskite octahedra. The structures are most often distorted so that the a and b -axes are now approximately $\sqrt{2}a_T$ ($a_T =$ tetragonal cell), shown as Figure-1.3.

1.2.1 Aurivillius Phases

The Aurivillius phases were first identified by Bengt Aurivillius in the late 1940's[1, 2]. These phases were shown to be composed of blocks of perovskite, n layers thick, of formula $[\text{A}_{n-1}\text{B}_n\text{O}_{3n+1}]$, separated by a $[\text{Bi}_2\text{O}_2]$ layer, with a fluorite type structure, as shown in Figure-1.4.

Most of the early work done on these structures involves the use of sin-

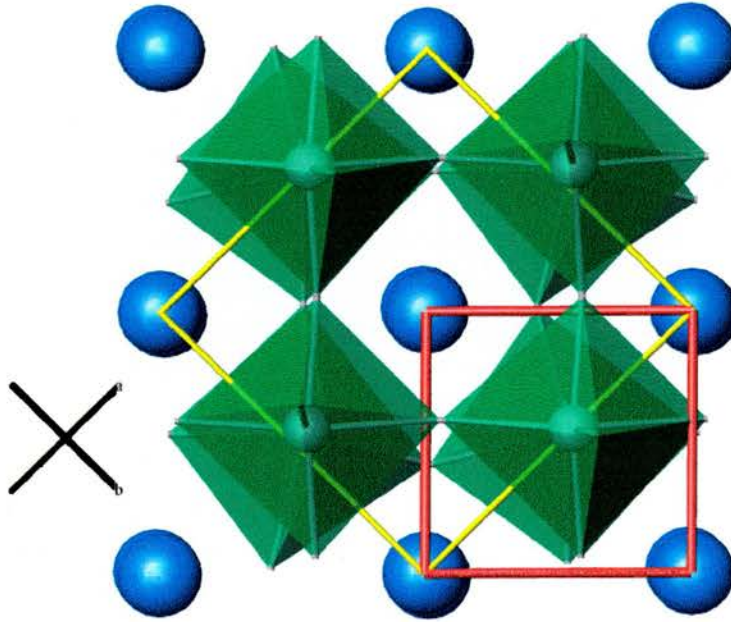


Figure 1.3: Aurivillius perovskite block, of $\text{Bi}_4\text{Ti}_3\text{O}_{12}$, viewed down the c -axis. Red lines are the tetragonal cell, yellow lines are the orthorhombic cell.

gle crystal X-ray diffraction. In a 1960's study[3] Aurivillius describes the structure of $\text{Ba}_2\text{Bi}_4\text{Ti}_5\text{O}_{18}$, a 5-layer structure, using single crystal diffraction. This structure would be the most complex Aurivillius phase described structurally for the next 30 years. However there are problems with the refinement, for example, one of the titanium atomic positions is almost identical to that of an oxygen atom. This can be attributed to the use of X-ray diffraction where the oxygen positions are difficult to identify, in the presence of heavier scatterers. However, more accurate work using single crystal X-ray diffraction is possible. In the early 1990's work was performed by Rae,

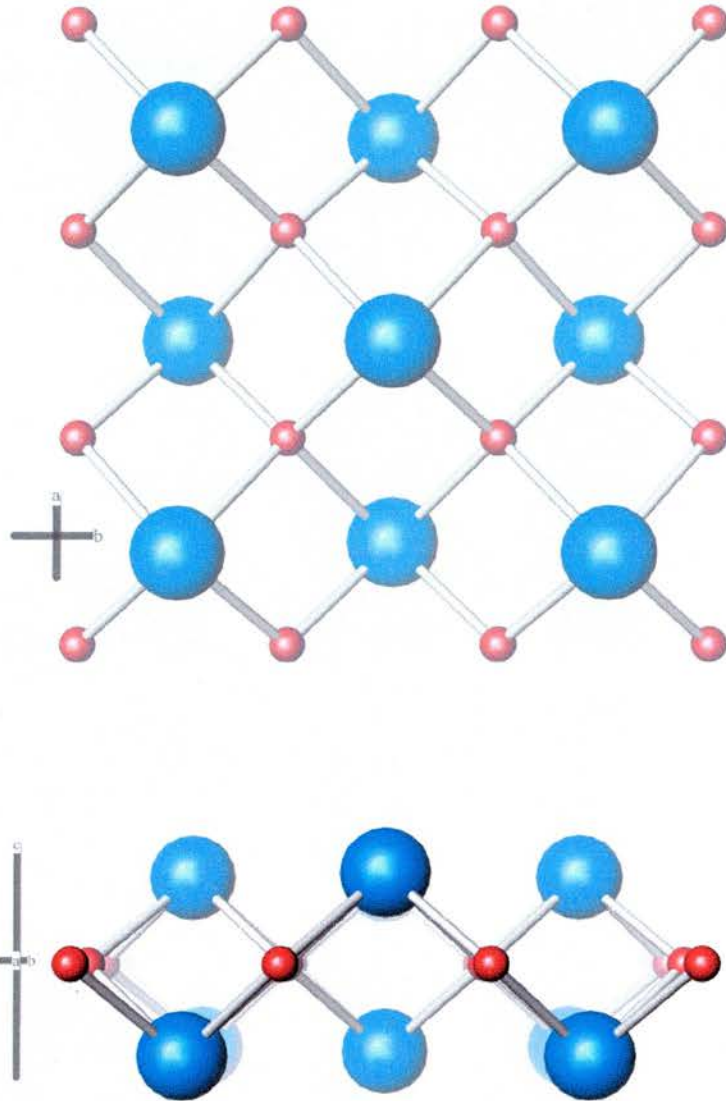


Figure 1.4: $[Bi_2O_2]$ structure, bismuth atoms in blue, oxygen atoms are red.

Top, c -axis projection, bottom, ab -plane projection

Withers and Thompson using single crystal X-ray diffraction to analyse the structure of 1, 2 and 3-layer Aurivillius phases[4, 5]. That work is discussed in more detail in later sections.

In the early 1960's there was an increasing focus on the properties of the Aurivillius phases, in particular the potential for use in ferroelectric materials. Two papers in particular[6, 7], detail the effect of composition and number of layers upon the ferroelectric behaviour of these phases. These properties would remain unharnessed until 1995, when a paper published by Scott and co-workers[8], detailed the suitability of these materials for use in 'fatigue free' ferroelectric memory applications. In these applications data are stored using the polarization state of the material, the information storage is subject, however, to a reduction of performance with use (fatigue). In this particular paper the material is the 2-layer phase $\text{SrBi}_2\text{Ta}_2\text{O}_9$ (SBT). In a later publication[9], the properties of the 3-layer $\text{Bi}_{3.25}\text{La}_{0.75}\text{Ti}_3\text{O}_{12}$ (BLT) material is compared against those of SBT, and it is found to also have a high fatigue resistance. Following on from these reports, investigations into the dielectric properties of other Aurivillius phases followed, for example, Nd doping into the $\text{Bi}_4\text{Ti}_3\text{O}_{12}$ (BTO) phase[10], Gd and Dy doping into BTO[11], Sm doping into BTO[12] and the 5-layer $\text{Sr}_2\text{Bi}_4\text{Ti}_5\text{O}_{18}$ [13].

Although less well documented, the Aurivillius family of structures have also been investigated for their other properties. Investigations have been made into the magnetic properties of the 4-layer $\text{Bi}_5\text{Ti}_3\text{FeO}_{15}$ [14, 15] and $\text{Bi}_5\text{Ti}_3\text{MnO}_{15}$ [16], the 5-layer $\text{Bi}_6\text{Ti}_3\text{Fe}_2\text{O}_{18}$ [15] and the 6-layer $\text{Bi}_7\text{Ti}_3\text{Fe}_3\text{Ti}_6\text{O}_{21}$ [17]. The possibility of creating oxide ion conductors by doping oxygen vacancies into Aurivillius structures has been examined[18]. In

that work the possibility of doping Ga^{3+} and Al^{3+} for Ti^{4+} was examined for the $\text{Bi}_2\text{Sr}_2\text{Nb}_2\text{TiO}_{12}$ structure[19, 20]. Doping of Sc, Al and Ga into the 4-layer $\text{BaBi}_4\text{Ti}_4\text{O}_{15}$ [21] has also been reported. Further work on this subject is to be found in Chapter 3.

These studies of the properties of the Aurivillius phases, whether the electrical, magnetic or ionic properties, all feature little or no structural data. Some of the papers produced X-ray diffraction patterns, indexings and lattice parameters. Almost none of them gave complete structures. There are however many other reports focussing on the structures of 2, 3 and 4-layer Aurivillius phases, and of the mixed layer Aurivillius phases.

One of the earliest publications to use neutron diffraction to investigate the structures of Aurivillius phases, by Newnham et al.[22], produced a set of conclusions which hold true for almost all known examples. It stated that for an Aurivillius phase with an odd number of perovskite layers the most likely space group is B2cb , and for one with an even number of layers the most likely is $\text{A2}_1\text{am}$. These observations are made as for the odd layered compounds the $\text{A2}_1\text{am}$ space group has a mirror plane perpendicular to c . Due to the positioning of the B-site on this mirror plane the octahedra would not be able to rotate and would instead distort. It is argued that this would be energetically unfavourable. For the even-layered compounds the reverse argument is put forward, i.e. that the mirror plane does not interfere with octahedral rotations but that the 2-fold axis along a would prevent the rotation of the octahedra in B2cb but not for $\text{A2}_1\text{am}$. It is in this paper that two high-temperature phase transitions in $\text{Bi}_5\text{Ti}_3\text{FeO}_{15}$ are discussed, a topic which is to be investigated in this thesis. The work by Newnham deals with

phases where the $[\text{Bi}_2\text{O}_2]$ layer and perovskite A-site are entirely composed of Bi^{3+} cations. The structural distortions are rationalised in terms of bond strain. The bond strain is created by the desire of the 'apical' oxygen on the outer octahedron to shorten its bond to the B-site cation, the displacement of the B-site cation creates distortions in the 'equatorial' oxygen and thus the symmetry of the system is lowered from the tetragonal $I4/mmm$ 'parent' structure. This certainly must be the case in 1-layer phases, but for 2 or more layers the effect of the A-site cation in the perovskite block must be taken into account. The parent structure is the high temperature phase found for all Aurivillius phases where there is no polarisation. The space groups used to describe the ferroelectric behaviour of the Aurivillius phases are distorted supercells, based upon the 'parent' $I4/mmm$, as discussed earlier. This distortion is not exclusive to the Aurivillius phases and can be found in other layered perovskites and in the perovskite structure itself. It arises due to the octahedral tilting in the perovskite block.

1-Layer Phases

There are two well documented isostructural 1-layer Aurivillius phases, Bi_2WO_6 and Bi_2MoO_6 . The 1-layer structures are set apart from most of the other Aurivillius phases as they do not require any perovskite A-site cations. This means that all the distortions of the perovskite octahedra are caused by the combined effect of the $[\text{Bi}_2\text{O}_2]$ layer and B-site bonding requirements. Some of the more recent work done on these structures [4, 23] would dispute the prior work of Newnham et al. and suggests that the two structures actually crystallise in $P2_1ab$, a subgroup of $B2cb$. The structure of

the Bi_2WO_6 phase[24] was rationalised using a bond valence approach. This is done by using the Bond Valence Sum (BVS) calculation (see Section 2.1.7) and the value of B established by Brown and Altermatt[25]. The values obtained for different space groups were compared and the best selected. It is demonstrated by this approach that the structure of Newnham et al. represents a false minimum. The bond valence summation and the use of a modulated structure approach are unusual, but here appear to give a more accurate re-interpretation of the previous model.

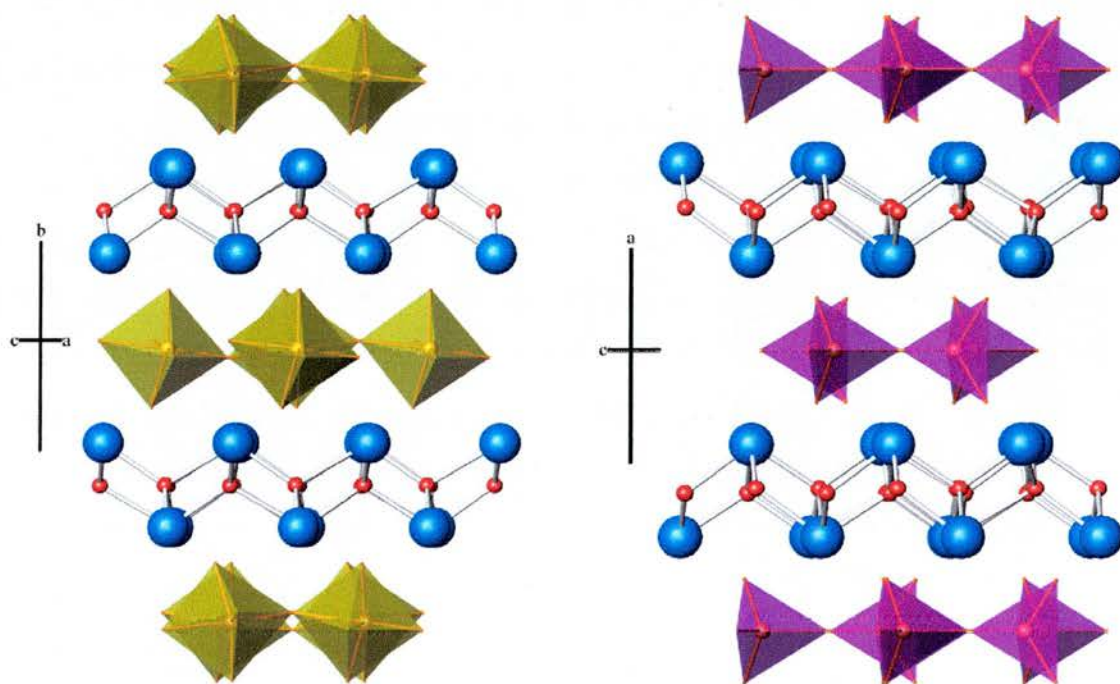


Figure 1.5: Bi_2WO_6 [26] and Bi_2GeO_5 [27] structures, Bi in blue, O in red, WO_6 octahedra in yellow, GeO_4 tetrahedra in purple

Occupancy of the B-site in the 1-layer Aurivillius phases is not limited to just the W^{6+} and Mo^{6+} cations as might be expected. There are other struc-

tures where Ge^{4+} or Si^{4+} [28] occupies the B-site. Here the structure must incorporate oxygen vacancies to achieve a charge balance, this is achieved by creating a series of connected tetrahedra instead of octahedra. The tetrahedral coordination would be expected for the Ge^{4+} and Si^{4+} , which are not normally found octahedrally coordinated. In the earlier paper and in a later combined refinement and simulation study[27], the space group is defined as $\text{Ccm}2_1$. $\text{Ccm}2_1$ is the standard setting of the $\text{A}2_1\text{am}$ space group, however, $\text{A}2_1\text{am}$ is used conventionally, to preserve a as the polar axis. Also found in the B-site is the V^{5+} cation, in the $\text{Bi}_2\text{VO}_{5.5}$ phase[29]. This structure has led to other structures where the B-site cation is partially filled by transition metal cations, possible as one of the sites is now tetrahedrally coordinated[30]. Some structures are reported with halide anions[31]. These structures are known as the BiMeVOX series, and can be thought of as a defect 1-layer Aurivillius structure. That work is not discussed in detail here.

2-Layer Phases

There are considerably more 2-layer phases than 1-layer phases, due to the increase in the combinations of cations that can give charge balance. The most investigated 2-layer structures are based around $\text{SrBi}_2\text{Ta}_2\text{O}_9$ (SBT). This structure was the first Aurivillius phase to be identified as a ‘fatigue free’ ferroelectric for use in non-volatile FeRAMs[8]. This compound, and indeed almost all other 2-layer Aurivillius phases, match to the space group proposed by Newnham et al.[22], $\text{A}2_1\text{am}$. From the $\text{SrBi}_2\text{Ta}_2\text{O}_9$ composition research has been done to investigate the effect of the A-site and B-site cation on both structure and T_C (see Chapter 2 for an explanation of T_C).

Prior work has been carried out on the nominal composition $\text{Sr}_{0.8}\text{Bi}_{2.2}\text{Ta}_2\text{O}_9$ [32]. Examining the structural data given the composition actually appears to be $\text{Sr}_{0.82}\text{Bi}_{2.12}\text{Ta}_2\text{O}_9$, which is an A-site deficient structure. In this case the crystallographic interest is two-fold, firstly, where are the vacancies? Secondly, is there any disorder of the Sr and Bi? The structure given has a purely Bi-containing $[\text{Bi}_2\text{O}_2]$ layer, with a perovskite A-site composition of 0.82 Sr / 0.12 Bi / 0.06 vacancy. This structure, whatever doubts there may be about its composition, possesses a larger spontaneous polarisation, a larger dielectric constant and a higher T_C than SBT. In an attempt to understand the underlying crystal chemistry of the ferroelectric phase change, a sample of $\text{Sr}_{0.85}\text{Bi}_{2.1}\text{Ta}_2\text{O}_9$ [33] was examined using both a.c. impedance and variable temperature powder neutron diffraction. The ferroelectric phase change appears to be at $T_C = 375\text{ }^\circ\text{C}$ from a.c. impedance. The structure at room temperature and up to $350\text{ }^\circ\text{C}$ was refined as $A2_1am$, above T_C it was refined as $Amam$ and then at $550\text{ }^\circ\text{C}$ a second phase change to the tetragonal $I4/mmm$ was observed.

Investigations into the effect of the divalent cation on the structure and ferroelectric properties of the 2-layer phases has been explored. In one study[34] the crystal structures of $\text{ABi}_2\text{Ta}_2\text{O}_9$ ($A = \text{Ca}, \text{Sr}$ and Ba) were examined, and can be rationalised in terms of size matching of the fluorite and the perovskite blocks. The Ca and Sr containing phases were found to be present in $A2_1am$, but the Ba phase was described as $I4/mmm$ at room temperature. Most probable is that at some lower temperature the structure of $\text{BaBi}_2\text{Ta}_2\text{O}_9$ transforms to $A2_1am$, and that its T_C is below room temperature. A second study[35] using synchrotron X-ray diffraction established the extent of cation

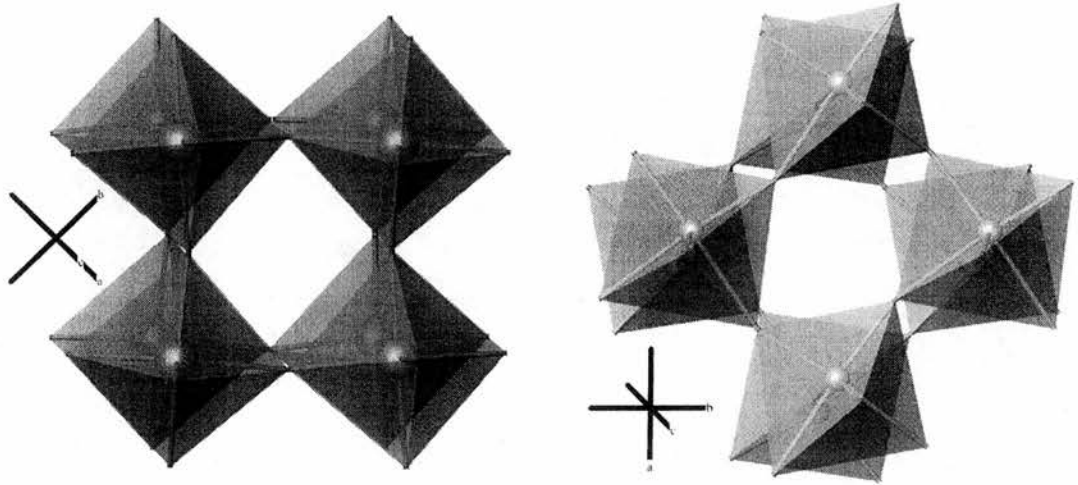


Figure 1.6: $\text{SrBi}_2\text{Ta}_2\text{O}_9$ and $\text{Bi}_2\text{W}_2\text{O}_9$ perovskite blocks viewed down the c -axis, SBT left, BWO right

disorder between the $[\text{Bi}_2\text{O}_2]$ layer and the perovskite A-site. The amount of disorder was found to increase with ionic radius, Ca with the least disorder, Ba with the most. This agrees with an earlier study on the analogous $\text{ABi}_2\text{Nb}_2\text{O}_9$ ($A = \text{Ca}, \text{Sr}, \text{Ba}$)[36]. The Nb^{5+} containing phases have also been studied to examine the effect of quenching on the cation distribution[37] and the cation disorder of Pb and Sr in $\text{Pb}_x\text{Sr}_{1-x}\text{Bi}_2\text{Nb}_2\text{O}_9$ [38].

Two-layer structures with no divalent cation have been examined structurally. The composition $\text{Bi}_3\text{TiNbO}_9$ was reported by Thompson and co workers[5], the structure was found to adopt the $A2_1am$ space group. This results in no ordering of perovskite blocks with Ti^{4+} and Nb^{5+} , as there is

only one crystallographic site. The A-site and interlayer are both by necessity completely Bi^{3+} . A more unusual 2-layer phase is $\text{Bi}_2\text{W}_2\text{O}_9$. This can be regarded as an Aurivillius phase in which the perovskite A-site is vacant, analogous to the ReO_3 structure. The structure was confirmed using single crystal X-ray diffraction, the space group being assigned as $\text{Pna}2_1$ [39]. Importantly, it is different to $\text{A}2_1\text{am}$, as reported for other 2-layer phases, in two key respects, firstly, rotations of the octahedra are different along c ; in $\text{A}2_1\text{am}$ they are in-phase but in $\text{Pna}2_1$ they are out of phase. Secondly the polar axis is c , rather than a , although $\text{Bi}_2\text{W}_2\text{O}_9$ was not seen to be ferroelectric.

3-Layer Phases

The 3-layer Aurivillius phases can be thought of as being based on the $\text{Bi}_4\text{Ti}_3\text{O}_{12}$ composition. This structure adopts the space group $\text{B}2\text{cb}$ at room temperature, as predicted[22], and transforms to $\text{I}4/\text{mmm}$ at $T_C = 675^\circ\text{C}$, with no intermediate phase transitions[40], as shown in Figure-1.7. The composition can be altered to attempt to induce different distortions. This can be done by replacing Bi^{3+} by a divalent cation and Ti^{4+} by either Nb^{5+} or Ta^{5+} . The original work on this was done by Aurivillius[2] and it details also the possibility of phases with $x > 0$ for the solid solution $\text{Bi}_{2-x}\text{Sr}_{2+x}\text{Ti}_{1-x}\text{Nb}_{2+x}\text{O}_{12}$. More recent work proposed compositions of up to $x = 0.6$ [41] in the series. A detailed neutron powder refinement for the composition $\text{Bi}_{1.8}\text{Sr}_{2.2}\text{Ti}_{0.8}\text{Nb}_{2.2}\text{O}_{12}$ was performed. This refinement gave a tetragonal structure in $\text{I}4/\text{mmm}$ with some A-site cation disorder. Also reported in the same paper are the X-ray refinements of $\text{Bi}_3\text{LaTi}_3\text{O}_{12}$ and

$\text{Bi}_2\text{La}_2\text{Ti}_3\text{O}_{12}$, both structures being given as $I4/mmm$. Earlier work by Wolfe and Newnham[42] gives solution limits, as given in Table-1.1, for the insertion of several rare earths into the $\text{Bi}_{4-x}\text{R}_x\text{Ti}_3\text{O}_{12}$.

Table 1.1: Rare Earth Solution Limits into $(\text{Bi}_2\text{O}_2)\text{R}_2\text{Ti}_3\text{O}_{12}$

Element	La	Pr	Nd	Sm	Eu	Gd	Tb
Solution Limit (x)	2.8	2.5	.24	2.0	2.0	1.4	1.0

Element	Dy	Ho	Er	Tm	Yb	Lu
Solution Limit (x)	1.0	0.6	0.4	0.2	0.1	0.1

Only one structural report has been produced of an oxygen deficient Aurivillius phase (with n greater than 1), $\text{Bi}_2\text{Sr}_2\text{Nb}_2\text{MnO}_{12-\delta}$ [43]. This structure is given as being orthorhombic $Fmmm$ with ordered Bi^{3+} and Sr^{2+} , i.e. Bi^{3+} in the $[\text{Bi}_2\text{O}_2]$ layer and Sr^{2+} in the perovskite A-site. The Nb^{5+} and Mn^{3+} are suspected to be ordered, so the Nb^{5+} is in the outer perovskite layer and Mn^{3+} is in the inner site. The MnO_x layer is also where the oxygen vacancies are proposed. The temperature dependance of resistivity and the magnetic susceptibility are also given. However, since the structure refinement has been performed using powder X-ray diffraction, the assignment of the $Fmmm$ space group may be incorrect and the oxygen vacancies are difficult to locate in the presence of Bi^{3+} .

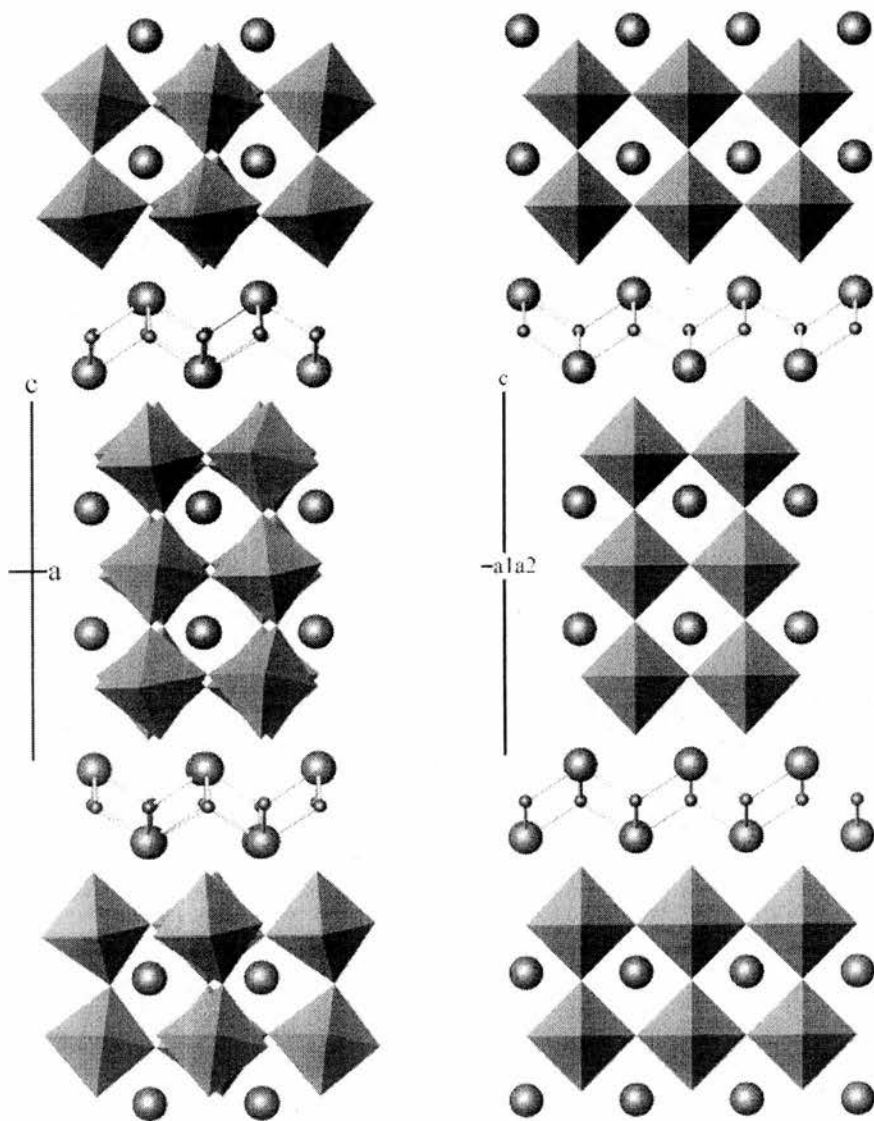


Figure 1.7: $\text{Bi}_4\text{Ti}_3\text{O}_{12}$; left, $B2cb$ 25 °C structure and right, $I4/mmm$ 800 °C structure

4-layer Phases

There are very few reports of 4-layer Aurivillius phases, one is the single crystal structure of the 4-layer Aurivillius phase $\text{Bi}_5\text{Ti}_3\text{FeO}_{15}$ by Kubel and Schmid[44]. In this study the space group $\text{Fm}2\text{m}$ was assigned to the room temperature phase. Two phase transitions were also proposed, the higher temperature of which was suggested to be the ferroelectric transition. Both this transition and the space group are unusual for even-layered Aurivillius phases. The use of X-ray radiation limits the ability to correctly identify the oxygen atomic positions thus limiting the ability to correctly identify the phase transitions taking place. This is why neutron diffraction is preferred over X-ray diffraction for these materials. Work performed here can be found in Chapter 3.

Mixed Layer Aurivillius Phases

Aurivillius phases can be found not only as structures with n layers of perovskite separated by the $[\text{Bi}_2\text{O}_2]$ layer. It is possible to intergrow perovskite blocks of different sizes to produce compositions $(\text{A}_{n-1}\text{B}_n\text{O}_{3n+1}) [\text{Bi}_2\text{O}_2] (\text{A}_n\text{B}_{n+1}\text{O}_{3(n+1)+1}) [\text{Bi}_2\text{O}_2]$, i.e. the two perovskite blocks may only differ by one layer. This is clear, as an attempt to make a 2 and 4-layer intergrowth phase would more likely result in a 3 layer phase[45]. These phases are written as Ax Ay , to indicate the alternating number of layers, x and y , in the perovskite blocks.

The $\text{A}_2 \text{A}_3$ phases are the most reported of the mixed layer compounds. Compositions tend to be intergrowths of $\text{Bi}_4\text{Ti}_3\text{O}_{12}$ and a two layer phase

such as $\text{BaBi}_2\text{Nb}_2\text{O}_9$. These phases have been studied mainly by high resolution electron microscopy. More recent crystallographic studies have been performed on these phases using both powder X-ray diffraction and powder neutron diffraction. A recent investigation focussed on the composition $\text{Bi}_7\text{Ti}_4\text{NbO}_{21}$, nominally an intergrowth of $\text{Bi}_4\text{Ti}_3\text{O}_{12}$ and $\text{Bi}_3\text{TiNbO}_9$. The resultant phase is known to be a ferroelectric material and therefore could only be described in a polar space group. The space group which has been selected by a combined single crystal X-ray, neutron and electron diffraction study[46], is $I2cm$, a non standard version of $Ima2$. Due to the presence of the body centering the unit cell has a c -axis equal to the sum of the two constituent cells. For Aurivillius phases with only one size of perovskite block there needs to be two perovskite and two fluorite layers in the unit cell. This occurs as the two fluorite layers will 'point' in opposing directions. For the mixed-layer structures there is required a minimum of two fluorite layers and one perovskite block of each size. The expected cell of this would have a c -axis half the length of the sum of the two intergrown compositions. A cell with the c -axis length the sum of the two intergrown compositions will contain four fluorite units and two perovskite units of each size. The ferroelectric nature of $\text{Bi}_7\text{Ti}_4\text{NbO}_{21}$ is expected to be caused by octahedral distortions in the perovskite blocks. This is indeed found to be the case.

In the 3-layer perovskite block the rotation is in antiphase along c , but, in the 2-layer block it is in-phase. This ordering of the rotations along c is the same as is found for the two separate intergrown structures. It is also found that the Nb^{5+} is located solely on the B-site in the 2-layer block, and is not spread over the B-sites in the 3-layer block. This would indicate that the

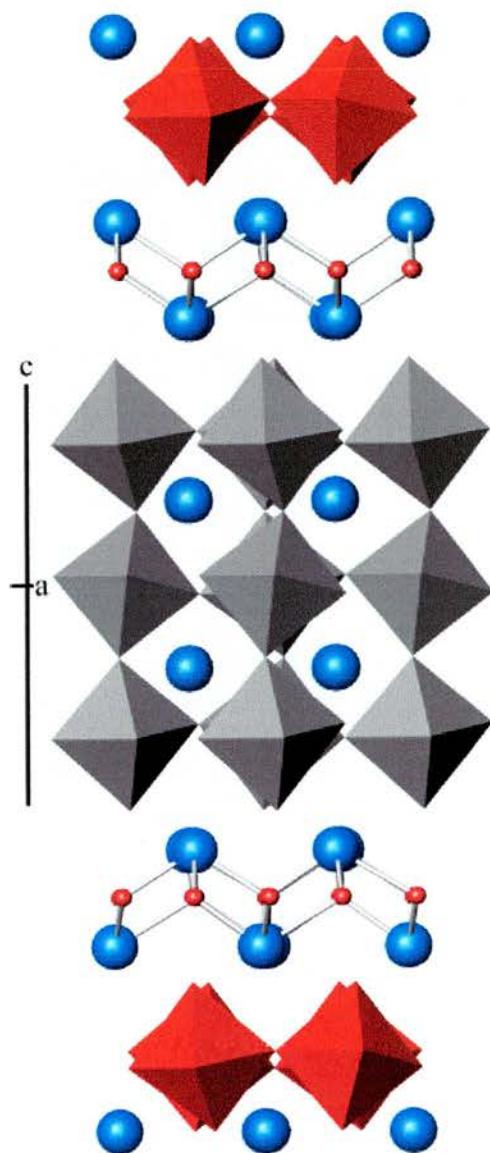


Figure 1.8: $\text{Bi}_7\text{Ti}_4\text{NbO}_{21}$ structure, Bi in blue, O in red, TiO_6 octahedra in grey, $(\text{Nb}_{0.5}\text{Ti}_{0.5})\text{O}_6$ octhedra in red

theoretical composition of the two Aurivillius phases being intergrown are retained. The structure is given in Figure-1.8.

Recent work has examined the structure of the composition $\text{Bi}_7\text{Ti}_{4.5}\text{W}_{0.5}\text{O}_{21}$ [47].

This structure is identified in the $P2_1am$ space group with the c -axis equal to the two intergrown phases. This is incongruous as the removal of body centring should result in the c -axis not being required to be doubled. It is noted that this study is a powder X-ray diffraction study and this could be the cause for this confusion. Also reported is the presence of two peaks in the dielectric permittivity versus temperature. This could initially be thought of as being due to the presence of another phase, for example one or both of the two intergrown compositions. The dielectric response versus temperature is also given for the two intergrown Aurivillius phases, it is clear that these do not coincide with the peaks from the mixed layer phase. The evidence presented does, however, leave several unanswered questions about the ferroelectric properties and the phase purity.

1.2.2 Ruddlesden-Popper Phases

The Ruddlesden-Popper phases arose from research into what was known as the K_2NiF_4 structure, layers of corner-sharing NiF_6 octahedra with rocksalt-like interlayers containing potassium. Attempts to make oxide variants of these resulted in the successful preparation of compositions Sr_2TiO_4 , Ca_2MnO_4 and SrLaAlO_4 [48]. With the successful structure determination of the $\text{Sr}_3\text{Ti}_2\text{O}_7$ phase in 1958 [49] it became apparent that this would give rise to a larger family of layered perovskites, general formula $\text{M}_2'[\text{A}_{n-1}\text{B}_n\text{O}_{3n+1}]$.

1-Layer Phases

Soon after the early work of Ruddlesden and Popper the indexing of other single layer phases was completed. The phases of composition NaLnTiO_4 were reported[50], the a parameter was found to increase and the c -axis to decrease with decreasing lanthanide ionic radius. This occurs as the decrease in the c -axis length is caused by distortions in the B-site cation environment, with apical bond lengths decreasing, equatorial bond lengths increase, leading to the increase in length of the a -axis. The volume of the unit cell is decreasing as would be expected with decreasing ionic radius.

There have been attempts to ion-exchange H^+ into the structure of NaYTiO_4 [51], to introduce Ca into $\text{Na}_{1-x}\text{Ca}_x\text{LaTiO}_4$ [52] and to prepare MLaTiO_4 ($M = \text{Li, Na, K}$) by hydrothermal synthesis[53], but these studies do not provide structural data. In 1996 a report on the structures of NaLnTiO_4 ($\text{Ln} = \text{La, Pr, Nd, Sm, Eu, Gd}$ and Y)[54] suggested the structures of the early lanthanides as tetragonal, space group $P4/nmm$. The later lanthanides such as Eu, Gd and Y (classed here by its ionic radius) were not tetragonal and were indexed as orthorhombic, space group $Pbcm$. The difference between these structures is shown in Figure-1.9. This X-ray study still remains the most complete to date of the Ti^{4+} containing phases.

There was considerable interest in the Ru^{4+} containing phases when Sr_2RuO_4 was found to be a very low temperature (1 K) superconductor[55]. This prompted a lot of interest in the magnetic structure of this and related compounds[56]. That work is not discussed here as it is not pertinent to the content of this study.

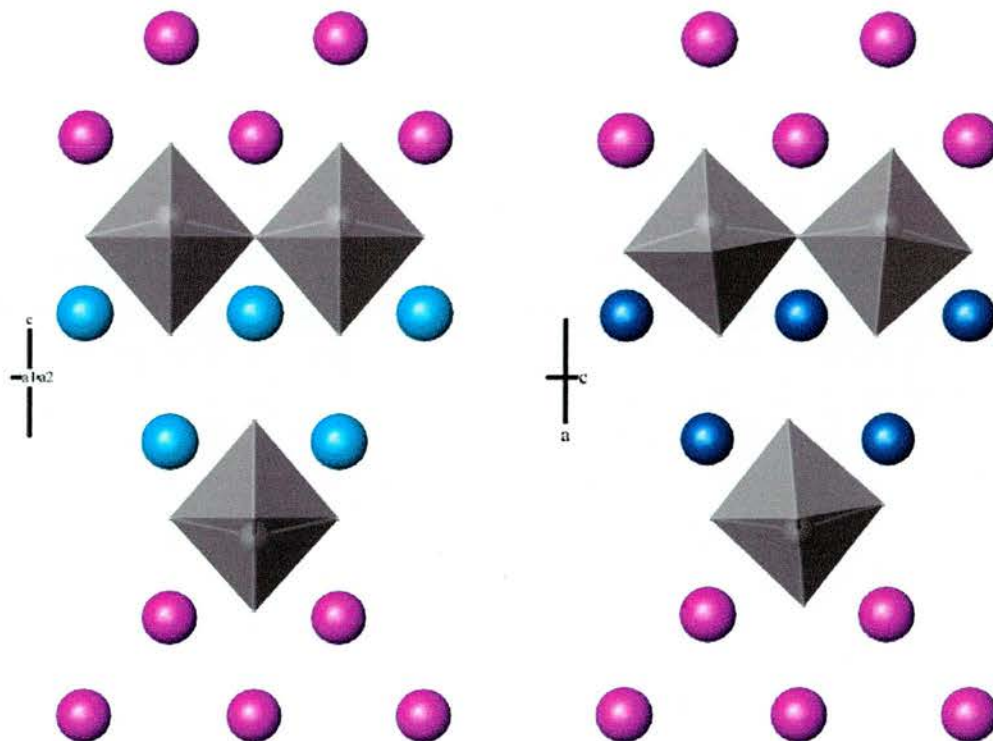


Figure 1.9: NaLaTiO_4 (left) and NaEuTiO_4 (right) structures, Na is purple, La is light blue, Eu is dark blue, TiO_6 octahedra in grey. Note the off-centre displacements of the Ti towards the Na containing layer.

2-Layer Phases

The report of the $\text{Sr}_3\text{Ti}_2\text{O}_7$ 2-layer phase[49] was the first of many 2-layer phases, most of the publications have however not been focussed on phases containing Ti^{4+} . One notable report details the structure of both $\text{Sr}_3\text{Ti}_2\text{O}_7$ and $\text{Ca}_3\text{Ti}_2\text{O}_7$ by electron and neutron diffraction[57]. This describes the Sr phase in the tetragonal, $I4/mmm$, space group with the Ca phase in $\text{Cmc}2_1$. $\text{Cmc}2_1$ is equivalent to $A2_1am$, therefore the rotations of the octahedra in

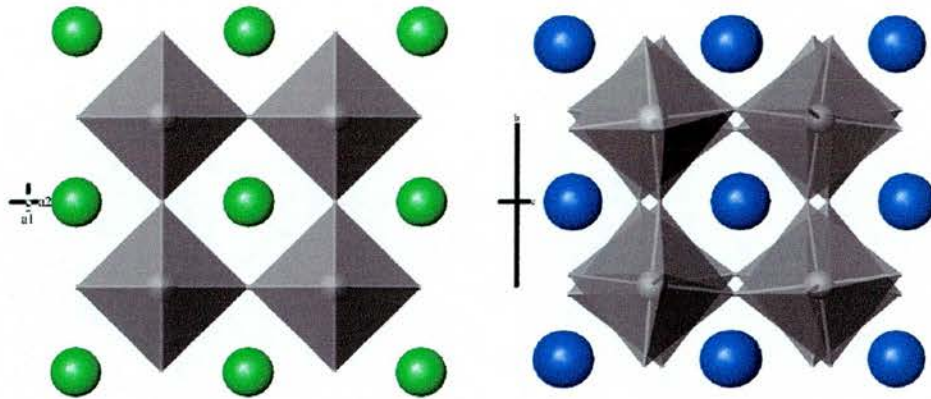


Figure 1.10: $\text{Sr}_3\text{Ti}_2\text{O}_7$ (left, tetragonal $I4/mmm$) and $\text{Ca}_3\text{Ti}_2\text{O}_7$ (right, orthorhombic $Ccm2_1$) perovskite blocks Sr is green, Ca is blue and TiO_6 octahedra are grey

the $\text{Ca}_3\text{Ti}_2\text{O}_7$ structure are analogous to those found in 2-layer Aurivillius phases.

Most of the work reported on 2-layer Ruddlesden-Popper phases has been done on samples containing Fe[58], Fe and Ru[59,] or Mn[60, 61, 62]. These samples have been studied as they have been found to possess Colossal Magnetoresistance (CMR), a property useful in applications such as computer hard disk read heads. Also known for 2-layer Ruddlesden-Popper phases are $\text{K}_2\text{SrTa}_2\text{O}_7 \cdot m\text{H}_2\text{O}$ ($m = 0, 2$)[63] and the potential of ion exchanging the K^+ for H^+ to give proton conductors[64]. Work on these proton conductors is at an early stage and structural elucidation is hampered by the potential presence of disordered water.

3-Layer Phases

Structural work on the the 3-layer examples of the Ruddlesden-Popper phases are the most prevalent. In the same paper that details the structure of $\text{Sr}_3\text{Ti}_2\text{O}_7$ and $\text{Ca}_3\text{Ti}_2\text{O}_7$ [57], the structures of $\text{Ca}_4\text{Ti}_3\text{O}_{10}$ (shown as Figure-1.11) and $\text{Ca}_{3.6}\text{Sr}_{0.4}\text{Ti}_3\text{O}_{12}$ are also discussed. Both are refined as orthorhombic $Pcab$ structures, but it is noted that a 2-layer impurity phase is present in each refinement. For the Mn analogue $\text{Ca}_4\text{Mn}_3\text{O}_{10}$ the structure has been refined as $Pbca$ [65]. This is the same space group with the cell reset so that the c -axis is the longest axis, unlike the $Pcab$ structures. The room temperature structures of $\text{Ca}_4\text{Mn}_2\text{FeO}_{9.75}$ and $\text{Sr}_4\text{Mn}_2\text{FeO}_{9.8}$ have been analysed[66] using powder neutron diffraction and are given as $I4/mmm$. In this work the key points are the ordering of the B-site cations and the location of the oxygen vacancies. The oxygen vacancies are identified around the Fe^{3+} sites, the Fe^{3+} is disordered over both sites, but has a slight preference for the inner octahedral site.

In the three layer phases there is a rapidly expanding interest in the phases which have alkali metal cations in the interlayer and lanthanides in the perovskite A-site. The size and charge discrepancy between these two cations results in ordering of the sites. In a powder neutron diffraction study on $\text{Na}_2\text{La}_2\text{Ti}_3\text{O}_{10}$ [67] this ordering was observed and the structure was recorded as a tetragonal cell with space group $I4/mmm$, see Figure-1.11. Reports of 3-layer Ruddlesden-Popper phases which contain iron, ruthenium or manganese are very few. However, Ru^{4+} has been inserted into the $\text{Na}_2\text{La}_2\text{Ti}_{3-x}\text{Ru}_x\text{O}_{10}$ structure[68]. The structure retains the parent structure's $I4/mmm$ symme-

try. The Ru^{4+} inserts into both perovskite sites although there is a preference for the inner perovskite site. Work inserting Mn^{4+} , producing phases of composition $\text{Na}_2\text{Ln}_2\text{Ti}_{3-x}\text{Mn}_x\text{O}_{10}$ ($\text{Ln} = \text{Sm}, \text{Eu}, \text{Gd}$ and Dy)[69] has been explored. In this work the authors detail the formation of 28 3-layer phases, in some of these phases the Na^+ has been ion-exchanged and replaced with Li^+ or NH_4^+ . The paper produces no full structural refinements, however, lattice parameters have been given. For all 28 phases the patterns have been indexed as tetragonal with the a parameter approximately twice that of the ideal value at 7.5 Å. This indexing is unlikely for the tetragonal cell. It would appear that either the samples are orthorhombic and distorted or impure. Interest in the 3-layer Ruddlesden-Popper phases with alkali metals as the interlayer and lanthanides as the perovskite A-site have been widely studied. The main interest is in their potential for ion exchange to introduce layers of protons. The materials themselves have also been studied for their intrinsic ionic conductivity. A study examining the effect of various lanthanides on the structure and ionic conductivities of the 3-layer structures was performed[70]. From this study it was found by powder X-ray diffraction that the structures are all tetragonal, $I4/mmm$, for $\text{Ln} = \text{La}, \text{Nd}, \text{Sm}$ and Gd and that the cell volume decreased with the ionic radius of the lanthanide. The decrease in lanthanide ionic radius was accompanied by an increase in the ionic conductivity of the material. Work on confirming the structure of the 3-layer phases obtained by powder X-ray diffraction has been done by employing powder neutron diffraction[71]. The neutron diffraction of $\text{A}_2\text{La}_2\text{Ti}_3\text{O}_{10}$ ($\text{A} = \text{Na}, \text{K}, \text{Rb}$) yields the tetragonal $I4/mmm$ space group with no interlayer / A-site disorder. Ionic conduction is assumed to take place within the interlayer

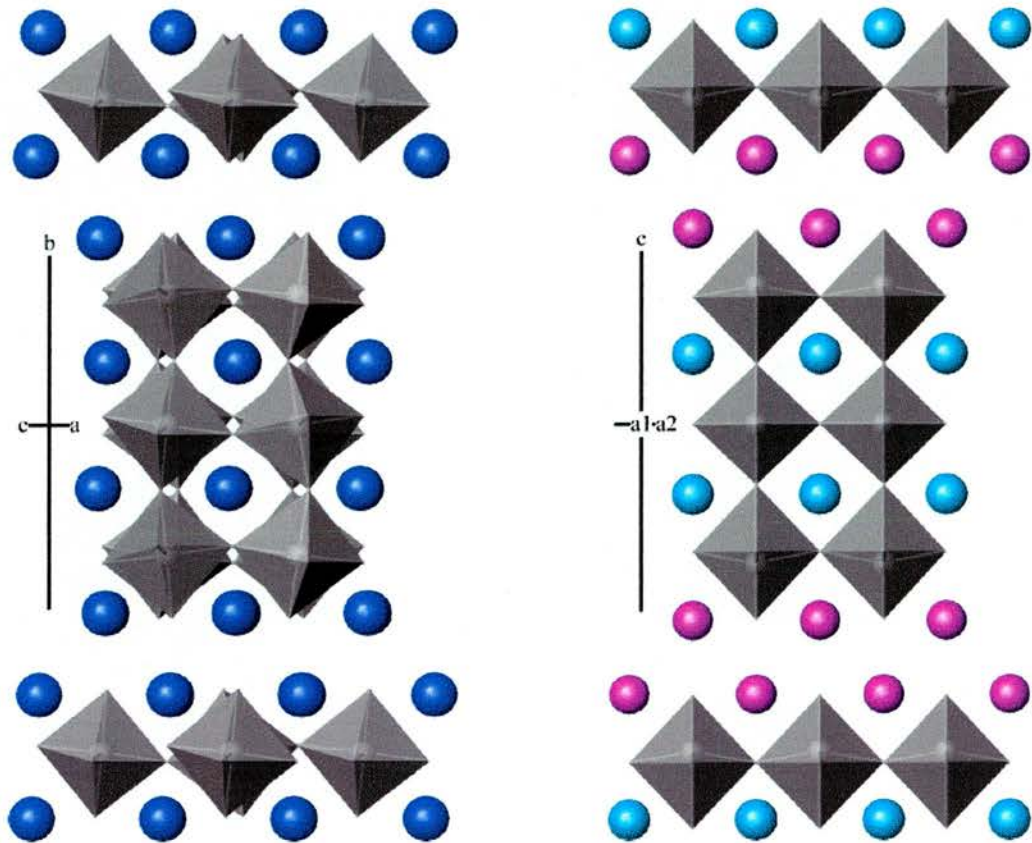


Figure 1.11: $\text{Ca}_4\text{Ti}_3\text{O}_{10}$ (left, $Pcab$) and $\text{Na}_2\text{La}_2\text{Ti}_3\text{O}_{10}$ (right, $I4/mmm$), Na is light purple, La is light blue, Ca is dark blue and TiO_6 octahedra are in grey

and not through the perovskite block. Further studies examining proton conduction[72], the structure of $\text{Li}_2\text{La}_2\text{Ti}_3\text{O}_{10}$ [73], Nd containing phases[74] and $\text{Rb}_2\text{La}_2\text{Ti}_3\text{O}_{10}$ [75], have all been reported widening the areas of interest in these phases. There has also been reported the structure both hydrated and dehydrated of $\text{K}_2\text{Sr}_{1.5}\text{Ta}_3\text{O}_{10}$ [76], the dehydrated structure again being identified as the tetragonal $I4/mmm$ structure. Work has also been performed to ion-exchange these structures[77].

The 3-layer alkali metal-containing structures are predominantly reported as $I4/mmm$. Some structures, particularly K^+ containing phases, appear to be hydrated. Work continues on both the CMR and ionic conduction properties of the Ruddlesden-Popper phases.

1.2.3 Dion-Jacobson Phases

The Dion-Jacobson phases[78, 79] are closely related to the Ruddlesden-Popper phases, having a general formula $\text{A}'[\text{A}_{n-1}\text{B}_n\text{O}_{3n+1}]$. Instead of a double layer of monovalent interlayer cations there is a single layer of monovalent interlayer cations. Like the Ruddlesden-Popper phases the interlayer cations are alkali metals, however due to there only being a single layer of cations it is possible for some of the larger group 1 metals to be accommodated. There are documented no occurrences of any 1-layer Dion-Jacobson phases, the projected formula of this being $\text{A}'\text{B}^{VII}\text{O}_4$. There are no suitable B site cations available for this formula, which would adopt octahedral symmetry.

2-Layer Phases

The smallest cation to be inserted into the interlayer of the Dion-Jacobson phases by solid state sintering is K^+ , as shown in $NaLaNb_2O_7$ [80], where the Na phases can only be produced via ion-exchange. The $NaLaNb_2O_7$ phase is not found until it is heated to above 250 °C to fully dehydrate the sample, which contains $16H_2O$ at room temperature. Examining the structure shown by Toda et al.[73] and the atomic co-ordinates it is clear that there exists two layers of Na^+ , which are apparently only partially occupied. One of the layers is assigned as also possessing oxygen from the water molecules. This hydrated interlayer structure bears close resemblance to the Ruddlesden-Popper interlayer structure. The dehydrated phase, however, appears unambiguously to be a Dion-Jacobson interlayer structure and has been assigned $I4/mmm$ symmetry. The perovskite blocks are arranged so that the octahedra are staggered, $1/2$ along a and $1/2$ along b as shown in Figure-1.12. The ability of the Dion-Jacobson phases to have the perovskite blocks staggered or eclipsed is not found in either the Ruddlesden-Popper or Aurivillius phases.

The next larger of the alkali metals, K^+ , can be inserted into the Dion-Jacobson family of structures and its ability to ion-exchange with H^+ has been reported[81]. The structure of $KLaNb_2O_7$ was reported by Sato et al.[82] as a slightly orthorhombic structure with a/b unit cell parameters still approximately 3.9 Å. This unusual distortion and the selection of the $C222$ space group would make it seem as if either the structure is hydrated, or that there is a subtle supercell distortion in the structure that cannot be

correctly assigned using powder X-ray diffraction. The assignment of the staggering of the perovskite blocks is possible using powder XRD and the structure appears to have the octahedra staggered along only one of the two shorter axes, shown as Figure-1.12, as opposed to two for the Na^+ analogue.

The Rb^+ containing $\text{RbLaNb}_2\text{O}_7$ [83] is considered the most reliable of the structures published due to it's having been performed using powder neutron diffraction. This resulted in a centrosymmetric orthorhombic structure, assigned the space group Imma . The orthorhombic distortion of this structure is very small and it is doubtful it could have been observed using powder X-ray diffraction. In this structure the octahedra in the perovskite blocks are not staggered along either of the shorter axes but are instead eclipsing each other. For $\text{CsLaNb}_2\text{O}_7$ [84] the compound was identified as P4/mmm , a tetragonal phase. As found for the Rb^+ containing phase the perovskite blocks are eclipsed, as shown in Figure-1.12.

It may be that the lack of distortion for the Na^+ and Cs^+ samples reflect their bonding stability in their environments. Or, the K^+ and Rb^+ sites are both strained in their bonding environments and require distortions of the perovskite block help reduce that strain. The distortions and staggering of the perovskite blocks can be examined using the bonding requirements of the interlayer cations which are dictated by cation size. The Na^+ cation is bound to four oxygen atoms in a tetrahedral arrangement. The K^+ cation is bound to six oxygens. It is a prism so the structure is bound to four oxygen atoms in one block and two in the other. The Rb^+ and Cs^+ cations are bound to eight oxygen atoms, four above and four below, in a cubic arrangement, and

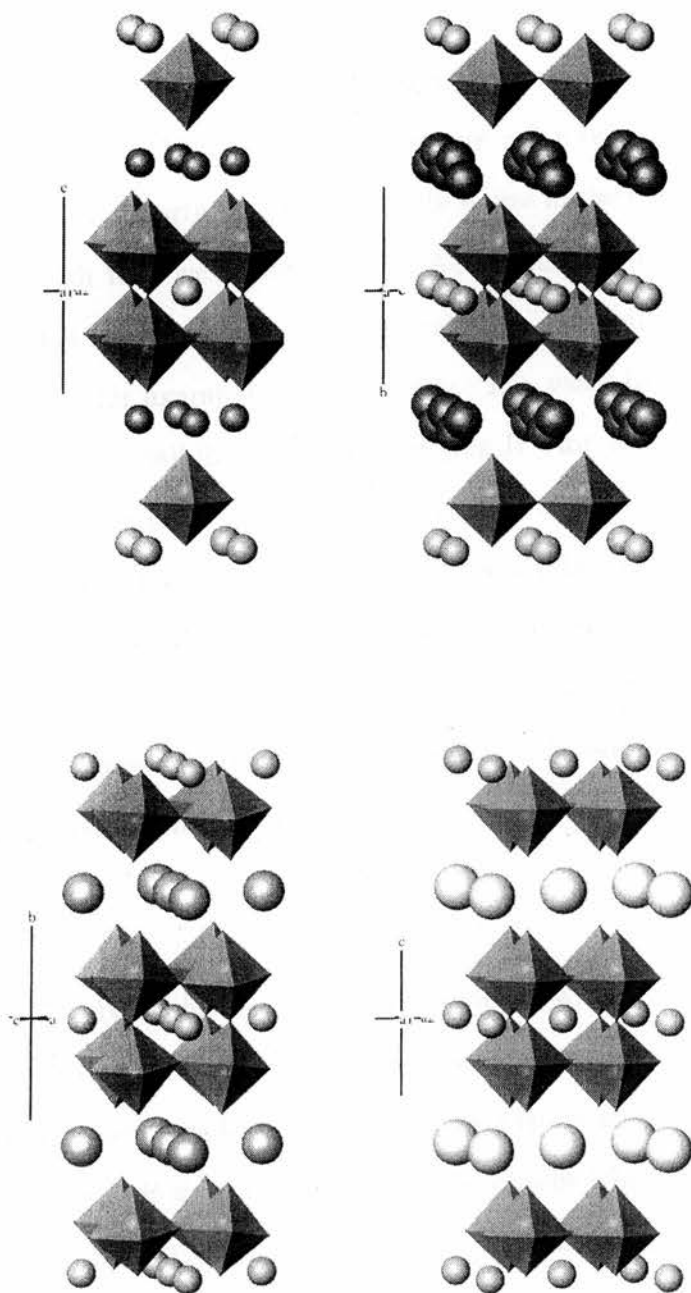


Figure 1.12: Structures of $\text{NaLaNb}_2\text{O}_7$ (top left), KLaNb_2O_7 (top right), $\text{RbLaNb}_2\text{O}_7$ (bottom left), $\text{CsLaNb}_2\text{O}_7$ (bottom right), showing the effect of the cation size on the arrangement of the perovskite block.

so the perovskite blocks are eclipsed.

Also mentioned for the 2-layer Dion-Jacobson phases is a report of indexings of ABiNb_2O_7 ($A = \text{Rb}$ or Cs)[85]. These structures are interesting as the Bi^{3+} cation has not been reported at the perovskite A-site in the Ruddlesden-Popper phases, though it is well known in the Aurivillius phases. The insertion of Bi^{3+} and its lone-pair into the perovskite A-site could result in interesting properties, for example ferroelectricity. The work by Subramanian et al. reports the possibility of ion-exchanging H^+ for Rb^+ and Cs^+ . The study focuses on the ionic conduction capabilities of the materials, no mention is made of any ferroelectric properties. The analysis of the structures only proceeds as far as the identification of lattice parameters. These are orthorhombic with the a and b axes at approximately twice that of the tetragonal parent. It is unlikely that this indexing is correct. A re-examination of this work is performed in Chapter 6.

3-Layer Phases

The 3-layer Dion-Jacobson phases can have compositions with divalent cations in the perovskite A-site and hence the B-site is occupied totally by Nb^{5+} or Ta^{5+} . They can also have trivalent cations occupying the A-site and are then of mixed valence in the B-site. In the case of the phases where the B-sites are totally occupied by either Nb^{5+} or Ta^{5+} , the structures are not complicated by issues of B-site cation ordering. The structures of the compounds $\text{ACa}_2\text{Ta}_3\text{O}_{10}$ ($A = \text{Li}, \text{Na}, \text{K}, \text{Rb}$ and Cs)[86] have been examined, the coordination of the interlayer cations follows the same pattern as found in the 2-layer structures. In addition Li^+ is found to occupy the same tetragonal

co-ordination as Na^+ . The alkali metal bonding environments are shown as Figure-1.13. In another study the structure of $\text{KCa}_2\text{Nb}_3\text{O}_{10}$ [87] is described as orthorhombic, space group Cmcm , different to the Ta^{5+} analogue. The structure is also given with the c -axis as twice that of the tetragonal parent, an unlikely possibility. However, the environment around the K^+ is similar to that of the Ta^{5+} variant. These phases, as for most of the Dion-Jacobson structures, have been examined for their ionic conductivity, either the alkali metal containing compounds[88, 89] or the ion-exchanged proton containing phases[90].

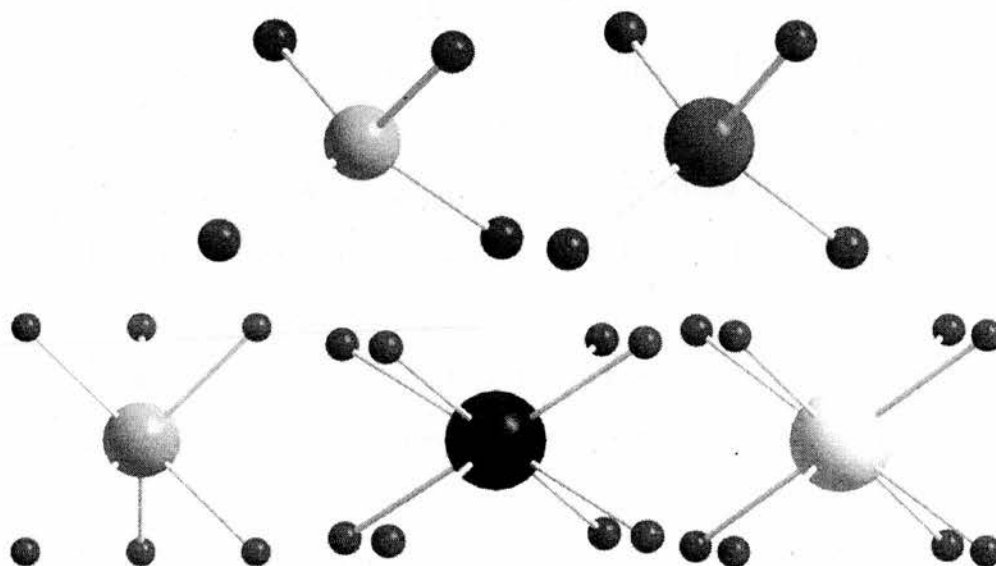


Figure 1.13: Alkali metal bonding environments in 3-layer phases; Li, top left; Na, top right; K, bottom left; Rb, bottom middle; Cs, bottom right

For the 3-layer structures where the B-site is occupied by both Ti^{4+} and Nb^{5+} or Ta^{5+} , the structure has the potential to be ordered in the B-sites. Three

possible alternatives were highlighted by Hong and co-workers[91]. Firstly, that the structure may be disordered over the two sites, such that both the inner and outer octahedra are occupied by $1/3 \text{ Ti}^{4+}$ and $2/3 \text{ Nb}^{5+}$. Secondly, the structure may be ordered, with all of the Nb^{5+} in the inner octahedra and all of the Ti^{4+} in the outer octahedra. Lastly, the structure may be ordered, with the inner octahedra occupied solely by Ti^{4+} and the outer octahedra $1/2 \text{ Ti}^{4+}$ and $1/2 \text{ Nb}^{5+}$. For the structure $\text{CsLa}_2\text{Ti}_2\text{NbO}_{10}$ the octahedra were found to be occupied in the third way; with the inner site Ti and the outer octahedra occupancy split evenly, shown in Figure-1.14. The structure is also given as tetragonal $I4/mmm$. This ordering is peculiar to the Dion-Jacobson phases, as the Aurivillius and Ruddlesden-Popper phases do not demonstrate this definite ordering. The same ordering was observed for the $\text{RbLa}_2\text{Ti}_2\text{NbO}_{10}$ structure[92]. In another paper Hong et al. discuss the Ta^{5+} analogues of the two previous compounds[93], again they are found to exhibit the ordering of the B-site cation.

The $\text{NaLa}_2\text{Ti}_2\text{TaO}_{10} \cdot x\text{H}_2\text{O}$ ($x = 2, 0.9, 0$) structure was examined and it was found to exist with varying water content at varying temperatures. The fully dehydrated form is $I4/mmm$, the $x = 0.9$ form is $P4/mmm$ and the $x = 2$ form is $I4/mmm$. This loss and regaining of the body-centering is unusual, but may be explained by the ordering of the water towards saturation and then loss of ordering at lower x . A similar two stage loss of water is found for the lanthanide series $\text{NaLn}_2\text{TiNb}_2\text{O}_{10}$ ($\text{Ln} = \text{La, Pr, Nd, Sm}$)[94], the structures are also identified as initially $I4/mmm$, then $P4/mmm$ and finally $I4/mmm$ when fully dehydrated. All of these structures appear to show the same B-site ordering found for $\text{CsLa}_2\text{Ti}_2\text{NbO}_{10}$. Work has been done on these 3-layer

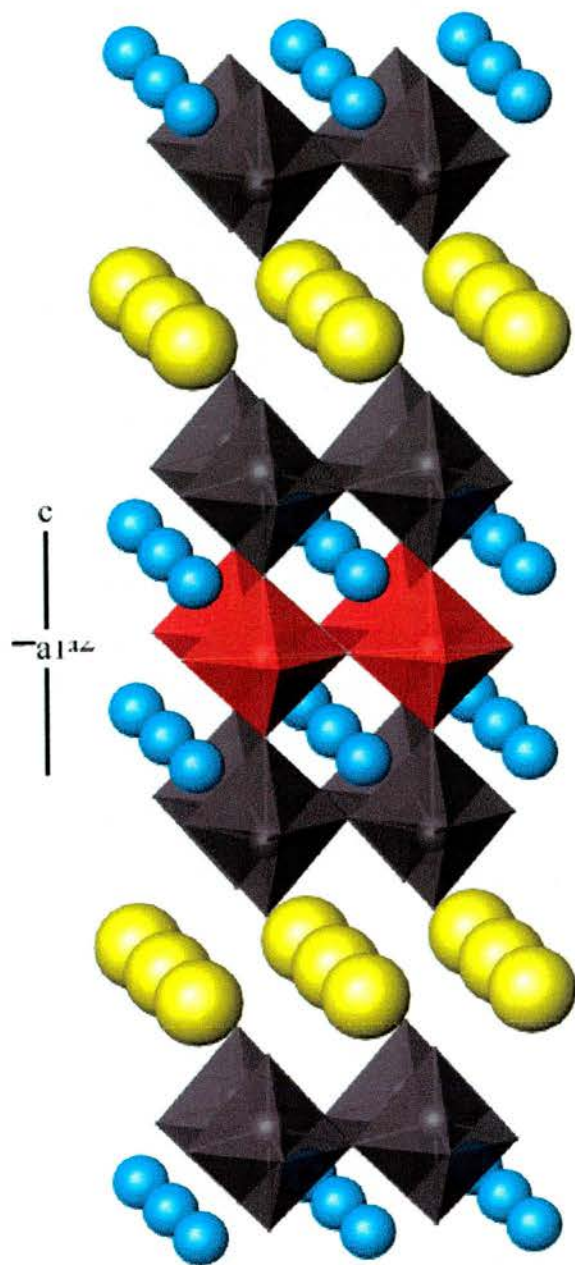


Figure 1.14: Structure of $\text{CsLa}_2\text{Ti}_2\text{NbO}_{10}$, Cs in yellow, La in light blue, TiO_6 octahedra in red, $(\text{Nb}, \text{Ti})\text{O}_6$ octahedra in dark grey

structures to ion-exchange protons for the alkali metal interlayer cations[95]. The use of the protonic phases as solid acids for intercalation of amines is described. In similar work the formation of layered brownmillerite phases (defect perovskite with tetrahedra as well as octahedra) with Al^{3+} and Fe^{3+} doping is attempted[96], these structures are then ion-exchanged to include protons and are used to intercalate amines. In both of these intercalation studies the compounds have been indexed and are found to adopt tetragonal unit cells. There are however no space groups given and no structural models given in the papers. The possibility of using divalent transition metal cations in both the B-site[97] and the interlayer[98] has been examined, again there are no definitive structures reported.

Phases of More Than 3-Layers

Papers detailing 4 or more layers are not very common for the Dion-Jacobson phases. In one early paper the series $\text{K}[\text{Ca}_2\text{Na}_{n-3}\text{Nb}_n\text{O}_{3n+1}]$ ($3 \leq n \leq 7$) was described[79], with details of the lattice parameters of the series, the proton exchanged phases and the result of intercalation. In a following paper[99] the delamination of the phases into perovskite sheets was identified. As in the first paper no structural data are produced. Other papers discussing the series $\text{K}[\text{Ca}_2(\text{Ca},\text{Sr})_{n-3}\text{Nb}_3\text{Ti}_{n-3}\text{O}_{3n+1}]$ ($n = 4, 5$)[100], $\text{A}[\text{Bi}_3\text{Ti}_4\text{O}_{13}]$ and $\text{A}[\text{Bi}_3\text{PbTi}_5\text{O}_{16}]$ ($\text{A} = \text{K}, \text{Cs}$ and $n = 4, 5$)[101] detail the lattice parameters for phases but offer no other structural information. Only one paper to date offers a full scale structural refinement, this was done using powder X-ray diffraction on the samples $\text{RbCa}_2\text{Na}_{1-x}\text{Sr}_x\text{Nb}_4\text{O}_{13}$ ($x = 0, 0.2, 0.4$)[102]. Clearly for the $x = 0.2$ and 0.4 samples the structure is not charge balanced

and no explanation is offered for how this is consolidated. The structures are given with the interlayer site as Rb^+ and the perovskite A-sites as randomly distributed Na^+ , Ca^{2+} and Sr^+ . All three structures were refined in the $P4/mmm$ tetragonal space group. These results are the most complete study of a 4-layer Dion-Jacobson phase published.

References

- [1] B. Aurivillius, *Ark. Kemi.*, 1949, **1**, 463.
- [2] B. Aurivillius, *Ark. Kemi.*, 1949, **1**, 499.
- [3] B. Aurivillius and P. H. Fang, *Phys. Rev.*, 1962, **126**, 893.
- [4] R. L. Withers, J. G. Thompson, and A. D. Rae, *J. Solid State Chem.*, 1991, **94**, 404.
- [5] J. G. Thompson, A. D. Rae, R. L. Withers, and D. C. Craig, *Acta Cryst. B*, 1991, **47**, 174.
- [6] E. C. Subbarao, *J. Phys. Chem. Solids*, 1962, **23**, 665.
- [7] G. A. Smolenskii, V. A. Isupov, and A. I. Agranovskaya, *Sov. Phys. - Solid State*, 1961, **3**, 651.
- [8] C. A.-P. de Araujo, J. D. Cuchiaro, L. D. McMillan, M. C. Scott, and J. F. Scott, *Nature*, 1995, **374**, 627.
- [9] B. H. Park, B. S. Kang, S. D. Bu, T. W. Noh, J. Lee, and W. Jo, *Nature*, 1999, **401**, 682.
- [10] U. Chon, H. M. Jang, M. G. Kim, and C. H. Chang, *Phys. Rev. Lett.*, 2002, **89**, 087601.
- [11] J. L. Pineda-Flores, E. Chavira, and A. Huanosta-Tera, *Physica C*, 2001, **364-365**, 674.
- [12] O. Alvarez-Fregoso, *J. Appl. Phys.*, 1997, **81**, 1387.
- [13] K. Srinivas and A. R. James, *J. Appl. Phys.*, 1999, **86**, 3885.
- [14] R. S. Singh, T. Bhimasankaram, G. S. Kumar, and S. V. Suryanarayana, *Solid State Comm.*, 1994, **91**, 567.
- [15] A. Srinivas, S. V. Suryanarayana, G. S. Kumar, and M. M. Kumar, *J. Phys. Condens. Mater.*, 1999, **11**, 3335.
- [16] M. M. Kumar, A. Srinivas, G. S. Kumar, and S. V. Suryanarayana, *Solid State Comm.*, 1997, **104**, 741.
- [17] A. Srinivas, M. M. Kumar, S. V. Suryanarayana, and T. Bhimasankaram, *Mat. Res. Bull.*, 1999, **34**, 989.
- [18] K. R. Kendall, C. Navas, J. K. Thomas, and H.-C. zur Loye, *Chem. Mater.*, 1996, **8**, 642.

- [19] K. R. Kendall, J. K. Thomas, and H.-C. zur Loye, *Solid State Ionics*, 1994, **70/71**, 221.
- [20] K. R. Kendall, J. K. Thomas, and H.-C. zur Loye, *Chem. Mater.*, 1995, **7**, 50.
- [21] J. K. Thomas, K. R. Kendall, and H.-C. zur Loye, *Solid State Ionics*, 1994, **70/71**, 225.
- [22] R. E. Newnham, R. W. Wolfe, and J. F. Dorrian, *Mat. Res. Bull.*, 1971, **6**, 1029.
- [23] J. G. Thompson, S. Schmid, R. L. Withers, A. D. Rae, and J. D. Fitzgerald, *J. Solid State Chem.*, 1992, **101**, 309.
- [24] A. D. Rae, J. G. Thompson, and R. L. Withers, *Acta Cryst. B*, 1991, **47**, 870.
- [25] I. D. Brown and D. Aldermatt, *Acta Cryst. B*, 1985, **41**, 244.
- [26] K. S. Knight, *Miner. Mag.*, 1992, **56**, 399.
- [27] C. Pirovano, M. S. Islam, R.-N. Vannier, G. Nowogrocki, and G. Mairesse, *Solid State Ionics*, 2001, **140**, 115.
- [28] B. Aurivillius, C.-I. Lindblom, and P. Sténson, *Acta Cryst. B*, 1964, **41**, 244.
- [29] K. Sooryanarayana, T. N. G. Row, and K. B. R. Varma, *Mat. Res. Bull.*, 1997, **32**, 1651.
- [30] I. Abrahams and F. Krok, *Solid State Ionics*, 2003, **157**, 139.
- [31] A. V. Akopjan, T. V. Serov, V. A. Dolgikh, E. I. Ardaschnikova, and P. Lightfoot, *J. Mater. Chem.*, 2002, **12**, 1490.
- [32] Y. Shimakawa, Y. Kubo, Y. Nagagawa, T. Kamiyama, H. Asano, and F. Izumi, *Appl. Phys. Lett.*, 1999, **74**, 1904.
- [33] C. H. Hervoches, J. T. S. Irvine, and P. Lightfoot, *Phys. Rev. B*, 2001, **64**, 100102.
- [34] Y. Shimakawa, Y. Kubo, Y. Nakagawa, S. Goto, T. Kamiyama, H. Asano, and F. Izumi, *Phys. Rev. B*, 2000, **61**, 6559.
- [35] R. Macquart, B. J. Kennedy, and Y. Shimakawa, *J. Solid State Chem.*, 2001, **160**, 174.
- [36] S. M. Blake, M. J. Falconer, M. McCree, and P. Lightfoot, *J. Mater. Chem.*, 1997, **7**, 1609.
- [37] Ismunandar and B. J. Kennedy, *J. Mater. Chem.*, 1999, **9**, 541.
- [38] B. J. Kennedy and B. A. Hunter, *Chem. Mater.*, 2001, **13**, 4612.
- [39] J.-L. Champarnaud-Mesjard, B. Frit, and A. Watanabe, *J. Mater. Chem.*, 1999, **9**, 1319.
- [40] C. H. Hervoches and P. Lightfoot, *Chem. Mater.*, 1999, **11**, 3359.
- [41] C. H. Hervoches and P. Lightfoot, *J. Solid State Chem.*, 2000, **153**, 66.
- [42] R. W. Wolfe and R. E. Newnham, *J. Electrochem. Soc. : Solid State Sciences*, 1969, p. 832.
- [43] W. J. Yu, Y. I. Kim, D. H. Ha, J. H. Lee, Y. K. Park, S. Seong, and N. H. Hur, *Solid State Comm.*, 1999, **111**, 705.

- [44] F. Kubel and H. Schmid, *Ferroelectrics*, 1992, **129**, 101.
- [45] B. Frit and J. P. Mercurio, *J. Alloys Compd.*, 1992, **188**, 27.
- [46] D. Mercurio, G. Trolliard, T. Hansen, and J. P. Mercurio, *Int. J. Inorg. Mater.*, 2000, **2**, 397.
- [47] S. Luo, Y. Noguchi, M. Miyama, and T. Kudo, *Mat. Res. Bull.*, 2001, **36**, 531.
- [48] S. N. Ruddlesden and P. Popper, *Acta Cryst.*, 1957, **10**, 538.
- [49] S. N. Ruddlesden and P. Popper, *Acta Cryst.*, 1958, **11**, 54.
- [50] G. Blasse, *J. Inorg. Nucl. Chem.*, 1967, **30**, 656.
- [51] M. Richard, G. Goglio, and L. Brohan, *Mat. Res. Bull.*, 1995, **30**, 925.
- [52] R. A. McIntyre, A. U. Falster, S. Li, W. B. Simmons, C. J. O'Connor, and J. B. Wiley, *J. Am. Chem. Soc.*, 1998, **120**, 217.
- [53] D. Chen, X. Jiao, and R. Xu, *Mat. Res. Bull.*, 1999, **34**, 685.
- [54] K. Toda, Y. Kameo, S. Kurita, and M. Sato, *J. Alloys Compd.*, 1996, **234**, 19.
- [55] Y. Maeno, H. Hashimoto, K. Yoshida, N. S. T. Fujita, J. G. Bednorz, and F. Lichtenberg, *Nature*, 1994, **372**, 532.
- [56] M. Braden, G. André, S. Nakatsuji, and Y. Maeno, *Phys. Rev. B*, 1998, **58**, 847.
- [57] M. M. Elcombe, E. H. Kisi, K. D. Hawkins, T. J. White, P. Goodman, and S. Matheson, *Acta Cryst. B*, 1991, **47**, 305.
- [58] E. Lucchini, D. Minichelli, and G. Slocari, *Acta Cryst. B*, 1973, **29**, 2356.
- [59] P. D. Battle, S. K. Bollen, and A. V. Powell, *J. Solid State Chem.*, 1992, **99**, 267.
- [60] P. D. Battle, M. A. Green, N. S. Laskey, J. E. Millburn, L. Murphy, M. J. Rosseinsky, S. P. Sullivan, and J. F. Vente, *Chem. Mater.*, 1997, **9**, 552.
- [61] M. A. Green and D. A. Neumann, *Chem. Mater.*, 2000, **12**, 90.
- [62] J. F. Mitchell, J. E. Millburn, M. Medarde, S. Short, J. D. Jorgensen, and M. T. Fernández-Díaz, *J. Solid State Chem.*, 1998, **14**, 599.
- [63] T. A. Kodenkandath and J. B. Wiley, *Mat. Res. Bull.*, 2000, **15**, 1737.
- [64] M.-P. Crosnier-Lopez, F. L. Berre, and J.-L. Fourquet, *J. Mater. Chem.*, 2001, **11**, 1146.
- [65] P. D. Battle, M. A. Green, J. E. Millburn, M. J. Rosseinsky, and J. F. Vente, *Chem. Mater.*, 1998, **10**, 658.
- [66] P. D. Battle, W. R. Branford, A. Mihut, M. J. Rosseinsky, J. Singleton, J. Sloan, L. E. Spring, and J. F. Vente, *Chem. Mater.*, 1999, **11**, 674.
- [67] A. J. Wright and C. Greaves, *J. Mater. Chem.*, 1996, **6**, 1823.
- [68] J. N. Lalena, A. U. Falster, W. B. Simmons, E. E. Carpenter, J. Wiggins, S. Hariharan, and J. B. Wiley, *Chem. Mater.*, 2000, **12**, 2418.
- [69] R. E. Schaak, D. Azfal, J. A. Schottenfeld, and T. E. Mallouk, *Chem. Mater.*, 2002, **14**, 442.

- [70] K. Park and S.-H. Byeon, *Bull. Korean Chem. Soc.*, 1996, **17**, 168.
- [71] S.-H. Byeon and H.-J. Nam, *Chem. Mater.*, 2000, **12**, 1771.
- [72] V. Thangdurai, A. K. Shukla, and J. Gopalakrishnan, *Solid State Ionics*, 1994, **73**, 9.
- [73] K. Toda, J. Wanatabe, and M. Sato, *Mat. Res. Bull.*, 1996, **31**, 1427.
- [74] M. Richard, L. Brohan, and M. Tournoux, *J. Solid State Chem.*, 1994, **112**, 345.
- [75] J. Gopalakrishnan and V. Bhat, *Inorg. Chem.*, 1987, **26**, 4299.
- [76] F. L. Berre, M. P. Crosnier-Lopez, and J. L. Fourquet, *J. Mater. Chem.*, 2002, **12**, 258.
- [77] R. E. Schaak and T. E. Mallouk, *J. Solid State Chem.*, 2000, **155**, 46.
- [78] M. Dion, M. Ganne, and M. Tournoux, *Mat. Res. Bull.*, 1981, **16**, 1429.
- [79] A. J. Jacobson, J. W. Johnson, and J. T. Lewandowski, *Inorg. Chem.*, 1985, **24**, 3727.
- [80] M. Sato, J. Abo, and T. Jin, *Solid State Ionics*, 1992, **51**, 285.
- [81] J. Gopalakrishnan, V. Bhat, and B. Raveau, *Mat. Res. Bull.*, 1987, **22**, 413.
- [82] M. Sato, J. Abo, T. Jin, and M. Ohta, *Solid State Ionics*, 1992, **51**, 85.
- [83] A. R. Armstrong and P. A. Anderson, *Inorg. Chem.*, 1994, **33**, 4366.
- [84] N. Kumada, N. Kinomura, and A. W. Sleight, *Acta Cryst. C*, 1996, **52**, 1063.
- [85] M. A. Subramanian, J. Gopalakrishnan, and A. W. Sleight, *Mat. Res. Bull.*, 1988, **23**, 837.
- [86] K. Toda, T. Teranishi, Z.-G. Ye, M. Sato, and Y. Hinatsu, *Mat. Res. Bull.*, 1999, **34**, 971.
- [87] H. Fukuoka, T. Isami, and S. Yamanaka, *J. Solid State Chem.*, 2000, **151**, 40.
- [88] V. Thangadurai and W. Weppner, *J. Mater. Chem.*, 2001, **11**, 636.
- [89] V. Thangadurai, P. Schmid-Beurmann, and W. Weppner, *J. Solid State Chem.*, 2001, **158**, 279.
- [90] M. Fang, C. H. Kim, and T. E. Mallouk, *Chem. Mater.*, 1999, **11**, 1519.
- [91] Y.-S. Hong, S.-J. K. and S.-J. Kim, and J.-H. Choy, *J. Mater. Chem.*, 2000, **10**, 1209.
- [92] Y.-S. Hong and K. Kim, *Chem. Lett.*, 2000, p. 690.
- [93] Y.-S. Hong, C.-H. Han, and K. Kim, *J. Solid State Chem.*, 2001, **158**, 290.
- [94] Y.-S. Hong and K. Kim, *Mat. Res. Bull.*, 2001, **36**, 1325.
- [95] J. Gopalakrishnan, S. Uma, and V. Bhat, *Chem. Mater.*, 1993, **5**, 132.
- [96] S. Uma and J. Gopalakrishnan, *Chem. Mater.*, 1994, **6**, 907.
- [97] J. Gopalakrishnan, S. Uma, N. Y. Vasanthacharya, and G. N. Subbanna, *J. Am. Chem. Soc.*, 1995, **117**, 2353.

- [98] K.-A. Hyeon and S.-H. Byeon, *Chem. Mater.*, 1999, **11**, 352.
- [99] M. M. J. Treacy, S. B. Rice, A. J. Jacobson, and J. T. Lewandowski, *Chem. Mater.*, 1990, **2**, 279.
- [100] R. A. M. Ram and A. Clearfield, *J. Solid State Chem.*, 1991, **94**, 45.
- [101] J. Gopalakrishnan, T. Sivakumar, V. Thangadurai, and G. N. Subbanna, *Inorg. Chem.*, 1999, **38**, 2902.
- [102] W. Sugimoto, H. Ohkawa, M. Naito, Y. Sugahara, and K. Kuroda, *J. Solid State Chem.*, 1999, **148**, 508.

Chapter 2

Techniques for Materials Analysis

2.1 Structural Analysis

In all materials the relationship between structure and properties is fundamental. Without a good knowledge of the structure it would not be possible to correctly understand the properties. For polycrystalline materials like those in this work, the main methods employed to establish structural models are diffraction methods. These methods rely on the crystalline nature of the materials.

2.1.1 Crystals, Symmetry and Space Groups

Crystals

The scientific analysis of crystals has been dated as far back as 1669[1]. However, before any analysis can be performed upon a crystal, what constitutes a crystal must be defined. A crystal is a periodic arrangement of some *motif*. The motif, or more commonly the asymmetric unit, is the description of some section of a structure, that when translated, rotated or reflected, yields the

unit cell of the structure. The unit cell can then be translated to produce an infinite lattice. Shown as Figure-2.1 is the structure of CsCl showing the unit cell which when repeated gives the structure.

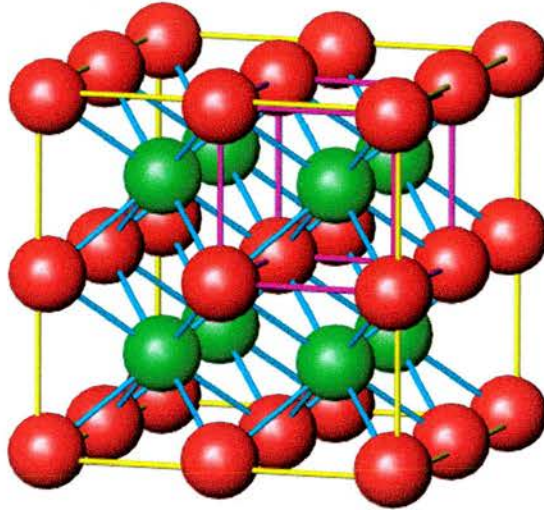


Figure 2.1: CsCl structure, unit cell is outlined in purple, Cs is red, Cl is green.

Lattices

The unit cell of a structure must be able to be arranged in three dimensions to give an infinite lattice filling all space, i.e. no gaps. The space must be filled by only one type of cell for this to be the unit cell. There are seven crystal systems, shapes of unit cell, that are possible. These are specified by three axes a , b and c and three angles α , β and γ . These, however, are not what define the seven systems, instead they are defined by a minimum number of symmetry operations that the system must contain, given in Table-2.1. The a , b and c values represent three vectors, the three angles, α , β and γ , are

Table 2.1: The Seven Crystal Systems

Crystal System	Minimum Symmetry Requirements	Conditions Imposed on Cell Geometry[2]
Triclinic	None	None
Monoclinic	One twofold axis or one symmetry plane	$\alpha = \gamma = 90^\circ$ (b unique) $\alpha = \beta = 90^\circ$ (c unique)
Orthorhombic	Any combination of three mutually perpendicular twofold axes or symmetry planes	$\alpha = \beta = \gamma = 90^\circ$
Tetragonal	One fourfold axis or one fourfold improper axis	$a = b; \alpha = \beta = \gamma = 90^\circ$
Trigonal	One three fold axis	$a = b; \alpha = \beta = 90^\circ; \gamma = 120^\circ$ (hex. axes) $a = b = c; \alpha = \beta = \gamma$ (rhomboh. axes)
Hexagonal	One sixfold or one sixfold improper axis	$a = b; \alpha = \beta = 90^\circ; \gamma = 120^\circ$
Cubic	Four threefold axis at 109.28° to each other	$a = b = c; \alpha = \beta = \gamma = 90^\circ$

the angles between the vectors. The α is the angle between b and c , and so on. The systems and the restrictions on the cell geometry are tabulated as Table-2.1.

Crystals are also described using one of four different classes or lattice types; primitive, P, where an atom on $(0,0,0)$ is only on the corners of the cell. Body-centred, I, where an atom on $(0,0,0)$ is equivalent to $(\frac{1}{2}, \frac{1}{2}, \frac{1}{2})$, Face-centred, F, where $(0,0,0)$ is equivalent to $(\frac{1}{2}, \frac{1}{2}, 0)$, $(\frac{1}{2}, 0, \frac{1}{2})$ and $(0, \frac{1}{2}, \frac{1}{2})$, C-centred, C, where $(0,0,0)$ is equivalent to $(\frac{1}{2}, \frac{1}{2}, 0)$. There are A and B equivalents to C, but these are treated as the same class.

Point Groups

To fully describe a crystal correctly more than just the system and the lattice type is required. To obtain the 230 space groups the system and lattice must be combined with the 32 point groups and other symmetry elements. The point groups give the 'families' of permitted operations for a given system. Point Group symmetry is specified with only proper or improper rotations and mirror planes. To obtain the full 230 space groups the mirror planes can be replaced by other translational elements, e.g. glide planes, and the proper and improper rotation axes can be replaced by other rotational elements, e.g. screw axes. It is possible to classify the 32 point groups into 11 Laue Groups, these Laue groups are the highest symmetry group in a set of point groups. For example, the orthorhombic Laue Group mmm is used to describe the point groups, mmm , 222 and $mm2$ ($m2m$ and $2mm$). The Laue group represents the symmetry of the diffraction pattern and this is always centrosymmetric.

Space groups can be described as being either centrosymmetric or non-centrosymmetric. Non-centrosymmetric space groups may have a polarisation, i.e. the centre of positive charge does not coincide with the centre of negative charge. Non-centrosymmetric space groups can be described in terms of four separate physical properties; polarity, circular dichroism, enantiomorphism and piezoelectricity. For this work it is the polar space groups that are of most importance. There are identified 11 polar point groups; 1, 2, 3, 4, 6, m , $mm2$, $3m$, $4mm$, $6mm$ and $\bar{4}2m$. Common to all of these groups is that for a given point (x,y,z) at least one coordinate will not be inverted to

-x, -y or -z, giving a net polarisation and the potential to display ferroelectric behaviour.

Miller Planes

The surface of a crystal does not necessarily correspond to the cell edge of the crystal, instead it may correspond to some other plane. For this reason, and reasons explained later, it is necessary to have a system to label the planes in a crystal. There is a convention by which the points at which a plane intercepts all three axes are expressed in terms of the axis length. These numbers are then converted to their reciprocals and the lowest set of integer values are taken, these are called the Miller indices. For example if a set of planes intercepts the axes at $\frac{1}{2}a$, $\frac{1}{3}b$ and $\frac{1}{4}c$, then the lowest set of reciprocals for this would be 2 3 and 4. These are enclosed in brackets as (hkl), in the example the plane would be given as (234).

The Bragg Equation

Use of these space groups and characterisation of the space groups is possible due to the use of diffraction techniques. These techniques all rely upon a beam of some particles (or wave) being refracted by the crystal. The equation governing this behaviour is the Bragg equation, Equation-2.1.

$$n\lambda = 2d\sin\theta \quad (2.1)$$

Where n is some integer value, λ is the wavelength of the radiation, d is the

d-spacing and θ is the angle between the incident radiation and the sample. The d-spacing is a distance between two crystal planes in a sample, for a pictorial representation see Figure-2.2. Diffraction will only occur for an integer n , when the waves of radiation constructively interfere to produce intensity.

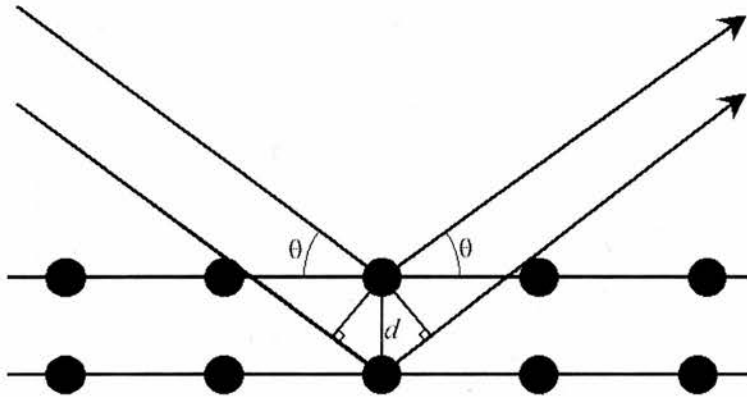


Figure 2.2: Diagram of Bragg Diffraction, showing d-spacing and θ

The Reciprocal Lattice[3]

The Bragg equation is able to provide the d-spacings of the reflections, but it is unable to determine the scattering intensities. To determine the scattering intensities it first must be understood that the diffraction pattern does not show the real-space reflections of a crystal. Instead it is showing a map of the reciprocal lattice, which is the Fourier transform of the real-space lattice. If the real-space crystal lattice can be thought of as being a series of planes, of some hkl , then the corresponding reciprocal lattice point is given by the line perpendicular to this plane that meets the origin. This gives the direction

of the reciprocal lattice vector, the distance is given by $1/d_{hkl}$ where d_{hkl} is the spacing of the planes in real-space.

Structure Factors[4]

The diffraction pattern of the crystal is given by the product of the Fourier transform of the lattice multiplied by the Fourier transform of the motif. The scattering density of a point x,y,z in the crystal is given by Equation-2.2.

$$\rho(x, y, z) = \frac{1}{V} \sum_h \sum_k \sum_l F_{hkl} \exp[-2\pi i(hx + ky + lz)] \quad (2.2)$$

The scattering from all hkl reflections are not the same, these different values are termed structure factors and are given by Equation-2.3.

$$F_{hkl} = V \int \int \int \rho(x, y, z) \exp[2\pi i(hx + ky + lz)] dx dy dz \quad (2.3)$$

In a single crystal experiment as many structure factors are sampled as possible and converted into real-space electron density maps, from which to solve the structure.

Thermal Parameters

The atoms in a structure are not stationary upon a single position. They are in fact vibrating around this point, in a temperature dependent fashion. The vibration of the atoms leads to a distribution of the scattering intensity and to a reduction of the structure factor, given as Equation-2.4.

$$(F_{hkl})_T \sim \exp\left[-B\left(\frac{\sin^2\theta}{\lambda^2}\right)\right] F_{hkl} \quad (2.4)$$

The thermal parameter refined, U_{ij} , is related to the thermal parameter for each atom, B_{ij} , by Equation-2.5

$$U_{ij} = \frac{B_{ij}}{8\pi^2} \quad (2.5)$$

2.1.2 X-rays

Properties of X-rays

X-rays are a part of the electromagnetic spectrum with a wavelength $\sim 10^{-10}$ m (1 Å). This is the same order of magnitude as a chemical bond, making X-rays ideal for probing the structure of crystals. Most X-ray diffraction experiments are performed using either a Cu or Mo source, Cu being a very common choice as it is cheap and produces good levels of intensity.

The X-ray scattering intensity is dependent upon the atomic number of the atom. This is due to the interaction of the X-rays with the electron clouds of atoms. This presents certain problems for X-ray diffraction. It is very difficult to ascertain the correct location of a light atom in the presence of a heavy one, as most of the observed intensity will be created by the heavier atom. It is difficult to determine the difference between neighbouring atoms in the periodic table, due to the similarity of the scattering. It is not possible using X-rays to determine any magnetic structure, as the X-ray radiation does not have any magnetic moment. Despite those problems X-ray diffraction is still

a very powerful tool for routine structural analysis.

Generation of X-rays

X-rays are generated by heating a metal coil, which gives off electrons which accelerate down a large potential difference towards a cooled anode. The anode then releases a stream of white X-rays within which are peaks corresponding to discrete emissions. These emissions are created by the generated electrons removing a core electron from the anode, and an electron from an outer shell filling the space. The energies of these transitions are consistent and are specific for a selected metal. There are two primary transitions, one from the $n = 2$ shell and one from the $n = 3$ shell, which produce K_α and K_β radiation respectively. The alpha and beta lines are actually pairs of lines $K_{\alpha 1}$, $K_{\alpha 2}$ and $K_{\beta 1}$, $K_{\beta 2}$. The radiation is filtered using a monochromator to give only one wavelength, either α or β . On some machines the α_1 and α_2 radiations are filtered.

Details of Machines Used

The machines used to perform X-ray powder analysis were Stoe STADI-P diffractometers, using Cu anodes, with primary beam (Ge Crystal) monochromation to give Cu $K_{\alpha 1}$ radiation (1.5406 Å) only. Data are recorded in a transmission geometry with the sample mounted between two Polythene disks, held in place with VaselineTM.

2.1.3 The Neutron

Properties of Neutrons[5]

The neutron is a spin $\frac{1}{2}$ uncharged particle with a mass of 1.67×10^{-27} kg. As the neutron interacts with the nucleus of an atom the scattering from different isotopes of an element are different. Neutrons are able to detect light elements as the scattering cross-section does not vary systematically with atomic number. This also means that it is possible to determine the difference between atoms with similar atomic number. The neutron is spin $\frac{1}{2}$ so it will interact with magnetic species making magnetic structure solution possible. All these points are advantageous over X-rays, the disadvantages are the cost and complexity of generating neutrons.

Generation of Neutrons[6]

The neutron is generated from one of two sources, either a nuclear reactor or a spallation source. The nuclear reactor sources rely on a controlled chain reaction of neutron-induced fission of ^{235}U . The fission processes produce a continuous source of neutrons for diffraction, however, these neutrons are of too high an energy. This makes them of too short a wavelength to be used in diffraction techniques. Therefore, the neutrons have to be slowed using a moderator. At the Institut Laue-Langevin (ILL) in Grenoble three different moderators are used to produce differing wavelengths of neutrons. A graphite moderator is used to produce 2000 K neutrons, a D_2O moderator is used to produce 300 K neutrons and a D_2 moderator is used to produce 25 K neutrons. The neutron beam at a reactor source is commonly monochro-

mated to give a narrow range of wavelengths. This monochromation results in the loss of large amounts of the flux.

The spallation source works by creating a beam of highly energised protons (~ 50 MeV) using a linear accelerator and bombarding a heavy metal target to produce the neutrons. This is an older design, modern spallation sources use a synchrotron in combination with the the linear accelarator to produce higher energies (~ 800 MeV). Spallation sources are often pulsed (~ 50 Hz). A pulsed signal makes the source ideal for the use of time-of-flight neutron diffraction. Using this technique the neutron wavelength can be found for an elastic collision over a defined length by measuring the time taken. The use of the pulses and time-of-flight means that the neutron beam is not monochromated. The result is that although the initial flux is less than for a reactor source the final flux is comparable.

Details of Machines Used

Three separate neutron powder diffractometers have been used in the course of this project. The D2B diffractometer at the ILL in Grenoble, is a fixed wavelength machine ($\lambda = 1.594$ Å) with a moving detector bank of 64 ^3He tubes. The POLARIS instrument at ISIS, a time-of-flight diffractometer has three fixed detector banks. These banks are fixed at $130\text{-}160^\circ$, $85\text{-}95^\circ$ and $28\text{-}42^\circ$, composed of 58 ^3He tube, 216 ZnS scintillator and 80 ^3He tube detectors respectively. The HRPD diffractometer at ISIS also has three detector banks, at $160\text{-}176^\circ$, $87\text{-}93^\circ$ and $28\text{-}32^\circ$. The banks are composed of 720 ZnS scintillator, 396 ZnS scintillator and 72 ^3He tube detectors respectively. The resultant resolutions of these detectors are given as Table-2.2.

Table 2.2: Neutron Detector Bank Resolutions

Instrument	Detector Bank	Resolution $\delta d/d$
D2B	moving	5×10^{-4}
Polaris	130-160 $^{\circ}$	5×10^{-3}
	85-95 $^{\circ}$	7×10^{-3}
	28-42 $^{\circ}$	2×10^{-2}
HRPD	160-176 $^{\circ}$	4.5×10^{-4}
	87-93 $^{\circ}$	2×10^{-3}
	28-32 $^{\circ}$	1×10^{-2}

2.1.4 Powder Diffraction

Powder diffraction data can be collected using both X-ray and neutron instruments. The data points are collected using either constant wavelength, variable 2θ or constant 2θ , variable wavelength (time-of-flight). In a powder diffraction pattern the observed intensities for a 3-dimensional sample are compressed along 1 dimension. This occurs as the grains of the sample powder are randomly oriented and although they diffract as for normal crystals they do not do so along a single direction. A single reflection will be seen as a cone of intensity, the diffraction pattern being a slice through several cones. However, using Bragg's law it is possible to determine the d-spacing required for the reflection. By indexing all the peaks the unit cell can be identified, several algorithms having been created for this purpose. In 1969 a paper was published detailing a method of structure refinement from powder neutron data[7].

2.1.5 Rietveld Refinement

The Rietveld Method

Rietveld noted that many of the reflections occurring from the polycrystalline samples overlapped, particularly at lower d-spacings, and it would not be possible to match individual reflections. His method relies on fitting a structural model to the whole pattern, not by matching individual peaks, but by simulating the entire pattern. The pattern can then be matched by fitting certain parameters. The parameters able to be refined are such as the atomic coordinates, thermal factors, the background (which is modelled by a cosine fourier series), a preferred orientation coefficient, the lattice parameters, the peak profile shape and, for X-ray diffraction, the detector zero-point. As previously mentioned thermal parameters are able to be refined, either isotropically or anisotropically. The anisotropic refinement requires 6 times as many variables to describe the thermal parameters.

The pattern calculated from the structural model is compared against the experimental data using a least squares minimisation. The quantity being minimised is the residual S_y [8], which is the sum over all points of one over the observed intensity, y_i , multiplied by the square of the difference between the experimental and calculated intensities, y_{ci} , given by equation-2.6.

$$S_y = \sum_i \frac{1}{y_i} (y_i - y_{ci})^2 \quad (2.6)$$

This residual is a value that can be minimised, however, it is not used as a measure of the overall quality of the fit. For this the R-factors are used,

which are values calculated along similar lines to the residuals, giving a measure of the quality of the fit. The two R-factors commonly used are the R_p and R_{wp} , the R-pattern and R-weighted pattern, respectively. R_{wp} is a better measure of the fit as it includes the residual value in the numerator. The χ^2 test is used as a statistical measure of fit quality as it factors in the number of parameters and data points (N = number of points, P = number of variables, C = number of constraints).

$$R_p = \frac{\sum |y_i(obs) - y_i(calc)|}{\sum y_i(obs)} \quad (2.7)$$

$$R_{wp} = \left\{ \frac{\sum \frac{1}{y_i} (y_i(obs) - y_i(calc))^2}{\sum \frac{1}{y_i} (y_i(obs))^2} \right\}^{\frac{1}{2}} \quad (2.8)$$

$$\chi^2 = \frac{1}{N - P + C} \sum \frac{1}{y_i} (y_i(obs) - y_i(calc))^2 \quad (2.9)$$

Profiles

The profile shapes of samples can vary substantially. Peak shapes for a certain sample on an instrument will not be the same as those obtained on another. The shape is affected by the sample crystallinity, the radiation used and the instrument geometry. The peak profile most often used for time-of-flight neutron diffraction is a Pseudo-Voigt profile. This is a convolution of

the Gaussian and Lorentzian peak shapes, incorporating the Ikeda-Carpenter function. The Gaussian function is a natural symmetric distribution curve, the Lorentzian distribution is also symmetric but is much sharper in profile, i.e. more triangular and less like a natural distribution. The Ikeda-Carpenter function was designed to simulate the sharp increase in flux created by a pulsed source and the longer tailing off of the flux created by the moderation process.

Using the GSAS program[9] this function presents 15 parameters for refinement, though not all are frequently used. The parameters are α_0 , α_1 , β_0 , κ , σ_0^2 , σ_1^2 , σ_2^2 , γ_0 , γ_1 , γ_2 , γ_{1e} , γ_{2e} , DIFC, DIFA and ZERO. The α_0 and α_1 parameters are part of the Ikeda-Carpenter function, which is a convolution of two functions, representing the fast leakage from the moderator. The β_0 corresponds to the other part of the Ikeda-Carpenter function, representing the slow leakage from the moderator. The κ parameter is associated with the mixing parameter for the two parts of the Ikeda-Carpenter function. The σ_0^2 , σ_1^2 and σ_2^2 parameters are related to the Gaussian part of the profile function. The γ parameters relate to the Lorentzian part of the profile. The DIFC, DIFA and ZERO parameters are diffractometer constants. Normally for a refinement only σ_1^2 , σ_2^2 , γ_1 and γ_2 are refined, as these are sample dependent. Values that are machine dependent are not refined.

2.1.6 Glazer Notation

In perovskite based materials the tilting of the octahedra in the structure is key to many of the interesting properties. A method was established by

Glazer[10] to describe the relative tilting of the octahedra. In this method two octahedra that tilt in-phase are described as + and out of phase is -. This is a useful way in which to examine the relationship of various structures to one another.

2.1.7 Bond Valence Calculations

It is desirable to understand the actual valence of the atoms in a structure. This can be particularly of interest if there are atoms where more than one valence is feasible. Calculation of the Bond Valence Sum (BVS) is performed to examine the bonding environment around an ion and to infer its oxidation state from the length of the bonds present. The method proposed by Brown and Altermatt[11], involves the initial assumption of the oxidation state of an ion and the use of an established bond length for a valence of 1. Using Equation-2.10, the established value for B (0.38), the bond lengths, r_j , of the structural model and the tabulated values for r_0 [11], the theoretical valence of an ion can be calculated.

$$V_{ij} = \sum_j e^{r_0 - r_j/B} \quad (2.10)$$

2.2 Physical Property Analysis

In the course of this work two physical properties were encountered; ferroelectricity and oxide ion conduction, properties that are well known for

perovskite based systems.

2.2.1 Ferroelectricity

A ferroelectric crystal has a permanent electric dipole which exists even in the absence of an external electric field. This is common also to pyroelectrics. The separate domains of polarity in the ferroelectric material will align with an applied field, and also display hysteresis behaviour, i.e. the polarisations will realign in the opposing direction as the field direction is changed. This behaviour is not observed for a pyroelectric material. Ferroelectric behaviour is found in the dielectric state below the Curie Temperature, T_C , above which the material is paraelectric.

2.2.2 Oxide Ion Conduction

Oxide ion conductors permit the movement of oxide ions through the material, creating a conduction of charge. This conduction can be achieved by a variety of methods, the method proposed for the materials in this work is the hopping mechanism. For the hopping mechanism the material must possess oxygen vacancies, which can be either intrinsic or extrinsic, extrinsic vacancies usually being created by doping or reduction of one of the metal cations. The oxide ion is believed then to move through the material along these vacancy sites, this has also been termed vacancy migration.

2.2.3 a.c. Impedance Spectroscopy[12]

In the course of this work it has been necessary to characterise the electrical properties of certain materials. To do this a.c. impedance spectroscopy has been used. This technique was selected as it is possible to separate the electrical properties of the bulk material from other electrical components. Components are able to be separated due to each individual RC (resistive / capacitive) component possessing a characteristic time constant, τ , given by Equation-2.11

$$\tau = RC \quad (2.11)$$

The RC elements can be separated with frequency due to the relationship given as equation-2.12. This holds for the angular frequency where the maximum impedance signal is recorded, ω_{MAX} .

$$\omega_{MAX}RC = 1 \quad (2.12)$$

$$\omega_{MAX} = 2\pi f_{MAX} \quad (2.13)$$

Scans are performed over a range of frequencies, however, data are normally plotted as Z'' versus Z' where:

$$Z^* = Z' - iZ'' \quad (2.14)$$

Plots of Z'' versus Z' typically show two semicircles, these can be assigned to regions of the sample based on the magnitude of the capacitance, obtained by applying equation-2.12 to the semicircles. The grain boundary would be expected to be in the order of 10^{-11} - 10^{-8} F, with the bulk at 10^{-12} F. For a ferroelectric material the bulk capacitance can be 10^{-10} - 10^{-9} F, leading to only one observable semicircle. In these cases the data can be examined using a plot of the imaginary component of the electrical modulus, M'' , versus $\log f$. Where the complex electrical modulus is given by Equation-2.15.

$$M^* = i\omega C_0 Z^* \quad (2.15)$$

Where $\omega = 2\pi f$, $C_0 = \epsilon_0 A/l$ and $i^2 = -1$.

The plot of M'' versus $\log f$ will normally produce two peaks, as opposed to the plot of Z'' versus $\log f$, which produces one peak. For the M'' plot the higher frequency peak represents the bulk structure. This is possible as the impedance plot picks out the most resistive elements, but the modulus plot picks out the smallest capacitances. For samples in this work capacitances were able to be obtained from Z'' versus Z' .

To use a.c. impedance spectroscopy to investigate a potential ferroelectric phase change capacitances are measured as described, but at various temperatures. The permittivity, ϵ' , of the sample is calculated using equation-2.16

$$C = \epsilon' \epsilon_0 \frac{A}{l} \quad (2.16)$$

Where ϵ_0 is the permittivity of free space, $8.854 \times 10^{-14} \text{ Fcm}^{-1}$, A is the surface area of the electrode and l is the length of the pellet.

For the ferroelectric phase change ϵ' is plotted against T and a peak in this plot will correspond to the Curie temperature T_C .

References

- [1] N. N. Greenwood, *Ionic Crystals, Lattice Defects and Nonstoichiometry*, Butterworth and Co., London, 1968.
- [2] ed. T. Hahn, *International Tables for Crystallography*, Vol. A : Space Group Symmetry, Kluwer Academic Publishers, Dordrecht, 1995.
- [3] C. Kittel, *Introduction to Solid State Physics*, Wiley, New York, 1996.
- [4] C. C. Wilson, *The Neutron Training Course : Single Crystal Diffraction*, ISIS, 2001.
- [5] S. M. Bennington, *The Neutron Training Course : The Neutron*, ISIS, 2001.
- [6] A. C. Hannon, *The Neutron Training Course : Neutron Sources*, ISIS, 2001.
- [7] H. M. Rietveld, *J. Appl. Cryst.*, 1969, **2**, 65.
- [8] ed. R. A. Young, *The Rietveld Method*, Oxford Science Publications, Oxford, 1996.
- [9] A. C. Larson and R. B. V. Dreele, *Report No. LA-U-86-748*, 1987.
- [10] A. M. Glazer, *Acta Cryst. B.*, 1972, **28**, 3384.
- [11] I. D. Brown and D. Altermatt, *Acta Cryst. B*, 1985, **41**, 244.
- [12] J. T. S. Irvine, D. C. Sinclair, and A. R. West, *Adv. Mater.*, 1990, **3**, 132.

Chapter 3

Aurivillius Phases Containing Trivalent Cations

3.1 Ga³⁺ Containing Aurivillius Structures

In 1994 and 1995 zur Loye et al. reported the synthesis of two new Ga³⁺ containing Aurivillius phase oxide ion conductors. These two compounds, Bi₂Sr₂Nb₂GaO_{11.5}[1, 2] and BaBi₄Ti₃GaO_{14.5}[3], are members of the solid solutions of the two families Bi₂Sr₂Nb₂Ti_{1-x}Ga_xO_{12-x/2} and BaBi₄Ti_{4-x}Ga_xO_{15-x/2} where x=1. The doping of Ga³⁺ for Ti⁴⁺ in the perovskite B-site was suggested to create the vacancies required for the oxygen conduction via a hopping mechanism.

These compounds are unusual as Ga³⁺ is often found in tetrahedrally coordinated sites, so when it is placed into an octahedral site it is expected that the octahedron will be distorted. Such a distortion would lead to oxygen displacements and octahedral BO₆ rotations, and the unit cell would be expected to be an orthorhombic cell with *a* and *b* approximately $\sqrt{2}a_t$ (*a_t* = *a* of tetragonal cell). Indeed the original model proposed for Bi₂Sr₂Nb₂GaO_{11.5} is orthorhombic and has lattice parameters *a* = 5.528(2) Å, *b* = 5.534(2)

Å and $c = 33.29(1)$ Å. The figure presented by zur Loye[1] shows the octahedra in the perovskite block as being tilted. However, in a later paper[2] the structure is indexed as tetragonal with $a = 3.913(1)$ Å and $c = 33.29(1)$ Å, where tilting of the octahedra is not permitted. So it would appear that there is some confusion as to the precise oxygen locations, as is to be expected for an X-ray study. However it is also possible that the assignment of both tetragonal and orthorhombic unit cells indicates a possible problem with the purity of the compound. Also in the same paper the difficulty of indexing reflections (106) and (216) in $\text{Bi}_2\text{Sr}_2\text{Nb}_2\text{AlO}_{11.5}$ and $\text{Bi}_2\text{Sr}_2\text{Ta}_2\text{AlO}_{11.5}$ is discussed. Although not explicitly stated it appears to be implied that there is some similar difficulty in indexing the Ga^{3+} containing compounds also. Mention is made that at high 2θ there appears to be peak splitting for $\text{Bi}_2\text{Sr}_2\text{Nb}_2\text{GaO}_{11.5}$, again it may be that the peak splitting and indexing problems are due to incorrect lattice assignment or an impurity. This indexing was the most complete structural study to date and is clearly insufficient. Preferable would be a full structural refinement.

For the 4-layer phase no diffraction pattern has been published, though some unit cell parameters are given[3]. $\text{BaBi}_4\text{Ti}_4\text{O}_{15}$; $a=5.682(3)$ Å and $c=41.74(3)$ Å. $\text{BaBi}_4\text{Ti}_3\text{GaO}_{14.5}$; $a=5.447(2)$ Å and $c=41.80$ Å. These would indicate a tetragonal unit cell which would not permit octahedral rotations, which seems unlikely given the bonding requirements of Ga^{3+} . Given that the a parameter proposed is $\sqrt{2}$ that for the tetragonal cell it could be proposed that the cell is actually orthorhombic with a very small difference between a and b . Such a difference would be difficult to detect from powder X-ray diffraction, neutron diffraction having the advantage of more easily-observable superlattice peaks.

Reference is made in the paper that it is not possible to determine ordering of B-site cations but that previous experience would indicate that there is no ordering in the B-site, hence there would probably be no ordering of the oxygen vacancies in the unit cell.

Reported here is the presence of a second phase in both the $\text{Bi}_2\text{Sr}_2\text{Nb}_2\text{GaO}_{11.5}$ and $\text{BaBi}_4\text{Ti}_3\text{GaO}_{14.5}$ X-ray data. This second phase has been identified and refined as $\beta\text{-Bi}_2\text{O}_3$, a well known oxide ion conductor, the presence of which casts doubt on the ionic conductivity of the two Aurivillius phases. Also it is no longer clear what the composition of those phases formed is. Work has been done on samples where $x=0, 0.2, 0.5$ and 1 for the two families $\text{Bi}_2\text{Sr}_2\text{Nb}_2\text{Ti}_{1-x}\text{Ga}_x\text{O}_{12-x/2}$ and $\text{BaBi}_4\text{Ti}_{4-x}\text{Ga}_x\text{O}_{15-x/2}$, these samples have been analysed by powder X-ray diffraction except for $\text{BaBi}_4\text{Ti}_4\text{O}_{15}$ where additional neutron diffraction data were collected.

3.2 Crystallography

3.2.1 $\text{BaBi}_4\text{Ti}_4\text{O}_{15}$

X-ray Refinement

This compound was originally reported by Aurivillius in 1950[4]. It was identified at that time by powder X-ray diffraction as being tetragonal with the space group, $I4/mmm$. Later it was identified as ferroelectric at room temperature and therefore a centrosymmetric space group like $I4/mmm$ would appear incorrect. This compound was remade in St. Andrews by Dr. Susan Blake. It was examined closely using X-ray and neutron diffraction, the original model was found to be incorrect and the orthorhombic

A2₁am space group, as predicted by Newnham[5], was assigned.

Refinement began by adjusting the A2₁am model for the 4-layer Aurivillius structure, Bi₅Ti₃FeO₁₅ already obtained by powder neutron diffraction, to fit the desired stoichiometry. This model was used to refine the lattice parameters but not atomic data, which were fixed. The atomic occupancy of the mixed Ba/Bi sites were examined by setting the sites to purely Bi and refining the occupancies. This is done as the total scattering from these sites will decrease as the percentage of Ba in the site increases. This indicated that the interlayer sites were tending to be purely Bi, with the Ba spread over the remaining two sites. A model with the interlayer site purely set as Bi and the perovskite A-sites permitted to refine for the Ba/Bi ratio was created and compared with a model where all sites have an identical occupancy of Ba/Bi. The disordered model possessed $\chi^2=2.53$ and the refined model possessed $\chi^2=2.52$. This difference is not significant enough to justify the continuation of the ordered model, henceforth the disordered model is used. At this point it was not possible to refine accurately the positions of the oxygen atoms. However, as the compound appeared pure it was taken forward to be analysed by powder neutron diffraction.

Neutron Refinement

The sample was measured for 100 μ Ahr on the POLARIS station at ISIS. The backscattering and 90° banks were used for data analysis. Using the model from the X-ray data the lattice parameters were refined, followed by the atomic co-ordinates and then SIG2 and GAM2, peak profile coefficients. At this point the fit was acceptable with $\chi^2=10$. With a chemically logical

model now established, it was then possible to go on to refine the isotropic thermal parameters for the model. This resulted in a lower χ^2 of approximately 7. This is already a good model of the structure, however it can be improved by refining the thermal parameters as anisotropic. With the exception of the three mixed Ba/Bi sites the thermal parameters for the atoms were permitted to refine anisotropically, this produced a final χ^2 of 4.29 for 115 variables. Attempts to refine the thermal parameters anisotropically for the mixed Ba/Bi sites would be unsuccessful, as although they are stated as being on the same position, it is not necessarily the case that they will be, due to local coordination preferences. For the final refinement the R_{wp} was 2.47 % and 2.94 % for the backscattering and 90° banks respectively.

After this refinement was completed it was left for a duration of time in what was believed to be a satisfactory state. Whilst this work was ongoing two papers reporting the structure were published. The first a synchrotron X-ray study assigned the polar orthorhombic space group $F2mm$ [6]. The second study done using a lab X-ray source reported the structure as $I4/mmm$ [7]. With these suggested structures it was decided to return to the refinement. When re-examining the POLARIS data (Figure-3.1) it was found that it was difficult to convince ourselves of the validity of the $A2_1am$ space group. Looking at the data it was not possible to see any additional peaks due to the orthorhombic distortion and no splitting of any peaks was observed. At this point it was decided to examine data from HRPD, which would be as decisive a test as was possible, as it is the highest resolution powder neutron diffractometer available. It is important to determine whether the structure is present in either $A2_1am$ or $F2mmm$. The $A2_1am$ group will

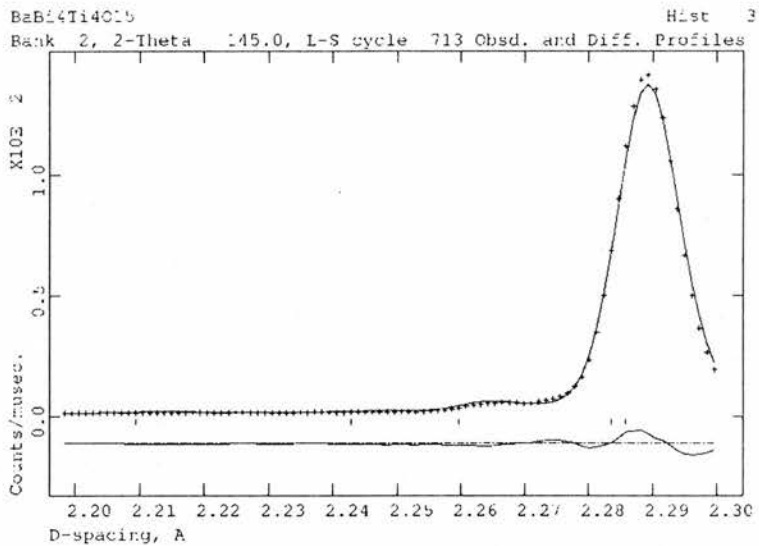


Figure 3.1: BaBi₄Ti₄O₁₅ POLARIS data, 2.2 to 2.3 Å, showing reflections for A2₁am

permit octahedral rotations, the F2mm group permits movement along the polar *a*-axis but not rotation of the octahedra.

The data obtained from HRPD were analysed using only the highest resolution backscattering bank. Before analysing the data it is apparent that the data were of a significantly higher resolution, and a peak splitting can be observed for the most intense peak, as shown in Figure-3.2. The model initially used was that obtained from the A2₁am refinement of POLARIS data. This demonstrated a good fit to the data, but contained many additional possible reflections that were not observed. Hence it was decided to attempt fitting to three higher symmetry space groups, namely F2mm with $a > b$, $b > a$ and Fmmm. Also a fit was attempted for the tetragonal 'parent' group I4/mmm, this refinement was so unstable it would not converge to any minimum value. Previously all 2 and 4-layer Aurivillius phases which have been identified as

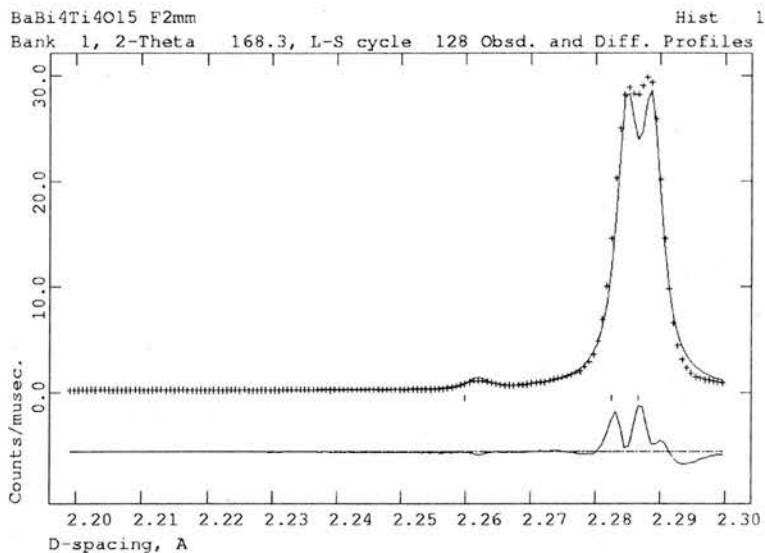


Figure 3.2: BaBi₄Ti₄O₁₅, HRPD data, orthorhombic peak splitting (0 2 10) and (2 0 10). Reflection marks shown for A2₁am

orthorhombic have been described by the A-centred space group A2₁am[8, 9], with the exception of Bi₅Ti₃FeO₁₅. The assignment of F2mm to this structure using single crystal X-ray diffraction is now judged incorrect and is discussed later in the chapter. However, in this case the phase is not present in this space group. This has important implications for the ferroelectric nature of the compound. Most Aurivillius structures are orthorhombically distorted to satisfy the bonding conditions of the perovskite A-site cation. This distortion occurs via a shift of the atomic position of the cation leading to complementary rotations of the perovskite octahedra. It is the movement of the oxygens away from the crystallographic special positions that leads to the lowering of the space group symmetry from face-centred to A-centred. For BaBi₄Ti₄O₁₅ to be identified in any of the face-centred groups would

therefore indicate that the octahedra are less distorted with oxygens located on higher symmetry positions within the unit cell. Due to the ferroelectric behaviour of the compound it is known that it is not centrosymmetric and so would have to be in one of the previously unreported face-centred space groups.

For each of the three face-centred space groups the same refinement procedure was followed; first the lattice parameters then the GAM-1 peak shape were refined. At this point it was noted that the peak shape parameters were ill-behaved and needed to be heavily damped in order to obtain a suitable fit. It was also not possible to switch on all four SIG-1, SIG-2, GAM-1 and GAM-2 parameters. This was not due to an overall lowering of quality of the fit but due to the peak shape losing the peak splitting of the peak at 2.29 Å. Instead of refining the peaks as two separate and distinct peaks the refinement tended to 'smear' the intensity and lose the resolution of the two peaks. Clearly this loss of resolution was unacceptable as this is a key feature of the data collected, hence the refinement of only the GAM-1 parameter. Next the atomic parameters were permitted to refine for both atomic position and thermal coefficients. At this point the SIG-1 parameter was refined and was stable with respect to the splitting of the peak at 2.29 Å. It would appear that the early problems with the peak parameters were due to the inaccuracy of the unrefined model, which was adapted from the A2₁am model. At this point the refinement of the isotropic model was finished and the Rwp and χ^2 values of the refinements were compared, as given in Table-3.1. It was then decided to attempt to improve the fit by permitting the oxygen atom thermal parameters to refine anisotropically, again the Rwp and χ^2 values

are noted, data included in Table-3.1.

Table 3.1: Fit Data for $\text{BaBi}_4\text{Ti}_4\text{O}_{15}$, HRPD Refinements

Space Group	Isotropic		Anisotropic	
	Rwp	χ^2	Rwp	χ^2
F2mm $a>b$	10.69	16.32	9.75	13.66
F2mm $b>a$	10.52	15.80	9.78	13.70

It is not clear from the χ^2 values for the anisotropic refinement of the data as to which of the two settings for the F2mm space group is most likely. Looking at the isotropic refinement the $b>a$ setting is clearly better and hence this is the model that is put forward as the final result, the model is given as Table-3.2 and selected bond lengths as Table-3.3, and displayed as Figure-3.3. This was done as it was considered that the thermal parameters may have been being used in the $a>b$ refinement to ‘fudge’ the data slightly, and that the isotropic model requires a more accurate placement of atoms in the unit cell. As is clear from the Figures-3.4 to 3.6, Rwp and χ^2 values, the quality of the fit to the data collected is good.

Once the structure had been established by Rietveld refinement in the final F2mm space group ($b>a$) the structure was examined for interesting structural features. The Bi/Ba ordering had been re-examined during the previous refinements and it was found that the ordering suggested by the X-ray refinement was again favourable. When looking at layered perovskites most careful attention is paid to the perovskite block as this is the section within which the interesting properties are thought to originate. First, examining the overall structure it is clear the the octahedra are distorted, plotted here (Figure-3.3) is the view of the structure along the $[110]$ direction. It is clear

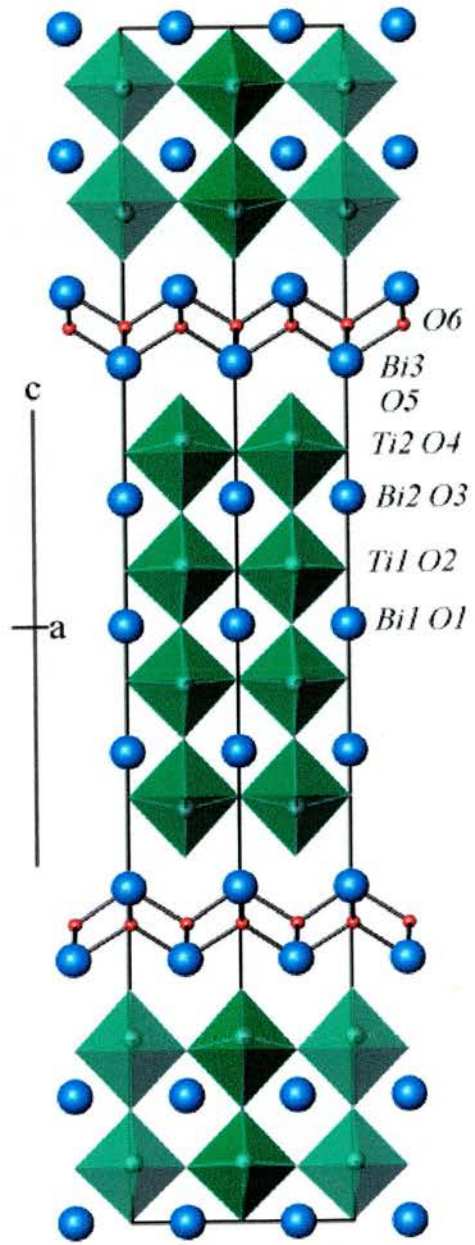


Figure 3.3: $\text{BaBi}_4\text{Ti}_4\text{O}_{15}$, cell view along $[100]$

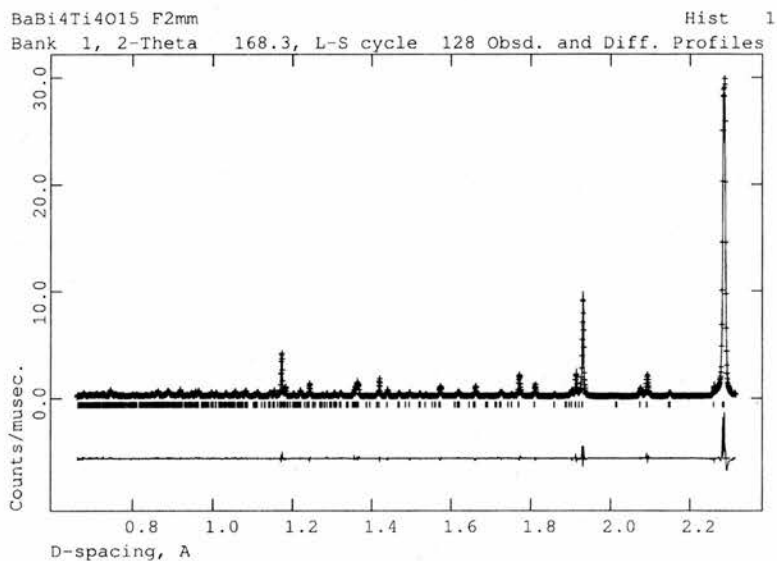


Figure 3.4: BaBi₄Ti₄O₁₅ Rietveld refinement, F2mm, HRPD backscattering data

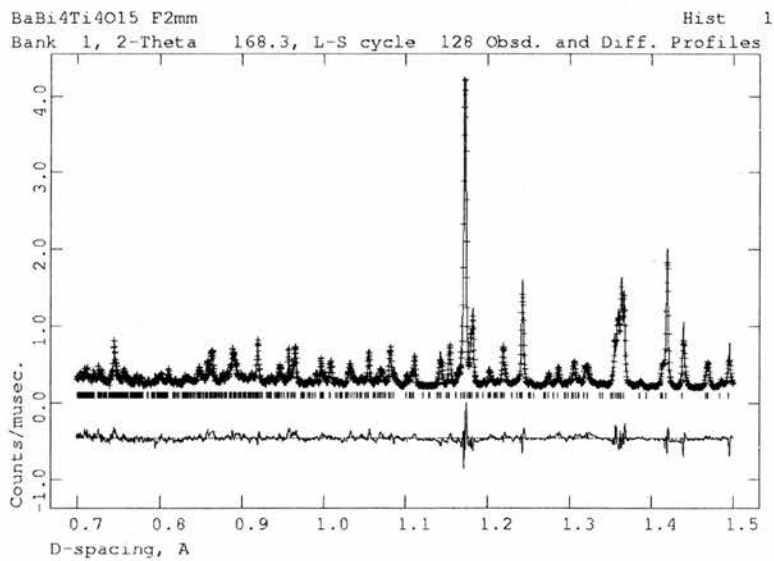


Figure 3.5: BaBi₄Ti₄O₁₅ Rietveld refinement, F2mm, 0.7 to 1.5 Å

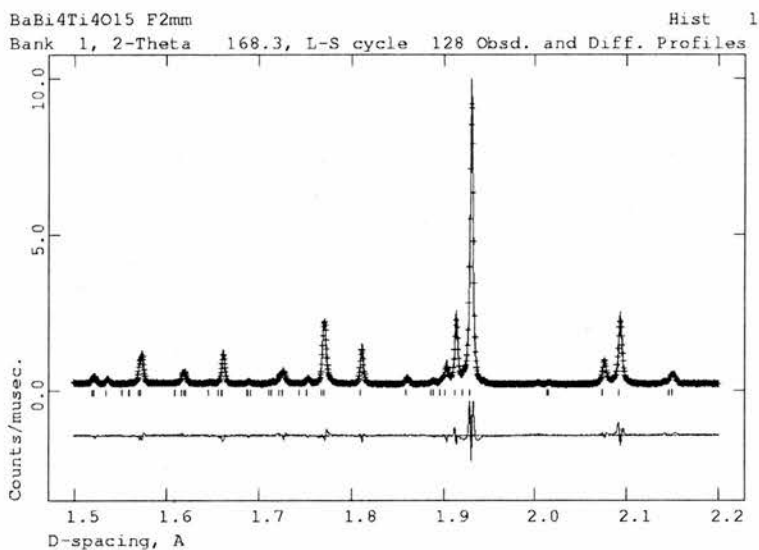


Figure 3.6: BaBi₄Ti₄O₁₅ Rietveld refinement, F2mm, 1.5 to 2.2 Å

from this picture that the Ti⁴⁺ cations are not lying on the exact centres of the perovskite octahedra, also the oxygens around these sites have changed from the ideal octahedral positions to compensate for this movement. Looking closely at just the perovskite sites (Figure-3.7), it can be seen that the mirror plane between the middle two octahedra leads the two inner octahedra to be identical and the two outer octahedra to be identical, but not the outer and inner octahedra. Clearly the inner octahedra appear to have larger displacements of the oxygens in the 'equatorial' position (relative to the *c*-axis), however this is apparently different to the Ti⁴⁺ position, which is closer to the idealised central position of the octahedra. This greater distortion in the octahedra is apparent in Figure-3.8, where the plan view of the outer octahedron is seen to be closer to a square and that of the inner octahedron has a parallelogram profile. Examining the bond distances in the

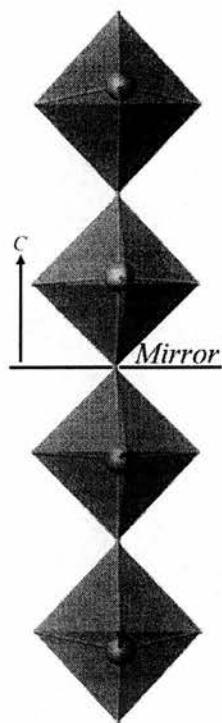


Figure 3.7: $\text{BaBi}_4\text{Ti}_4\text{O}_{15}$ octahedra, showing mirror plane

octahedra (Figure-3.9) it is clear why the outer octahedra appear to possess less distortion of the 'equatorial' oxygens; this due to the size of the 'axial' oxygen bond lengths. Whilst the perovskite B-site to oxygen bond length for the oxygen shared with the inner perovskite octahedra is lengthened, the oxygen adjacent to the interlayer is drastically reduced. Examining the two perovskite B-sites using a bond valence calculation it is found that the inner octahedron has a calculated value of 4.27 with a 7% error and the outer site has 4.14 with a 3% error. Both of these values are slightly higher than would be expected and may indicate a strain in the perovskite block.

The perovskite distortions are important not only in terms of their crystal-

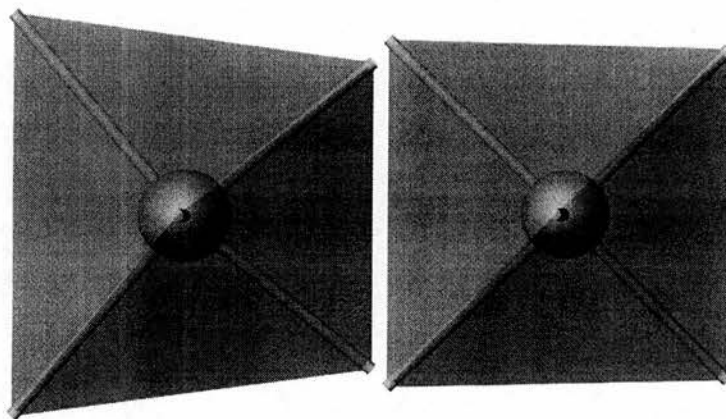


Figure 3.8: $\text{BaBi}_4\text{Ti}_4\text{O}_{15}$ outer(right) and inner(left) octahedra, polyhedra plan view

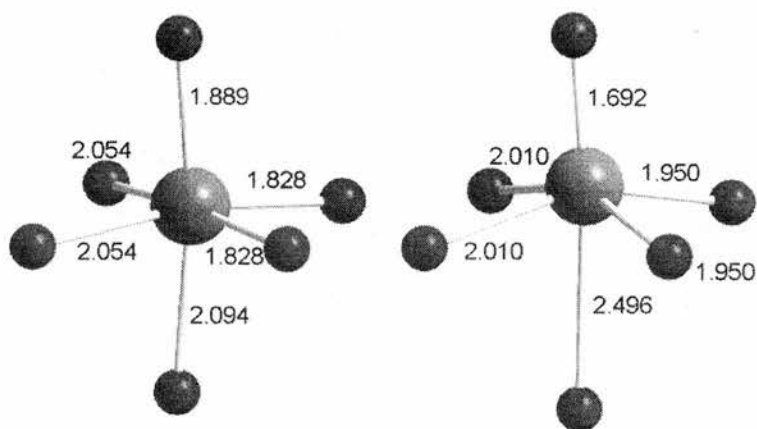


Figure 3.9: $\text{BaBi}_4\text{Ti}_4\text{O}_{15}$ outer(right) and inner(left) octahedra, ball and stick

Table 3.2: BaBi₄Ti₄O₁₅ Atomic Parameters from 25 °C HRPD Data, space group F2mm, a = 5.45083(5) Å, b = 5.46406(5) Å, c = 41.8542(4) Å. R_{WP} = 0.098, χ^2 = 13.7, for 3128 data points and 986 contributing reflections, 0.80 < d < 2.35 Å

Atom	Multiplicity	x	y	z	Uiso/Uequiv x 100
Bi1 ²	4	0.000000 ¹	0.000000	0.000000	4.8(1))
Bi2 ³	8	0.002(7)	0.000000	0.1060(1)	4.8(1)
Bi3 ⁴	8	0.002(7)	0.000000	0.2202(1)	4.0(1)
Ti1	8	0.009(7)	0.000000	0.4502(2)	1.4(2)
Ti2	8	0.019(7)	0.000000	0.3455(2)	1.4(2)
O1	4	0.486(9)	0.000000	0.000000	6.59*
O2	16	0.773(5)	0.216(1)	0.9539(2)	4.62*
O3	8	0.002(5)	0.000000	0.5949(1)	3.40*
O4	16	0.757(6)	0.244(2)	0.8558(1)	2.11*
O5	8	0.002(8)	0.000000	0.6950(1)	4.15*
O6	8	0.266(5)	0.250000	0.250000	1.43*

1. Fixed to define origin of polar axis
2. Occupancy refined to 0.12(4) Ba / 0.88(4) Bi
3. Occupancy refined to 0.44(2) Ba / 0.56(2) Bi
4. Occupancy fixed to 0.0 Ba / 1.0 Bi

Atom	U11	U22	U33	U12	U13	U23
O1	10(2)	4.8(9)	4.7(5)	0.00	0.00	0.00
O2	3.85	1.93	8.44	-1.77(4)	-2.8(6)	1.9(5)
O3	6.1(6)	2.5(4)	1.7(3)	0.00	1.5(9)	0.00
O4	1.7(3)	1.3(3)	3.5(2)	-1.1(2)	1.1(5)	1.2(4)
O5	5.6(6)	6.4(6)	1.1(3)	0.00	-2.7(8)	0.00
O6	1.3(5)	2.2(4)	0.8(2)	0.00	0.00	1.0(6)

Table 3.3: BaBi₄Ti₄O₁₅ Selected Bond Lengths

bond	length Å	bond	length Å	bond	length Å
Bi1 O1	2.80(5)	Bi2 O2	3.04(1)	Bi3 O5	2.928(2)
Bi1 O1	2.65(5)	Bi2 O2	3.04(1)	Bi3 O5	2.928(2)
Bi1 O1	2.733(1)	Bi2 O2	3.29(1)	Bi3 O5	2.92(3)
Bi1 O1	2.733(1)	Bi2 O2	3.29(1)	Bi3 O5	2.92(3)
Bi1 O2	2.58(2)	Bi2 O3	2.771(1)	Bi3 O6	2.34(1)
Bi1 O2	2.58(2)	Bi2 O3	2.771(1)	Bi3 O6	2.34(1)
Bi1 O2	2.58(2)	Bi2 O3	2.77(3)	Bi3 O6	2.25(1)
Bi1 O2	2.58(2)	Bi2 O3	2.76(3)	Bi3 O6	2.25(1)
Bi1 O2	2.89(2)	Bi2 O4	2.47(1)		
Bi1 O2	2.89(2)	Bi2 O4	2.47(1)		
Bi1 O2	2.89(2)	Bi2 O4	2.54(1)		
Bi1 O2	2.89(2)	Bi2 O4	2.54(1)		

bond	length Å	bond	length Å
Ti1 O3	2.496(8)	Ti2 O1	2.094(8)
Ti1 O4	2.01(2)	Ti2 O2	2.05(2)
Ti1 O4	2.01(2)	Ti2 O2	2.05(2)
Ti1 O4	1.95(2)	Ti2 O2	1.83(2)
Ti1 O4	1.95(2)	Ti2 O2	1.83(2)
Ti1 O5	1.692(8)	Ti2 O3	1.889(8)

lography but also in terms of the phenomena that these structural distortions imbue. In the case of $\text{BaBi}_4\text{Ti}_4\text{O}_{15}$ it has been previously documented to be ferroelectric[10]. Perovskites are known to be displacive ferroelectrics and the A-site cation's local environment is highly important. What can be noted is that the $\text{BaBi}_4\text{Ti}_4\text{O}_{15}$ structure is strongly affected by the $[\text{Bi}_2\text{O}_2]^{2+}$ layer and this in part has an influence on the distortion of the perovskite B-site. It is clear that the influence of the Aurivillius interlayer diminishes from the outer perovskite layer to the inner, this in turn leads to a greater distortion of oxygens in the ab -plane to accommodate the bonding requirements of the B-site cation.

3.2.2 $\text{BaBi}_4\text{Ti}_{4-x}\text{Ga}_x\text{O}_{15-x/2}$

X-ray Refinement

This series of compounds was made with $x = 1$ as per the original paper[3] and with $x = 0.2$ and 0.5 . The first step was to replicate the sample made by zur Loye et al. This synthesis was done by Dr. Susan Blake. The X-ray pattern of this structure was examined and compared to that obtained by zur Loye et al. As the two patterns matched, several attempts were made to index the pattern as a single phase, all of these were unsuccessful. The pattern appeared to be successfully indexed except for one peak at $d = 3.19$. This value of d-spacing was compared to those found for the most likely other products and the starting materials. A match was found for $\beta\text{-Bi}_2\text{O}_3$, so a two phase refinement was carried out using the $\text{BaBi}_4\text{Ti}_4\text{O}_{15}$ model and a model for $\beta\text{-Bi}_2\text{O}_3$ [11]. It is possible to extract weight percentages and

relative percentages in a two phase Rietveld refinement in GSAS. This is done by first refining the main phase to give the best quality of fit to the data possible. All possible refinable parameters are used at this point. Once this step is established, all parameters relating specifically to this phase are switched off, the only parameters left on are the background parameters and zero point. To perform the refinement using two phases the second phase is entered. A constraint must be set up such that the sum of the relative abundances of the two phases should equal 1. The refinement is then performed with the histogram scale factor turned off and the two phase scale factors turned on. For this refinement it was judged prudent to also turn on the lattice parameters for the second phase as it was suspected that the composition entered for this phase was not exact due to potential Ga^{3+} doping. The weight percentages of the two phases can then be found in the GSAS generated .LST file.

For the refinement of the single phase problems are created due to the number of peaks from the two phases which overlap. Initially it was attempted to refine both the histogram scale factor and the four peak profile coefficients (GV, GW, GY and LX). It was found that if all of these were refined freely the histogram scale factor was very small and the value of GW too large, this manifested itself in the inability of the refinement to match the intensity of the largest peak as shown in Figure-3.10. Hence the histogram scale factor was not permitted to refine for these refinements, for $x = 1$ it was held at a value of 0.8, when refined the figure was approximately half of this. By holding the value of the overall histogram scale factor to this value it was found that the peak profile parameters were less likely to be ill-defined, as can

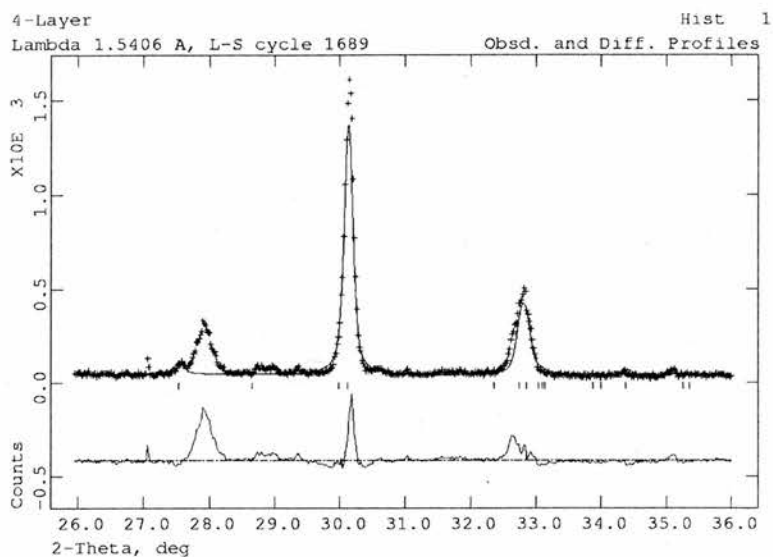


Figure 3.10: $\text{BaBi}_4\text{Ti}_3\text{GaO}_{15}$, poor match to histogram intensity for single phase refinement

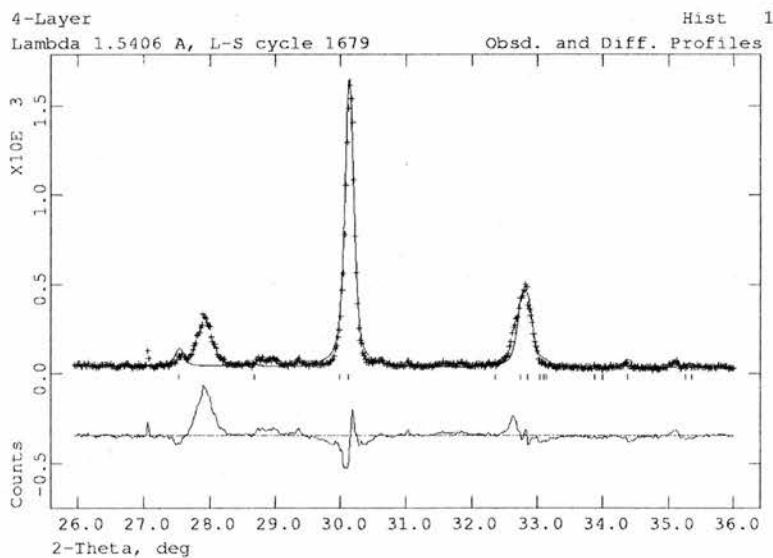


Figure 3.11: $\text{BaBi}_4\text{Ti}_3\text{GaO}_{15}$, improved match to histogram intensity by fixing the scale factor

be seen from Figure-3.11 the fit to the intensity is much better. Whilst the peak profile co-efficients are better behaved they are still not as well behaved as would be desired. It can be observed that the peak shape includes a leading and trailing edge, this is problematic due to the overlapping of so many peaks of the two phases. It has been decided that it is much better to refine the peak shape than to set it to an arbitrary value or not refine it at all, leading to a too narrow a peak profile. These problems with the intensity of the main phase are important, if the main phase is poorly defined then the predicted percentages of the two phases may be incorrectly estimated. This makes the choice of refinable parameters for the two phases very important. Here it was decided that the peak profile coefficients were combining with the histogram scale factor to give a lower χ^2 . This is not due to the peak profile giving a good estimate of all the recorded points, instead it is giving an excellent estimate of the lower portion of the peak slopes and a very poor estimate of the highest points of a peak. Together these are giving a better fit statistically, however, it is a less acceptable fit for the desired purpose of this refinement, where the whole peak must be matched.

Taking the values established for the single phase refinement, all parameters were switched off except the background and zero-point, at this point the second phase was introduced and the constraint set up. This was refined to check the stability and accuracy of the starting model for the second phase. The model was found to give a good fit and the lattice parameters were refined for the second phase to enable a more accurate fit. Attempting to improve the fit the next step was to refine the peak profile coefficients, which resulted in a terminal problem for the refinement. Instead of progressing to

a good match for the peak shape the parameters tended to flatten the peak, attempting to reduce the intensity down to zero. This happened regardless of what damping was applied or what peak profiles were refined. Attempting to estimate the relative percentages using an unrefined peak model of peak profile no. 2 (Pseudo-Voigt) is unrealistic as this results in a very sharp peak with a poor fit to the peak width, instead another peak profile was selected. Using peak profile no. 1 (Gaussian) the peak is fitted very well without the refinement of any parameters, therefore this was the final model used for the description of the peak shape of the second phase. This unusually wide peak shape may be attributed to the second phase being of lower crystallinity than the main phase.

The values extracted for the percentage of the β - Bi_2O_3 impurity phase can be plotted against the level of Ga^{3+} doping, from this it will be clear if the level of doping has an effect upon the formation of the impurity. If the presence of the β - Bi_2O_3 is independent of the Ga^{3+} content then the line will be flat, if the two are directly related there will be some line or curve decreasing with the value of x. Also the values of the lattice parameters for the main 4-layer phase can be compared against composition to ascertain whether this is the same phase in each refinement or not. Shown as Figure-3.12 is the single phase refinement, the improvement given by the two phase refinement is shown as Figure-3.13.

As can be seen from Figure-3.14 the percentage of impurity present is decreasing with decreasing Ga^{3+} content. Indeed the impurity is still decreasing at $x=0.2$ hence it can be said that if any Ga^{3+} is being inserted into the 4-layer phase it must be less than this value. From Table-3.4 it is clear that

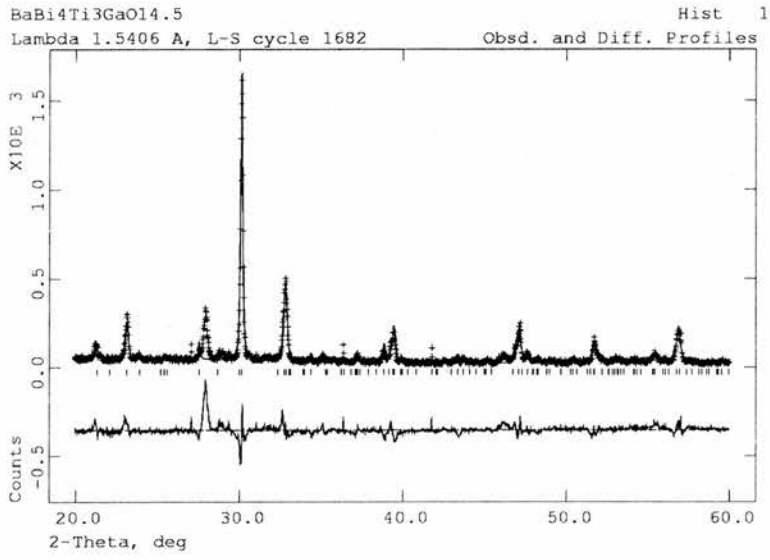


Figure 3.12: BaBi₄Ti₃GaO_{14.5}, single phase refinement

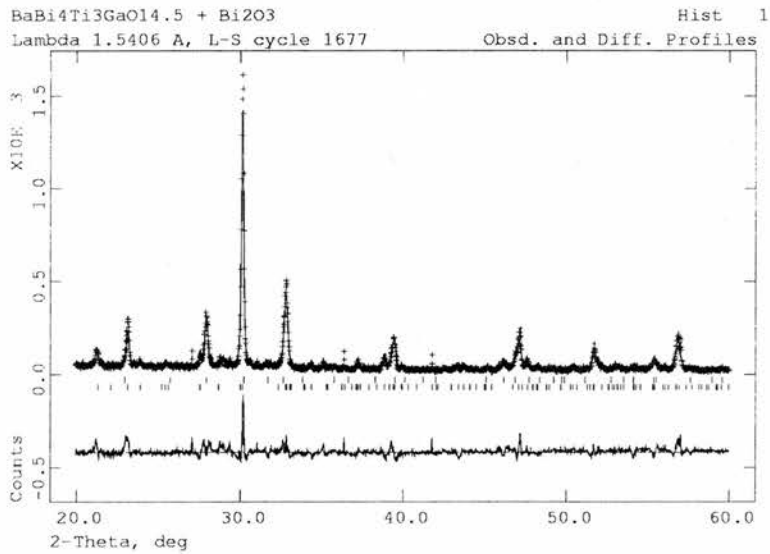


Figure 3.13: BaBi₄Ti₃GaO_{14.5}, two phase refinement

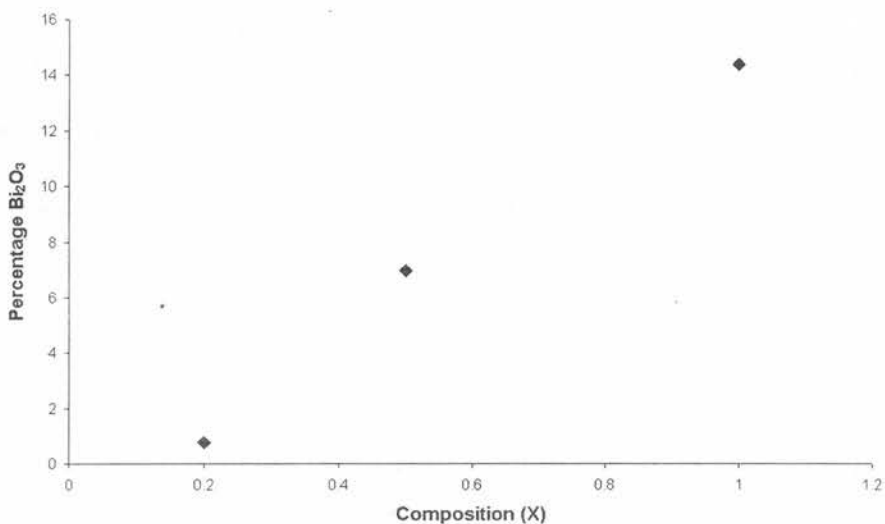


Figure 3.14: 4-Layer $\text{BaBi}_4\text{Ti}_{4-x}\text{Ga}_x\text{O}_{15-x/2}$. Ideal Ga^{3+} content (x) vs. percentage β - Bi_2O_3

Table 3.4: $\text{BaBi}_4\text{Ti}_{4-x}\text{Ga}_x\text{O}_{15-x/2}$ 4-layer unit cell parameters

X	a (Å)	b (Å)	c (Å)
1	5.470(1)	5.453(1)	41.744(8)
0.5	5.470(1)	5.452(1)	41.715(7)
0.2	5.446(1)	5.463(4)	41.770(3)

the lattice parameters of the 4-layer phase are not changing significantly with composition and are therefore in agreement with the idea that the doping limit is below $x = 0.2$. It is also noted that the lattice parameters a and b have switched in $x = 0.2$ so that $b > a$. This is due to the structure being only slightly metrically orthorhombic, the refinement has difficulty in determining a difference between a and b .

3.2.3 $\text{Bi}_2\text{Sr}_2\text{Nb}_2\text{Ti}_{1-x}\text{Ga}_x\text{O}_{12-x/2}$

Refinement

The synthesis of this 3-layer structure was attempted with Ga^{3+} doping levels of $x=1$, $x=0.5$ and $x=0.2$, the $x=1$ sample having been previously prepared by Dr. Susan Blake. Examining the powder pattern obtained from these syntheses it is clear that there is a second phase present in the pattern, assigned as $\beta\text{-Bi}_2\text{O}_3$. The refinement of the two phases was carried out as for the 4-layer phase (Section-3.2.2) to examine the limit of Ga^{3+} solubility in this system.

It was found that the refinement of the 3-layer phase progressed much more smoothly than that for the 4-layer, possibly due to the higher ($I4/mmm$) symmetry assigned to the main phase. It was possible for these structures to refine the histogram scale factor and lattice parameters, without the lattice parameters going outside acceptable limits. The second phase peak shape was defined with the pseudo-Voigt function as for the main phase and this was found to give an acceptable fit to the data. The single phase refinement is shown as Figure-3.15 and the two phase as Figure-3.16.

It can be observed from Figure-3.17 that the trend is for the presence of the impurity to diminish with decreasing Ga^{3+} concentration, to the extent that the impurity has almost vanished at $x = 0.2$. As for the 4-layer phase the conclusion must be that the maximum doping level in this system is below $x = 0.2$, this is backed up by the consistent lattice parameters obtained for the main phase, shown in Table-3.5.

Having now examined both 3 and 4-layer Aurivillius phases for the possibility of substituting Ga^{3+} for Ti^{4+} , it seems clear that the solubility of Ga^{3+} in these systems is very low. It can be stated that the phases published by zur Loye[1, 2, 3] are impure. The presence of an impurity which is itself a very good oxide ion conductor would suggest that the Aurivillius phases produced may not be good oxide ion conductors, as originally believed.

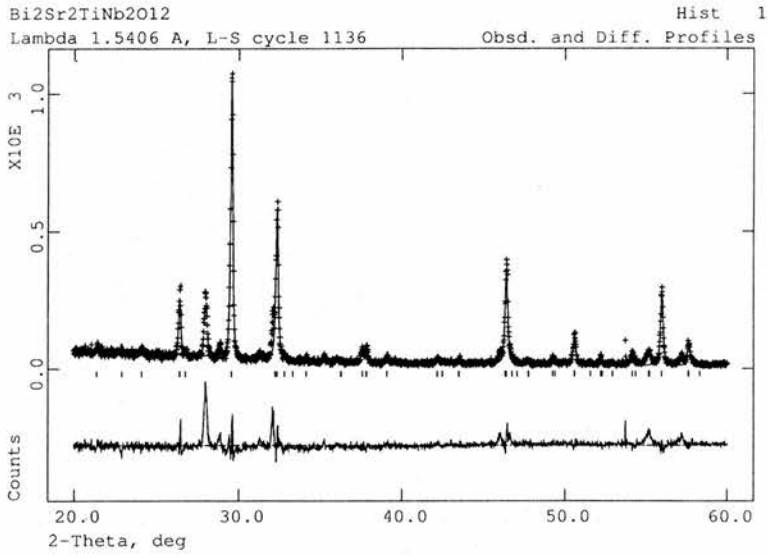


Figure 3.15: $\text{Bi}_2\text{Sr}_2\text{Nb}_2\text{GaO}_{11.5}$, single phase refinement

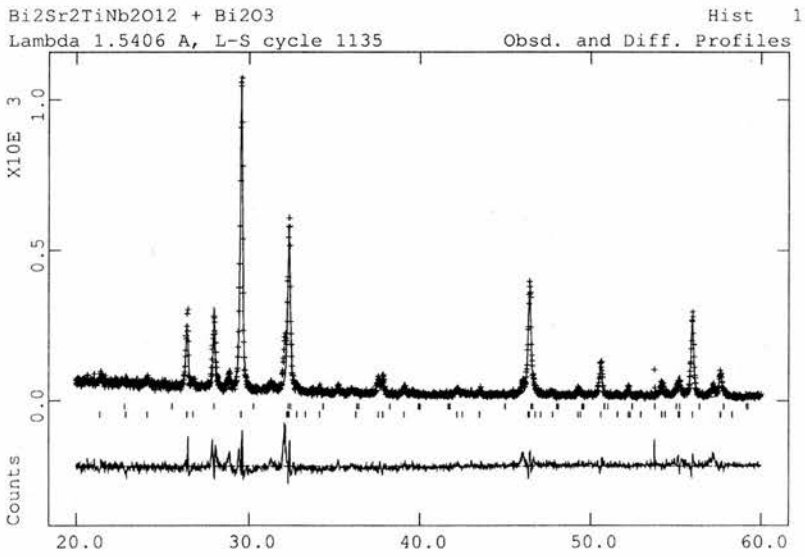


Figure 3.16: $\text{Bi}_2\text{Sr}_2\text{Nb}_2\text{GaO}_{11.5}$, two phase refinement

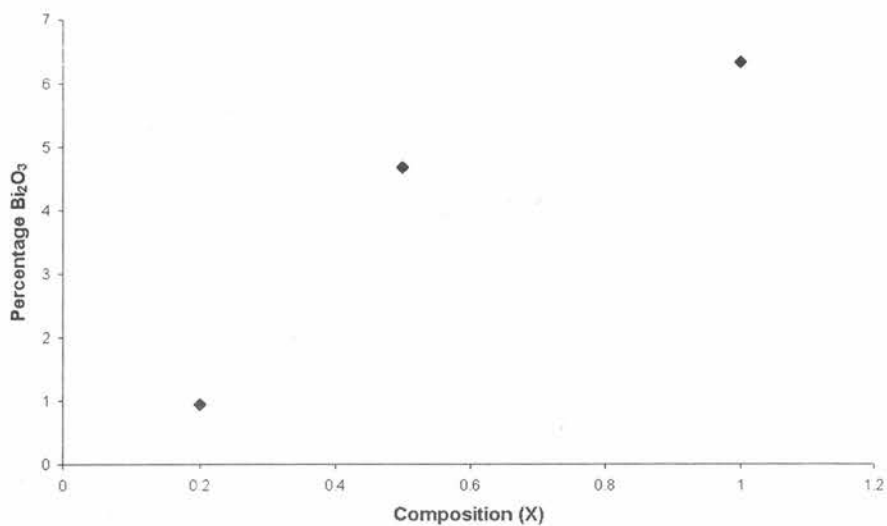


Figure 3.17: $\text{Bi}_2\text{Sr}_2\text{Nb}_2\text{Ti}_{1-x}\text{Ga}_x\text{O}_{12-x/2}$. Ideal Ga^{3+} content (x) vs. percentage $\beta\text{-Bi}_2\text{O}_3$

Table 3.5: $\text{Bi}_2\text{Sr}_2\text{Nb}_2\text{Ti}_{1-x}\text{Ga}_x\text{O}_{12-x/2}$ unit cell parameters

X	a (Å)	b (Å)	c (Å)
1	3.9102(1)	a	33.270(3)
0.5	3.8990(1)	a	33.187(1)
0.2	3.8967(1)	a	33.173(2)

3.3 Aurivillius Phases Containing Fe^{3+}

Aurivillius Phases containing transition metals are very rare. Fe^{3+} containing phases have been examined as the inclusion of a trivalent cation into the perovskite B-site will result in a different distortion of the octahedra. This distortion takes place in an attempt to adjust the bonding requirements for the site to those of the mixed $\text{Ti}^{4+}/\text{Fe}^{3+}$ occupancy. Octahedral distortions in perovskite type structures are known to give rise to ferroelectric character, hence it is for this property that most of the papers to date have focussed. There have been reported 4,5 and 6-layer Aurivillius phases containing Fe^{3+} . $\text{Bi}_7\text{Ti}_3\text{Fe}_3\text{O}_{21}$ [12] is a proposed 6-layer Aurivillius structure which has been examined for both dielectric and magnetic properties, this proposed structure would seem unlikely as no reports of any other 6-layer phases exist. Magnetoelectric measurements have been carried out for $\text{Bi}_6\text{Ti}_3\text{Fe}_2\text{O}_{18}$ and $\text{Bi}_5\text{Ti}_3\text{FeO}_{15}$ [13], 5 and 4-layer structures. All of these papers contain investigations into the properties of these compounds, however very little crystallographic work has been performed upon them. Without in-depth studies of the crystal structure of these phases it is difficult to comment accurately upon their electrical and magnetic properties. Also, increasing the number of layers in the perovskite block would make it more difficult to produce phase pure material as the desired composition becomes more akin to the infinite-layer, ABO_3 type perovskite.

The most detailed study of the crystal structure of these Fe^{3+} containing systems is the work done by Kubel and Schmid[14]. This single crystal X-ray study of the 4-layer $\text{Bi}_5\text{Ti}_3\text{FeO}_{15}$ indicated that at room temperature

the structure adopted Fmm2 symmetry (more commonly written as F2mm, with c as the long axis). It was suggested that there was an orthorhombic-orthorhombic phase transition from the non-centrosymmetric Fmm2 to the centrosymmetric Fmmm, observed at 560 °C by optical measurement. Also stated was the orthorhombic-tetragonal phase change at 750 °C, close to the ferroelectric Curie temperature of 720 °C[15]. This is contrary to more recent work done on other 4-layer Aurivillius phases and on 2-layer SrBi₂Ta₂O₉ (SBT), where it has been shown that an orthorhombic to orthorhombic phase transition corresponds to the ferroelectric transition[16]. Hence in this study we hope to clearly identify, using neutron diffraction, the space group of the room temperature phase and the phase transition(s) which the structure undergoes. By using powder neutron diffraction it is hoped that the space group of the compound and its transitions can be more clearly observed. This is due to the superiority of neutron scattering compared to X-ray scattering in the detection of oxygen atoms in these systems. The oxygen positions are of vital importance when attempting to identify the octahedral rotations and distortions taking place. Supplementary to the work done by Ismailzade an a.c. impedance experiment has been performed in order to determine T_C .

3.4 Bi₅Ti₃FeO₁₅

3.4.1 Neutron Data

Powder neutron diffraction data at 25 °C were collected on POLARIS, the variable temperature runs were collected on HRPD, both at ISIS.

25 °C Study

The room temperature structure proposed by Kubel and Schmid permits movement of all the atoms along the polar a axis, however, it does not permit rotations of the octahedra in the perovskite layer. So instead of beginning with the 'F2mm model', $A2_1am$, was used. It can be seen from Figure-3.18 that the F2mm space group does not adequately describe all of the peaks found in the neutron data, particularly those peaks at approximately 2.34 Å, and 2.37 Å. These additional peaks are due to the freedom of the oxygens within the octahedra to rotate, and are indicative of a lowering of symmetry away from face-centred. Once the basic model was entered the refinement was begun by checking that the new lattice parameters were accurate. Once these were acceptably close to the experimental findings, i.e. that the calculated and experimental peaks had begun to overlap, the lattice parameters were permitted to refine.

The next stage was to refine the atomic co-ordinates of the atoms in the unit cell except those for the B-site cations. The B-sites were not refined due to the scattering from mixed Ti^{4+} and Fe^{3+} , the neutron scattering length (b) for Ti^{4+} is -3.438×10^{-15} m, and 9.45×10^{-15} m for Fe^{3+} . Due to there being three times as much Ti^{4+} as Fe^{3+} the neutron scattering from the B-sites is effectively zero, making it impossible to refine them. Positions therefore are held at those values found for the X-ray refinement. Next the peak shape parameters GAM-1, GAM-2 and SIG-2 were refined, followed by the thermal parameters for all sites except the B-sites. This produced a good model, however, on close examination of the Rietveld plot it was found that certain

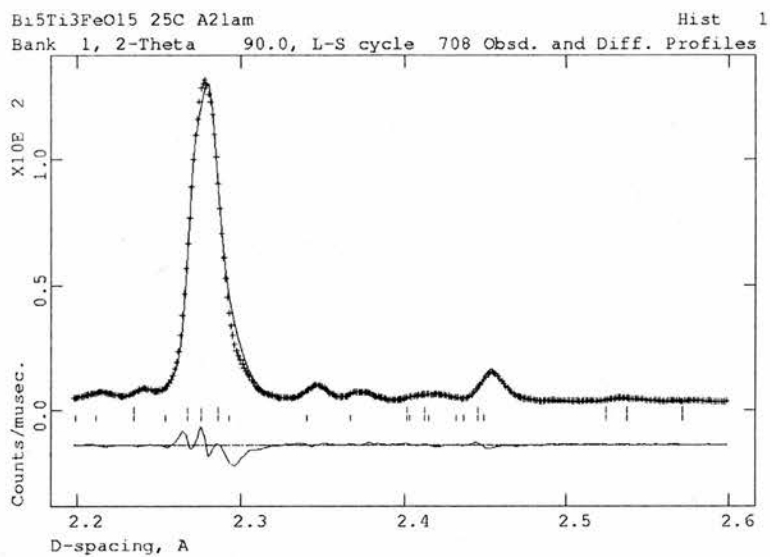


Figure 3.18: $A2_1am$ vs $F2mm$ space groups. Upper marks; $F2mm$, lower marks; $A2_1am$

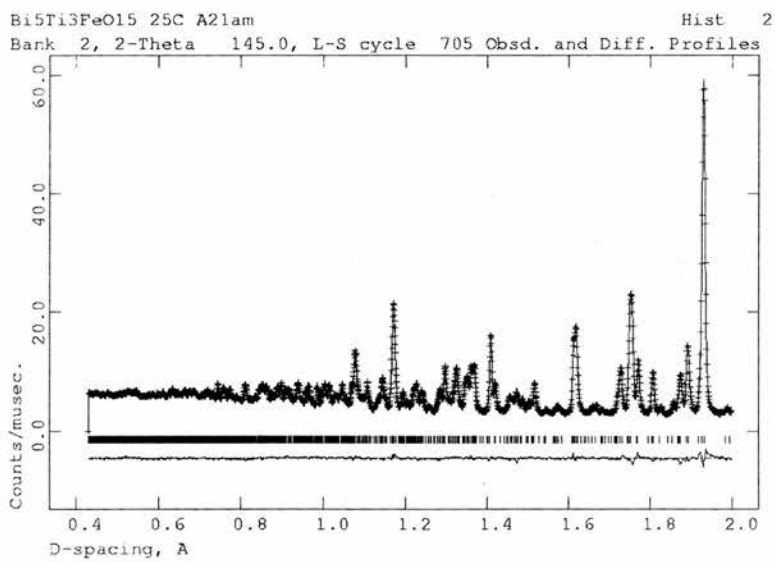


Figure 3.19: $Bi_5Ti_3FeO_{15}$, 0.4 to 2 Å, 145° bank

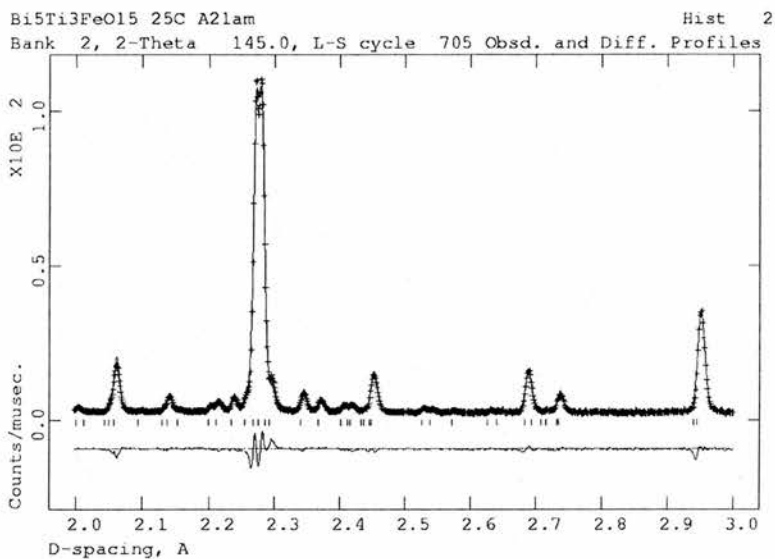


Figure 3.20: $\text{Bi}_5\text{Ti}_3\text{FeO}_{15}$, 2 to 3 Å, 145° bank

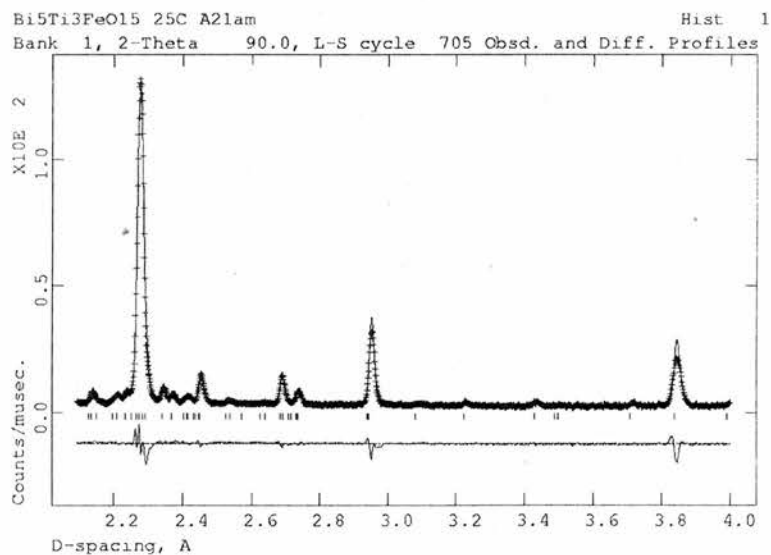


Figure 3.21: $\text{Bi}_5\text{Ti}_3\text{FeO}_{15}$, 2.1 to 4 Å, 90° bank

Table 3.6: $\text{Bi}_5\text{Ti}_3\text{FeO}_{15}$ atomic parameters from 25 °C neutron data, space group $A2_1am$, $a = 5.4698(1) \text{ \AA}$, $b = 5.4389(1) \text{ \AA}$, $c = 41.197(1) \text{ \AA}$. $R_{WP} = 0.032$, $\chi^2 = 5.3$, for 7878 data points and 4632 contributing reflections, $0.43 < d < 4.2 \text{ \AA}$

Atom	Multiplicity	x	y	z	Uiso*100
Bi1	4	0.250000 ¹	0.2494(7)	0.000000	1.28(5)
Bi2	8	0.2381(11)	0.2446(5)	0.1045(1)	0.73(3)
Bi3	8	0.2297(8)	0.2678(5)	0.2195(1)	1.07(4)
Ti1 ²	8	0.250000	0.250000	0.450000	0.50
Ti2 ²	8	0.250000	0.250000	0.350000	0.50
O1	4	0.3362(11)	0.1772(9)	0.500000	0.34(8)
O2	8	0.6073(9)	0.5460(7)	0.0518(1)	1.22(7)
O3	8	0.3250(10)	0.3060(7)	0.4050(1)	0.72(6)
O4	8	0.5325(9)	0.4854(6)	0.1385(1)	0.57(5)
O5	8	0.2911(11)	0.2034(7)	0.3049(1)	1.36(8)
O6	8	0.5045(8)	0.4888(6)	0.2506(1)	0.44(4)
O7	8	0.0333(11)	-0.0299(7)	0.0394(1)	1.17(6)
O8	8	0.0832(9)	0.0323(6)	0.1469(1)	0.43(5)

1. Fixed to define origin of polar axis
2. Occupancy fixed to 0.75 Ti / 0.25 Fe

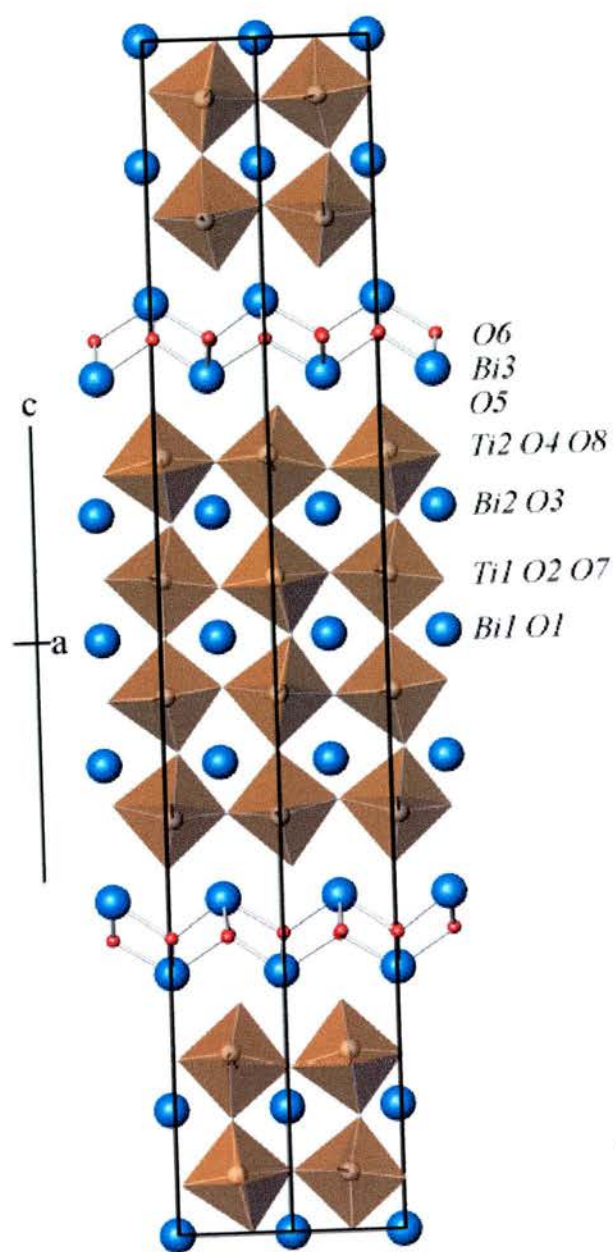


Figure 3.22: $\text{Bi}_5\text{Ti}_3\text{FeO}_{15}$ Cell View Along $[110]$

Table 3.7: Bi₅Ti₃FeO₁₅ bond lengths at 25 °C

bond	length Å	bond	length Å	bond	length Å
Bi1 O1	3.148(6)	Bi2 O2	3.388(4)	Bi3 O5	2.606(5)
Bi1 O1	2.374(7)	Bi2 O2	2.554(4)	Bi3 O5	3.235(5)
Bi1 O1	2.299(6)	Bi2 O3	2.310(5)	Bi3 O5	3.247(4)
Bi1 O1	3.231(6)	Bi2 O3	3.246(5)	Bi3 O5	2.596(4)
Bi1 O2	3.314(4)	Bi2 O3	2.464(5)	Bi3 O6	2.313(4)
Bi1 O2	2.531(4)	Bi2 O3	3.115(5)	Bi3 O6	2.217(4)
Bi1 O2	2.531(4)	Bi2 O4	2.502(4)	Bi3 O6	2.233(4)
Bi1 O2	3.314(4)	Bi2 O4	2.318(4)	Bi3 O6	2.466(4)
Bi1 O7	2.520(5)	Bi2 O7	3.268(4)		
Bi1 O7	2.542(5)	Bi2 O7	3.341(3)		
Bi1 O7	2.542(5)	Bi2 O8	2.259(4)		
Bi1 O7	2.520(5)	Bi2 O8	2.981(4)		

peaks were not being fitted accurately. This was examined and attributed to a false minimum created by the oxygen displacements. The oxygen atom (O8) in the refinement was moved by GSAS to below 0 for both the x and y co-ordinates and stabilised below that value at the false minimum. The true values were in fact higher than 0 and if started above 0 will stabilise there in what is an improved fit to the data, shown as Figures-3.19 to 3.21. The final structural model is tabulated in Tables-3.4.1 and 3.4.1, and shown as Figure-3.22. It is difficult to comment upon the octahedral distortions of the perovskite layer as it was not possible to accurately identify a definite position for the B-site cations. It is probable that the Fe³⁺ and Ti⁴⁺ do not actually occupy an absolutely identical position and are in fact on very slightly different positions favoured by their valencies. Due to this and the lack of strong scattering from the B-sites, analysis of the octahedral tilting is limited to examining the octahedra in relation to each other.

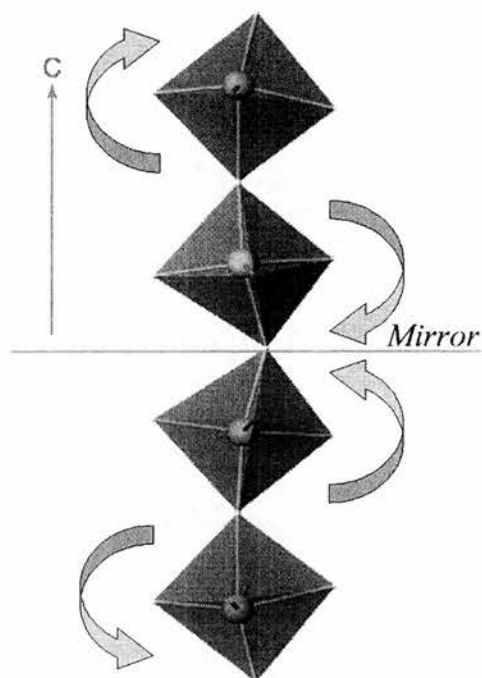


Figure 3.23: Effect of the mirror plane on octahedral rotations in the perovskite block of $\text{Bi}_5\text{Ti}_3\text{FeO}_{15}$

It can be observed that the octahedra of the perovskite block must obey the symmetry of the space group. Therefore the two inner octahedra must be mirror images of one another, also the outer octahedra must display the same behaviour. Here the outer octahedra can be seen to be rotating in the opposite direction to the inner octahedra. In notation analogous to that by Glazer[17] the octahedra can be described as being $- + -$, along the c -axis. This is highlighted in Figure-3.23. Next, the compound was examined using variable temperature powder neutron diffraction to examine the phase change(s) present.

Elevated Temperature Study

Data were collected at temperatures up to and including 800 °C, this is high enough to identify accurately the lattice transitions. The model used for the refinements up to and including 700 °C was the $A2_1am$ model from the room temperature refinement, above 700 °C the tetragonal $I4/mmm$ space group is assigned. It can be seen from Figure-3.24 that the additional peaks due to the orthorhombic distortion are present at both 650 °C and 700 °C but not at 750 °C. The data were examined carefully to see if the first phase transition reported by Kubel and Schmid (approximately 560 °C) could be identified. Clearly from Figure-3.25 and Table-3.4.1 there is no merging of the a and b axes. There is a slight decrease in the quality of the fit to the data around 560 °C, which is assumed to be due to the diminishing intensity of the weaker orthorhombic peaks. The plot of the c -axis against temperature (Figure-3.26) was examined, for a change in the slope of the graph similar to that found for the 2-layer $Sr_{0.85}Bi_{2.1}Ta_2O_9$. For $Sr_{0.85}Bi_{2.1}Ta_2O_9$ an orthorhombic to orthorhombic phase transition can be observed by the change in slope at the point where the phase change occurs. This change in slope is not present and neither is the slight increase in orthorhombicity found for the 2-layer analogue.

Due to the lack of any change in the slope of the c -axis (Figure-3.26) or an increase in the orthorhombicity (Figure-3.27), there is no evidence from the variable temperature powder neutron diffraction data for an intermediate phase transition. Due to this it would appear likely that the structure undergoes a ferroelectric transition at the orthorhombic to tetragonal phase

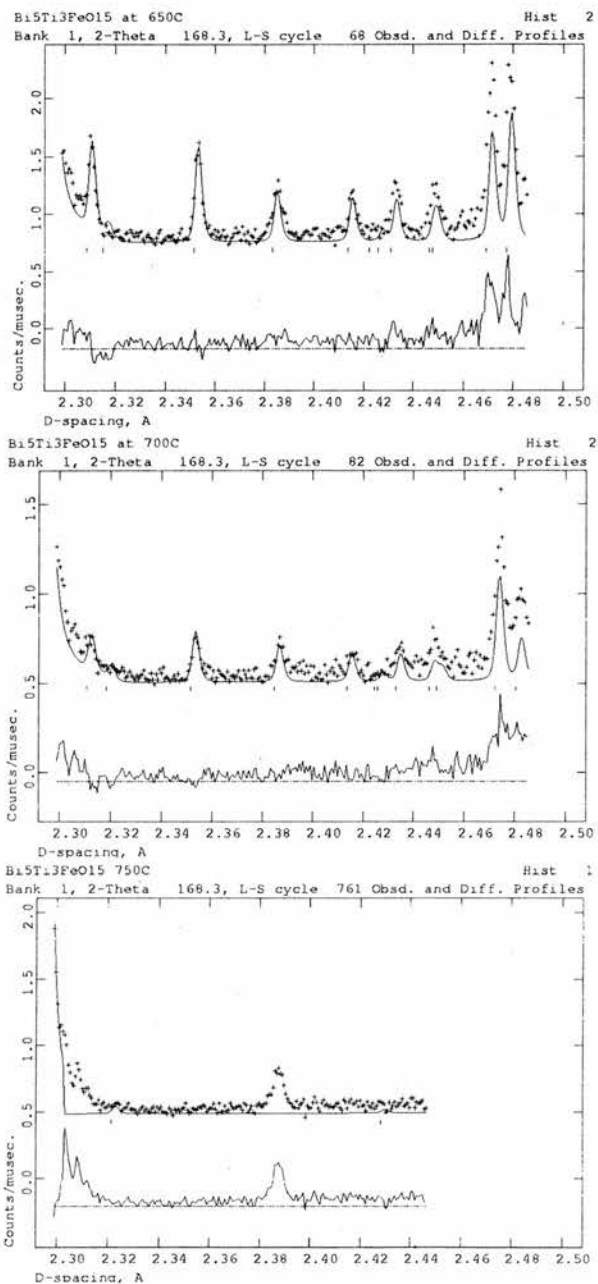


Figure 3.24: Bi₅Ti₃FeO₁₅ phase transition show by orthorhombic peaks present in 650 °C and 700 °C, A₂1am refinements, e.g. at 2.47 and 2.479 Å, no longer present in 750 °C, I4/mmm, refinement.

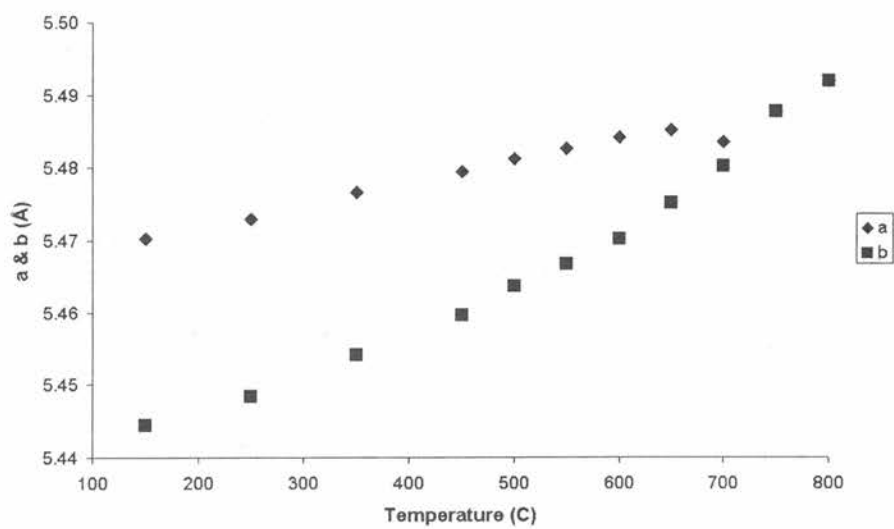


Figure 3.25: $\text{Bi}_5\text{Ti}_3\text{FeO}_{15}$, *a* and *b* vs temperature

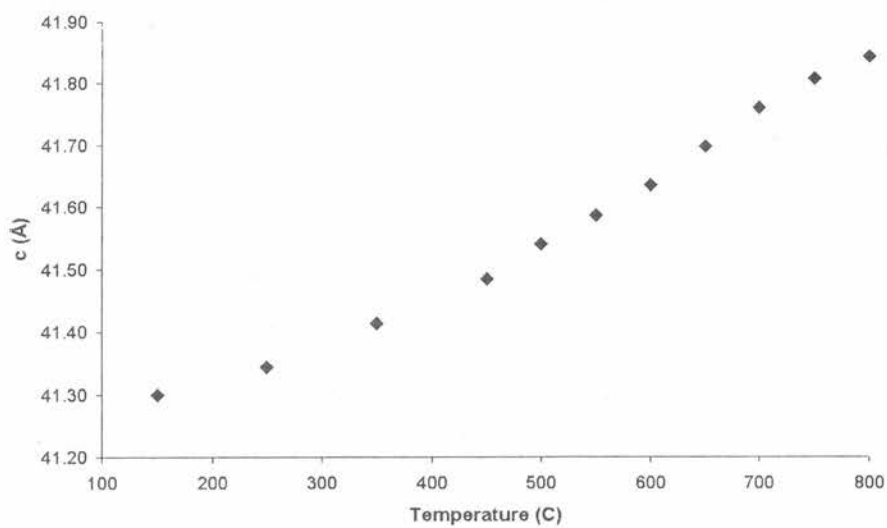


Figure 3.26: $\text{Bi}_5\text{Ti}_3\text{FeO}_{15}$, *c* vs temperature

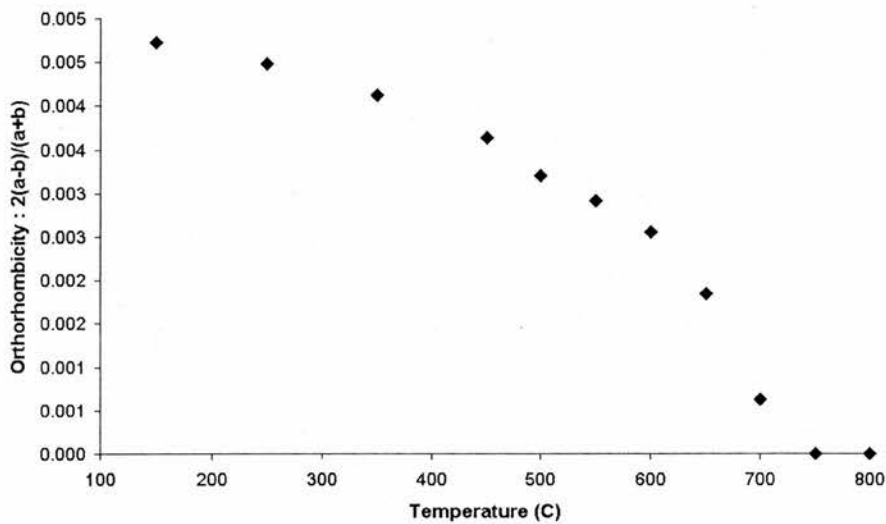


Figure 3.27: $\text{Bi}_5\text{Ti}_3\text{FeO}_{15}$, orthorhombicity ($2(a-b)/(a+b)$) vs temperature

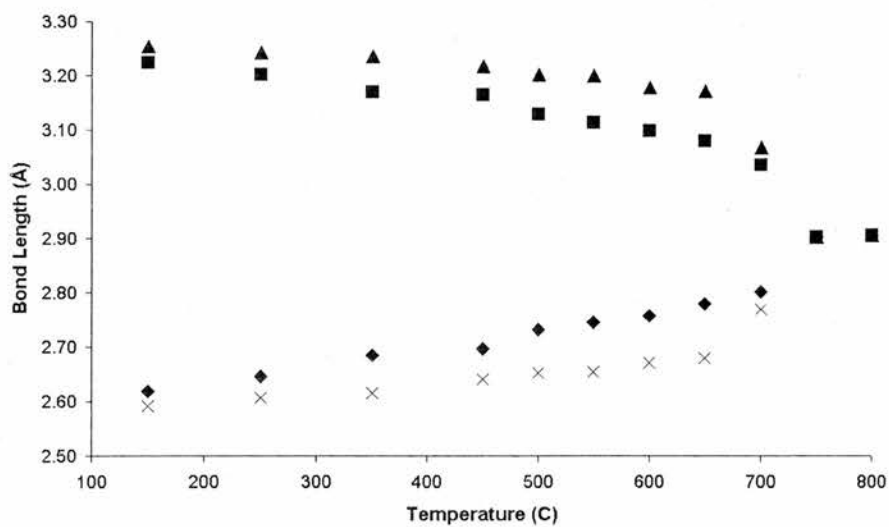


Figure 3.28: $\text{Bi}_5\text{Ti}_3\text{FeO}_{15}$, Bi3 apical Bi-O bond lengths vs. temperature

Table 3.8: Bi₅Ti₃FeO₁₅ Variable Temperature Lattice Data

Temp.	Sp. Grp.	a	b	c	χ^2
150	A2 ₁ am	5.47035(6)	5.44453(5)	41.2993(5)	1.597
250	A2 ₁ am	5.47299(6)	5.44845(5)	41.3444(5)	1.611
350	A2 ₁ am	5.47674(6)	5.45418(5)	41.4142(5)	1.532
450	A2 ₁ am	5.47950(5)	5.45956(5)	41.4864(4)	1.455
500	A2 ₁ am	5.48130(4)	5.46373(3)	41.5425(3)	2.653
550	A2 ₁ am	5.48268(4)	5.46677(3)	41.5879(3)	1.921
600	A2 ₁ am	5.48418(3)	5.47017(3)	41.6373(2)	3.428
650	A2 ₁ am	5.48518(4)	5.47500(4)	41.6983(3)	5.423
700	A2 ₁ am	5.48367(6)	5.47985(7)	41.7604(3)	3.687
750	I4/mmm	3.88035(2)	a	41.8076(4)	5.328
800	I4/mmm	3.88335(2)	a	41.8431(4)	4.266

transition. It can be considered that there is no phase transition present at 560°C therefore the ferroelectric phase transition would be expected at 720°C. The transition that Kubel and Schmid published may have appeared due to the incorrect assignment of the space group for the lower temperature data.

From the change in the apical Bi-O bond lengths, i.e. interlayer Bi3 to apical O of perovskite block, it should be possible to determine whether the phase transition is first or second-order. If the bond lengths are continuous in their change as they approach T_C then the change is second-order. Were the bond lengths not to change in a continuous fashion, but were instead to change suddenly then the transition would be first-order. From the plot of the Bi-O apical bond lengths (Figure-3.28) it can be seen that the transition is very difficult to define. Two of the bond lengths appear to show a first-order transition and the other two bond lengths show a second-order transition. It has been noted that the first and second-order transitions as are defined

classically are extremes. A first order transition may show some continuous change, this makes this method for the determination of the phase change open to some degree of interpretation. From the plot of apical Bi-O bond lengths it could be inferred that the phase transition is first-order. Therefore an intermediate phase, such as Amam as observed for $\text{Sr}_{0.85}\text{Bi}_{2.1}\text{Ta}_2\text{O}_9$, would not be expected.

Examining the effect of increasing temperature on the structure can be done by examining the Bi-O bond lengths. From these bond lengths the first-order nature of the phase transition will be apparent. Examining the change in the environment around the two 12-coordinate perovskite A-sites will demonstrate the effect of temperature at the local structural level. The bonds of the inner Bi^{3+} site can be plotted against temperature for the bonds in the Bi-O plane and for the bonds to oxygen ions in the Ti-O plane, above and below. From Figure-3.29 it is observed that the in-plane bonding, whilst not constrained by symmetry to be two pairs of equivalent bonds, appears to deviate only slightly from this arrangement. The increase in temperature has very little influence on the bonds until 700 °C where the bonds appear to be converging, at 750 °C, when the refinement is tetragonal, they are constrained equal. From these bond lengths it would appear as if the structure is undergoing a first-order transition. Figure-3.30 shows the plot of the out of plane bonding. Here, as the oxygens are placed on either side of an atom lying on a mirror-plane then the bond lengths will mirror one another. This results as can be seen from the plot, in four different sets of bond lengths, shown as Figure-3.31. It is interesting to note that there appears to be one distinctly longer bond length and three shorter distances. In this case the

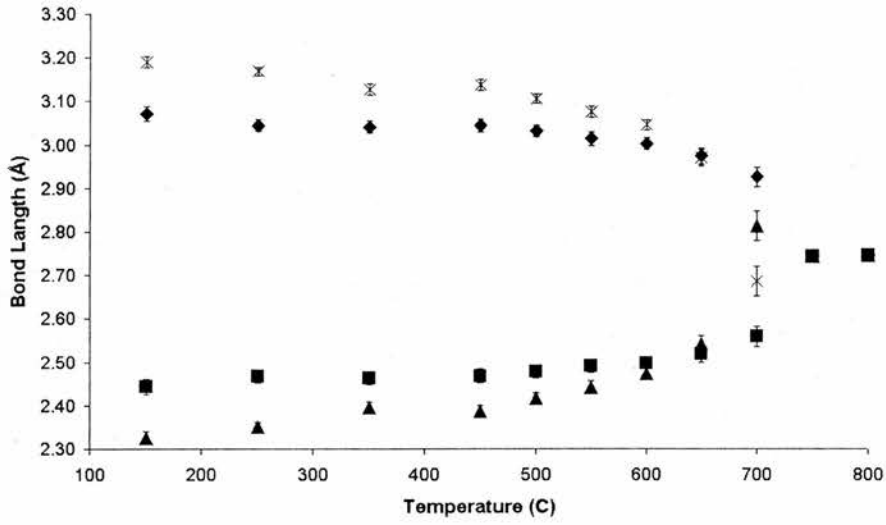


Figure 3.29: $\text{Bi}_5\text{Ti}_3\text{FeO}_{15}$, Bi1 equatorial bond lengths vs temperature

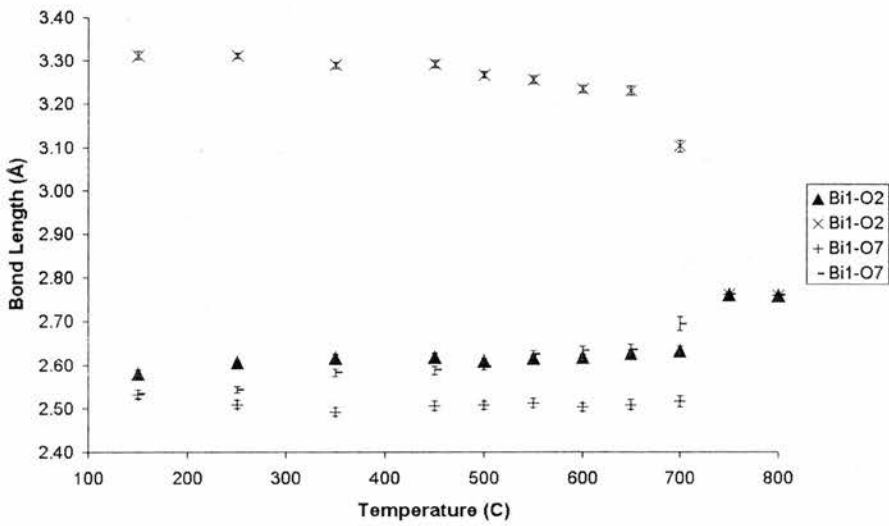


Figure 3.30: $\text{Bi}_5\text{Ti}_3\text{FeO}_{15}$, Bi1 to O2 and O7, bond lengths vs temperature

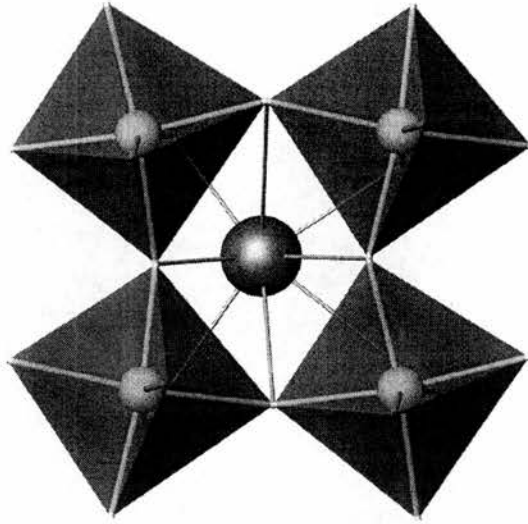


Figure 3.31: $\text{Bi}_5\text{Ti}_3\text{FeO}_{15}$, plan view of inner perovskite octahedra, showing off-centre displacement of Bi1

Bi is positioned closer on the ab -plane to one oxygen, the distortion of the BO_6 octahedra brings two other oxygens closer and one is necessarily further away. The behaviour of these bonds, and therefore the Bi^{3+} ion, is not discretely first-order, but appears predominantly so. In Figure-3.30 there are two pairs of bond lengths, one indicated by a X shape and the other by a triangle. These two bond lengths appear relatively unchanged by the increase in temperature, though they are slowly converging. The other two pairs, indicated as a cross and a dash, show a much larger effect and can be observed to converge also. The behaviour being more pronounced due to the large difference in the lower temperature bond lengths. The final tetragonal bond length is an approximate average of the two converged distances and corresponds to a definite discontinuity.

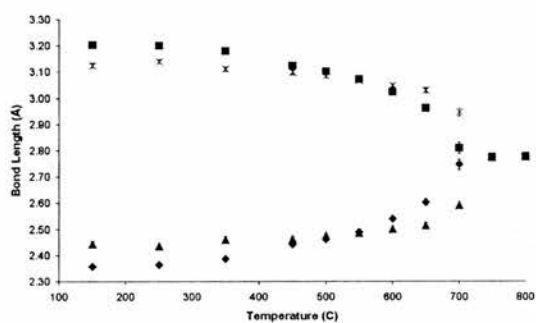


Figure 3.32: $\text{Bi}_5\text{Ti}_3\text{FeO}_{15}$, Bi2 equatorial bond lengths vs temperature

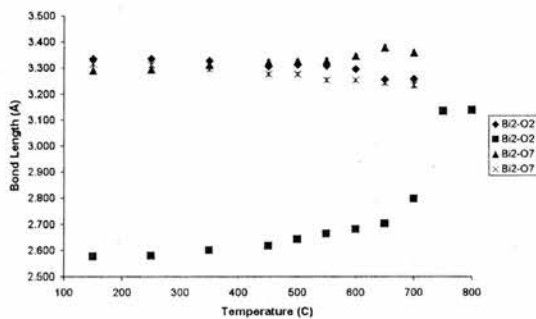


Figure 3.33: $\text{Bi}_5\text{Ti}_3\text{FeO}_{15}$, Bi2 to O2 and O7, bond lengths vs temperature

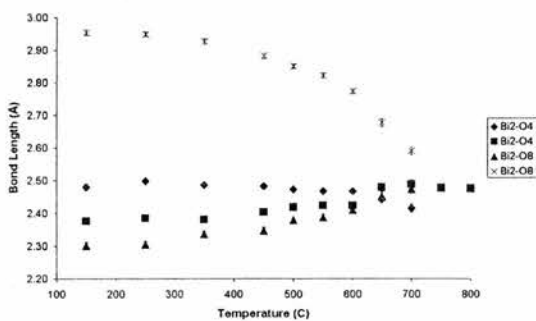


Figure 3.34: $\text{Bi}_5\text{Ti}_3\text{FeO}_{15}$, Bi2 to O4 and O8, bond lengths vs temperature

For the outer Bi^{3+} site, Bi1, the bonding is more complex as it is possible to have 12 different bond lengths. For ease of analysis these have been plotted as three graphs, corresponding to the three different oxygen positions found in the final tetragonal refinements. These correspond to the bonding in the plane and to the bond from above the Bi-O plane and also from below. The plot of the in-plane bonding, Figure-3.32, shows that the bonds are, though not constrained to be so, approximately 'paired'. This is similar to the inner Bi site, however, unlike the inner Bi site there is a definite gradual merging of these two pairs. The discontinuity of a first-order transition is harder to discern, indeed it is not possible to confidently describe this as showing first-order behaviour. The plot of the bonding to the oxygens in the inner BO_6 octahedra, Figure-3.33, shows that there are three longer bonds and one shorter one. The longer bonds are expected, as the perovskite block cations are all shifted along c towards the Bi_2O_2 interlayer. Correspondingly in the plot of the bonds to the oxygens in the outer BO_6 octahedra, Figure-3.34, there are three shorter bonds and one longer.

What is observed is behaviour not unlike that of the Bi1 site. Figure-3.33 shows that the shorter bond and one of the longer bonds appear to converge prior to the tetragonal phase change. As with the inner Bi site the other two bond distances are relatively unchanged. For Figure-3.34 the description is very similar, here the longer bond and one of the shorter bonds converge before T_C , the other two bonds remaining similar. In both of the out of plane plots the bonding appears to show some first-order and some second-order behaviour. It is noted that it is not unusual for a first-order transition to display some second-order behaviour.

3.4.2 a.c. Impedance

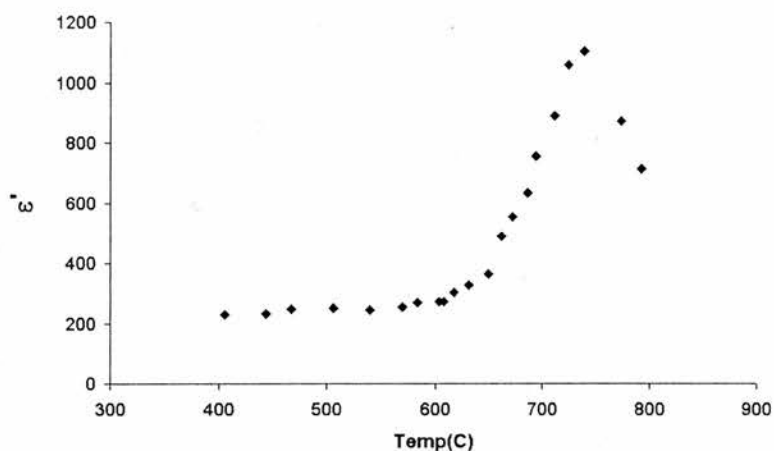


Figure 3.35: $\text{Bi}_5\text{Ti}_3\text{FeO}_{15}$ a.c. impedance plot

Data from an a.c. impedance experiment were measured over three sweeps, two in an increasing temperature gradient and one on a decreasing slope. The data obtained have been plotted as the curve of the sample permittivity against temperature, shown a Figure-??. Clearly the curve has a maximum point at around 710 - 720 °C. This is the ferroelectric Curie temperature (T_C) and coincides with the temperature of the phase transition from $A2_1am$ to $I4/mmm$.

3.5 Summary

The powder X-ray diffraction study of the Ga^{3+} doped phases shows that it is very difficult to obtain phase purity. For the two series $\text{BaBi}_4\text{Ti}_{3-x}\text{Ga}_x\text{O}_{15-x/2}$

and $\text{Bi}_2\text{Sr}_2\text{Nb}_2\text{Ti}_{1-x}\text{Ga}_x\text{O}_{12-x/2}$ it has been demonstrated experimentally that a phase pure compound has not been established, even for doping as low as $x = 0.2$. The main impurity phase in these reactions has been established as Bi_2O_3 , itself a very well known and good oxide ion conductor. With the presence of an oxide ion conductor, the main Aurivillius phase, the exact composition of which is still unknown, cannot be assumed to be an oxide ion conductor.

The 4-layer Aurivillius phase $\text{BaBi}_4\text{Ti}_4\text{O}_{15}$ has been identified in the $F2mm$ setting using powder neutron diffraction. It is clear from the ferroelectric behaviour of this material that it cannot be $I4/mmm$. However, at the time of writing this another paper has been published on the structure of $\text{BaBi}_4\text{Ti}_4\text{O}_{15}$ [18], this time reported in space group $A2_1am$. In this paper no attempt to identify the validity of $A2_1am$ versus $F2mm$ has been made. Although it is noted that the $A2_1am$ model fits the data well, it is possible that this is due to the large number of variables that the lower symmetry structure permits.

The structure of $\text{Bi}_5\text{Ti}_3\text{FeO}_{15}$ has been established as having $A2_1am$ symmetry at less than 750°C . The material has been identified as undergoing only one transition; from orthorhombic to tetragonal at T_C . Both of these findings are contrary to the single crystal study of Kubel and Schmid. The incorrect identification of the compound in $F2mm$ can be attributed to the use of X-ray data. The additional phase transition observed is also thought to have been due to incorrect assignment of the lower temperature space group. The T_c has been confirmed to be 720°C by a.c. impedance spectroscopy, in accordance with previous work.

References

- [1] K. R. Kendall, J. K. Thomas, and H.-C. zur Loye, *Solid State Ionics*, 1994, **70/71**, 221.
- [2] J. K. Thomas, K. R. Kendall, and H.-C. zur Loye, *Solid State Ionics*, 1994, **70/71**, 224.
- [3] K. R. Kendall, J. K. Thomas, and H.-C. zur Loye, *Chem. Mater.*, 1995, **7**, 50.
- [4] B. Aurivillius, *Ark. Kemi.*, 1950, **1**, 499.
- [5] R. E. Newnham, R. W. Wolfe, and J. F. Dorrian, *Mat. Res. Bull.*, 1971, **6**, 1029.
- [6] M. E. Fuentes, A. Mehta, L. Lascano, H. Camacho, R. Chianelli, J. F. Fernández, and L. Fuentes, *Ferroelectrics*, 2002, **269**, 159.
- [7] G. Nalini and T. N. G. Row, *Bull. Mat. Res.*, 2002, **25**, 275.
- [8] S. M. Blake, M. J. Falconer, M. McCreedy, and P. Lightfoot, *J. Mater. Chem.*, 1997, **7**, 1609.
- [9] J. G. Thompson, A. D. Rae, R. L. Withers, and D. C. Craig, *Acta. Cryst. B.*, 1991, **47**, 174.
- [10] G. A. Smolenskii, V. A. Isupov, and A. I. Agranovskaya, *Sov. Phys. - Solid State*, 1961, **3**, 651.
- [11] S. K. Blower and C. Greaves, *Acta. Cryst. C.*, 1988, **44**, 587.
- [12] A. Srinivas, M. M. Kumar, S. V. Suryanarayana, and T. Bhimasankaram, *Mat. Res. Bull.*, 1999, **34**, 989.
- [13] A. Srinivas, S. V. Suryanarayana, G. S. Kumar, and M. M. Kumar, *J. Phys.: Condens. Matter*, 1999, **11**, 3335.
- [14] F. Kubel and H. Schmid, *Ferroelectrics*, 1992, **129**, 101.
- [15] I. H. Ismailzade, *Kristallografiya*, 1967, **12**, 468.
- [16] C. H. Hervoches, J. T. S. Irvine, and P. Lightfoot, *Phys. Rev. B*, 2001, **64**, R100102.
- [17] A. M. Glazer, *Acta. Cryst. B.*, 1972, **28**, 3384.
- [18] B. J. Kennedy, Y. Kubota, B. A. Hunter, Ismunadar, and K. Kato, *Solid State Comm.*, 2003, **126**, 653.

Chapter 4

Mixed Layer Aurivillius Phases

The mixed layer Aurivillius phases are not particularly well studied structurally. The main work has been performed on $\text{Bi}_7\text{Ti}_4\text{NbO}_{21}$ [1], a structure which is an intergrowth of the 2-layer $\text{Bi}_3\text{TiNbO}_9$ and the 3-layer $\text{Bi}_4\text{Ti}_3\text{O}_{12}$. This structure is referred to as an A2 A3 phase, to represent the 2-layer Aurivillius then 3-layer Aurivillius blocks. The work performed in this study has been on two A1 A2 phases, $\text{Bi}_5\text{TiNbWO}_{15}$ and $\text{Bi}_5\text{Nb}_3\text{O}_{15}$. Powder neutron diffraction studies have been performed on all three samples. TEM images and electron diffraction of the $\text{Bi}_5\text{TiNbWO}_{15}$ phase have also been performed.

4.1 $\text{Bi}_5\text{TiNbWO}_{15}$

The $\text{Bi}_5\text{TiNbWO}_{15}$ phase is an intergrowth of Bi_2WO_6 and $\text{Bi}_3\text{TiNbO}_9$. Of interest in this sample is whether the W^{6+} is present in the single layer of perovskite, in the double layer or disordered over both. Arguments as to why ordering should occur are discussed later. There are very few papers which mention $\text{Bi}_5\text{TiNbWO}_{15}$ [2], and to date no structural studies have been performed.

X-ray Data

The X-ray powder diffraction pattern was examined in space group I2cm, based on the model of $\text{Bi}_7\text{Ti}_4\text{NbO}_{21}$ (a fuller description of the construction of this model is given later). The full refinement plot is shown in Figure-4.1, which reveals no visible impurities. Therefore the sample was taken forward to be analysed using powder neutron diffraction.

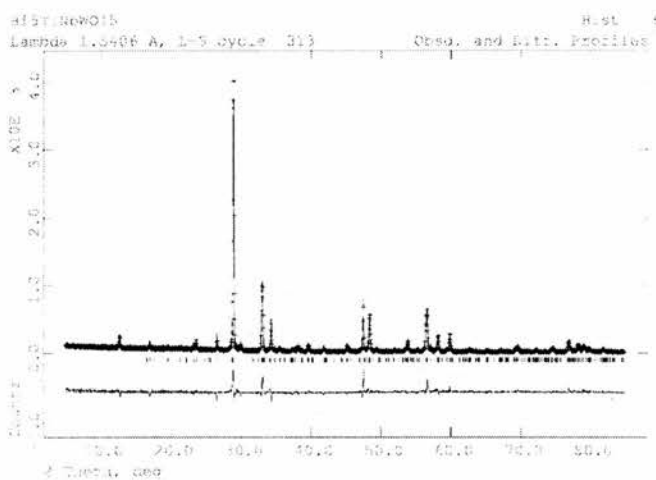


Figure 4.1: Full XRD refinement plot of $\text{Bi}_5\text{TiNbWO}_{15}$ in space group I2cm

Neutron Diffraction Data

The neutron diffraction data were collected at ISIS on the POLARIS diffractometer. The refinements were carried out using both the backscattering and 90° banks. The model proposed from the X-ray diffraction based on the I2cm model for the A2 A3 phase $\text{Bi}_7\text{Ti}_4\text{NbO}_{21}$ was used as a starting point for the neutron refinements.

The I2cm model for $\text{Bi}_7\text{Ti}_4\text{NbO}_{21}$ [1] was obtained using powder neutron and electron diffraction. The structure has the Ti^{4+} cation of the inner octahedra of the A3 block on the $z = 0$ and 0.5 positions along c . The c -axis is defined by the inclusion of two A2 and two A3 blocks. This is referred to as a 'doubling' of the c -axis leading to the I-centred cell observed. The model of the A1 A2 phase was based on this by placing the B-site of the A1 block on the $z = 0$ and 0.5 positions along c . The c -axis was shortened to an appropriate length (for A2A3 $c \sim 58 \text{ \AA}$, for A1A2 $\sim 41 \text{ \AA}$) and the relative atomic positions were based around those for $\text{Bi}_7\text{Ti}_4\text{NbO}_{21}$, see Figure-4.6 for atomic labelling.

The permitted reflections of the I2cm model were co-incident with the positions of intensity in the neutron data and it appeared that the structure could be described as I2cm. The analysis proceeded with the refinement of the lattice parameters, SIG-1 and GAM-1 profile coefficients for both histograms, a preferred orientation correction along the c -axis, the atomic positions and their isotropic thermal parameters. At this point in the refinement it is noted that the thermal parameters of the mixed Nb/Ti site and the W site, the two sites being identified as those of the two constituent Aurivillius phases, are constrained to be equal. The fit obtained from the refinement of these parameters is good, the atomic positions and the thermal parameters are generally very good, except that some of the thermal parameters are slightly larger than ideal. The Bi3 and O1 sites in particular have large thermal factors, see Table-4.1 for details.

To ensure that the large thermal parameters, observed for Bi3 and O1, were not due to the refinement finding a false minimum, a manual search was performed. Atoms were manually moved 'down' from the special position

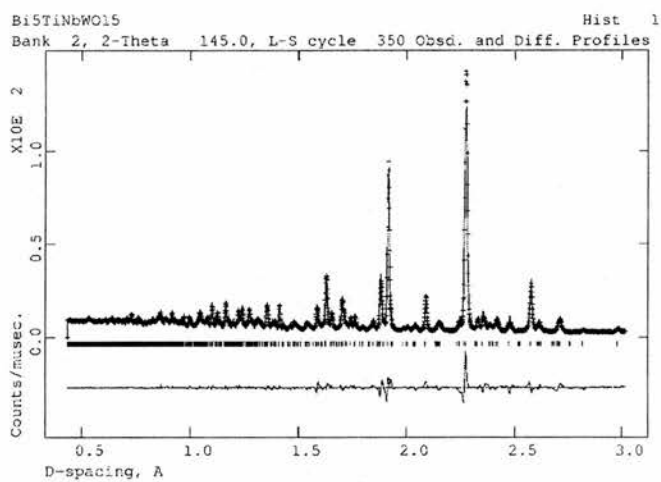


Figure 4.2: $\text{Bi}_5\text{TiNbWO}_{15}$ neutron refinement, 145° 0.4 to 3 Å

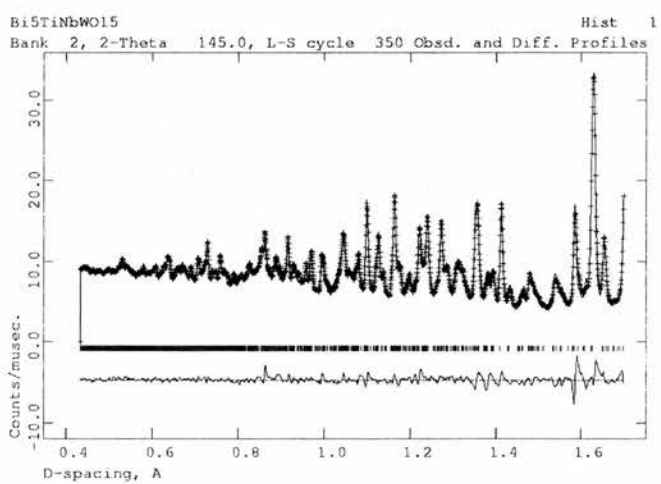


Figure 4.3: $\text{Bi}_5\text{TiNbWO}_{15}$ neutron refinement, 145° 0.4 to 1.7 Å

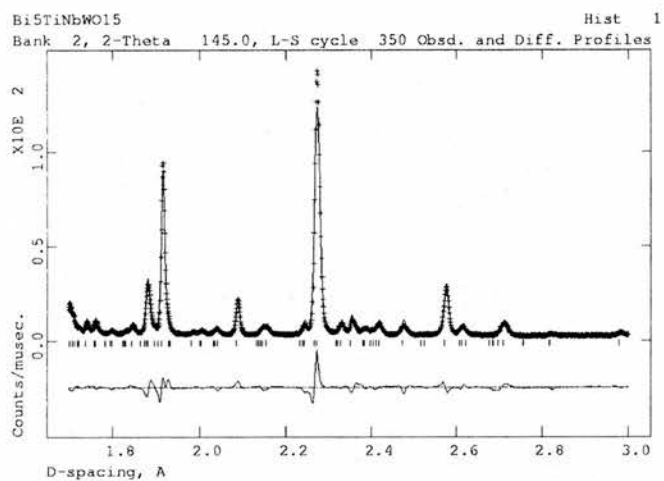


Figure 4.4: Bi₅TiNbWO₁₅ neutron refinement, 145 ° 1.7 to 3 Å

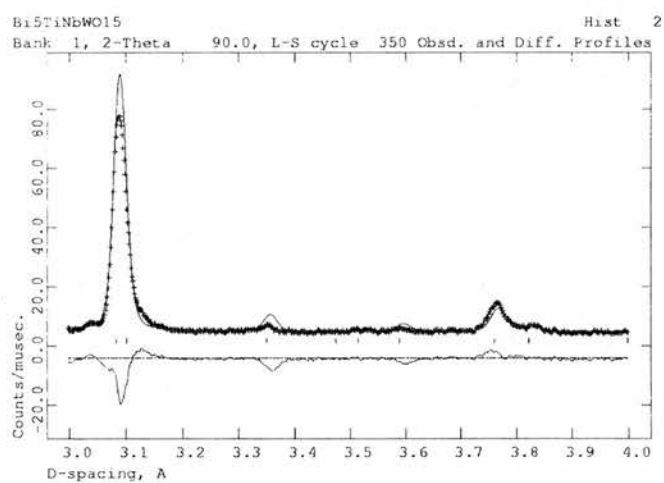


Figure 4.5: Bi₅TiNbWO₁₅ neutron refinement, 90 ° Bank 3 to 4 Å

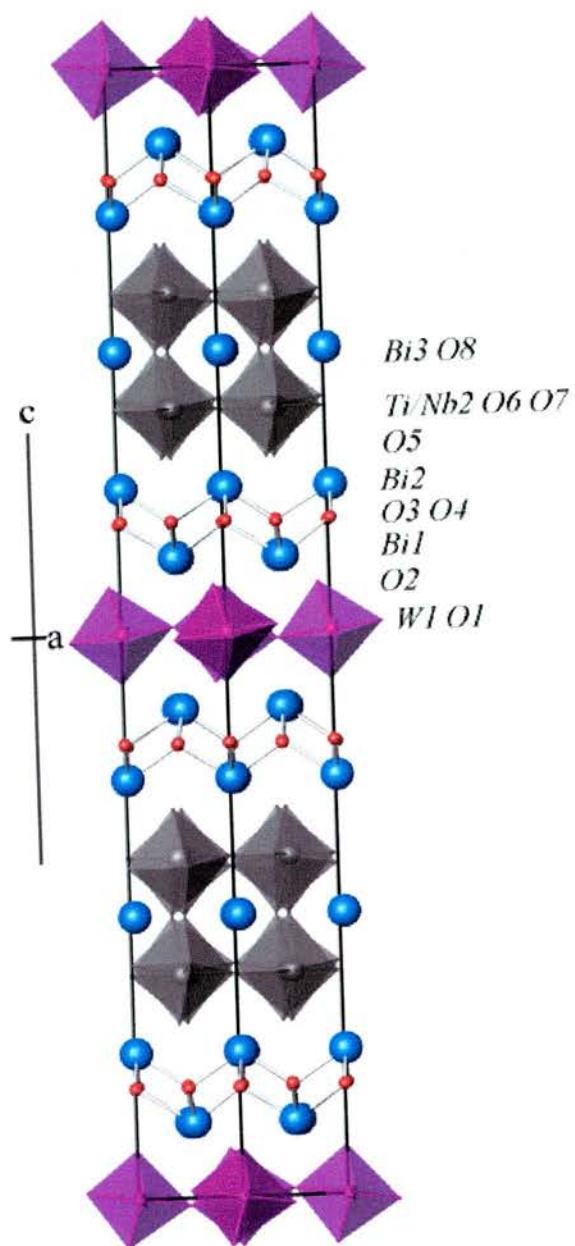


Figure 4.6: View along the $[1\ 1\ 0]$ direction of $\text{Bi}_5\text{TiNbWO}_{15}$

and refined to see where the refinement stabilises. If it stabilises at the same position then no false minimum has been found. If it stabilises at a value 'down' from the special position, then a comparison of the two minima in the refinement must be made to find the correct result. In this case the refinement always returned the same result, so it is taken as the final refinement, given as Figures-4.2 to 4.5.

Thermal parameters for the O1 atom were changed to anisotropic to see along which axis the scattering was present. It was found that the scattering was larger along both a and b than along c . O1 is in the plane of the W1 atom, it is noted that W1 has a very small thermal coefficient. An attempt to refine the thermal parameters for the W site separate to that for the Ti/Nb site was made, to see if the constraint was creating an artificially small W scattering. The result was a large thermal parameter for O1 and a small value for W1. So the constraint was reinserted.

It was decided that the thermal parameters of the Bi3 and O1 whilst being larger than would be desired, were not able to be reduced. The sites are not symmetrically constrained so no lowering of the symmetry would seem to help, no false minima were identified. The refinement was attempted with the thermal parameters anisotropic and this was found to be unsuccessful with the ellipsoids becoming non-positive-definite, also this refinement involves approximately 130 parameters, which is an unacceptably large amount. The final refinement is therefore the isotropic I2cm model, given as Table-4.1 and Figure-4.6 with selected bond lengths given as Table-4.2.

Table 4.1: Bi₅TiNbWO₁₅ atomic parameters from 25 °C neutron data, space group I2cm, a = 5.4231(2) Å, b = 5.4027(2) Å, c = 41.744(1) Å. R_{WP} = 0.041, $\chi^2 = 19.48$, for 7792 data points and 5079 contributing reflections, 0.43 < d < 4.16 Å

Name	Multiplicity	x	y	z	Uiso*100
Bi1	8	0.543(1)	0.016(1)	0.0671(1)	1.1(1)
Bi2	8	0.027(1)	-0.009(1)	0.1286(1)	1.4(1)
Bi3	4	0.035(2)	0.010(1)	0.250000	3.4(1)
W1	4	0.014(2)	0.000000	0.000000	0.1(1)
Nb/Ti2	8	0.502(3)	-0.035(2)	0.1983(2)	0.1(1)
O1	8	0.270(2)	0.231(3)	-0.0059(2)	5.7(2)
O2	8	-0.057(1)	0.057(1)	0.0440(2)	1.8(1)
O3	8	0.261(2)	0.241(1)	0.0992(1)	0.32(9)
O4	8	0.753(2)	0.755(1)	0.0975(1)	0.1(1)
O5	8	0.480(2)	-0.042(1)	0.1543(1)	1.2(1)
O6	8	0.180(1)	0.204(1)	0.1979(1)	0.3(1)
O7	8	0.774(1)	0.787(1)	0.2074(1)	-0.1(1)
O8	4	0.460(2)	0.060(2)	0.250000	1.7(2)

4.1.1 Electron Microscopy

One interesting result is the location of the Ti, Nb and W cations. Earlier, it was stated that the refinement began with the W in the 1-layer site and the Ti and Nb in the 2-layer site. The final refinement preserved this ordering of the cations. One argument for such ordering is based on the charges of certain blocks within the system, proposed by Zhou[3, 4]. The theory is that if there is no charge present when the charges of the neighbouring blocks are summed then there is no need for a structural distortion. However, if the sum of charges on neighbouring blocks do not equal zero then the structure will distort to isolate the areas of higher charge. This results in a stepped structure as shown in Figure-4.7. These steps occur for Aurivillius phases

Table 4.2: Bi₅TiNbWO₁₅ bond lengths

bond	length Å	bond	length Å	bond	length Å
Bi1 O2	3.397(7)	Bi2 O3	2.229(5)	Bi3 O6	2.537(6) x 2
Bi1 O2	2.385(8)	Bi2 O3	2.383(6)	Bi3 O6	3.270(7) x 2
Bi1 O2	3.275(8)	Bi2 O4	2.347(6)	Bi3 O7	2.569(6) x 2
Bi1 O2	2.568(9)	Bi2 O4	2.223(5)	Bi3 O7	2.736(8) x 2
Bi1 O3	2.360(6)	Bi2 O5	3.171(8)	Bi3 O8	3.12(1)
Bi1 O3	2.228(7)	Bi2 O5	2.672(8)	Bi3 O8	2.34(1)
Bi1 O4	2.219(7)	Bi2 O5	2.662(8)	Bi3 O8	3.13(1)
Bi1 O4	2.492(6)	Bi2 O5	3.177(8)	Bi3 O8	2.33(1)

bond	length Å	bond	length Å
W1 O1	1.90(1)	Nb2 O5	1.85(1)
W1 O1	1.90(1)	Nb2 O6	2.17(2)
W1 O1	1.99(1)	Nb2 O6	1.99(2)
W1 O1	1.99(1)	Nb2 O7	1.79(2)
W1 O2	1.895(6)	Nb2 O7	1.93(2)
W1 O2	1.895(6)	Nb2 O8	2.23(1)



Figure 4.7: Possible $\text{Bi}_5\text{TiNbWO}_{15}$ structures from charge ordering.

and have been documented for the A1 A2 structure $\text{Bi}_5\text{Nb}_3\text{O}_{15}$ [3]. From this charge ordering argument it would be expected that, if the structure is ordered, as is suggested from the X-ray diffraction data, then the bulk structure would not be stepped. To examine the structure for any domains of stepped defect, and to confirm the bulk structure, electron microscopy was performed by Dr Wuzong Zhou.

The view of the structure down the long c -axis shows no discernible defect structure, see Figure-4.8. However, in this case, as the structure is overlapping regularly, it is not expected that a defect would be observed even if one were present. The defect can only be observed looking along either of the two short axes. Figure-4.9 shows a regular structure for the bulk of $\text{Bi}_5\text{TiNbWO}_{15}$ and it is this kind of structure that is observed for most of the particles examined by the microscope. This agrees with the model established from the powder neutron diffraction data. Also observed, very occasionally, in small domains of certain particles are stepped structures. Some of the stepped structures look similar to those previously published by

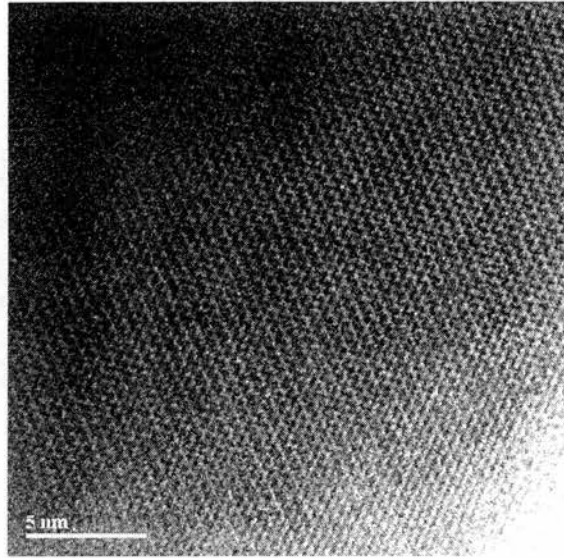


Figure 4.8: View down [001] for the bulk structure of $\text{Bi}_5\text{TiNbWO}_{15}$

Zhou[4] for the $\text{Bi}_2\text{Nb}_{0.5}\text{W}_{0.5}\text{O}_{5.75}$ structure. In these defects the defect is a continuous step, shown in Figure-4.10. For some of the defects there are stepped regions where the stepping forms a herringbone pattern, see Figure-4.11 and Figure-4.12. The presence of these defect regions within particles, but not as entire particles, suggests that the sample is mainly to be found as an ordered, pure, layered compound. It also suggests that these defect domains may be caused by an imbalance in the ratio of the B-site cations. Alternatively, there may be some degree of disorder among the B-site cations, leading to a less even charge distribution, then to the stepped defect structure. The fact that these defect domains are rare and small would suggest that the model obtained from the neutron diffraction data is correct for the bulk average structure.

This compound is believed to be ferroelectric as, in a previous paper[5], the

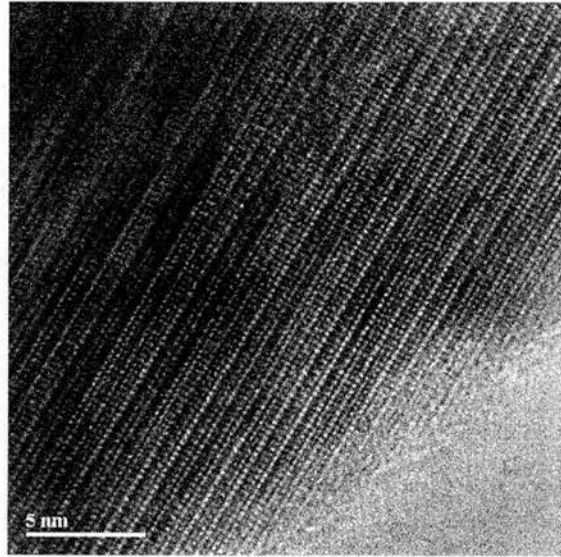


Figure 4.9: view down the a/b axis $\text{Bi}_5\text{TiNbWO}_{15}$

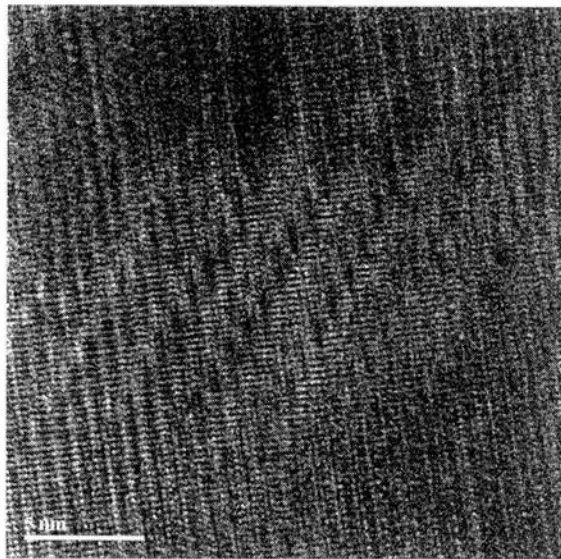


Figure 4.10: An area of the stepped structure found in $\text{Bi}_5\text{TiNbWO}_{15}$

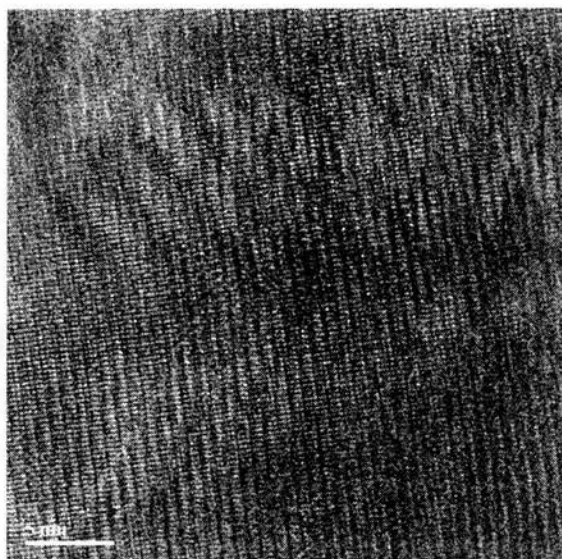


Figure 4.11: An area of herringbone stepped defect structure in $\text{Bi}_5\text{TiNbWO}_{15}$

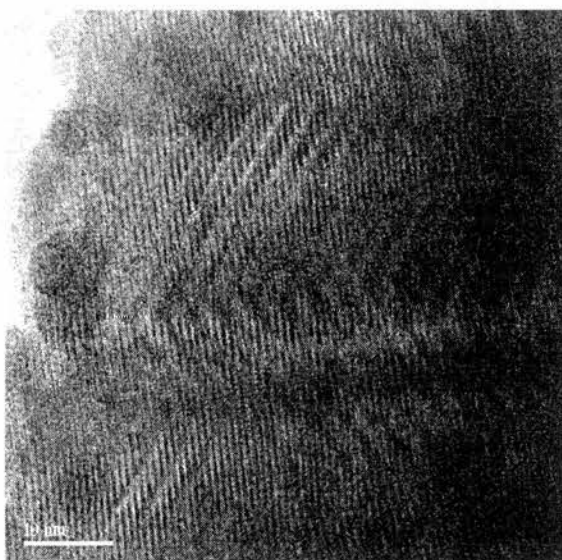


Figure 4.12: A larger area (lower magnification) of the herringbone stepped structure found in $\text{Bi}_5\text{TiNbWO}_{15}$

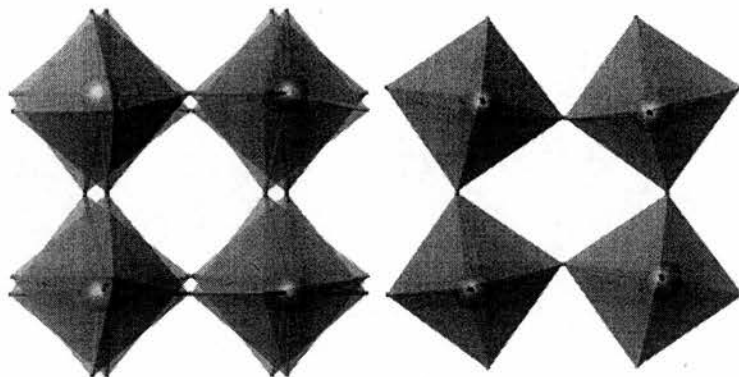


Figure 4.13: Octahedral rotations in the A2 layer of $\text{Bi}_5\text{TiNbWO}_{15}$. Left, view along tetragonal a -axis. Right, view along c -axis. Both pictures show a $2 \times 2 \times 2$ block of octahedra.

dielectric constant of the sample was rising with temperature. Conductivity measurements were carried out to 400°C , but were stopped without reaching any maximum due to a large increase in electrode interferences. The rotations in the 2-layer block have been examined and may be described as $a^-a^-c^+$ in Glazer[6] notation. This is the same as for the ferroelectric 2-layer Aurivillius phases. The in-phase rotation along the c -axis is described by the mirror plane between the two octahedra in the block. The 2-layer rotations are shown in Figure-4.13. The body-centering of the unit cell results in the WO_6 octahedra at the base of the unit cell being tilted in the opposing direction from those at the midpoint of the unit cell.

The component perovskite blocks of the $\text{Bi}_5\text{TiNbWO}_{15}$ phase can be compared to the perovskite blocks in the two intergrown phases. For the Ti/NbO_6

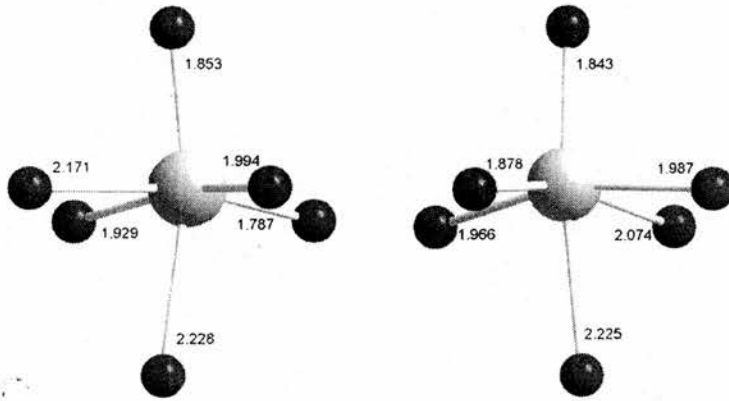


Figure 4.14: Comparison of Ti/NbO_6 octahedra for $\text{Bi}_5\text{TiNbWO}_{15}$ (left) and $\text{Bi}_3\text{TiNbO}_9$ (right)

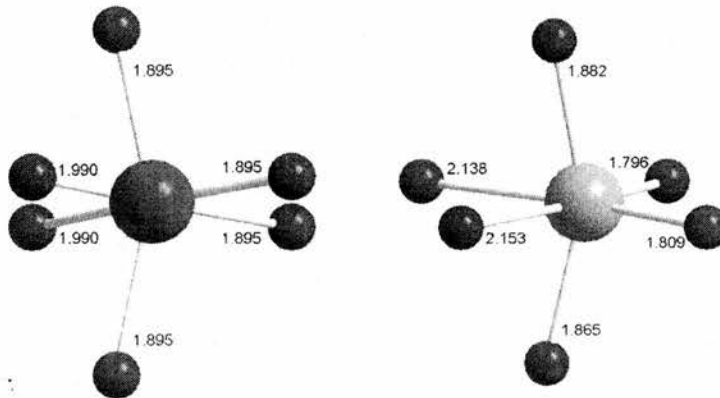


Figure 4.15: Comparison of WO_6 octahedra for $\text{Bi}_5\text{TiNbWO}_{15}$ (left) and Bi_2WO_6 (right)

octahedra (Figure-4.14) the octahedra are clearly very similarly distorted along the c -axis. The displacement of the Ti/Nb site within the ab -plane is greater for the $\text{Bi}_5\text{TiNbWO}_{15}$ phase than for $\text{Bi}_3\text{TiNbO}_9$. For the WO_6 octahedra the displacement along the c -axis is zero for the $\text{Bi}_5\text{TiNbWO}_{15}$ phase as it is constrained by a 2-fold axis. For the WO_6 octahedron in the Bi_2WO_6 phase, although there is no constraint the two corresponding bond lengths are very similar (Figure-4.15). For the W-O bonds within the ab -plane there is greater distortion in the Bi_2WO_6 phase. The Ti/Nb site is more distorted than expected and the W site is less distorted. It may be that in order to intergrow the two compositions, the distortions of the two perovskite blocks have had to compromise.

4.2 $\text{Bi}_5\text{Nb}_3\text{O}_{15}$

The $\text{Bi}_5\text{Nb}_3\text{O}_{15}$ phase is another A1 A2 mixed-layer Aurivillius phase, but in this case it is not composed of two previously identifiable structures. Previously the structure was identified as having a stepped defect structure when viewed along $[010]$ [7]. The composition was indexed with a unit cell; $a = 31.79 \text{ \AA}$, $b = 5.45 \text{ \AA}$, $c = 41.02 \text{ \AA}$. This represents a structure that is ordered, with similar periodicity to $\text{Bi}_5\text{TiNbWO}_{15}$ for b and c , however, the a -axis is $6\sqrt{2}a_0$. It was noted that the nature of the structure in the a direction means that it could be twice as large[7] as the stated cell. In the same paper the powder X-ray diffraction data were analysed at various temperatures. The structure was indexed as tetragonal with $a = 10.936 \text{ \AA}$, which is twice a_0 . It is unlikely that this is the correct indexing, the authors themselves

point out that for a high resolution dataset they are unable to index all of the peaks with this model. To date no accurate model of the bulk structure has been produced. Due to the stepped nature of sections of the structure, and the possibility of a very large unit cell, it may be that the structure is very difficult to characterise. In this study the structure has been examined using powder X-ray and neutron diffraction data.

4.2.1 Diffraction Data

For the X-ray diffraction data the compound could be indexed using a tetragonal cell, with $a = 3.86, 5.46$ or 7.73 \AA . It would appear that, whilst the tetragonal model matches the X-ray data there are very few peaks from which to get an accurate cell determination. Also the additional peaks which are referred to previously[7] are hard to identify in the data collected here.

The sample was taken to POLARIS at ISIS to be used for powder neutron diffraction. The data obtained from this experiment were compared against the tetragonal models and it was found that it was not possible to index the material as tetragonal. A check was performed to see if any of the additional peaks were due to other phases. This was done by displaying the permitted reflections for the Pmmm, 'single' c -axis cell, and the Immm cell, with a 'doubled' c -axis, see Figure-4.16. It was found that certain peaks could not be indexed by either system, therefore it is unlikely that the material is pure.

It was decided to attempt to fit an I2cm model based on the $\text{Bi}_5\text{TiNbWO}_{15}$ structure. This resulted in a reasonable fit to the experimental data, as

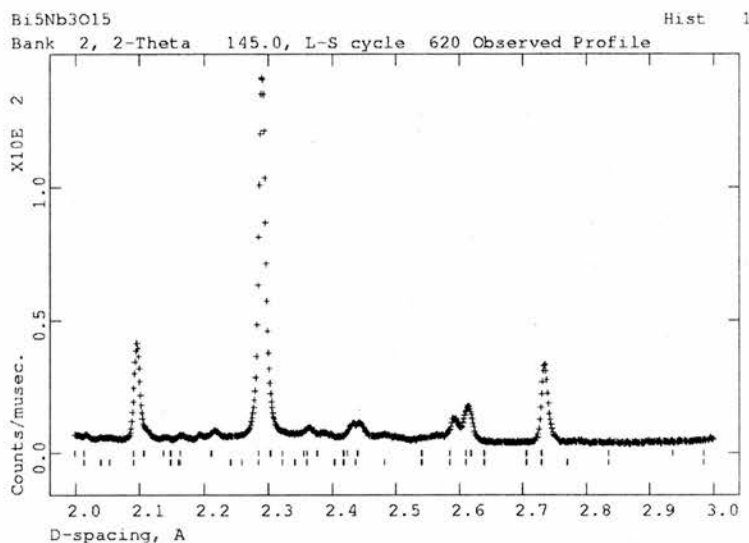


Figure 4.16: Plot of backscattering neutron data for $\text{Bi}_5\text{Nb}_3\text{O}_{15}$, 2 to 3 Å. Lower tick marks are for Immm, $c = 2C_O$. Upper tick marks are for Pmmm, $c = C_O$.

shown in Figure-4.17. On close inspection there were some problems with peak fitting (Figure-4.18) probably due to the presence of a second phase. From the data that are available it is not possible to determine unambiguously the structure of $\text{Bi}_5\text{Nb}_3\text{O}_{15}$. However, it has been modelled well by the I2cm structure, which would make it analogous to $\text{Bi}_5\text{TiNbWO}_{15}$. The orthorhombic distortion of the Nb^{5+} phase is very small, which has caused some of the difficulty in identifying the correct model. The final model obtained is given in Table-4.3, however, no detailed analysis of the structural distortions is performed due to the unreliable nature of these results. Given the uneven charge distribution in the layers of the compound, it is likely that far more of the $\text{Bi}_5\text{Nb}_3\text{O}_{15}$ would be found as the 'staggered' phase than for

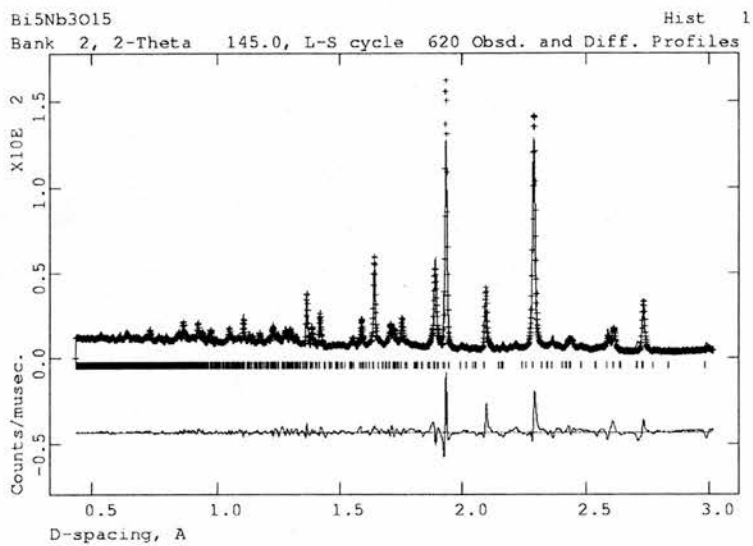


Figure 4.17: Plot of backscattering neutron data for $\text{Bi}_5\text{Nb}_3\text{O}_{15}$, I2cm model.

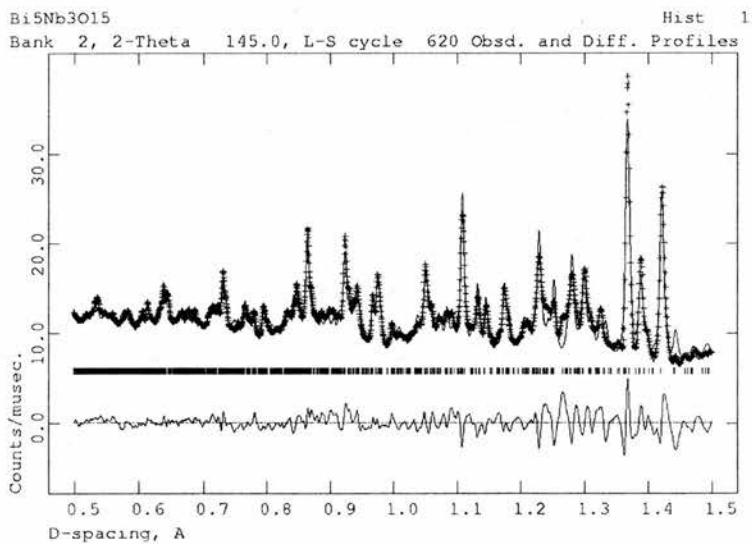


Figure 4.18: Plot of backscattering neutron data for $\text{Bi}_5\text{Nb}_3\text{O}_{15}$, 0.5 to 1.5 Å, I2cm model.

Table 4.3: Bi₅Nb₃O₁₅ atomic parameters from 25 °C neutron data, space group I2cm, a = 5.4647(7) Å, b = 5.4612(8) Å, c = 41.840(2) Å. R_{WP} = 0.0627, $\chi^2 = 49.85$, for 7792 data points and 5184 contributing reflections, 0.43 < d < 4.16 Å

Name	Multiplicity	x	y	z	Uiso*100
Bi1	8	0.498(2)	-0.003(3)	0.0644(2)	4.4(2)
Bi2	8	-0.006(2)	-0.010(2)	0.1274(1)	1.49(9)
Bi3	4	0.010(3)	-0.043(4)	0.250000	4.2(3)
Nb1	4	-0.014(2)	0.000000	0.000000	0.49(6)
Nb2	8	0.489(2)	0.011(2)	0.1959(1)	0.49(6)
O1	8	0.287(2)	0.200(2)	-0.0035(3)	0.8(2)
O2	8	-0.088(2)	-0.010(3)	0.0462(2)	1.9(2)
O3	8	0.246(4)	0.266(3)	0.0978(3)	2.6(3)
O4	8	0.730(2)	0.740(2)	0.0985(2)	-0.48(7)
O5	8	0.445(4)	0.045(4)	0.1522(3)	4.2(4)
O6	8	0.240(3)	0.270(2)	0.2083(2)	1.0(2)
O7	8	0.703(2)	0.720(3)	0.2046(2)	0.7(2)
O8	4	0.416(4)	-0.060(5)	0.250000	4.0(6)

Bi₅TiNbWO₁₅.

References

- [1] D. Mercurio, G. Trolliard, T. Hansen, and J. P. Mercurio, *Int. J. Inorg. Mater.*, 2000, **2**, 397.
- [2] B. Frit and J. P. Mercurio, *J. Alloys Compd.*, 1992, **188**, 27.
- [3] W. Zhou, *Adv. Mat.*, 1990, **2**, 94.
- [4] W. Zhou, *J. Solid State Chem.*, 1992, **163**, 479.
- [5] T. Kikuchi, A. Watanabe, and K. Uchida, *Mat. Res. Bull.*, 1977, **12**, 299.
- [6] A. M. Glazer, *Acta. Cryst. B.*, 1972, **28**, 3384.
- [7] W. Zhou, D. A. Jefferson, and J. M. Thomas, *Geophysics Monographs*, 1984, **45**, 113.

Chapter 5

Lanthanides in Aurivillius Phases

Aurivillius phases are known to be potential ‘fatigue free’ ferroelectrics, suitable for use in devices such as smart card memory. Two papers in Nature have highlighted the possibilities of such materials, one reporting $\text{SrBi}_2\text{Ta}_2\text{O}_9$ [1] and the other[2] reporting $\text{Bi}_{4-x}\text{La}_x\text{Ti}_3\text{O}_{12}$. It is on the materials with lanthanum doping that this chapter focuses. Two solid solutions have been investigated, the 2-layer, $\text{Bi}_{3-x}\text{La}_x\text{TiNbO}_9$ and the 3-layer, $\text{Bi}_{4-x}\text{La}_x\text{Ti}_3\text{O}_{12}$.

5.1 $\text{Bi}_{3-x}\text{La}_x\text{TiNbO}_9$

The solid solution $\text{Bi}_{3-x}\text{La}_x\text{TiNbO}_9$ was prepared for values $x = 0, 0.2, 0.4, 0.6, 0.8$ and 1 . The samples were analysed by powder X-ray and neutron diffraction, performed on HRPD at ISIS. It was believed that the samples would gradually decrease in orthorhombicity with increasing La^{3+} content. At some value of x a phase change was anticipated, from $A2_1am$ to $I4/mmm$. Previously recorded dielectric measurements on the series[3] had shown that at $x = 0.8$, it becomes difficult to discern a maximum in the plot of ϵ vs

temperature, indicating the loss of ferroelectric behaviour.

5.1.1 $\text{Bi}_3\text{TiNbO}_9$

The undoped phase has previously been studied using single crystal X-ray and electron diffraction methods[4]. The setting used here to describe the structure is different to the prior report. The structure used for the refinement is based on the model of $\text{SrBi}_2\text{Nb}_2\text{O}_9$ as given by Blake et al[5]. The atomic coordinates of the final model obtained are displayed as Table-5.1 and as Figure-5.1 and a plot of the final refinement is given as Figure-5.2.

Table 5.1: $\text{Bi}_3\text{TiNbO}_9$ atomic parameters from 25 °C HRPD data, space group $A2_1am$, $a = 5.44150(4)$ Å, $b = 5.40299(4)$ Å, $c = 25.1057(2)$ Å. $R_{WP} = 0.082$, $\chi^2 = 5.22$, for 4270 data points and 4495 contributing reflections, $0.70 < d < 2.5$ Å

Atom	Multiplicity	x	y	z	Uiso x 100
Bi1	4	0.195(1)	0.7607(6)	0.500000	1.07(4)
Bi2	8	0.204(1)	0.7315(4)	0.69903(6)	1.07(4)
Ti/Nb ¹	8	0.250000	0.241(2)	0.5873(2)	-0.5(2)
O1	4	0.288(2)	0.1815(8)	0.500000	0.8(1)
O2	8	0.257(2)	0.3040(5)	0.6595(1)	1.03(8)
O3	8	0.473(2)	0.5062(6)	0.2500(1)	0.60(6)
O4	8	0.481(2)	0.5333(6)	0.5680(1)	0.63(7)
O5	8	0.562(2)	0.0500(7)	0.5853(1)	0.97(8)

¹ occupancy is 0.5 Nb⁵⁺ / 0.5 Ti⁴⁺

There are no fundamental problems with the model. It is noted, however, that the thermal parameter for the Ti/Nb site has gone slightly negative. This model was used to give a starting structure for the La³⁺ doped compositions.

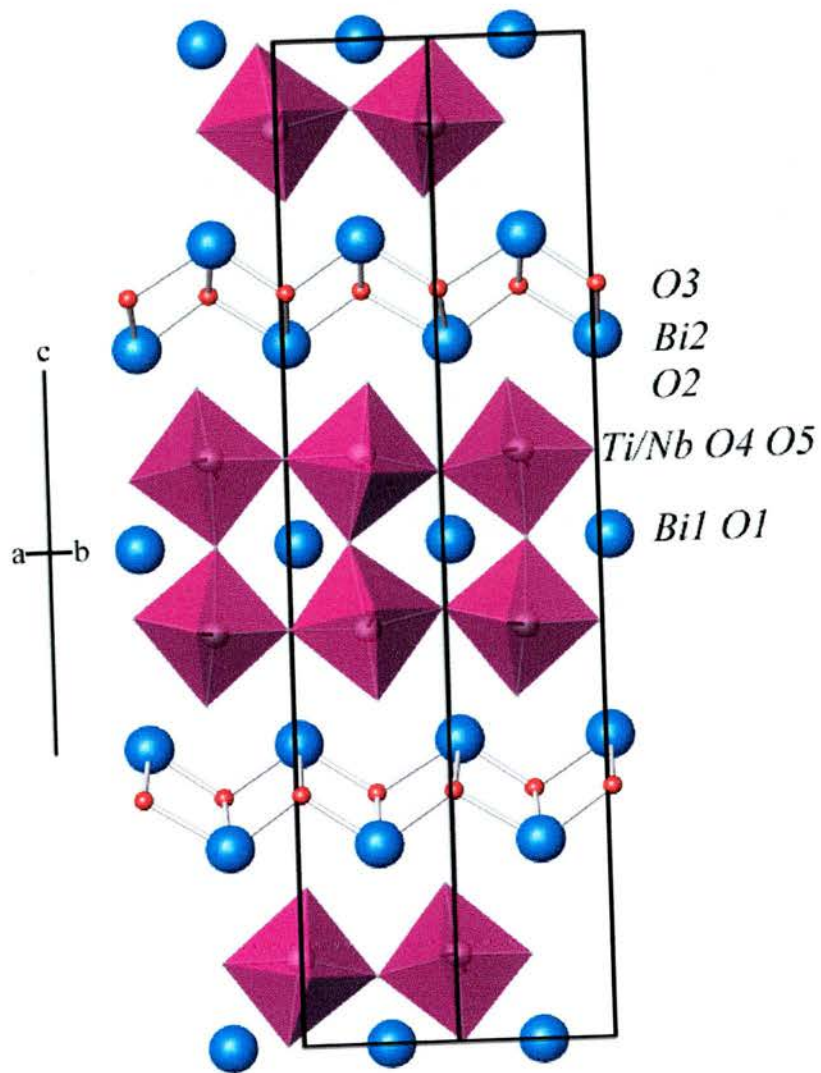


Figure 5.1: $\text{Bi}_3\text{TiNbO}_9$ structure; bismuth is blue, oxygen is red and the TiO_6 octahedra are in purple

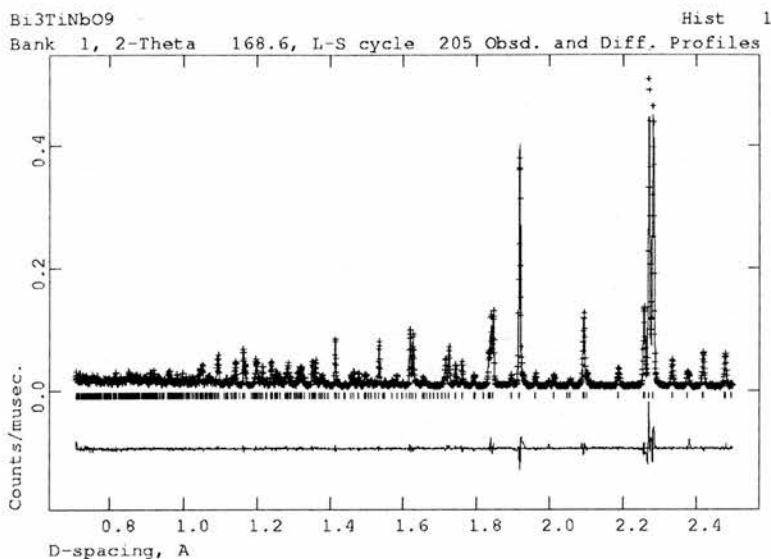


Figure 5.2: Bi₃TiNbO₉ neutron refinement plot, 0.7 to 2.5 Å. Tick marks are for A2₁am

5.1.2 Bi_{2.8}La_{0.2}TiNbO₉

For the $x = 0.2$ doped phase the compound was indexed as A2₁am. The structure was refined using a combined X-ray and neutron refinement, utilising an X-ray histogram, and the backscattering and 90° banks of the HRPD diffractometer at ISIS. This was deemed necessary to identify the level of disorder in the mixed Bi³⁺/La³⁺ sites. The discrimination between Bi³⁺ and La³⁺ using neutron data is limited as the scattering factors are 8.532×10^{-15} m and 8.24×10^{-15} m, respectively. To successfully perform a combined X-ray and neutron refinement it may be necessary to perform an absorption correction for the X-ray data. It was found for this dataset, and all others in this chapter, that this was not necessary. The refinements can be performed

as normal, except that the diffractometer constant, DIFC, is switched on for both the neutron histograms to avoid compromising the values of the unit cell parameters.

From Figures-5.3 and 5.4 it is clear that there is a second phase present in the $x = 0.2$ sample. This was unexpected at such a low dopant level. Examining the X-ray diffraction data (Figure-5.5) there is no obvious impurity present. At this point the impurity cannot be identified and it is uncertain if it is only present in the neutron data, possibly due to an unclean sample can.

Already the effect of the La^{3+} doping can be observed, there is a small decrease in the c -axis length and there is a large reduction of the orthorhombicity. These changes will be discussed in a more detailed fashion later. It is noted that the La^{3+} occupancy is given as -0.097 for the Bi/La2 site, this has been retained to highlight the difficulties in refining such a small dopant level. It is assumed that the refined levels can be approximated to an ordered structure with all of the La^{3+} located in the perovskite block, i.e. Bi1 site.

5.1.3 $\text{Bi}_{2.6}\text{La}_{0.4}\text{TiNbO}_9$

The $x = 0.4$ phase was also refined using the polar $A2_1am$ space group. Examining the backscattering bank, shown as Figure-5.6, an impurity similar to that for the $x = 0.2$ phase is observed. Examining Figure-5.7 it is clear that this impurity is not identifiable in the X-ray data. It seems unlikely that the impurity is due to an unclean sample can for both samples, far more likely is that this is some systematic impurity phase. The impurity remains unknown due to a lack of clearly identifiable peaks. Still observable, from

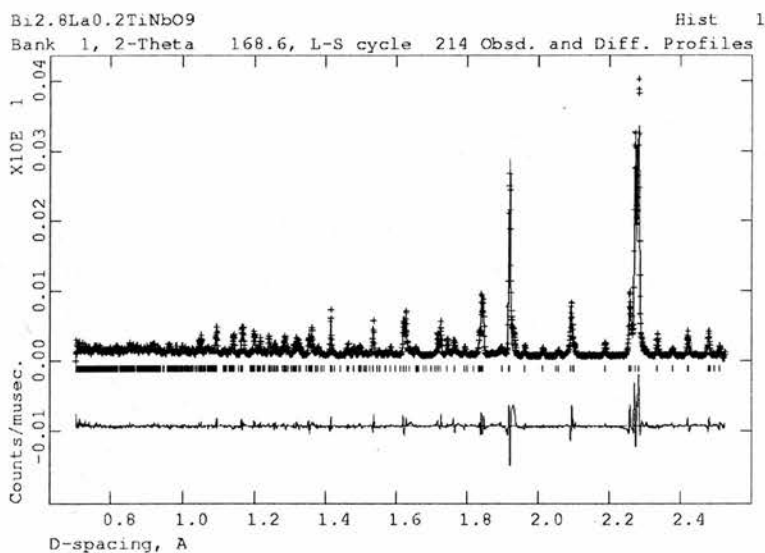


Figure 5.3: Bi_{2.8}La_{0.2}TiNbO₉ neutron refinement plot, 0.7 to 2.5 Å, backscattering bank. Tick marks are for A2₁am

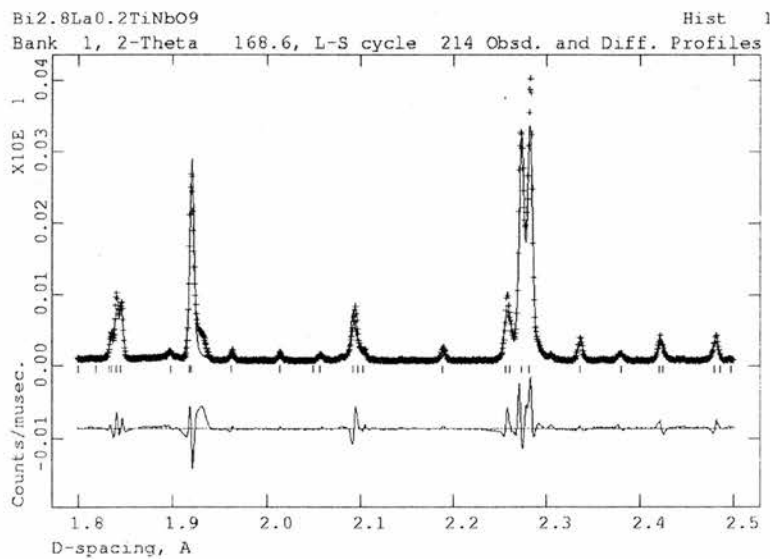


Figure 5.4: Bi_{2.8}La_{0.2}TiNbO₉ neutron refinement plot, 1.8 to 2.5 Å, showing the impurity peaks. Tick marks are for A2₁am

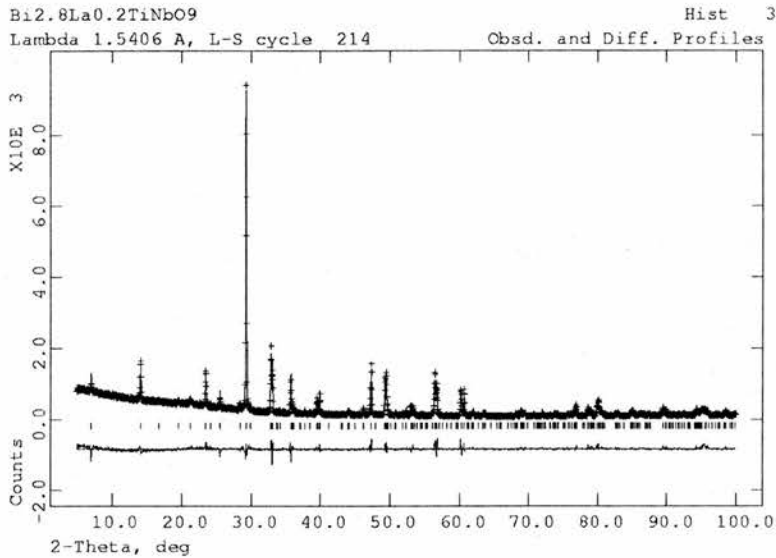


Figure 5.5: $\text{Bi}_{2.8}\text{La}_{0.2}\text{TiNbO}_9$ X-ray refinement plot, showing no impurity peaks. Tick marks are for $A2_1am$

Figure-5.6, are the superstructure peaks which indicate the orthorhombic supercell, which requires the $A2_1am$ symmetry. Again the Bi/La2 site has a negative occupancy of La, this is assumed to indicate an ordering of the perovskite A-site and the $[\text{Bi}_2\text{O}_2]$ layer site.

5.1.4 $\text{Bi}_{2.4}\text{La}_{0.6}\text{TiNbO}_9$

For the $x = 0.6$ phase the orthorhombic distortion is reduced to almost zero. It would appear from the plot of the neutron data that there is still some orthorhombic distortion present in the sample, observable as superlattice reflections, observable in Figure-5.8. Also, the impurity that was found for both the $x = 0.2$ and $x = 0.4$ sample does not appear to be present in this

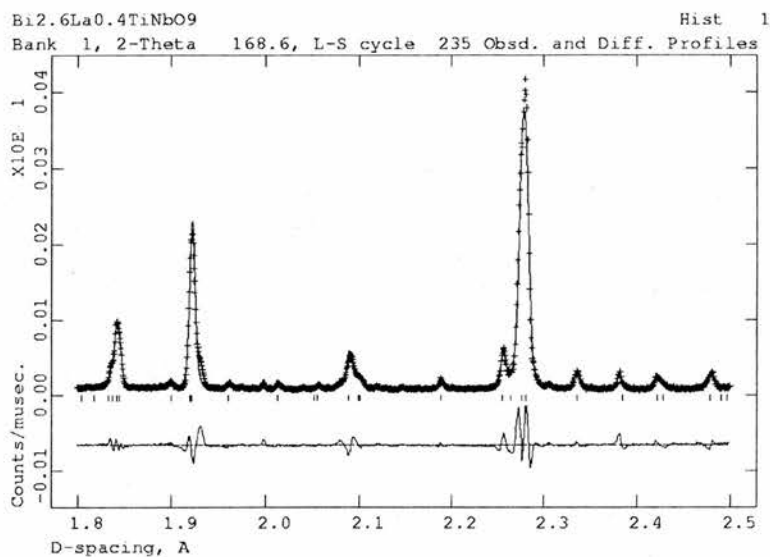


Figure 5.6: Bi_{2.6}La_{0.4}TiNbO₉ neutron refinement plot, backscattering data, from 1.8 to 2.5 Å. Tick marks are for A₂₁am

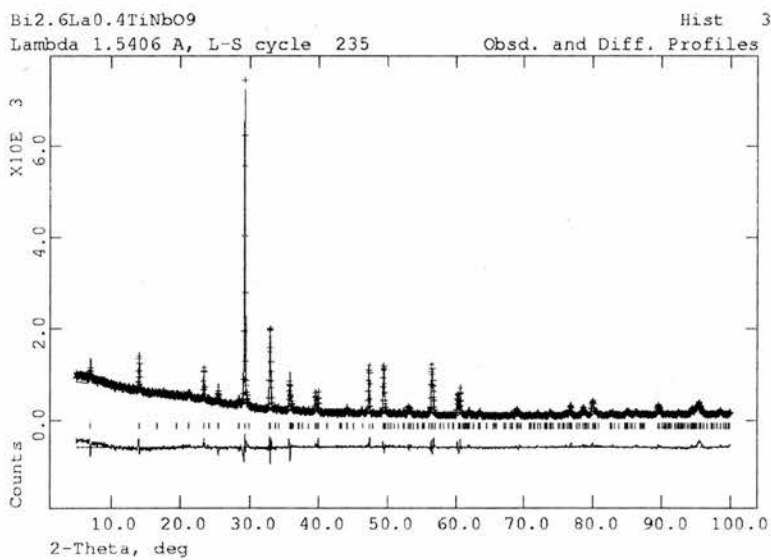


Figure 5.7: Bi_{2.6}La_{0.4}TiNbO₉ X-ray refinement plot, showing no impurity peaks. Tick marks are for A₂₁am

sample.

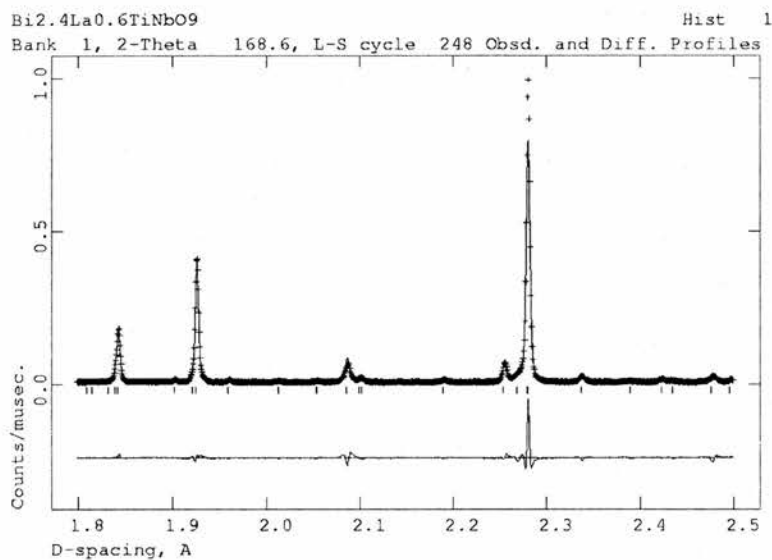


Figure 5.8: $\text{Bi}_{2.4}\text{La}_{0.6}\text{TiNbO}_9$ neutron refinement plot, backscattering bank, 1.8 to 2.5 Å. Tick marks are for $A2_1am$

5.1.5 $\text{Bi}_{2.2}\text{La}_{0.8}\text{TiNbO}_9$

The $x = 0.8$ sample was the most difficult to justify as either the orthorhombic or the tetragonal phase. However, during refinement the lattice parameters were very close to tetragonal. Also the additional orthorhombic peaks could not be seen as clearly as for the $x = 0.6$. Analysis was complicated by some small impurity peaks in the same region as the superstructure peaks. However, the structure was refined as $I4/mmm$, shown as Figure-5.9, as the use of the lower symmetry $A2_1am$, could not be justified.

It can be seen by examining the Rietveld plots for the refinements, that the fit to the intensity of the main peak, just below 2.3 Å, is decreasing in quality

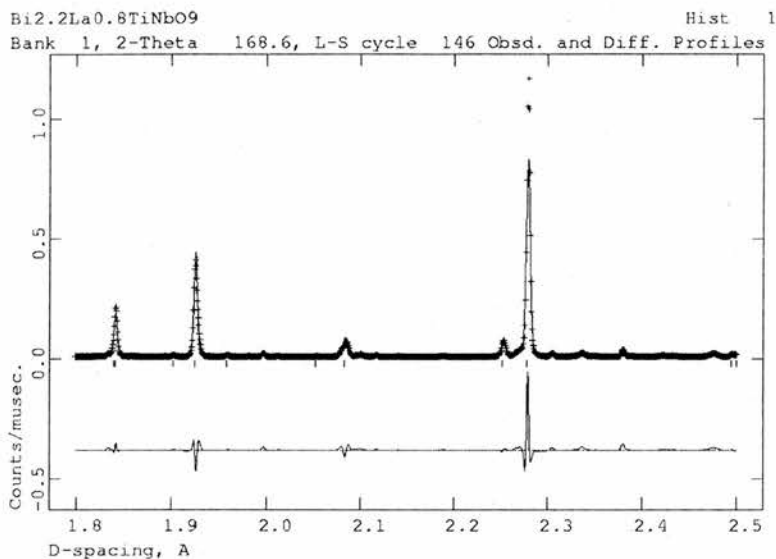


Figure 5.9: Bi_{2.2}La_{0.8}TiNbO₉ neutron refinement plot, backscattering bank, 1.8 to 2.5 Å. Tick marks are for I4/mmm

with increasing x . The reason for this is unknown, it could be that there is some overlapping intensity with the impurity phase. The shape of the peak may also be changing, so the refined peak shape coefficients are not correctly fitting the experimental profiles.

A potential problem with the refinements could be the ALPHA-1 parameter, which was manually adjusted. The ALPHA-1 value is specified in an instrument parameter file supplied by ISIS. On the visit to HRPD, where most of the data in this chapter were collected, the normalization procedure had been altered to an automated sequence, included in the Ariel software. The change of normalization procedure resulted in a change of instrument parameter file. The manual adjustment was necessary as the peak shapes given by the ALPHA-1, in the new instrument parameter file, gave peak

shapes where the curve diverged; into the separate Gaussian and Lorentzian parts (for a fuller explanation on peak profiles see Section-2.1.5). Examining the new and old instrument parameter files; the ALPHA-1 value in the new file was approximately one order of magnitude larger than the old value. For this reason the value was manually reset from 2.56 to 0.256. This resulted in an immediate improvement to the fit of the data, however, the value of ALPHA-1 could still be incorrect. Attempts were made to refine ALPHA-1 to compensate for this, but these were unsuccessful.

5.1.6 $\text{Bi}_2\text{LaTiNbO}_9$

For the $x = 1$ sample it appears, without ambiguity, to be metrically tetragonal and not orthorhombic. From Figure-5.10 it is clear that there is also a small amount of an impurity phase present. It is also clear that the fit to the most intense reflection is much better for this sample. Whatever strain has been caused on either side of the phase transition may account for the diminishing quality of the fit to the most intense peak. It does appear unlikely that it is an effect of the impurity phase, as this is least prevalent for the $x = 0.8$ sample, where the fit to the main peak is of lowest quality.

5.1.7 Comparison of La^{3+} Doped Samples

Having looked at each of the refinements individually, here the trends occurring with doping are analysed. The results are presented in graphical form. Tables of these values and the experimental models are given in the appendices.

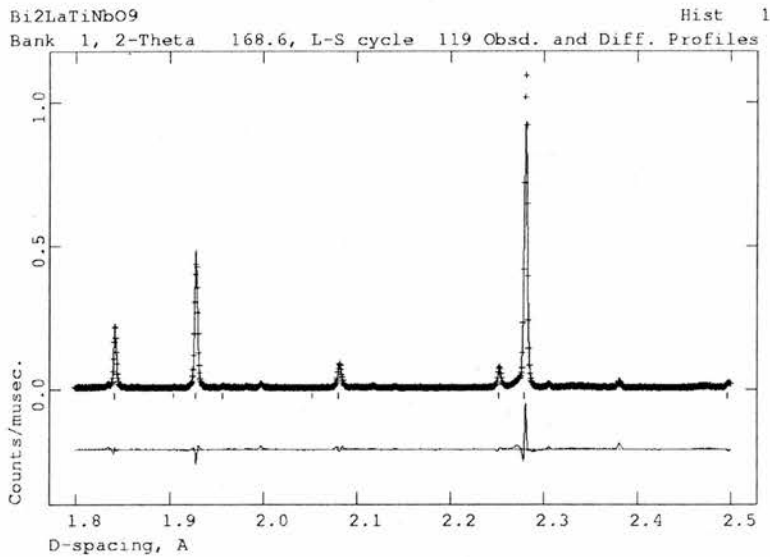


Figure 5.10: Bi₂LaTiNbO₉ neutron refinement plot, backscattering bank, 1.8 to 2.5 Å. Tick marks are for I4/mmm

The Unit Cell

The effect of the doping on the unit cell can be examined through the unit cell parameters. For the plot of a and b against x (Figure-5.11) the graph shows a gradual merging of the lattice parameters. A more subtle point is the slightly anomalous a and b parameters for the $x = 0.6$, both values appear higher than may have been expected. However, the a for $x = 0.6$ is still larger than b . This is important as it is sometimes found that models near an orthorhombic to tetragonal phase transition have the values of a and b 'crossing over'. In these cases the refinement is having difficulty identifying the orthorhombic nature of the sample. For the $x = 0.6$ sample this was not a problem, hence, the result is taken as valid. It is possible that the unexpected

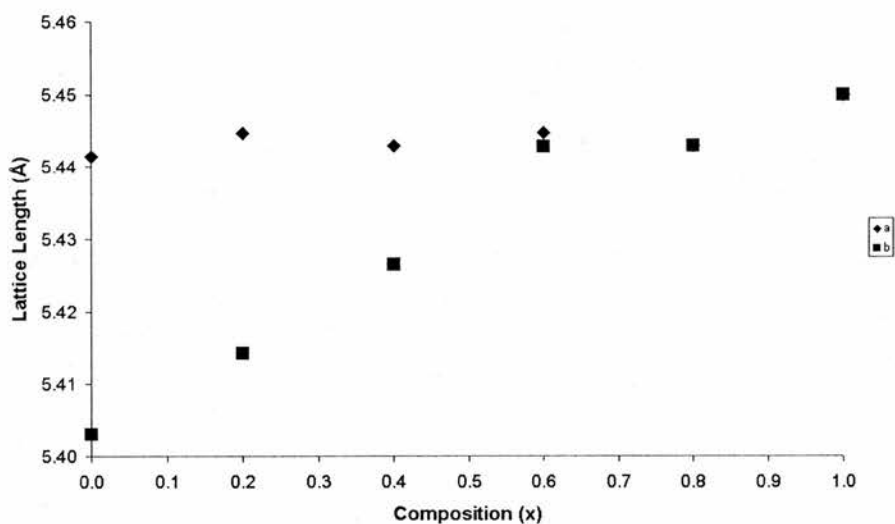


Figure 5.11: Plot of a and b against x for $\text{Bi}_{3-x}\text{La}_x\text{TiNbO}_9$. Tetragonal models are lotted as $\sqrt{2} \times a_T$.

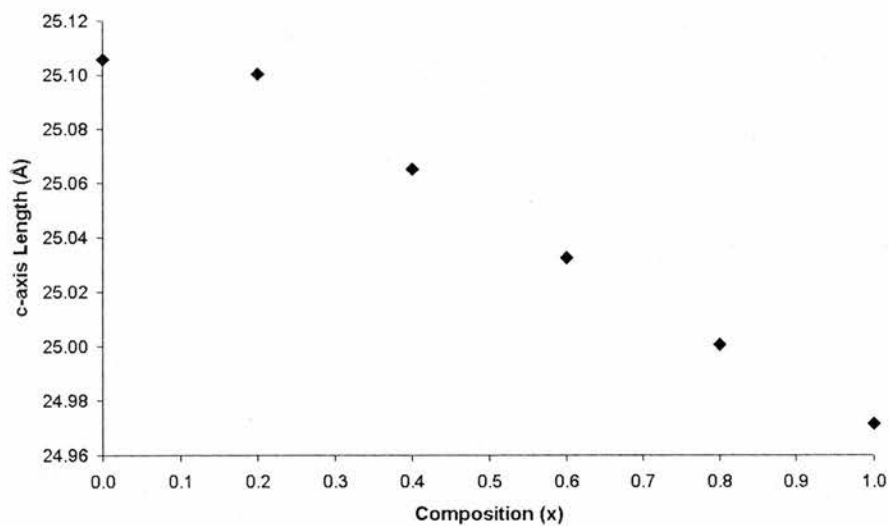


Figure 5.12: Plot of c against x for $\text{Bi}_{3-x}\text{La}_x\text{TiNbO}_9$.

size of the $x = 0.6$ cell can be explained by the poor quality of the fit to the most intense peak in the refinement. This fit may be symptomatic of a small discrepancy in the lattice parameters caused by the combined neutron and X-ray refinement, and a potential impurity phase. For the c -axis the behaviour is much simpler, Figure-5.12 clearly shows a linear decrease in the value of c . For the plot of unit cell volume against x , Figure-5.13 clearly shows the effect of the unexpectedly large a and b values for $x = 0.6$. Here the plot shows the large volume of the unit cell of $x = 0.6$, which is larger than even the $x = 1$ phase. Splitting the change in the c -axis length into the perovskite block, Figure-5.14, and non-perovskite section, Figure-5.15. The perovskite block encompasses the octahedra height from O2 to O2, the non perovskite space is the remaining cell height. The two plots show that the contraction in the structure along c is almost entirely due to the contraction of the perovskite block and at higher values of x , a small contraction in the $[\text{Bi}_2\text{O}_2]$ layer site.

B-site Bonding Environment

In the orthorhombic structures, where octahedral tilting is permitted, there are six distinct bond distances. For the tetragonal model the bonds in the the Ti-O plane are all equivalent. In Figure-5.16 the two apical bonds are represented by a square and a diamond. The square is the long bond to the oxygen linking the polyhedra and the short bond is that to the oxygen adjacent to the $[\text{Bi}_2\text{O}_2]$ layer.

The in-plane bonds are behaving as two pairs, one pair is represented by the star and the cross. These start out far apart from one another and come

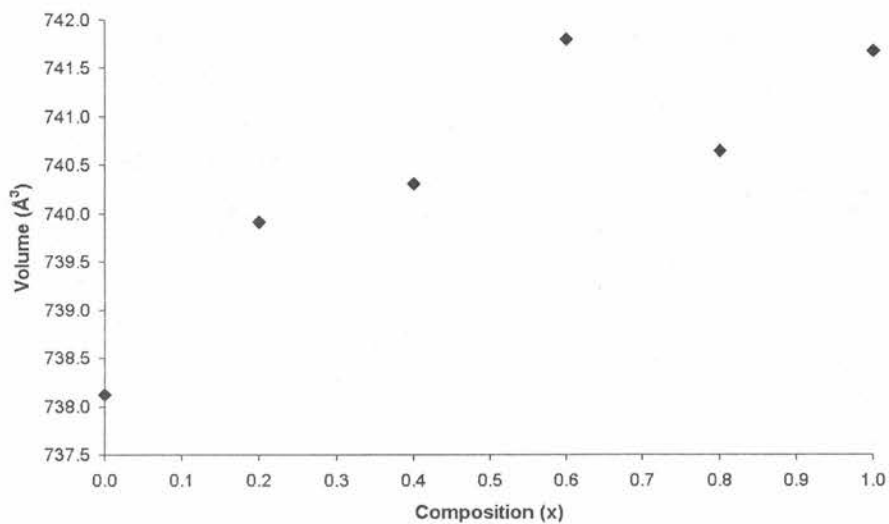


Figure 5.13: Plot of unit cell volume against x for $\text{Bi}_{3-x}\text{La}_x\text{TiNbO}_9$.

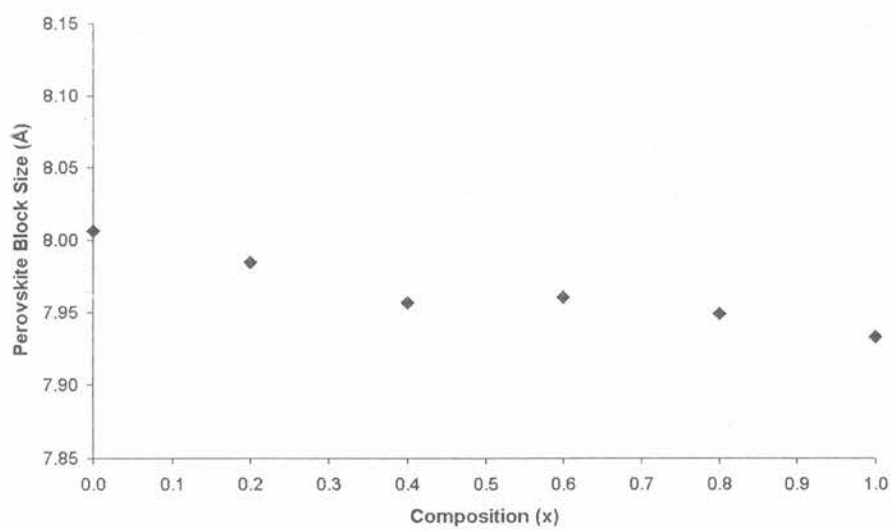


Figure 5.14: Plot of perovskite block height against x for $\text{Bi}_{3-x}\text{La}_x\text{TiNbO}_9$.

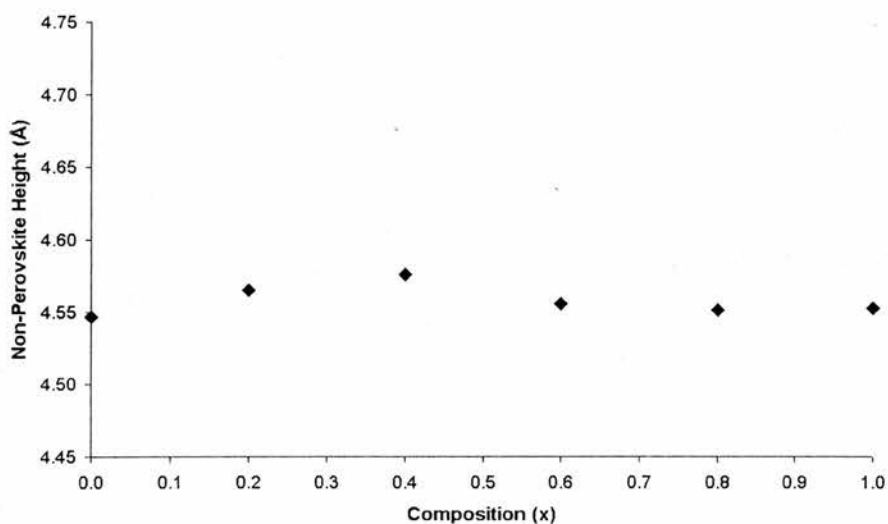


Figure 5.15: Plot of non-perovskite height against x for $\text{Bi}_{3-x}\text{La}_x\text{TiNbO}_9$.

together as the doping increases, this indicates that initially the Ti^{4+} is off centre towards one of the oxygens, creating a long and short bond within the plane. The other pair are represented by the triangle and the circle. The lengths of these bonds begin as close together, they then spread apart as the oxygens rotate and the Ti^{4+} moves. Then as the structure becomes less distorted they become gradually more similar.

For the equatorial bond angles there is no discernible pattern to be seen in Figure-5.17. However, it can be observed that the introduction of La^{3+} into the system creates a greater distortion in the equatorial bond angles. From the axial bond angles there is a clear trend as the octahedra become more regular as the La^{3+} content is increased, given as Figure-5.18. As for the equatorial bond angles the introduction of La^{3+} has created greater distortion than for the undoped sample. For both the equatorial tilting (Figure-5.19)

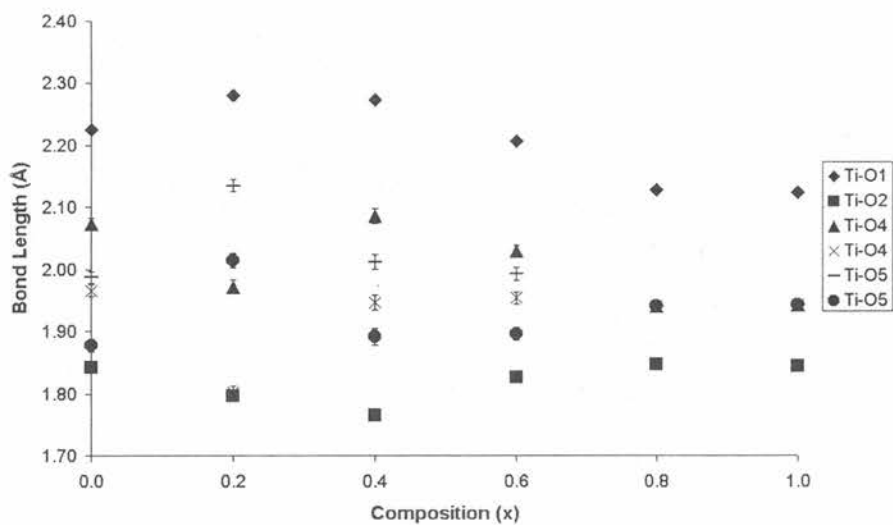


Figure 5.16: Plot of Ti-O bond lengths against x for $\text{Bi}_{3-x}\text{La}_x\text{TiNbO}_9$.

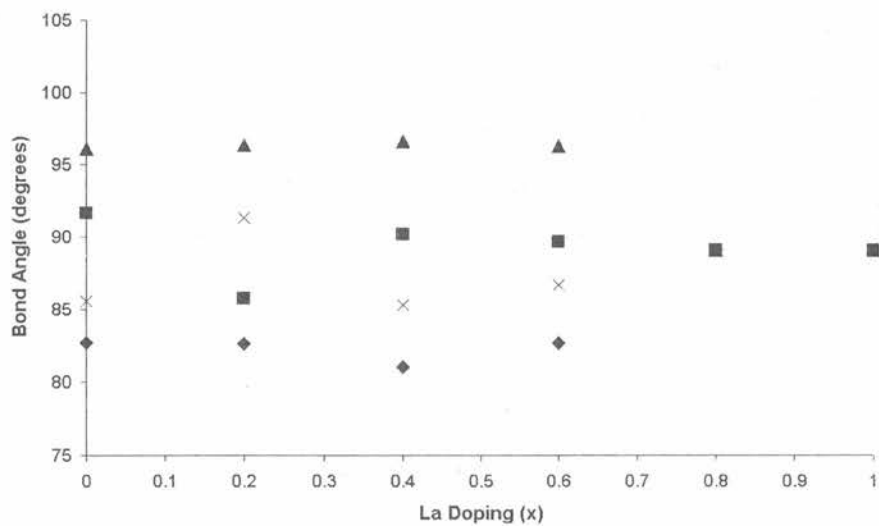


Figure 5.17: Plot of equatorial O-Ti-O bond angles against x for $\text{Bi}_{3-x}\text{La}_x\text{TiNbO}_9$.

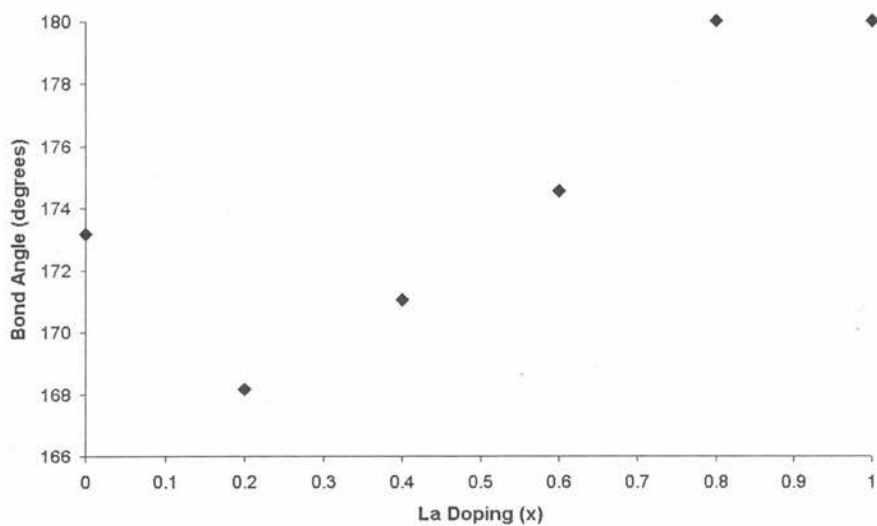


Figure 5.18: Plot of axial O1-Ti-O2 bond angle against x for $\text{Bi}_{3-x}\text{La}_x\text{TiNbO}_9$.

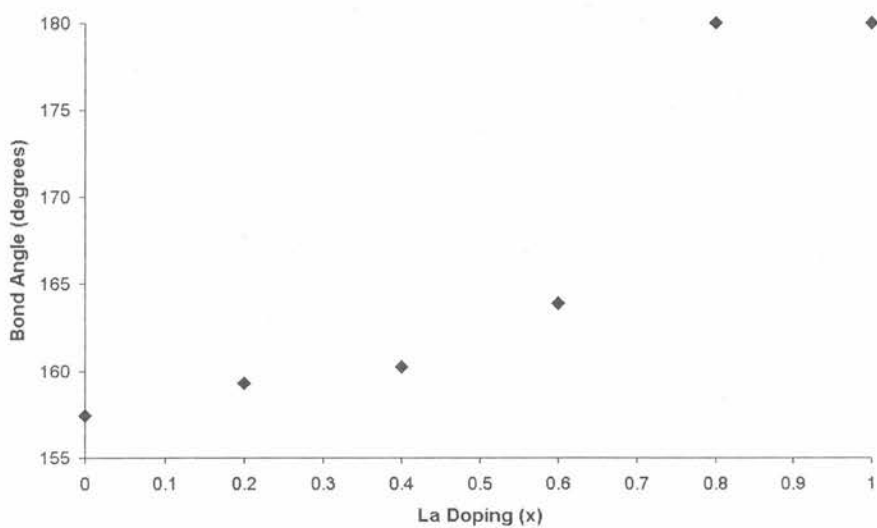


Figure 5.19: Plot of equatorial tilting in octahedra against x for $\text{Bi}_{3-x}\text{La}_x\text{TiNbO}_9$.

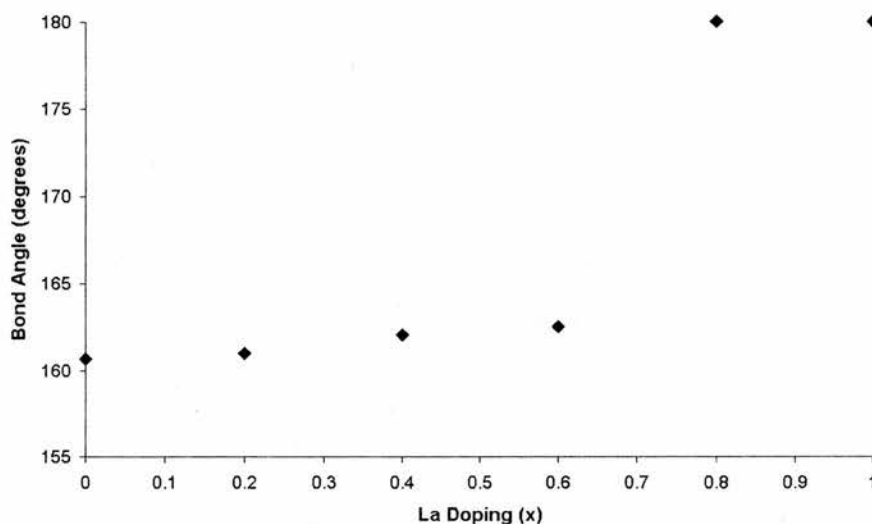


Figure 5.20: Plot of axial tilting, O2-O1-O2, in octahedra against x for $\text{Bi}_{3-x}\text{La}_x\text{TiNbO}_9$.

and the axial tilting (Figure-5.20) there is a gradual increase in the tilt angle before $x = 0.8$.

A-site Bonding Environment

The A-site cation bonding environment is plotted as the in-plane and out-of-plane Bi-O distances against x . For the in-plane oxygens (Figure-5.21) there are two longer Bi-O bonds and two shorter bonds, these abruptly change to a single bond length at the phase transition. Examining closely it can be seen that those bond lengths represented by the cross and the triangle are converging faster than the other two bonds. The two bonds that are converging faster lie along the a -axis from the Bi1 site. The out of plane bonding, shown as Figure-5.22, shows three very similar shorter bonds and

one longer bond. It is noted that due to the mirror symmetry element there are two bonds of each type present. The longer bond is steadily decreasing and the three shorter bonds homogenise, with increasing x . There is a clearly observable discontinuity at the orthorhombic to tetragonal phase change, indicating that as the Bi1 cation moves to the tetragonal position its movement is greater along the polar a -axis.

Bi₂O₂ Site Bonding Environment

Examining the plot of the apical Bi2-O2 bond lengths (Figure-5.23) there are four distinct bond lengths, as the Bi is displaced along both a and b . The bonds are grouped into two shorter and two longer bonds, the distortion being slightly greater, at lower x values, for the b -axis. The a -axis shows a slightly higher tendency to homogenise with increasing La³⁺ content, however none of the bonds vary much in length. As the bonds are consistently split into shorter and longer bonds, the O²⁻ site is therefore remaining displaced along both a and b , whilst the structure is orthorhombic. The bonding within the [Bi₂O₂] layer is shown as Figure-5.24. There is clearly one long bond and three short bonds, indicating that the distortion is inclined towards one corner. However, the movement of the oxygens has resulted in three bonds of relatively equal length. With increasing La³⁺ content the longest bond is seen to decrease slowly and the shorter bonds homogenise.

Lanthanum Occupancies

The lanthanum occupancies obtained by refinement are plotted in Figures-5.25 and 5.26. It can be observed that the refinements for the $x = 0.2, 0.4$

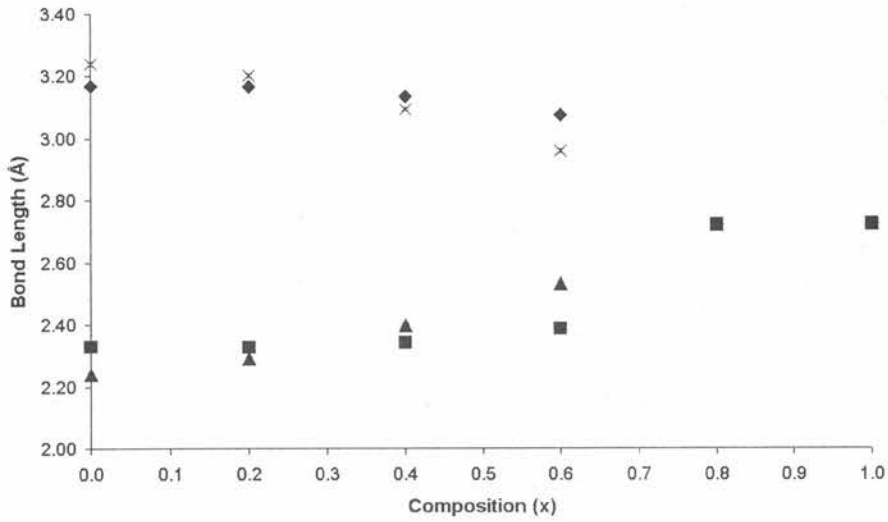


Figure 5.21: Plot of Bi1-O1 bond lengths against x for Bi_{3-x}La_xTiNbO₉.

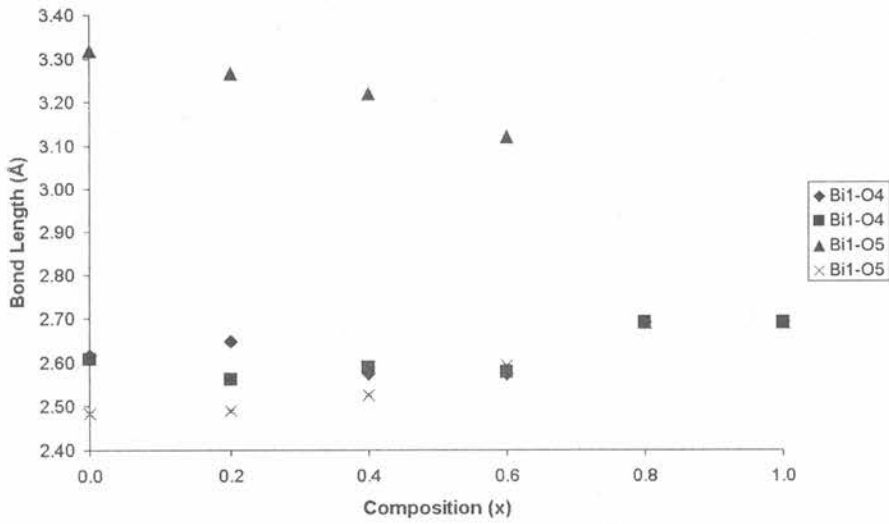


Figure 5.22: Plot of Bi1-O out-of-plane bond lengths against x for Bi_{3-x}La_xTiNbO₉.

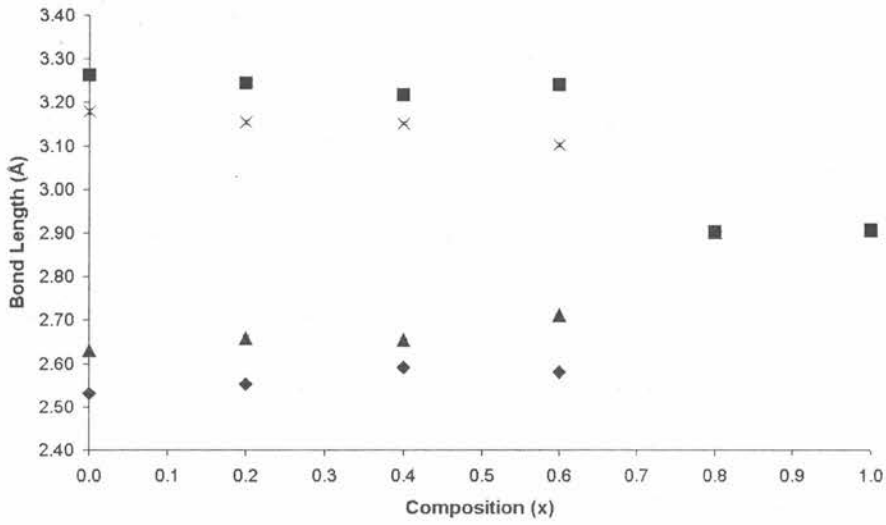


Figure 5.23: Plot of Bi2-O2 apical bond lengths against x for $\text{Bi}_{3-x}\text{La}_x\text{TiNbO}_9$.

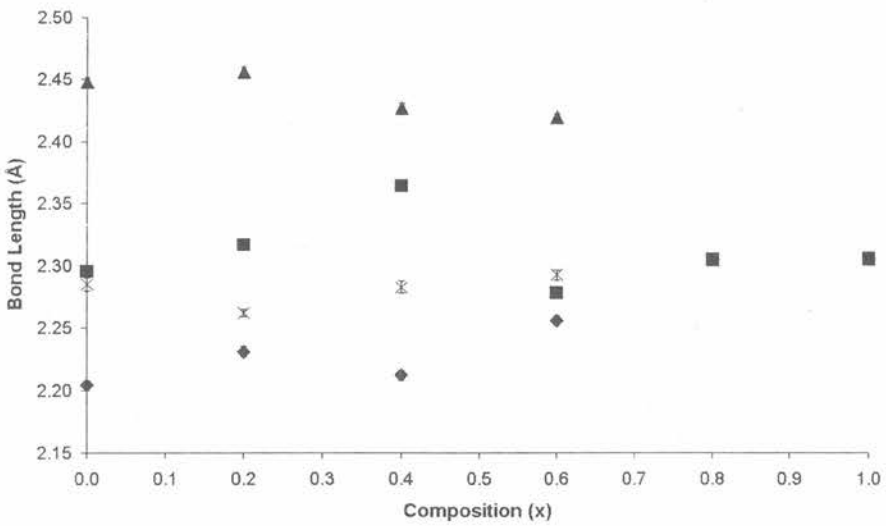


Figure 5.24: Plot of Bi2-O3 bond lengths against x for $\text{Bi}_{3-x}\text{La}_x\text{TiNbO}_9$.

and 0.6 phases are not exact. Due to the low levels of doping no definite value can be established. The refined values for the Bi/La2 site are below zero, an impossibility. It is assumed that in these refinements the structure actually has the La^{3+} content solely in the perovskite A-site, and that the $[\text{Bi}_2\text{O}_2]$ layer is composed solely of Bi^{3+} . What appears to be suggested from Figure-5.25 is that the orthorhombic structure does not wish to permit the inclusion of La^{3+} into the $[\text{Bi}_2\text{O}_2]$ layer. Conversely, when the La^{3+} content is sufficiently large some La^{3+} is inserted onto the $[\text{Bi}_2\text{O}_2]$ layer site and the structure prefers to adopt the tetragonal symmetry.

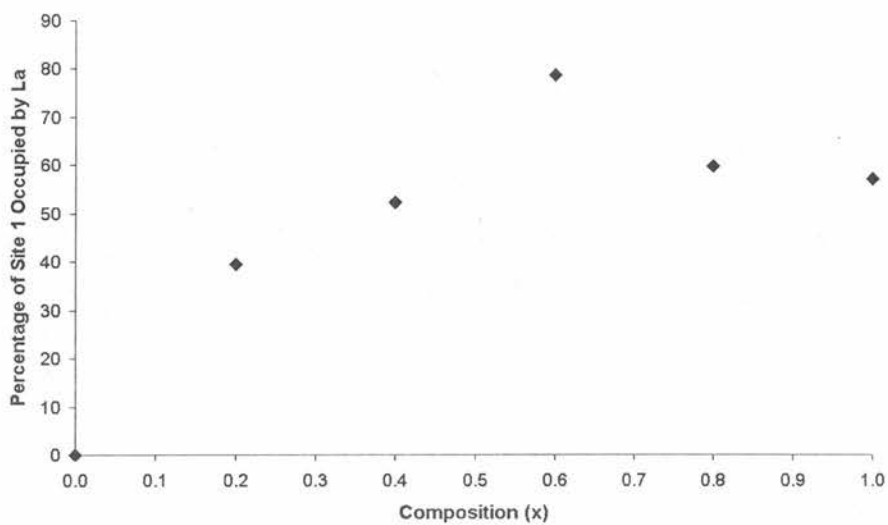


Figure 5.25: Plot of La^{3+} content in the perovskite A-site in $\text{Bi}_{3-x}\text{La}_x\text{TiNbO}_9$.

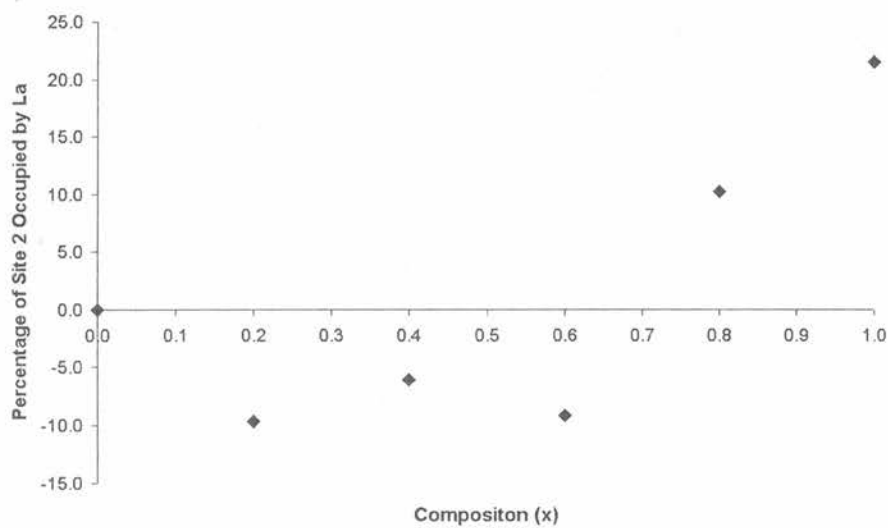


Figure 5.26: Plot of La^{3+} content in the $[\text{Bi}_2\text{O}_2]$ layer site in $\text{Bi}_{3-x}\text{La}_x\text{TiNbO}_9$.

5.2 $\text{Bi}_{4-x}\text{La}_x\text{Ti}_3\text{O}_{12}$

The paper published by Park et al[2] is an examination of the composition $\text{Bi}_{3.25}\text{La}_{0.75}\text{Ti}_3\text{O}_{12}$. This poses certain questions. In the paper no explanation is offered as to why the composition $x = 0.75$ was chosen, does this have the largest ferroelectric polarisation? Is it the most resistant to fatigue? Or is it a good compromise to both of these? Most importantly of all is what effect does altering the La^{3+} composition have on the structure and properties of the material?

The structure of the parent $\text{Bi}_4\text{Ti}_3\text{O}_{12}$ (BTO) phase has been well established[6]. Within our group preliminary powder XRD refinements of the $x = 1$ and $x = 2$ $\text{Bi}_{4-x}\text{La}_x\text{Ti}_3\text{O}_{12}$ structures have been published[7]. The parent phase is an orthorhombic phase, in space group B2cb. This polar group permits displacement of the A and B-site cations and rotations of the octahedral sites. The $x = 1$ and $x = 2$ La^{3+} doped structures were suggested as I4/mmm, the 'parent' tetragonal phase, where no distortions are permitted. The I4/mmm structures are not polar and hence are not ferroelectric. However, the studies on these two phases were done using powder XRD and hence would not be expected to provide accurate oxygen positions. For this reason a powder neutron diffraction study was performed. In a more recent study[8] using Convergent Beam Electron Diffraction (CBED) it was suggested that the structure of $\text{Bi}_3\text{LaTi}_3\text{O}_{12}$ was B121, a monoclinic group. This was based on the absence the c -axis plane of symmetry, in the CBED experiment. As the distortion is very subtle and cannot be observed using the diffraction techniques presented here, the B2cb model has been retained.

5.2.1 X-ray and Neutron Diffraction Data

From the X-ray data it appeared that all of the phases were pure, though no accurate assignment of the structure could be performed due to the limitations of using X-rays. The compositions were $x = 0.1, 0.3, 0.5, 0.7, 0.9, 1.1, 1.3, 1.5$ and, in addition, an $x = 2.0$ sample as made by Dr. Charles Hervoches. Identification of the Bi/La ratio in the $[\text{Bi}_2\text{O}_2]$ layer and perovskite A-site were established using powder X-ray data, with the model first established from neutron data. This was done as there is a very small difference between the neutron scattering lengths of Bi and La, 8.532 and 8.24×10^{-15} m respectively. The samples were analysed on the HRPD and POLARIS diffractometers at ISIS. HRPD data were collected for the $x = 0.3$ to 1.3 and POLARIS for the $x = 0.1, 1.5$ and 2.0 .

The refinements began with the $\text{Bi}_{3.9}\text{La}_{0.1}\text{Ti}_3\text{O}_{12}$ sample. This structure was refined using a version of the parent structure, adjusted for the La^{3+} content and the lattice parameters. Initially the structure was refined using the backscattering bank of the neutron data only. For this refinement the fractional occupancies of the Bi/La sites were not varied. The model obtained from this refinement was then used to perform an X-ray refinement, where the lattice parameters, preferred orientation, zero point and peak profile coefficients (GX, GY, GZ, LX) were refined. Also, the thermal parameters and fractional occupancies of the Bi/La sites were refined, with the thermal parameters all constrained to be equal. It was found that by using this method of refinement for such a low quantity of La, the final occupancies were dependent on the initial starting occupancies. Clearly this was unacceptable. It

was decided to perform a combined X-ray and neutron refinement. A problem with this method of refinement is that the thermal parameters obtained are affected by the absorption of the X-rays by the sample. In the case of these refinements a correction is not required. So the combined X-ray and neutron refinements were carried out, using the variables discussed in Section-5.1.2. The structure was refined as $A2_1am$ without problems Figure-5.27 shows the [110] view of the structure. For the $x = 0.1$ phase the orthorhombic peaks are clearly visible in Figure-5.28.

For the samples $x = 0.1, 0.3, 0.5, 0.7$ and 0.9 the orthorhombic reflections are unambiguously identified and the sample can be refined as $A2_1am$. For the $x = 0.1$ and 0.3 refinements no other phase is observed. Starting with the $x = 0.5$ sample a second phase can be identified. This is identified by the most intense peak at $d = 2.30$, clearly observable for $x = 0.5$ in Figure-5.28. Also observable is a loss of fit to two peaks due to their merging with larger peaks. This is seen for the reflections at around 2.36 and 2.43 . For the $x = 0.7$ and 0.9 samples the main impurity peak is still able to be observed, also a smaller peak at $d = 2.35$ is present. Whilst intensity in this position is permitted by symmetry it is not observed for samples of lower La^{3+} content. It is therefore considered to be due to some impurity phase.

For the $x = 1.1$ refinement (Figure-5.29) the peak at $d = 2.40$ is no longer able to be observed and the peak at 2.418 is also noticeably weaker. The main impurity peak is also very weak. This suggests that the impurity is not increasing with increasing La^{3+} content, and is therefore not caused by the level of the La^{3+} doping. The diminishing of these peaks may be linked to the presence of two broader peaks at 2.35 and 2.41 . These peaks can

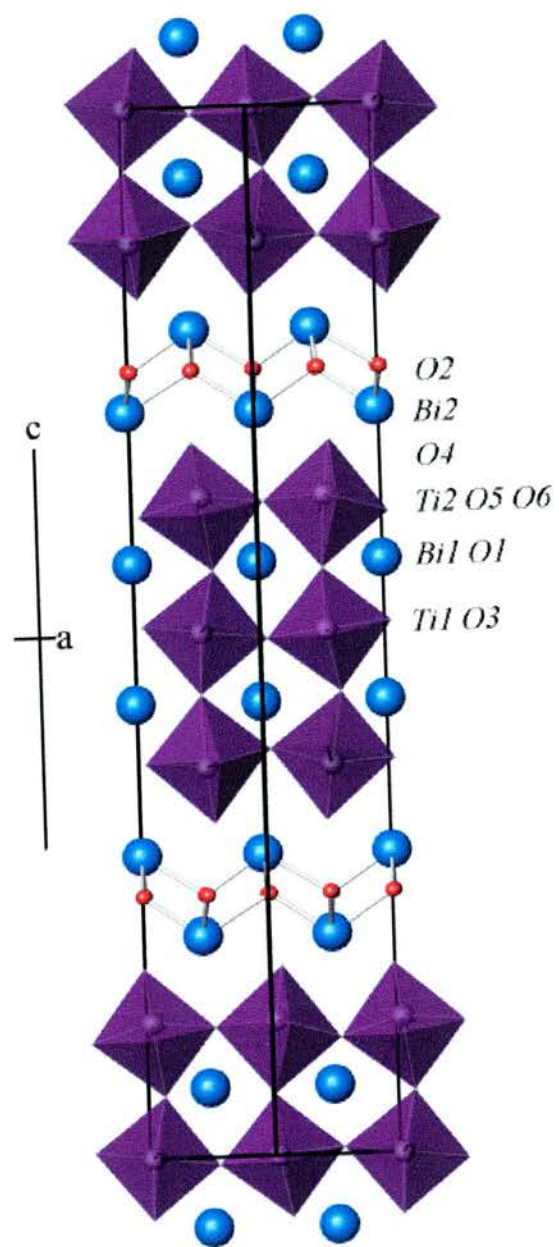


Figure 5.27: View along $[110]$ of orthorhombic $\text{Bi}_{4-x}\text{La}_x\text{Ti}_3\text{O}_{12}$

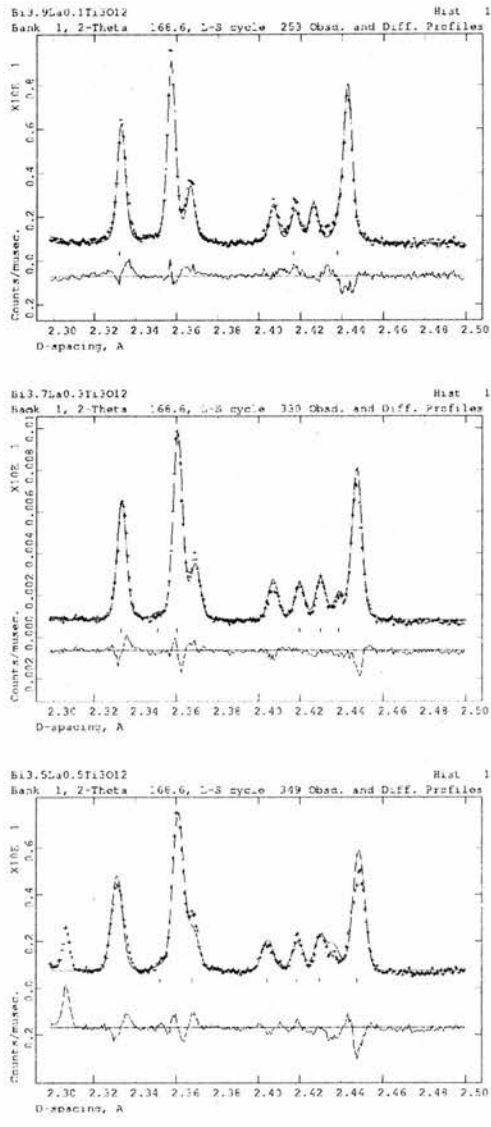


Figure 5.28: Rietveld refinements of HRPD data for the $x = 0.1, 0.3$ and 0.5 (top to bottom) members of the series $\text{Bi}_{4-x}\text{La}_x\text{Ti}_3\text{O}_{12}$, for 2.3 to 2.5 Å. Tick marks are for B2cb.

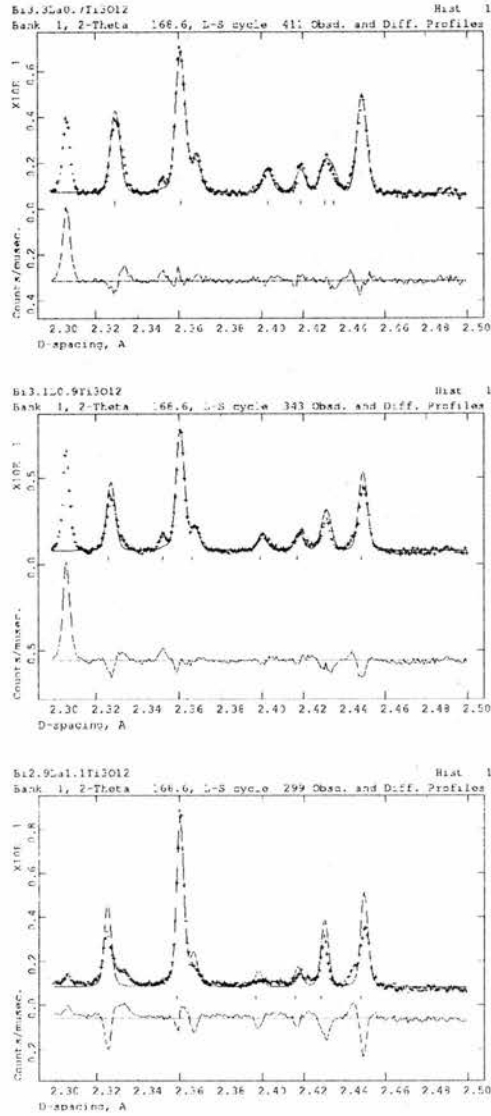


Figure 5.29: Rietveld refinements of HRPD data for the $x = 0.7, 0.9$ and 1.1 (top to bottom) members of the series $\text{Bi}_{4-x}\text{La}_x\text{Ti}_3\text{O}_{12}$, for 2.3 to 2.5 \AA . Tick marks are for B2cb.

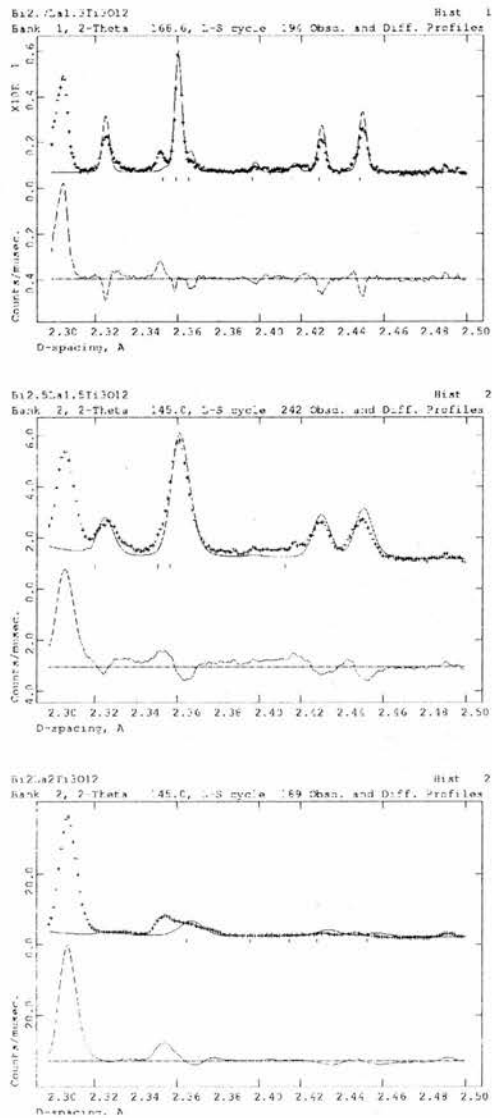


Figure 5.30: Rietveld refinements of the $x = 1.3, 1.5$ and 2.0 (top to bottom) members of the series $\text{Bi}_{4-x}\text{La}_x\text{Ti}_3\text{O}_{12}$, for 2.3 to 2.5 \AA , showing the diminishing orthorhombic reflections. Tick marks are for B2cb for $x = 1.3$ and $x = 1.5$, $x = 2.0$ is given as I4/mmm.

also be weakly observed for the $x = 0.7$ phase. For the $x = 1.3$ phase the impurity peaks at 2.30, 2.35 and 2.45 are all clearly observable. Both the 2.40 and 2.42 orthorhombic reflections are hard to discern, the $d = 2.43$ and 2.45 reflections are both clearly still present. The structure still appears to be orthorhombic.

For the $x = 1.5$ and 2.0 samples (Figure-5.30) the neutron diffraction data were collected on POLARIS at ISIS. The difference in the resolution can be clearly observed from Figure-5.30. For the $x = 1.5$ sample the impurity peak at $d = 2.30$ is still present. Also present are the orthorhombic reflections at $d = 2.43$ and 2.45, hence, the structure was refined as $A2_1am$. For the $x = 2.0$ sample the impurity peak at 2.30 is present, however, the orthorhombic supercell peaks have gone. The structure now appears to be tetragonal, and was refined as $I4/mmm$.

5.2.2 Effect of Composition on Structure

Unit Cell

The a and b parameters versus composition, given as Figure-5.31, show a merging of the a and b -axes at the $x = 1.1$ sample. At this point, and for the $x = 1.3$ and 1.5 samples, the a and b parameters were constrained to be equivalent. This was done to prevent the b -axis from becoming larger than the a -axis. 'Crossing over' of the axes can occur when the orthorhombicity ($2[a-b/a+b]$) of the samples is so low that the refinement cannot identify it. The orthorhombicity is plotted as Figure-5.32, this clearly shows the steady decrease of the orthorhombicity of the sample with La^{3+} content. Clearly

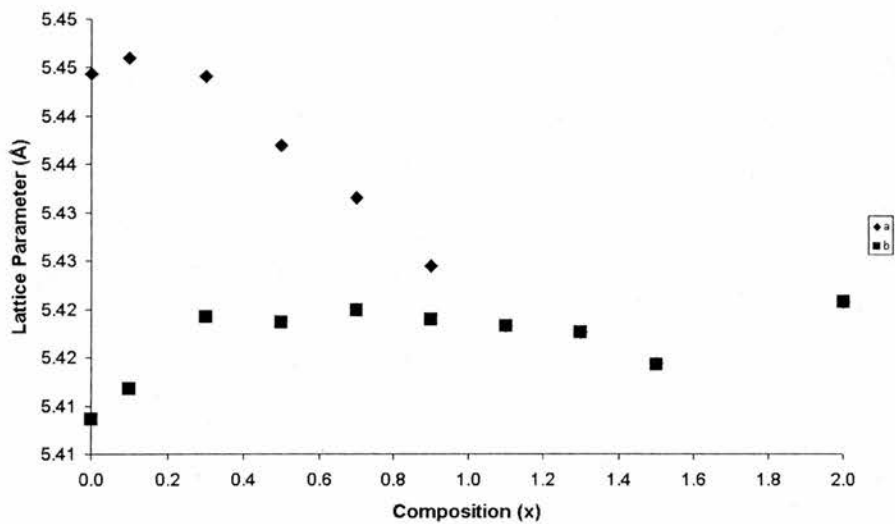


Figure 5.31: a and b parameters versus composition for $\text{Bi}_{4-x}\text{La}_x\text{Ti}_3\text{O}_{12}$

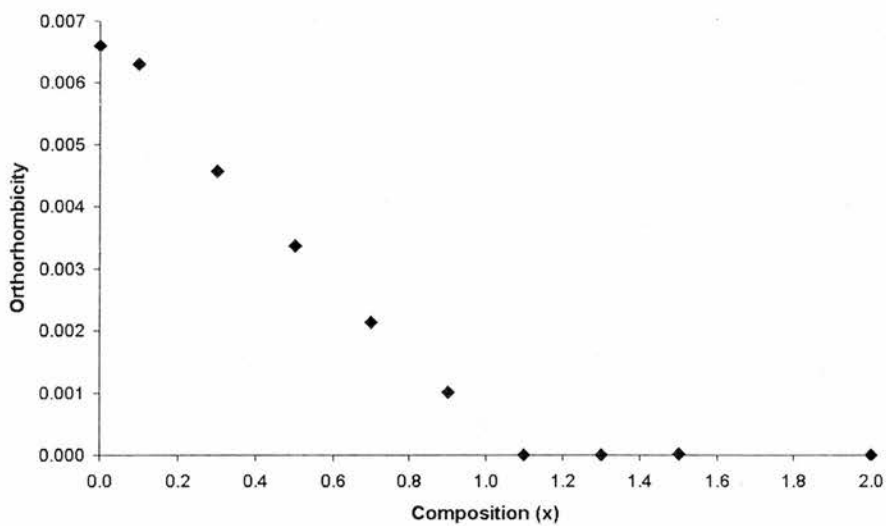


Figure 5.32: Orthorhombicity versus composition for $\text{Bi}_{4-x}\text{La}_x\text{Ti}_3\text{O}_{12}$

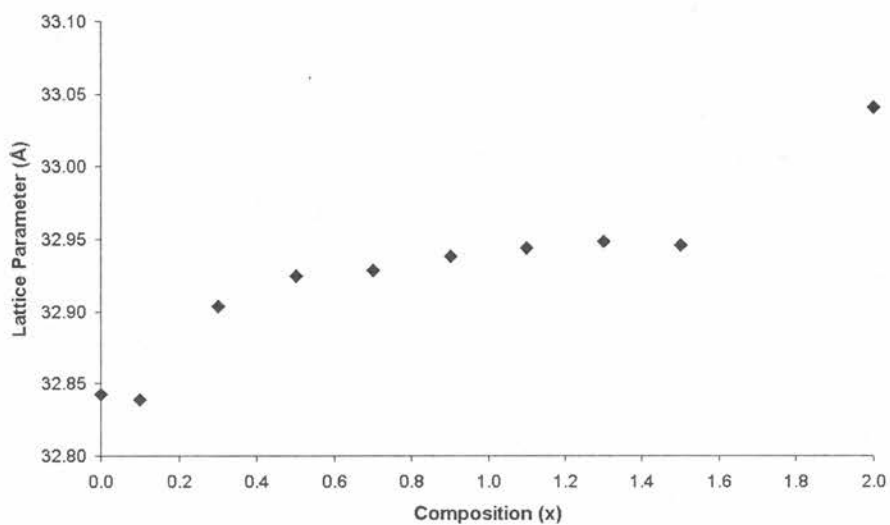


Figure 5.33: *c*-axis versus composition for $\text{Bi}_{4-x}\text{La}_x\text{Ti}_3\text{O}_{12}$

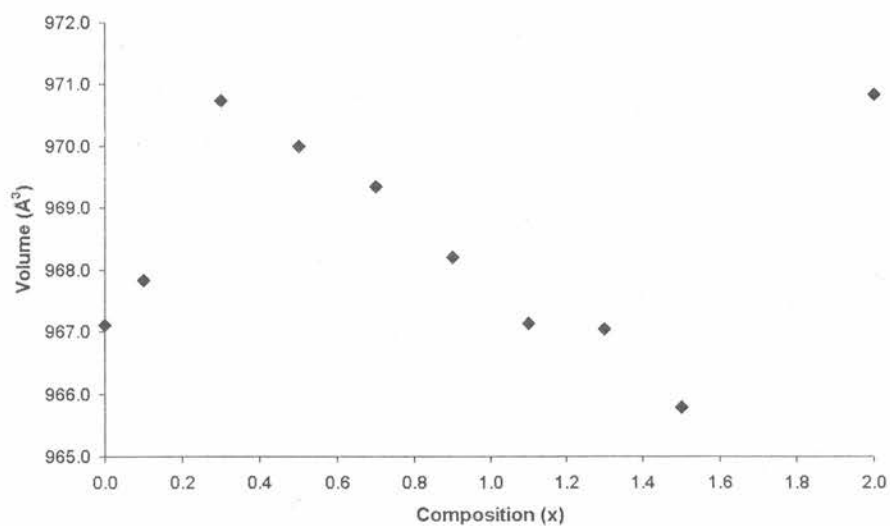


Figure 5.34: Unit cell volume versus composition for $\text{Bi}_{4-x}\text{La}_x\text{Ti}_3\text{O}_{12}$

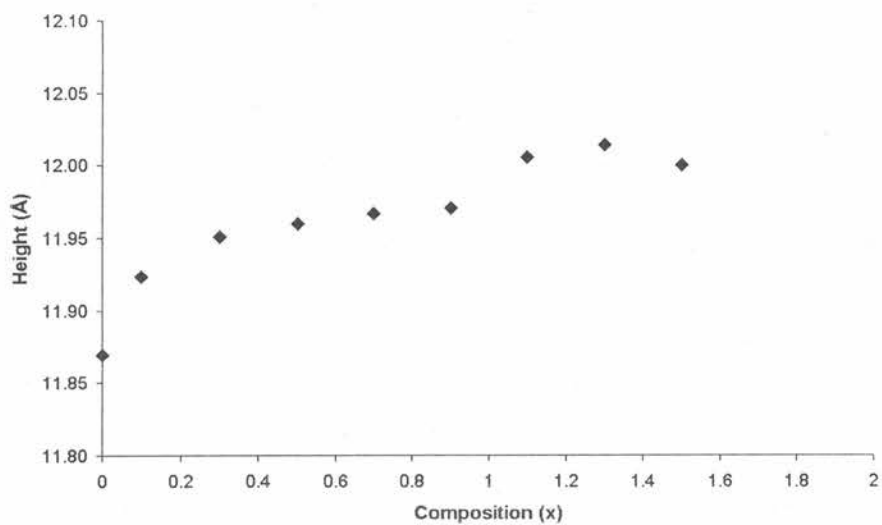


Figure 5.35: Perovskite block height versus composition for $\text{Bi}_{4-x}\text{La}_x\text{Ti}_3\text{O}_{12}$

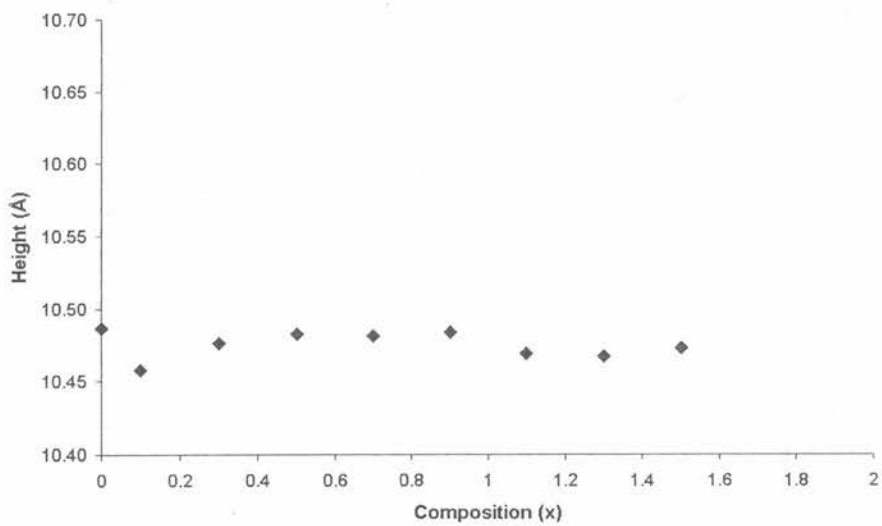


Figure 5.36: Non-perovskite block height versus composition for $\text{Bi}_{4-x}\text{La}_x\text{Ti}_3\text{O}_{12}$

the sample is metrically tetragonal, however, as shown previously there are clearly orthorhombic superstructure peaks still present until $x = 2.0$.

The change in the c -axis with composition, see Figure-5.33, shows a large increase with the initial La^{3+} doping and then a slower increase with higher dopant concentration. The unit cell volume appears erratic (Figure-5.34) but across most of the compositions the volume is decreasing. Dividing the c -axis into the perovskite and non-perovskite sections. As for the 2-layer structures these lengths are defined by the distance from apical (O4) oxygens. It can be observed (Figures-5.35 and 5.36) that it is the behaviour of the perovskite block that is dominating the c -axis behaviour. For the volume, other than the $x = 0.1$, the trend is decreasing with increasing La^{3+} content. This trend is the opposite of that observed for the 2-layer phase.

Perovskite A-site Bonding Environment

The bonding to the A-site is from the oxygen atoms in-plane (O1) with the site, the oxygens in the outer perovskite octahedron (O5 and O6) and the oxygens in the inner octahedron (O3). The in-plane bonding (Figure-5.37) displays no large changes with the increasing La^{3+} content. One bond remains longer and one shorter, there are some fluctuations in the difference between the two intermediate bond lengths, though, not enough to extrapolate any trend. For the bonding to O3 (the oxygen in the inner perovskite octahedron, given as Figure-5.38), there are two shorter and two longer bonds. Due to the oxygen atoms being located on a mirror plane there is no displacement along c . This results in two of the oxygens mirroring one another. As the bond to the oxygen represented by the cross decreases in length, the

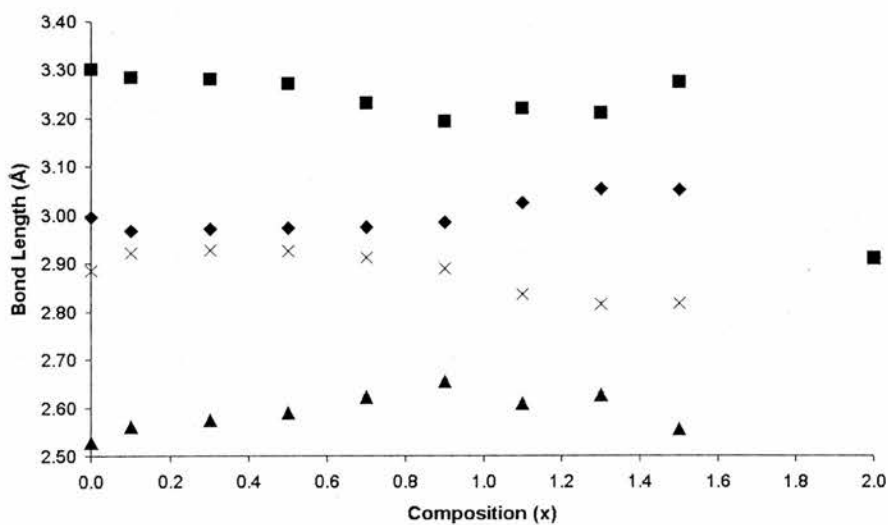


Figure 5.37: Perovskite A-site in-plane bond lengths versus composition for $\text{Bi}_{4-x}\text{La}_x\text{Ti}_3\text{O}_{12}$

bond represented by the triangle increases in length. Similar mirroring is observed for the other two bond lengths. This homogenising of the two bond lengths occurs along the a -axis, the two bond lengths along b are far less similar. It is observed that even though the models of $x = 1.1, 1.3$ and 1.5 are constrained with a and b equal the bonds are still non-homogenous. For the bonding to the oxygens in the outer perovskite octahedra (Figure-5.39) the movement of the A-site cation along the a -axis is again observed with the drastic shortening of the one long bond present and the compensating small increases of the three shorter bonds.

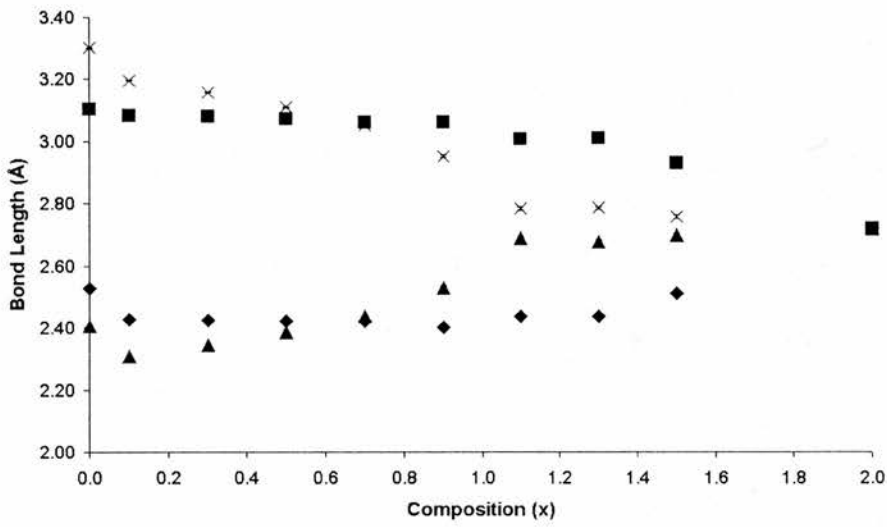


Figure 5.38: Perovskite A-site to O3 (inner perovskite octahedra) bond lengths versus composition for $\text{Bi}_{4-x}\text{La}_x\text{Ti}_3\text{O}_{12}$

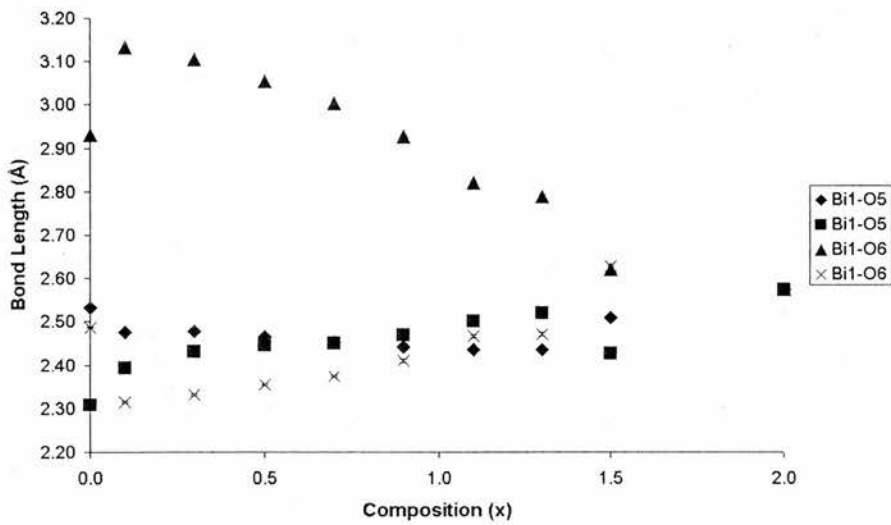


Figure 5.39: Perovskite A-site to O5 and O6 (outer perovskite octahedra) bond lengths versus composition for $\text{Bi}_{4-x}\text{La}_x\text{Ti}_3\text{O}_{12}$

[Bi₂O₂] Layer Site Bonding Environment

From the subtle changes in the lengths of the bonding within the [Bi₂O₂] layer, the Bi/La site appears to be displaying greater movement along the *a*-axis. From Figure-5.40 it is clear that even after $x = 1.1$ the refinements are still producing an unambiguously orthorhombic structure. For the bonding to the apical oxygen (O4) of the outer octahedron of the perovskite block the bonds are slowly converging, but, have not yet merged by $x = 1.5$. The plot of the bonding within the [Bi₂O₂] layer (Figure-5.41) shows that there are clearly two long and two short bonds. This splitting into the two long and short bonds indicates that the Bi/La site is displaced along both *a* and *b*. The bonds along the *a* axis are those represented by the triangle and the cross, these two bonds show far greater change with *x* than the bonds along the *b*-axis. It is therefore believed that movement is greater along *a* with increasing La³⁺ content. There is also a sudden decrease in the length of the bond represented by the cross, and a corresponding increase in that of the triangle, when the *a* and *b*-axes are constrained to be equal.

Perovskite Octahedral Distortions

For the inner perovskite octahedra the B-O bonds are constrained by symmetry to be three pairs, two pairs in plane with Ti1 and one pair representing the apical oxygens. The in-plane bonding, shown as Figure-5.42, is represented by the square and the diamond. These converge towards one another to $x = 0.9$, then at $x = 1.1$ they diverge again. The apical bond lengths are relatively constant throughout, with only a slight decrease. Evidently constraining the

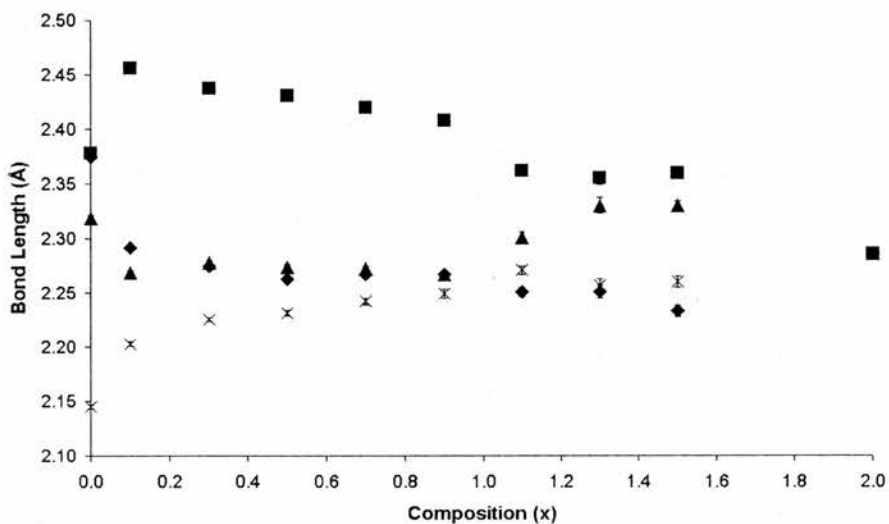


Figure 5.40: $[\text{Bi}_2\text{O}_2]$ layer to O_2 bond lengths versus composition for $\text{Bi}_{4-x}\text{La}_x\text{Ti}_3\text{O}_{12}$

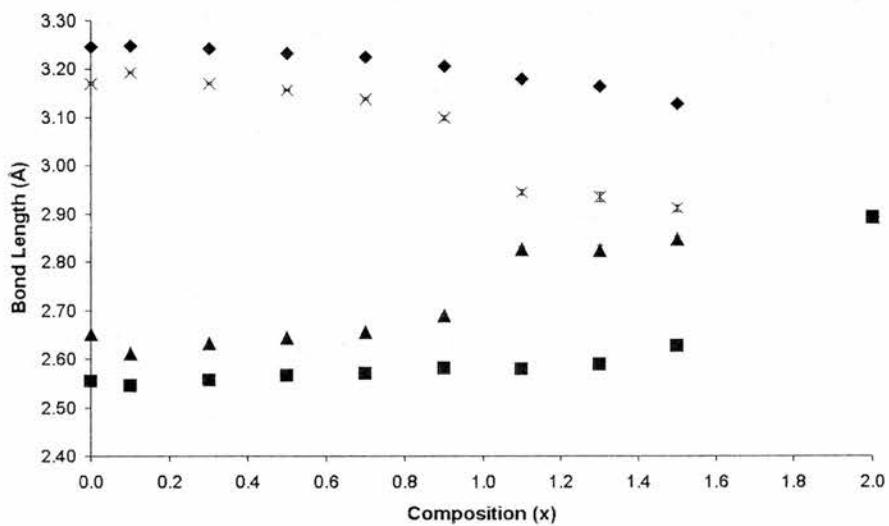


Figure 5.41: $[\text{Bi}_2\text{O}_2]$ layer to O_4 (in the outer perovskite octahedra) bond lengths versus composition for $\text{Bi}_{4-x}\text{La}_x\text{Ti}_3\text{O}_{12}$

refinement to have both a and b equal has created some problems for the refinements. From Figure-5.44 it can be seen that the initial doping of La^{3+} leads to an increase in the distortion of the inner octahedron. This distortion then decreases until the refinements are constrained with a and b equal, whereupon the distortion dramatically increases. As yet the exact cause for this remains unknown.

For the outer octahedral site the longer apical bonds, shown as the diamond in Figure-5.43, are increasing only very slightly. The in-plane bonding begins to decrease at around $x = 0.9$, before which it is constant. The inner octahedral bond angles (Figure-5.44) are consistent until the constraining of a and b , where they diverge. The outer octahedral equatorial bond angles (Figure-5.45) are decreasing in disorder, showing that the addition of the lanthanum has decreased the need for distortion in the outer octahedra. The perovskite octahedra do not appear to show any clearly identifiable trends in terms of geometry. It may be that the presence of the impurity phases is hindering correct identification of trends in the perovskite octahedra. Also noted is the effect of constraining the $x = 1.1, 1.3$ and 1.5 refinements with a and b equal.

Three tilt angles are measured the outer octahedral tilt, O5-O6-O5, the inner octahedral tilt, O3-O3-O3 and the axial tilt, O4-O4-O4. All of the octahedral tilt angles are increasing (Figure-5.46) towards a regular tetragonal structure. The axial angle is the slowest increasing, indicating that the distortion is retained most along c . The inner equatorial site is the least distorted, due in some part to the fixed c parameter for the B-site. This behaviour is closely related to the axial bond angles (Figure-5.47) where the inner octahedral site

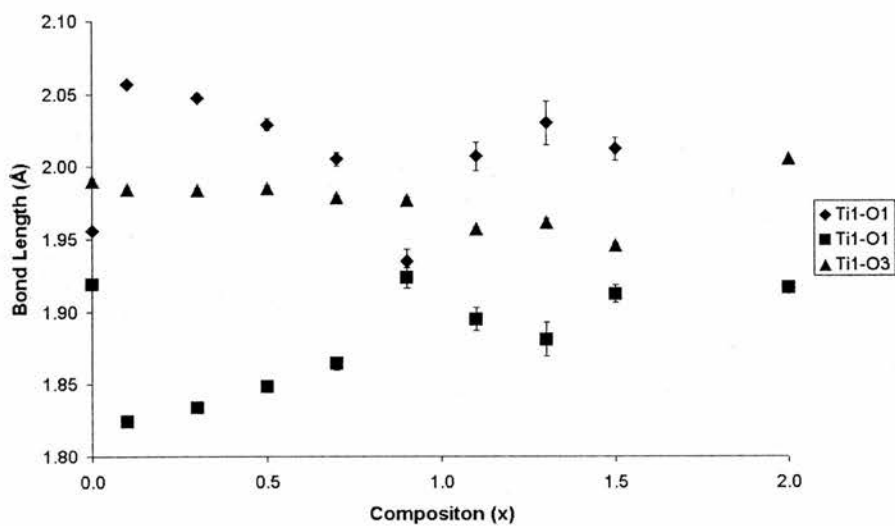


Figure 5.42: Inner perovskite layer Ti-O bond lengths versus composition for $\text{Bi}_{4-x}\text{La}_x\text{Ti}_3\text{O}_{12}$

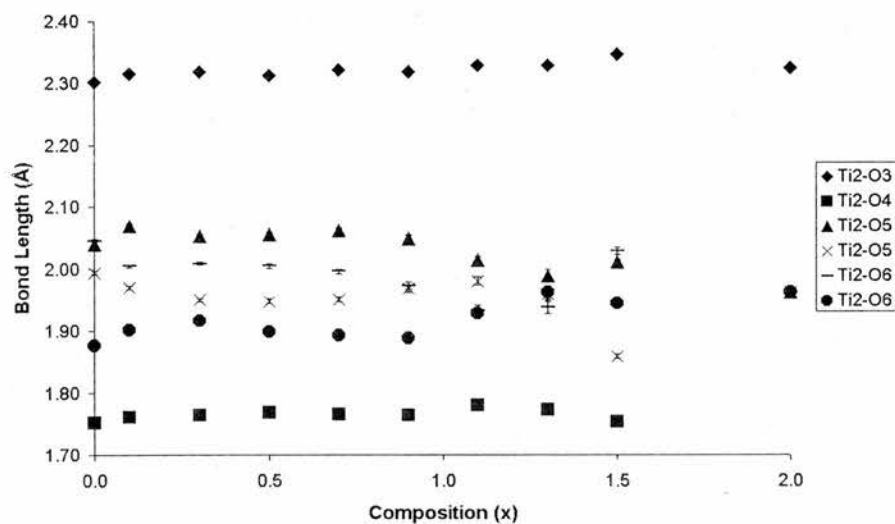


Figure 5.43: Outer perovskite layer Ti-O bond lengths versus composition for $\text{Bi}_{4-x}\text{La}_x\text{Ti}_3\text{O}_{12}$

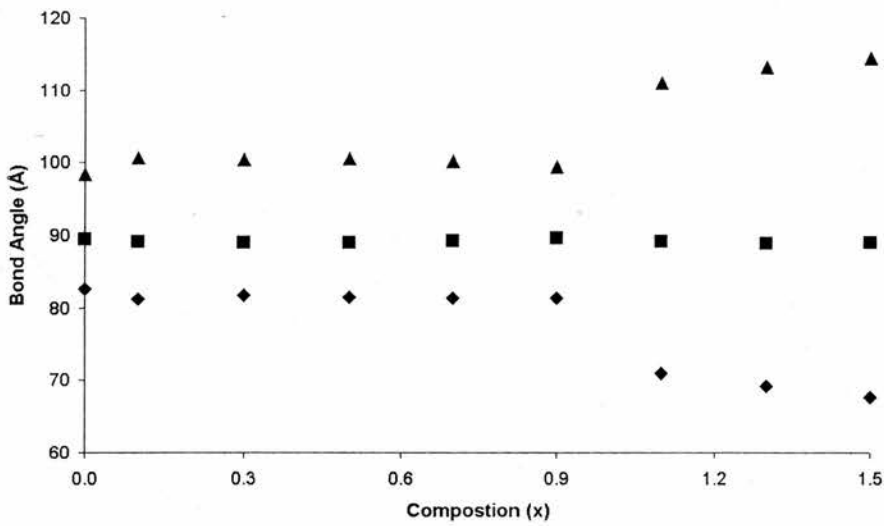


Figure 5.44: Inner octahedron equatorial bond angles, O3-Ti1-O3, versus composition for $\text{Bi}_{4-x}\text{La}_x\text{Ti}_3\text{O}_{12}$

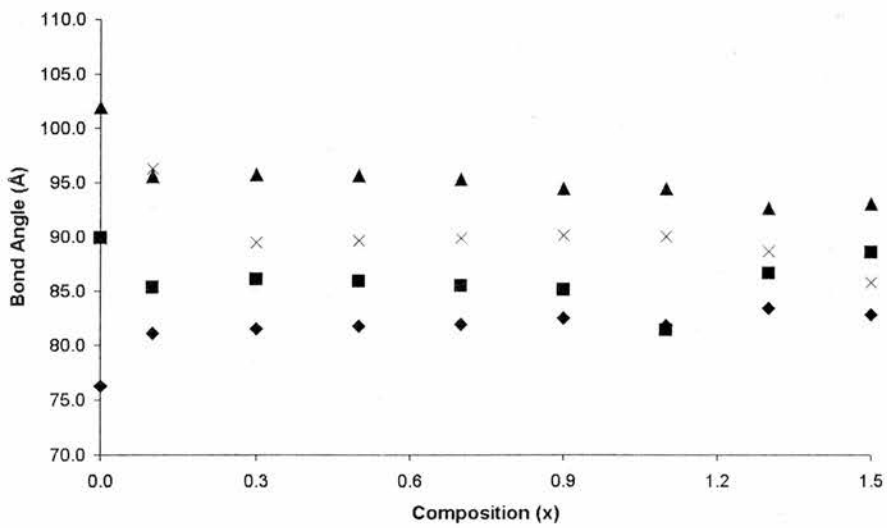


Figure 5.45: Outer octahedron equatorial bond angles, O5-Ti2-O6, versus composition for $\text{Bi}_{4-x}\text{La}_x\text{Ti}_3\text{O}_{12}$

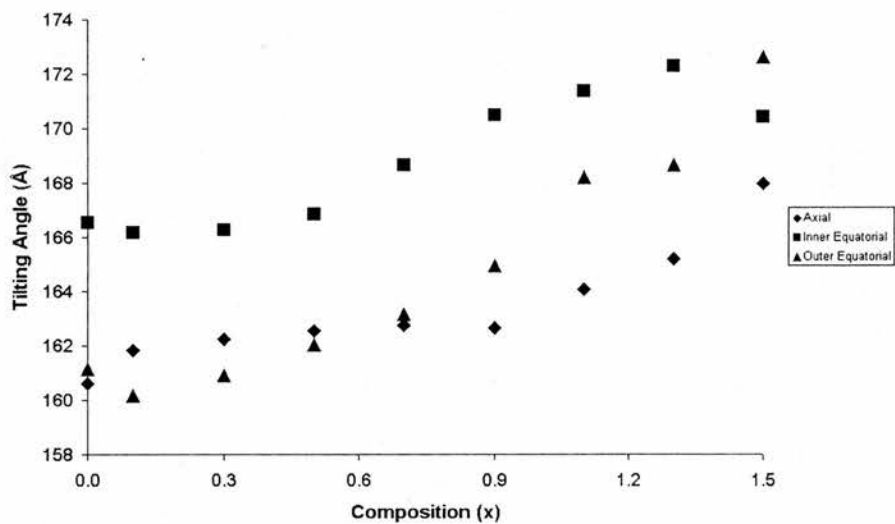


Figure 5.46: Octahedral tilting versus composition for $\text{Bi}_{4-x}\text{La}_x\text{Ti}_3\text{O}_{12}$

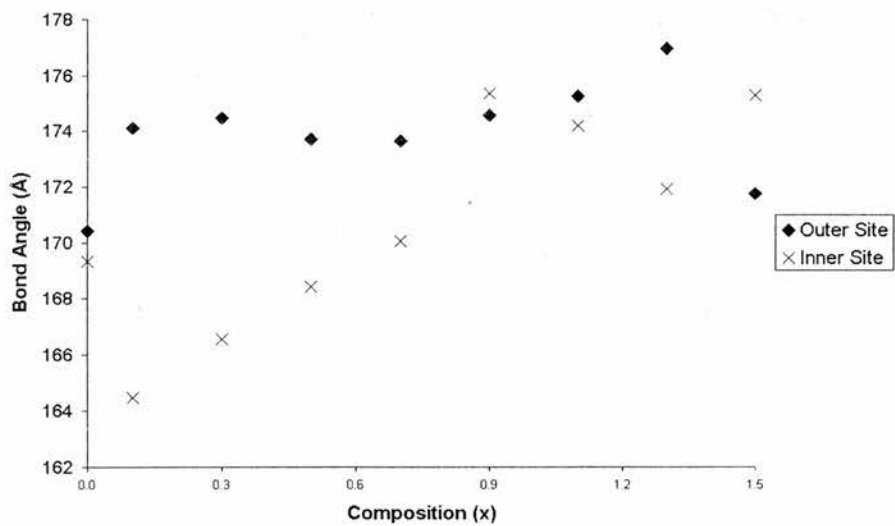


Figure 5.47: Octahedra axial bond angles, outer site, O4-Ti2-O1, inner site, O1-Ti1-O1, versus composition for $\text{Bi}_{4-x}\text{La}_x\text{Ti}_3\text{O}_{12}$

is not as heavily distorted as the outer site.

Lanthanum Distribution

The distribution of La^{3+} over the two sites is showing a clear preference for the A-site of the perovskite block over the $[\text{Bi}_2\text{O}_2]$ layer. At low values of x correctly identifying the distribution of La^{3+} is difficult, with several of the values obtained for the occupancy of the $[\text{Bi}_2\text{O}_2]$ layer being negative, see Figure-5.48. For the perovskite A-site, as observed in the 2-layer sample, there is a linear increase in the occupancy with the increase in dopant level, shown as Figure-5.49. One point is clearly incongruous, at $x = 1.3$ there is a large increase in the amount of La^{3+} in the $[\text{Bi}_2\text{O}_2]$ layer and a corresponding decrease in the A-site occupancy. It is unclear why the refinement has stabilised at these values, but it appears to be a stable minimum.

5.2.3 Discussion

Initially it was hoped that some values of x would be established for the change from an orthorhombic structure to a tetragonal structure. For the $\text{Bi}_{3-x}\text{La}_x\text{TiNbO}_9$ series for x up to 0.6 the structure appears to be orthorhombic, at $x = 0.8$ it would appear to be tetragonal. For the $n = 3$ $\text{Bi}_{4-x}\text{La}_x\text{Ti}_3\text{O}_{12}$ at values up to $x = 1.5$ the structure appears to be orthorhombic, by $x = 2$ it appears tetragonal. In both series the presence of small impurities in the samples hampered the identification. One point to arise from these investigations was the question of the change of the c -axis. For the $n = 2$ series this can be seen to decrease, shown in Figure-5.12. In the case of the $n = 3$

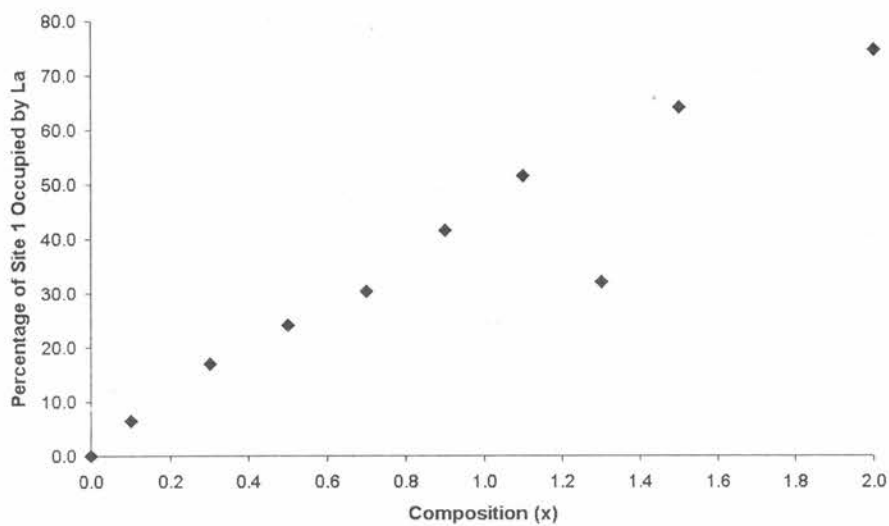


Figure 5.48: Percentage of A-site occupied by La^{3+} versus composition for $\text{Bi}_{4-x}\text{La}_x\text{Ti}_3\text{O}_{12}$

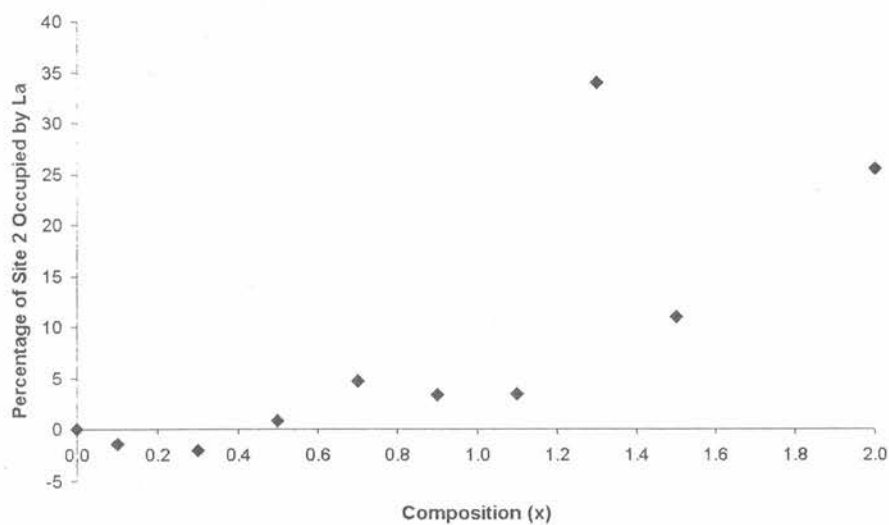


Figure 5.49: Percentage of $[\text{Bi}_2\text{O}_2]$ layer site occupied by La^{3+} versus composition for $\text{Bi}_{4-x}\text{La}_x\text{Ti}_3\text{O}_{12}$

series it is seen to increase, given as Figure-5.33. From the plots of the La^{3+} occupancies (Figures-5.25, 5.26, 5.48 and 5.49) it is suggested that the La^{3+} is initially, and predominantly to be found in the A-site of the perovskite block. It is then to be considered why a cation which will desire a more central position in a site, thus less space, can create both expansion and contraction along the c -axis.

For the $\text{Bi}_{3-x}\text{La}_x\text{TiNbO}_9$ series examining Figure-5.20 there is very little change in the axial tilting. A larger change in the axial tilt would suggest the structure was moving towards a more vertically straight alignment of the octahedra. In this case there is little change and the La^{3+} would be expected to have a contracting effect on the lattice parameters. The equatorial tilting is increasing a faster rate than the axial tilting, Figure-5.19, this may explain why the b -axis appears to be increasing towards the a -axis. In the case of the $\text{Bi}_{4-x}\text{La}_x\text{Ti}_3\text{O}_{12}$ series the axial tilting increases more than for the two layer, Figure-5.46. It can also be observed that the axial (apical) bond angle for the octahedral sites is increasing, Figure-5.47, particularly for the inner site. This would be indicative of an aligning of the octahedra with the c -axis, thus creating an increase in the overall c -axis length.

References

- [1] C. A.-P. de Araujo, J. D. Cuchiaro, L. D. McMillan, M. C. Scott, and J. F. Scott, *Nature*, 1995, **374**, 627.
- [2] B. H. Park, B. S. Kang, S. D. Bu, T. W. Noh, J. Lee, and W. Jo, *Nature*, 1999, **401**, 682.
- [3] B. Frit and J. P. Mercurio, *J. Alloys Compd.*, 1992, **188**, 27.
- [4] J. G. Thompson, A. D. Rae, R. L. Withers, and D. C. Craig, *Acta Cryst. B*, 1991, **47**, 174.
- [5] S. M. Blake, M. J. Falconer, M. McCree, and P. Lightfoot, *J. Mater. Chem.*, 1997, **7**, 1609.
- [6] C. H. Hervoches and P. Lightfoot, *Chem. Mater.*, 1999, **11**, 3359.
- [7] C. H. Hervoches and P. Lightfoot, *J. Solid State Chem.*, 2000, **153**, 66.
- [8] M.-W. Chu, M. T. Calades, Y. Piffard, A.-M. Marie, E. Gautier, O. Joubert, M. Ganne, and L. Brohan, *J. Solid State Chem.*, 2003, **172**, 389.

Chapter 6

Other Layered Phases

Whilst most of the work presented in this thesis has been done on Aurivillius phases, a significant amount of work has been carried out on both Dion-Jacobson and Ruddlesden-Popper phases. This work was carried out to examine the different distortions present in the layered phases, that is the work presented here.

6.1 Dion-Jacobson Phases

The Dion-Jacobson phases are a family of layered perovskites of general formula $A'[A_{n-1}B_nO_{3n+1}]$, where the perovskite blocks are separated by a single layer of large monovalent cations, e.g. Rb^+ or Cs^+ . Previous structural work on the Dion-Jacobson phases has focused on the potential for B-site ordering, and the inclusion of differing A-site cations to produce different structural distortions. The B-site ordering is a previously documented phenomenon for 3-layer structures, with 2 Ti and 1 Nb in the B-site. These previous studies were done using powder X-ray diffraction. For this study it was attempted to ascertain if there were actually some subtle structural distortions

of the structures, hence, neutron diffraction has been performed upon the $\text{CsLa}_2\text{TiNb}_2\text{O}_{10}$ sample.

It is common that the A-site cation should either be a lanthanide or a divalent metal such as Sr or Ca, however, it is unusual to find any report of Bi as the A-site cation in Dion-Jacobson phases. A previous study by Subramanian[1] reports the indexing of the 2 and 3-layer Dion-Jacobson phases $\text{CsBiNb}_2\text{O}_7$ and $\text{CsPb}_2\text{Nb}_3\text{O}_{10}$. In this previous study the $\text{CsBiNb}_2\text{O}_7$ structure is metrically orthorhombic. However, the lattice parameters for a and b are given as 7.599 Å, and 7.714 Å, respectively, i.e. approximately $2a_T \times 2a_T$. If the structure is distorted so as to require being orthorhombic, it would be more normal for it to be with a and b approximately 5.4 Å, i.e. $\sqrt{2}a_T$. In the paper only lattice parameters are given. Since these structures are potentially very interesting as a comparison to the Aurivillius phases, a full structural refinement was required. It was decided to prepare the 2-layer $\text{CsBiNb}_2\text{O}_7$ and $\text{CsNdNb}_2\text{O}_7$ and the 3-layer $\text{CsLa}_2\text{TiNb}_2\text{O}_{10}$, $\text{CsNd}_2\text{TiNb}_2\text{O}_{10}$ and $\text{CsBi}_2\text{TiNb}_2\text{O}_{10}$ samples.

Also documented previously are indexings of powder X-ray diffraction patterns for $\text{CsBi}_3\text{Ti}_4\text{O}_{13}$ and $\text{CsBi}_3\text{PbTi}_5\text{O}_{16}$ [2], $n = 4$ and 5-layer phases respectively, these two structures are both described as tetragonal. Here the $n = 4$ phase $\text{CsBi}_3\text{Ti}_4\text{O}_{13}$ was prepared and analysed using powder neutron diffraction.

6.1.1 CsMnNb₂O₇

CsNdNb₂O₇

This compound was analysed using powder X-ray diffraction to identify whether it appeared to be either tetragonal ($a = a_T$) or orthorhombic ($a, b \sim \sqrt{2}a_T$). It is clear from Figure-6.1 that the structure cannot be described by P4/mmm, the space group observed for the La³⁺ containing analogous compound, as there are unmatched intensities. It is believed that if the structure is distorted then it will be found in an orthorhombic space group. Also, the orthorhombic Pmmm space group has too many permitted reflections, as was expected, Pmmm is not often observed for layered perovskites. Hence the actual space group is probably of higher symmetry than Pmmm and lower than P4/mmm. To establish which space group requires the use of powder neutron diffraction.

This sample was analysed by powder neutron diffraction at the HRPD station at ISIS. Already, using powder X-ray diffraction, we have been able to discount the tetragonal structure of CsLaNb₂O₇[3]. Therefore, a small change in the size of the lanthanide has resulted in a significant change in the structure of this phase. Another structural refinement of a 2-layer Dion-Jacobson phase, RbLaNb₂O₇[4], was previously performed using powder neutron diffraction. The model for the Rb phase is orthorhombic, with the b -axis set as the long axis, space group Imma. The Imma spacegroup is centrosymmetric and so the RbLaNb₂O₇ phase is not ferroelectric. This structure was examined against our neutron data and found to be an unsuitable model. In this case a change in the size of the alkali metal cation has also produced a

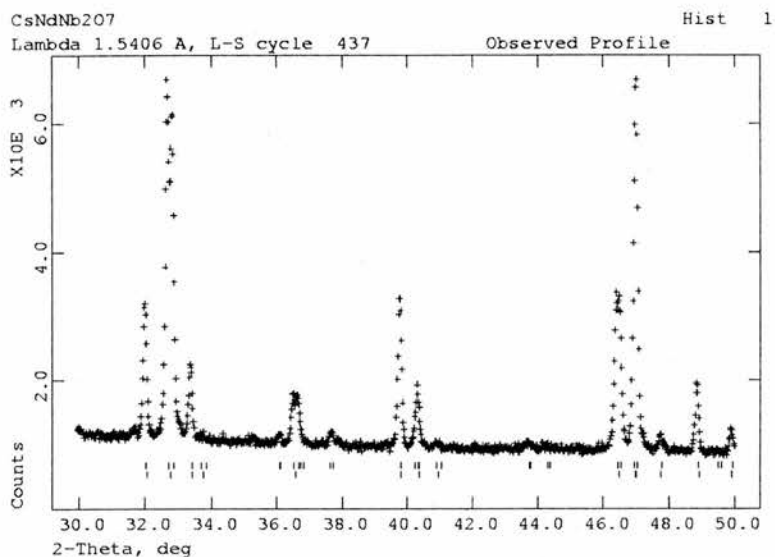


Figure 6.1: $\text{CsNdNb}_2\text{O}_7$ XRD data, showing $P4/mmm$ permitted reflections (lower marks) and $Pmmm$ supercell permitted reflections (upper marks)

notable structural change. This, along with the change caused by altering the A-site cation, demonstrates that the structural behaviour of these phases is very sensitive to composition. Using the absences, two space groups were identified as possibilities for modelling the structure, the centrosymmetric $Pm\bar{m}$ and the non-centrosymmetric $P2_1am$. These two space groups have the same absences, however, the $Pm\bar{m}$ group will not permit rotations of the octahedra around the c -axis. The $P2_1am$ space group permits octahedral rotations around all three axes, though the tilting must be in phase along c due to the mirror plane. This behaviour is analogous to that observed for the 2-layer Aurivillius phases.

Fitting the simpler centrosymmetric model to the data resulted in certain fitting problems. Notably the χ^2 was 6.8, which is a good value, so the model

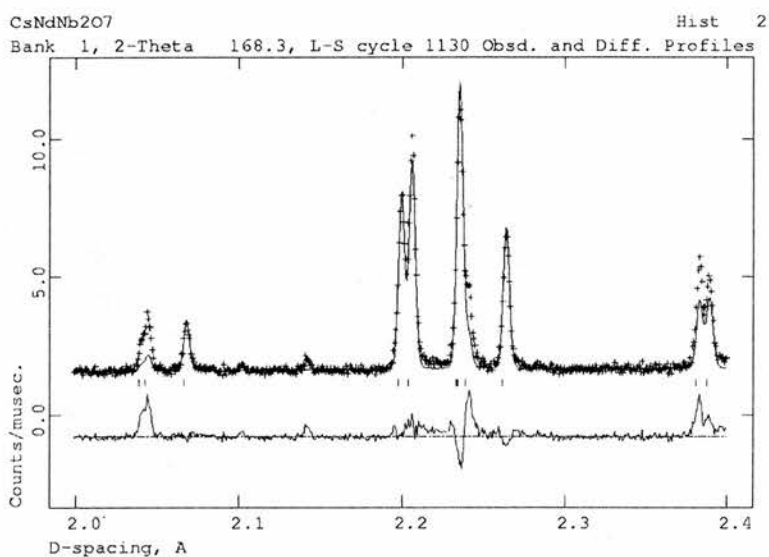


Figure 6.2: CsNdNb₂O₇, Pmam refinement from 2 to 2.4 Å, showing unfitted intensities

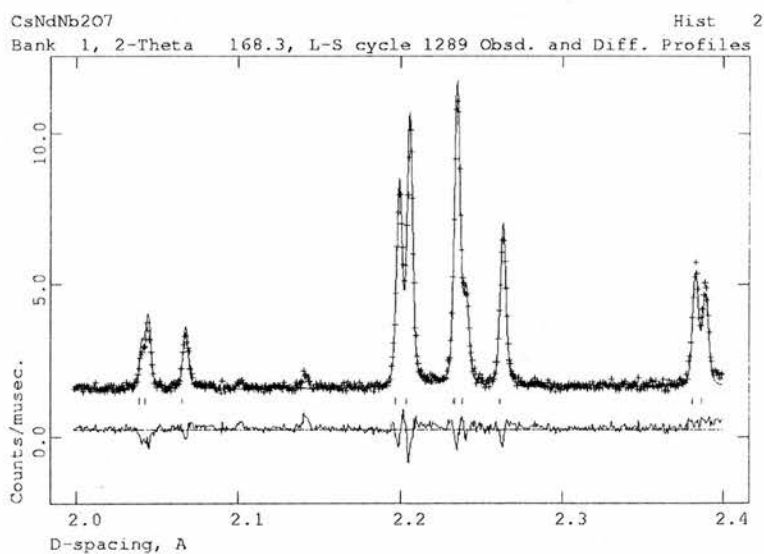


Figure 6.3: CsNdNb₂O₇, P2₁am refinement from 2 to 2.4 Å, showing correctly fitted intensities

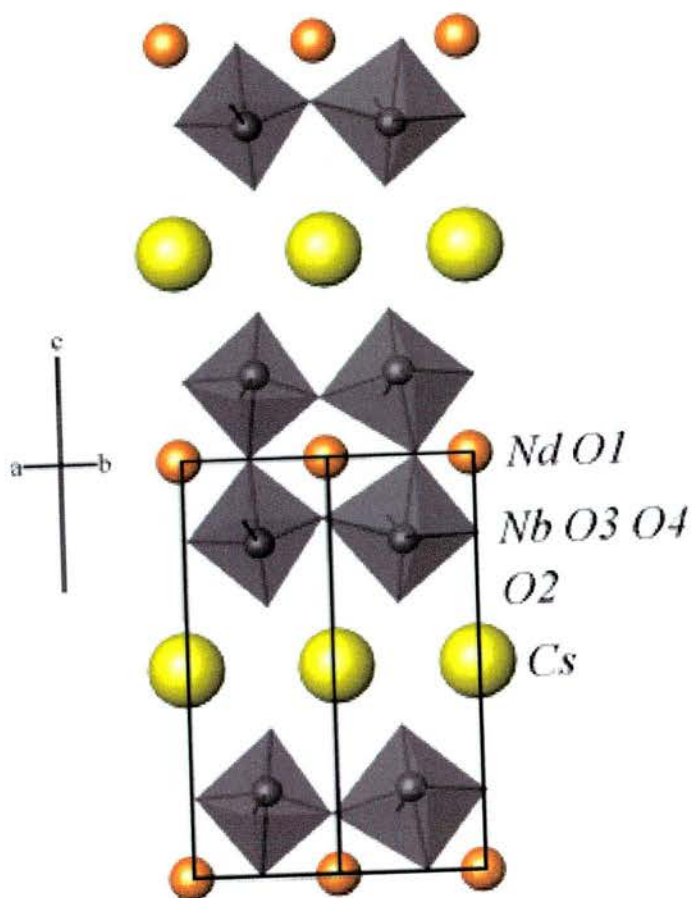


Figure 6.4: $\text{CsNdNb}_2\text{O}_7$ structure, Cs = yellow, Nd = orange Nb = grey, O = red

Table 6.1: CsNdNb₂O₇ atomic parameters from 25°C HRPD data, space group P2₁am, a = 5.4722(1) Å, b = 5.4474(1) Å, c = 11.1695(1) Å. R_{WP} = 0.043, $\chi^2 = 3.36$, for 7667 data points and 3001 contributing reflections, 0.4 < d < 3.3 Å

Atom	Multiplicity	x	y	z	Uiso/Uequiv x 100
Cs	2	0.245(1)	0.2655(6)	0.500000	1.95(7)
Nd	2	0.2645(6)	0.2552(4)	0.000000	0.90(5)
Nb	4	0.2451(5)	0.7537(4)	0.2020(1)	0.98(3)
O1	2	0.220(1)	0.6791(5)	0.000000	2.38
O2	4	0.2454(6)	0.8021(4)	0.3552(2)	1.46
O3	4	0.0072(6)	0.0278(6)	0.1443(2)	1.71
O4	4	0.4323(4)	0.4532(5)	0.1906(2)	2.16

Atom	U11	U22	U33	U12	U13	U23
O1	2.4(3)	1.9(2)	2.8(2)	-0.4(2)	0.00	0.00
O2	1.6(1)	1.0(2)	1.8(1)	-0.5(2)	1.7(2)	-0.7(1)
O3	0.4(1)	2.4(2)	2.4(1)	0.0(1)	-0.9(2)	-0.5(2)
O4	2.7(2)	1.7(2)	2.2(1)	-1.0(1)	0.1(1)	-0.5(1)

Table 6.2: CsNdNb₂O₇ selected bond lengths

bond	length Å	bond	length Å	bond	length Å
Cs O2	2.998(4) x 2	Nd O1	3.148(3)	Nb O1	2.297(1)
Cs O2	3.341(4) x 2	Nd O1	2.322(4)	Nb O2	1.731(2)
Cs O2	3.198(6) x 2	Nd O1	3.002(7)	Nb O3	2.083(4)
Cs O2	3.202(6) x 2	Nd O1	2.517(7)	Nb O3	1.972(5)
		Nd O3	2.473(4) x 2	Nb O4	1.935(4)
		Nd O3	2.596(3) x 2	Nb O4	2.053(4)
		Nd O4	2.558(2) x 2		
		Nd O4	3.219(3) x 2		

is fitting most of the data well. However, looking at the plot of the refinement it is clear that although the general fit is good it appears to be failing to fit some of the structural data, see Figure-6.2. These small discrepancies in the fit quality are most likely caused by the inability of the centrosymmetric model to accommodate the oxygen displacements required by the structure. Therefore the next step was to attempt a fit to the data with a $P2_1am$ model and compare the result. The non-centrosymmetric model for $P2_1am$ gave a χ^2 of 3.2, which is a significant improvement on the Pm model. Examining the fit it is clear that those peaks not fitted by the Pm model are now being fitted, shown as Figure-6.3. The subtle differences between the two models shows up clearly in the plots of the Rietveld refinements. It can be stated unambiguously that the $P2_1am$ model provides a better representation of the structure, shown as Figure-6.4 and Tables-6.1 and 6.2.

CsBiNb₂O₇

The Bi^{3+} variant of the 2-layer structure was examined using powder X-ray and neutron diffraction. From the X-ray diffraction data (Figure-6.5) it is clear that the structure is orthorhombic, $a = \sqrt{2}a_T$. The neutron analysis followed the same pattern as for the Nd^{3+} analogue, with the two space groups, Pm and $P2_1am$ being selected. It was found for these two groups that generally the fit of the Bi^{3+} sample was of poorer quality than the Nd^{3+} sample. However, the same conclusion was reached and the $P2_1am$ model was found to produce a superior fit, the χ^2 actually halving from the Pm to $P2_1am$ model. The two fitted histograms are shown as Figure-6.6 and Figure-6.7, with data given as Tables-6.3 and 6.4. The structure displays

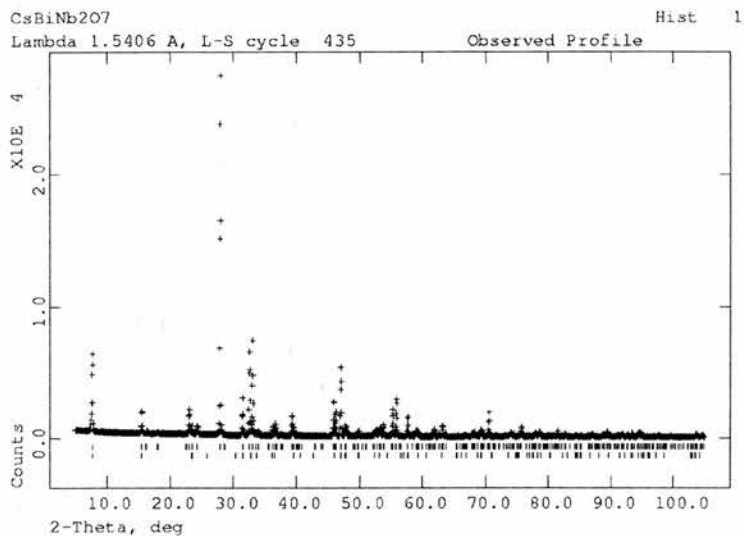


Figure 6.5: X-ray diffraction pattern of $\text{CsBiNb}_2\text{O}_7$. Upper marks are Pmmm, lower marks are I4/mmm

similar distortions of the perovskite layer to those observed for $\text{CsNdNb}_2\text{O}_7$, shown as Figure-6.8.

From Figure-6.9 the relative rotations of the two perovskite blocks can be examined. It would appear that the Nd^{3+} sample has larger tilting of the octahedra than the Bi^{3+} sample. The ionic radius of the Bi^{3+} cation is slightly larger than that of the Nd^{3+} , so it would be expected that it may require a larger site and thus create smaller octahedral tilting. For both the a and c axes the $\text{CsNdNb}_2\text{O}_7$ phase is smaller than the $\text{CsBiNb}_2\text{O}_7$ phase. the situation is reversed for the b -axis. This is believed to be due to the Cs layer only tolerating a certain range of values for the ab -plane, so as the a -axis contracts the b -axis expands to compensate.

Bi^{3+} also has a lone pair, this has a strong effect on the bonding of the Bi^{3+} .

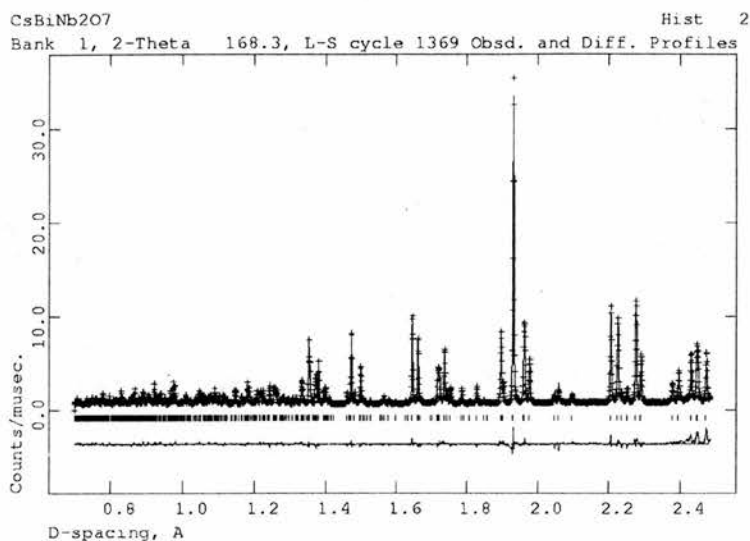


Figure 6.6: Neutron diffraction pattern of $\text{CsBiNb}_2\text{O}_7$, backscattering bank, showing fit of $\text{P2}_1\text{am}$ model

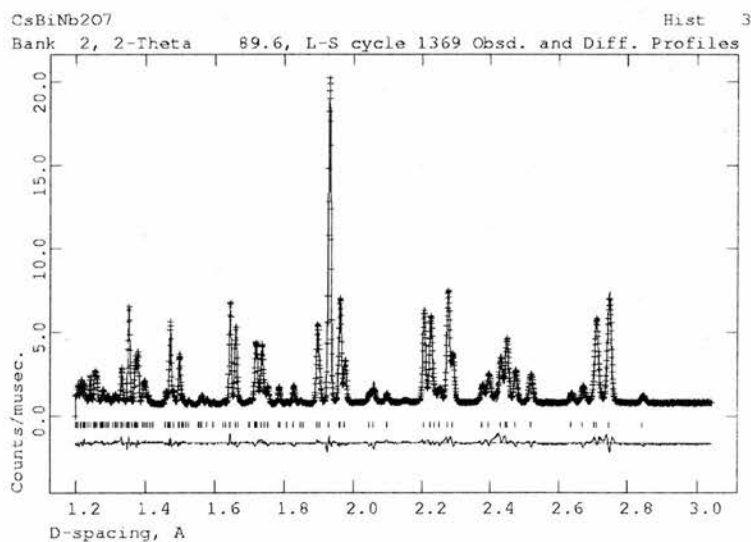


Figure 6.7: X-ray diffraction pattern of $\text{CsBiNb}_2\text{O}_7$, 90° bank, showing fit of $\text{P2}_1\text{am}$ model

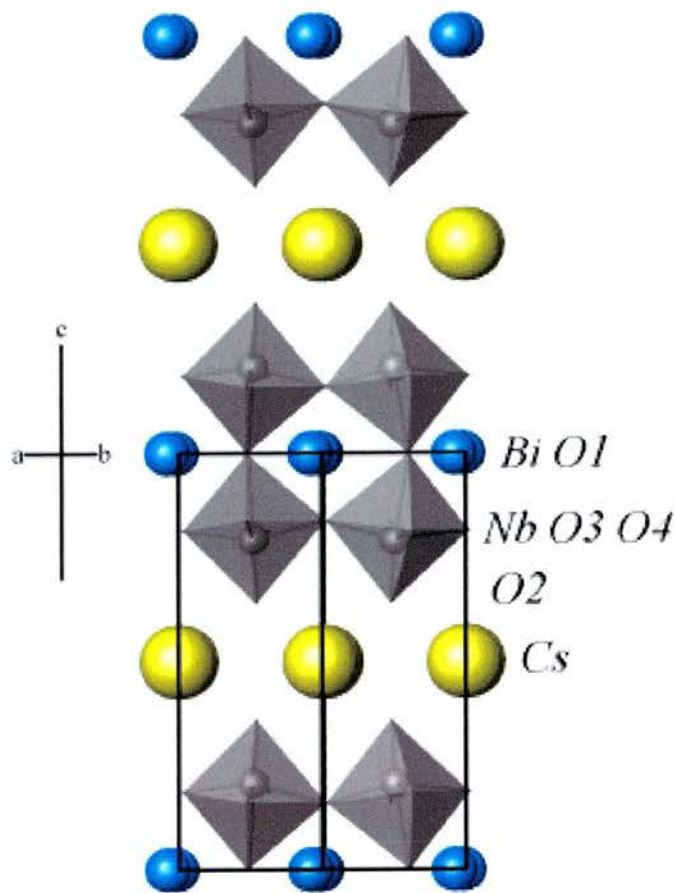


Figure 6.8: $\text{CsBiNb}_2\text{O}_7$ structure, Cs = yellow, Bi =blue Nb = grey, O = red

Table 6.3: CsBiNb₂O₇ atomic parameters from 25°C HRPD data, space group P2₁am, a = 5.4953(1) Å, b = 5.4225(1) Å, c = 11.3766(1) Å. R_{WP} = 0.063, $\chi^2 = 7.60$, for 7326 data points and 627 contributing reflections, 0.70 < d < 3.1 Å

Atom	Multiplicity	x	y	z	Uiso/Uequiv x 100
Cs	2	0.2536(7)	0.2590(5)	0.500000	2.18(7)
Bi	2	0.3045(3)	0.2776(3)	0.000000	1.43(6)
Nb	4	0.2456(4)	0.7577(4)	0.2078(1)	1.22(4)
O1	2	0.2157(5)	0.6840(5)	0.000000	1.65*
O2	4	0.2474(4)	0.7797(4)	0.3617(2)	1.41*
O3	4	0.0099(5)	0.0267(4)	0.1604(2)	1.72*
O4	4	0.4288(3)	0.4480(4)	0.1861(2)	2.64*

Atom	U11	U22	U33	U12	U13	U23
O1	1.9(2)	1.3(2)	1.7(2)	-1.2(2)	0.00	0.00
O2	1.6(1)	1.14(1)	1.5(1)	1.1(1)	-1.1(1)	0.2(1)
O3	1.5(1)	2.8(2)	0.9(1)	0.9(1)	-0.6(2)	-0.6(1)
O4	3.5(2)	1.6(2)	2.8(2)	1.6(1)	-0.9(1)	-0.8(1)

Table 6.4: CsBiNb₂O₇ selected bond lengths

bond	length Å	bond	length Å	bond	length Å
Cs O2	3.038(4) x 2	Bi O1	3.256(3)	Nb O1	2.403(1)
Cs O2	3.232(3) x 2	Bi O1	2.257(3)	Nb O2	1.755(2)
Cs O2	3.202(4) x 2	Bi O1	3.243(3)	Nb O3	2.024(4)
Cs O2	3.144(4) x 2	Bi O1	2.269(3)	Nb O3	1.941(3)
		Bi O3	2.794(3) x 2	Nb O4	1.973(3)
		Bi O3	2.707(3) x 2	Nb O4	2.082(3)
		Bi O4	3.311(3) x 2		
		Bi O4	2.409(2) x 2		

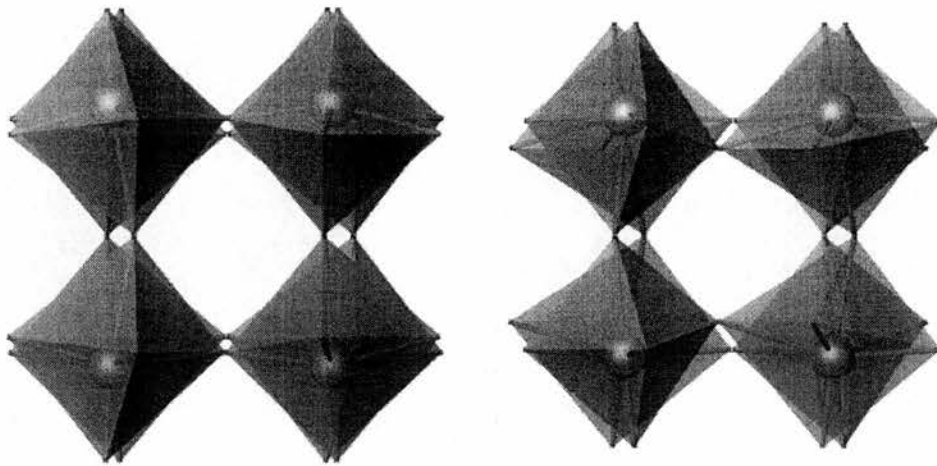


Figure 6.9: View along [110] for $\text{CsBiNb}_2\text{O}_7$ (left) and $\text{CsNdNb}_2\text{O}_7$ (right), showing the out of phase rotations of the octahedra along the tetragonal a -axis

From Figure-6.10 it is clear that the Bi^{3+} cation is more displaced from the idealised centre than the Nd^{3+} cation. It is most likely that this is an effect of the lone pair. These structures are distorted layered perovskites with distortions similar to ferroelectric 2-layer Aurivillius phases. To examine the samples for any potential similar ferroelectric behaviour an a.c. impedance experiment was performed.

A.C. Impedance

An a.c. impedance spectroscopy experiment was carried out on the $\text{CsNdNb}_2\text{O}_7$ sample. For this experiment no ferroelectric peak was observed in the plot of permittivity versus temperature, $\epsilon' \sim 4$. Therefore, there is no ferroelectric phase change over the range $150\text{ }^\circ\text{C}$ to $850\text{ }^\circ\text{C}$.

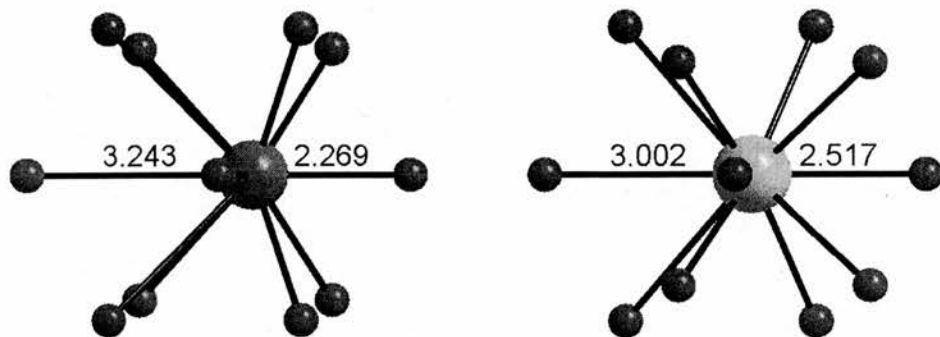


Figure 6.10: View along [010] for $\text{CsBiNb}_2\text{O}_7$ (left) and $\text{CsNdNb}_2\text{O}_7$ (right), showing the displacement of the A-site cation.

6.1.2 $\text{CsM}_2\text{Ti}_2\text{NbO}_{10}$ (M = La, Nd & Bi)

The three compositions $\text{CsM}_2\text{Ti}_2\text{NbO}_{10}$ (M = La, Nd & Bi) are 3-layer Dion-Jacobson phases, these have been analysed here using powder X-ray and neutron diffraction. The $\text{CsLa}_2\text{Ti}_2\text{NbO}_{10}$ sample was prepared previously by Richard Riggs.

$\text{CsLa}_2\text{Ti}_2\text{NbO}_{10}$

The 3-layer La^{3+} containing phase has been previously reported by powder X-ray diffraction as tetragonal, in the $P4/mmm$ space group, $a = 3.8495(1)$ Å, $c = 15.3927(2)$ Å [5]. B-site ordering was reported where the inner octahedral site is occupied solely by Ti^{4+} and the outer site is a 50/50 mix of Ti^{4+} and Nb^{5+} [5]. Examining laboratory X-ray diffraction data the sample prepared appeared to be tetragonal. In order to confirm this the sample was taken to POLARIS at ISIS where powder neutron data were collected. Using the model of Hong et al. it is clear that the structure is tetragonal, as no su-

perstructure peaks are able to be observed (Figure-6.11). There is one small impurity phase peak present at $d = 2.35$, shown in Figure-6.12. However, no other impurity peaks could be identified and so the second phase was not identified.

The ordering of the B-site was set initially as that proposed by Hong and co-workers. When the model was permitted to refine these occupancies, it was found that they retained the initial ordering. For this structure although no superstructure was found the neutron data analysis is certainly worthwhile to establish without doubt the validity of the Hong model. The final structural parameters are given as Table-6.5 and bond lengths as Table-6.6. For this structure the position of oxygen O1 is disordered away from the ideal tetragonal position at $x = 0$ for both the Hong model and that of this refinement. It was found that it was necessary to place oxygen O1 away from the ideal position or the thermal parameters for O1 would become very large. As this creates a site of twice the multiplicity of the idealised site, the occupancy is set to 0.5 to preserve the stoichiometry. The refinements continually proceed to the same minimum and so this result is viewed as valid. It may be that there is some degree of disorder on the ab plane for this position. The bond lengths produced by this displacement are still chemically sensible. The effect of the weak bonding of the Cs^+ layer can be seen from the large difference between the outer (shorter) and inner (longer) apical bond lengths in the outer octahedra. Evident from Figure-6.13 is the disorder of the O1 site and the displacement of the Ti/Nb site in the outer octahedra.

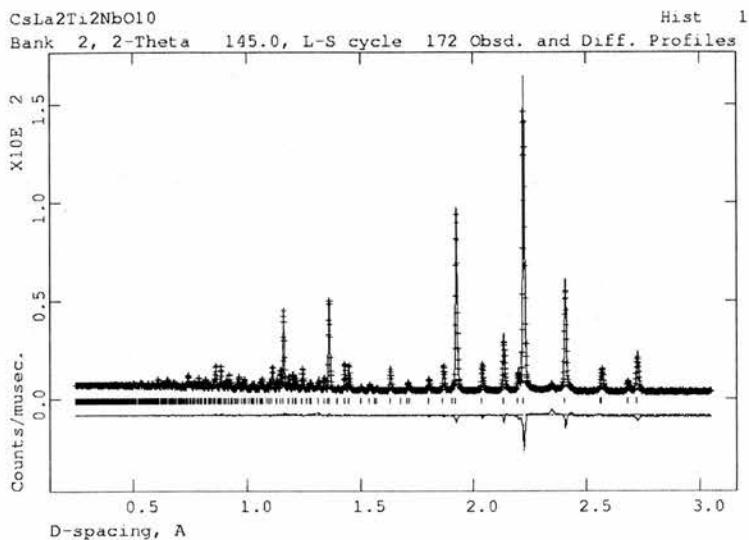


Figure 6.11: Rietveld refinement plot of P4/mmm model of CsLa₂Ti₂NbO₁₀, backscattering data

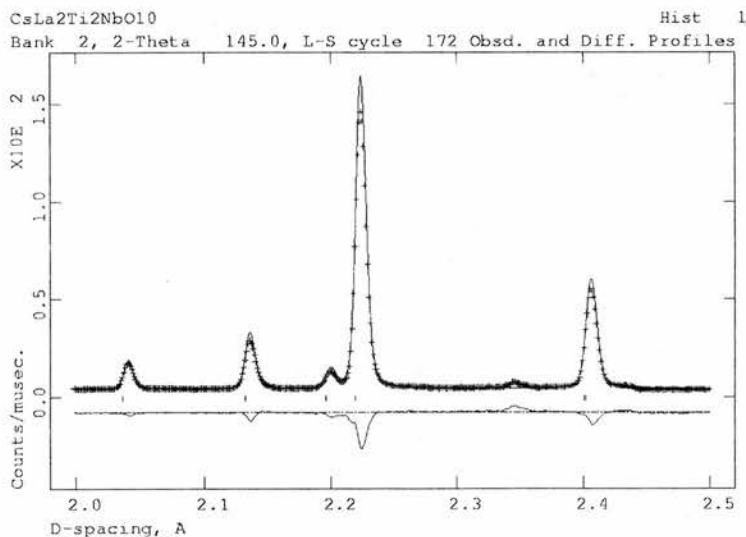


Figure 6.12: Rietveld refinement plot of P4/mmm model of CsLa₂Ti₂NbO₁₀, 2 to 2.5 Å

Table 6.5: CsLa₂Ti₂NbO₁₀ atomic parameters from 25 °C HRPD data, space group P4/mmm, a = 3.8499(1) Å, c = 15.3887(3) Å. $R_{WP} = 0.025$, $\chi^2 = 4.96$, for 9939 data points and 5719 contributing reflections, $0.70 < d < 4.2$ Å

Atom	Multiplicity	x	y	z	Uequiv x 100
Cs	1	0.500000	0.500000	0.500000	1.64
La	2	0.500000	0.500000	0.1406(1)	0.55
Ti/Nb1 ¹	1	0.000000	0.000000	0.000000	0.31
Ti/Nb2 ²	2	0.000000	0.000000	0.2810(2)	0.31
O1	4	0.1171(3) ³	0.500000	0.000000	0.73
O2	2	0.000000	0.000000	0.1238(1)	1.05
O3	4	0.000000	0.500000	0.2501(1)	0.67
O4	2	0.000000	0.000000	0.3955(1)	1.14

¹ fraction set to Nb 0.0 / Ti 1.0

² fraction set to Nb 0.5 / Ti 0.5

³ fraction set to 0.5

Atom	U11	U22	U33	U12	U13	U23
Cs	1.30(5)	1.30(5)	2.3(1)	0.00	0.00	0.00
La	0.48(2)	0.48(2)	0.69(3)	0.00	0.00	0.00
Ti/Nb1	0.33(4)	0.33(4)	0.27(7)	0.00	0.00	0.00
Ti/Nb2	0.33(4)	0.33(4)	0.27(7)	0.00	0.00	0.00
O1	0.93(4)	0.12(4)	1.15(6)	0.00	0.00	0.00
O2	1.37(3)	1.37(3)	0.40(6)	0.00	0.00	0.00
O3	0.80(2)	0.33(3)	0.87(4)	0.00	0.00	0.00
O4	1.47(3)	1.47(3)	0.47(5)	0.00	0.00	0.00

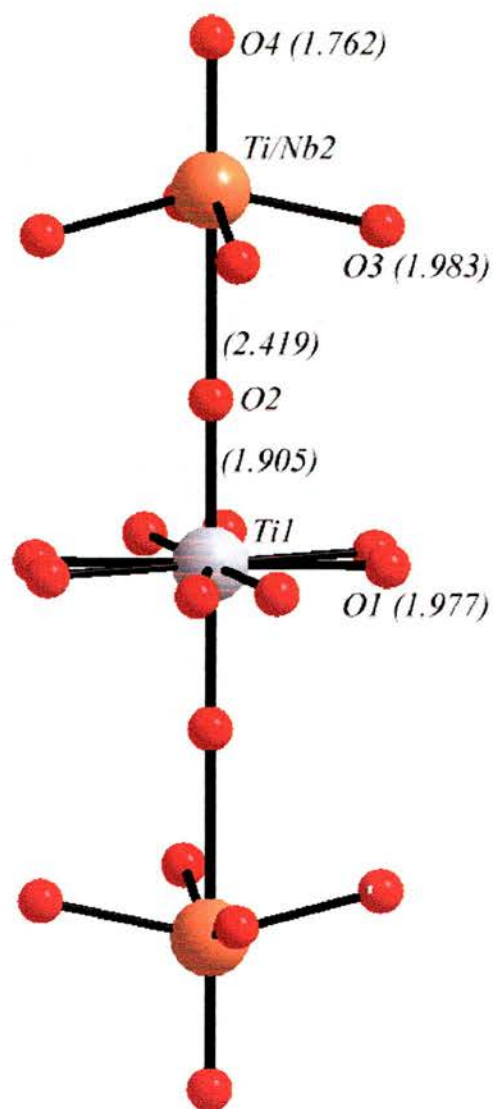


Figure 6.13: Perovskite block of $P4/mmm$ model of $\text{CsLa}_2\text{Ti}_2\text{NbO}_{10}$. Showing the effect of the O1 displacement and the displacement of the Ti/Nb site along c . Ti^{4+} site in grey, $\text{Ti}^{4+}/\text{Nb}^{5+}$ site in orange, oxygens in red.

Table 6.6: CsLa₂Ti₂NbO₁₀ selected bond lengths

bond	length Å
Cs O4	3.162(1)
La O1	2.618(1) x 4 ¹
La O1	3.213(1) x 4 ¹
La O2	2.735(1) x 4
La O3	2.558(1) x 4
Ti1 O1	1.977(2) x 8 ¹
Ti1 O2	1.905(1) x 2
Ti2 O2	2.419(3)
Ti2 O3	1.983(1) x 4
Ti2 O4	1.762(3)

¹ fractional occupancy of O1 is 0.5

CsNd₂Ti₂NbO₁₀

The 3-layer Dion-Jacobson structure with Nd³⁺ as the A-site cation has not previously been reported. Of interest was whether the reduction of the size of the A-site cation could create a lowering of the symmetry, and whether the ordering of the B-site cations, observed for CsLa₂Ti₂NbO₁₀, would be present.

From the X-ray data the sample appears to be tetragonal as for the La³⁺ composition, shown as Figure-6.14. There is however one very small additional peak at $2\theta = 28^\circ$. This is the only additional peak visible and the phase present is not able to be identified using only this peak.

The compound was taken to ISIS and neutron diffraction was performed using the HRPD instrument. The presence of the impurity phase complicated the structural refinement. The P4/mmm model of the CsLa₂Ti₂NbO₁₀ was

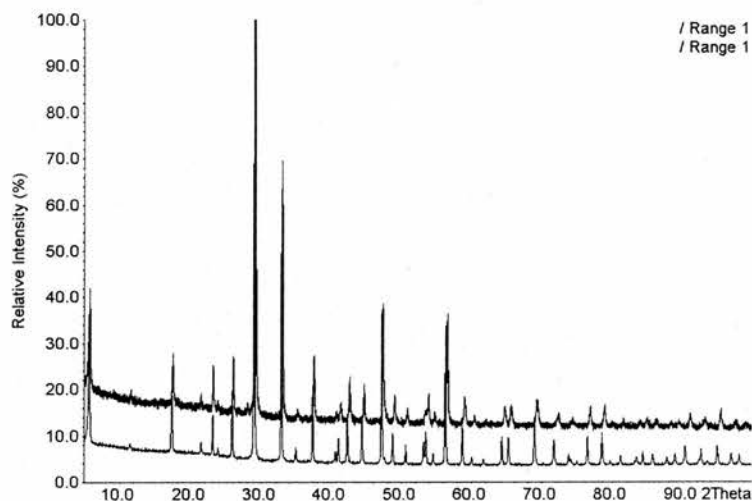


Figure 6.14: X-ray diffraction patterns of $\text{CsLa}_2\text{Ti}_2\text{NbO}_{10}$ (bottom) and $\text{CsNd}_2\text{Ti}_2\text{NbO}_{10}$ (top), from 5 to 100 2θ . No superstructure is observed in either case.

selected and a refinement performed. This results in a good fit to the experimental data, see Figure-6.15. From Figure-6.16 it can be seen that there are several peaks unmatched, all believed to be impurity peaks. Whilst it is believed that these additional peaks observed, on the neutron diffraction pattern, are from an additional phase, it does mean that the possibility of a subtle orthorhombic distortion may have been missed. In the presence of the impurity peaks there is no way to determine unambiguously any superstructure from the data.

$\text{CsBi}_2\text{Ti}_2\text{NbO}_{10}$

Like the Nd^{3+} containing structure, this composition has not previously been reported. For this composition it was felt that it would be much more likely

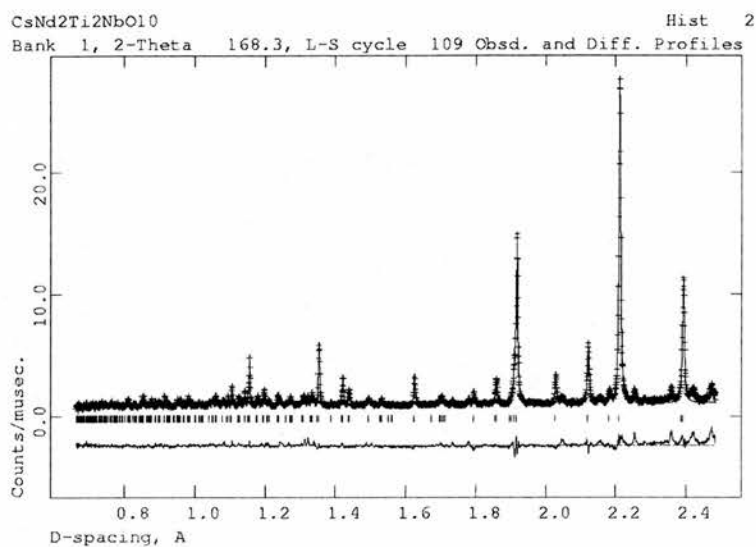


Figure 6.15: Rietveld refinement of CsNd₂Ti₂NbO₁₀, showing P4/mmm reflection marks.

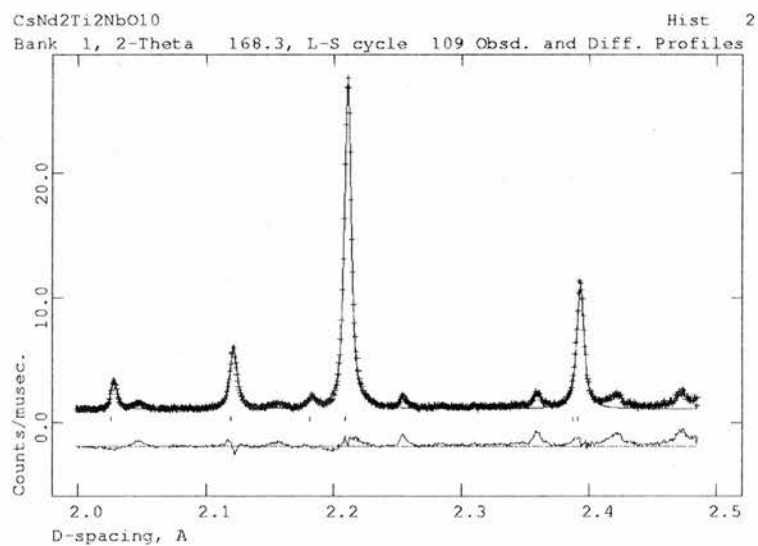


Figure 6.16: Rietveld refinement of CsNd₂Ti₂NbO₁₀, 2 to 2.5 Å, showing P4/mmm reflection marks and additional peaks.

to be orthorhombically distorted. It was considered that the lone-pair effect of the Bi^{3+} cation would help to create these distortions.

The X-ray data appear to support the hypothesis that this compound should be orthorhombic. From Figure-6.17 peak splitting at 32.6 and 37.3° can clearly be observed. The peaks can be indexed as orthorhombic with a small difference between a and b , with $a = \sqrt{2}a_T$.

Indexing the neutron data is not easy, as the additional peaks may prove to be orthorhombic superstructure peaks or impurities. As for the Nd^{3+} variant the identification of the structure was hindered by this problem. In the case of the $\text{CsBi}_2\text{Ti}_2\text{NbO}_{10}$ phase the structure is already appearing to be orthorhombically distorted. To correctly model the structure it must be decided if the c -axis is 'doubled' or not. Figure-6.18 shows the permitted reflections for both the Immm ('doubled' c -axis), $c \sim 31 \text{ \AA}$, and the Pmmm cells, $c \sim 15.5 \text{ \AA}$. For the Pmmm cell there are additional peaks, also, there are intensities at positions where no intensity is permitted, $d = 2.37$ and 2.38 . For the Immm cell, there are few additional peaks. The only potential additional intensities are very weak, $d = 2.32, 2.34$. Both space groups fail to match the intensity at $d = 2.26$, suggesting the presence of some impurity phase. The body-centred model with the 'doubled' c -axis was selected and the space group $\text{Ic}2\text{m}$ was identified from absences. As can be seen from Figure-6.19, the overall quality of the fit for the $\text{Ic}2\text{m}$ model is good. The superstructure peaks corresponding to the larger body-centred cell are also matched well, seen in Figure-6.20.

The Ti/Nb content of the two B-sites were refined for this model and the sites do tend towards the ordering previously observed for $\text{CsLa}_2\text{Ti}_2\text{NbO}_{10}$.

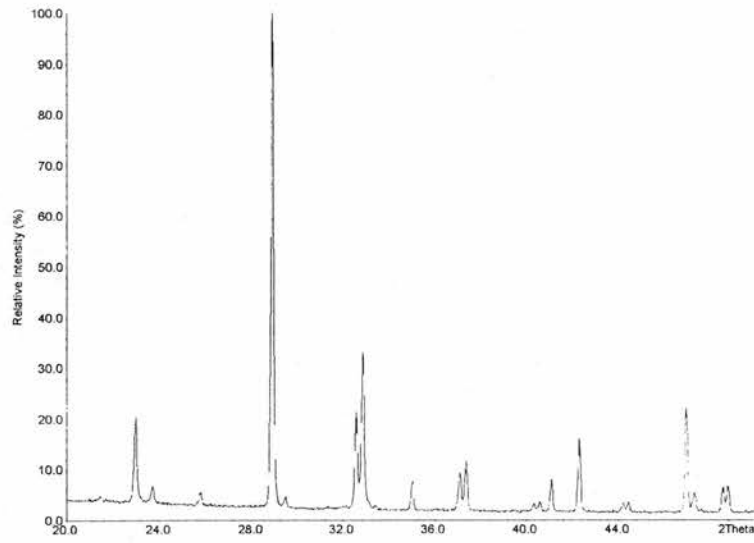


Figure 6.17: X-ray diffraction pattern of $\text{CsBi}_2\text{Ti}_2\text{NbO}_{10}$, from 20 to 50 2θ , showing orthorhombic peak splitting.

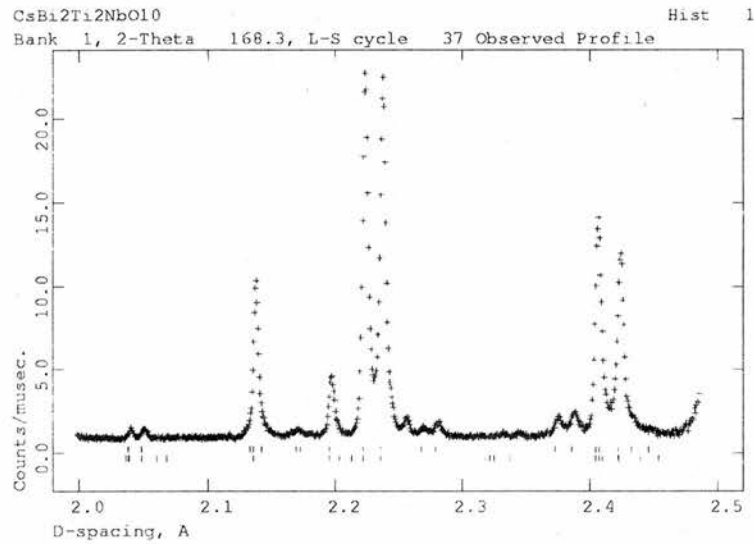


Figure 6.18: Neutron diffraction pattern of $\text{CsBi}_2\text{Ti}_2\text{NbO}_{10}$, from 2 to 2.5 Å. Upper marks, Immm, $c \sim 31$ Å. Lower marks, Pmmm, $c \sim 15.5$ Å.

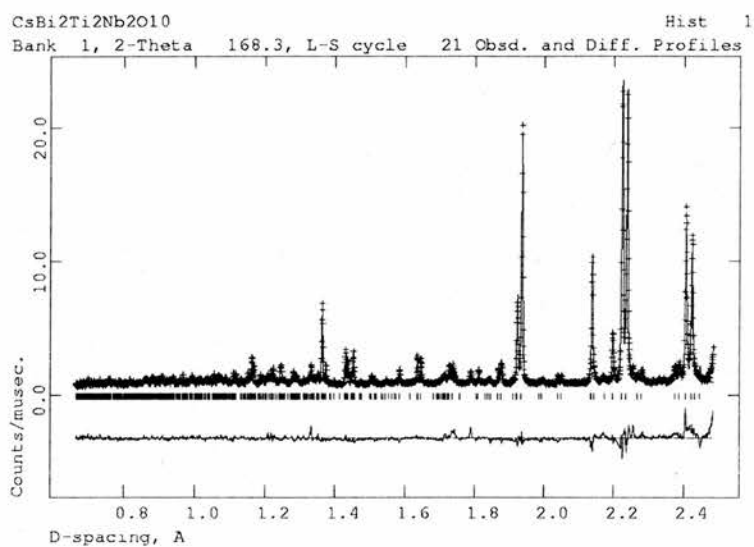


Figure 6.19: Neutron refinement of CsBi₂Ti₂NbO₁₀ in Ic2m.

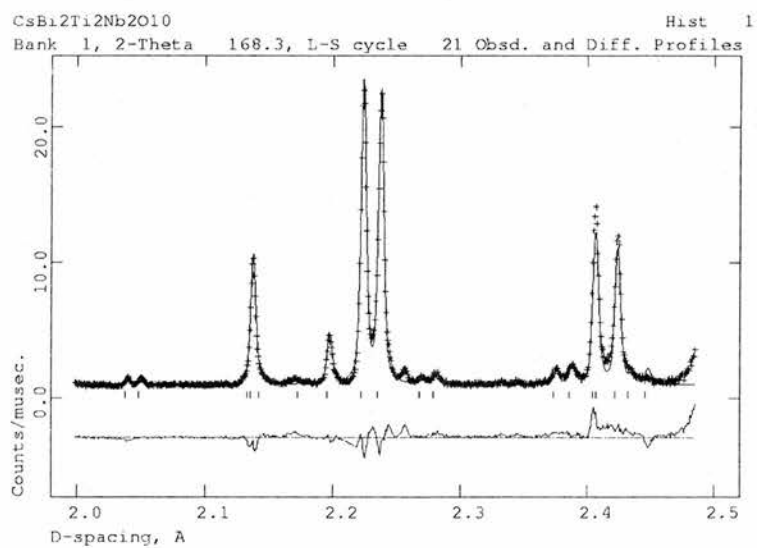


Figure 6.20: Neutron refinement of CsBi₂Ti₂NbO₁₀ in Ic2m, from 2 to 2.5 Å, showing the fit to the orthorhombic superstructure peaks.

However, there is observed a degree of disorder in the sites. Whilst it is thought that this result is correct, it would be unwise to assume the actual values of the occupancies are correct, due to the presence of the impurity. The final model is given in Table-6.7 and the selected bond distances in Table-6.8.

Comparing the distortions of the perovskite octahedra in $\text{CsBi}_2\text{Ti}_2\text{NbO}_{10}$, see Figure-6.21, with those of $\text{CsLa}_2\text{Ti}_2\text{NbO}_{10}$, see Figure-6.13, it is clear that the inner octahedral site remains heavily constrained. The $\text{CsLa}_2\text{Ti}_2\text{NbO}_{10}$ structure has the inner B-site and the oxygens in-plane (perpendicular to c) on a mirror plane, resulting in equal axial and equal equatorial bond lengths. The $\text{Ic}2\text{m}$ model for $\text{CsBi}_2\text{Ti}_2\text{NbO}_{10}$ results in three pairs of bond lengths. This is caused by the two-fold rotation axis along b , the B-site cation lies on this axis, with the result that the oxygen atoms are equivalent pairs. The outer site in the $\text{P}4/\text{mmm}$ model is able only to displace along the c -axis. For the $\text{Ic}2\text{m}$ model the distortion can occur along all three axes. The displacement of the mixed Ti/Nb site along the c -axis is greater in the $\text{CsLa}_2\text{Ti}_2\text{NbO}_{10}$ structure than for $\text{CsBi}_2\text{Ti}_2\text{NbO}_{10}$, as might be expected. Notable is that the shortest bond length for the outer octahedral site in $\text{CsBi}_2\text{Ti}_2\text{NbO}_{10}$ is not the apical bond to the oxygen nearest the Cs^+ layer, instead it is one of the equatorial bonds. The B-site cation has not moved very much along either the a or the b -axis, it is the displacement of the oxygens which has created the high degree of distortion in the outer octahedra of the perovskite block.

The Bi^{3+} containing structure is non-centrosymmetric and polar, and as such may be a ferroelectric. However, no a.c. impedance data were collected on

Table 6.7: CsBi₂Ti₂NbO₁₀ atomic parameters from 25 °C HRPD data, space group Ic2m, a = 5.5001(1) Å, b = 5.4499(1) Å, c = 30.7591(4) Å. R_{WP} = 0.092, χ^2 = 12.49, for 8356 data points and 4609 contributing reflections, 0.70 < d < 3.25 Å

Atom	Multiplicity	x	y	z	Uiso x 100
Cs	4	0.996(1)	0.033(3)	0.250000	2.6(2)
Bi	8	0.9643(5)	0.034(2)	0.0721(1)	2.97(9)
Ti/Nb1 ¹	4	0.500000	0.058(6)	0.000000	1.2(7)
Ti/Nb2 ²	8	0.492(4)	0.019(8)	0.1379(5)	1.2(7)
O1	8	0.202(1)	0.267(2)	0.0059(2)	4.7(2)
O2	8	0.488(1)	0.085(2)	0.0618(2)	9.2(3)
O3	8	0.224(1)	0.299(1)	0.1239(2)	1.7(1)
O4	8	0.717(1)	0.753(2)	0.1324(2)	3.2(2)
O5	8	0.495(1)	0.046(2)	0.1982(1)	3.3(1)

¹ Occupancy refined to Ti 0.842(9) / Nb 0.158(9)

² Occupancy refined to Ti 0.579(4) / Nb 0.421(4)

Table 6.8: CsBi₂Ti₂NbO₁₀ selected bond lengths

bond	length Å	bond	length Å
Cs O5	3.180(8) x 2	Bi O1	2.736(8)
Cs O5	3.178(8) x 2	Bi O1	2.865(8)
Cs O5	3.10(1) x 2	Bi O1	3.104(7)
Cs O5	3.22(1) x 2	Bi O1	3.154(8)
Ti/Nb1 O1	2.01(2) x 2	Bi O2	2.652(8)
Ti/Nb1 O1	1.94(2) x 2	Bi O2	2.913(8)
Ti/Nb1 O2	1.909(5) x 2	Bi O2	2.482(8)
Ti/Nb2 O2	2.37(2)	Bi O2	3.030(8)
Ti/Nb2 O3	2.16(4)	Bi O3	2.582(7)
Ti/Nb2 O3	1.75(4)	Bi O3	2.665(8)
Ti/Nb2 O4	1.91(4)	Bi O4	2.763(7)
Ti/Nb2 O4	2.05(4)	Bi O4	2.420(7)
Ti/Nb2 O5	1.86(2)		

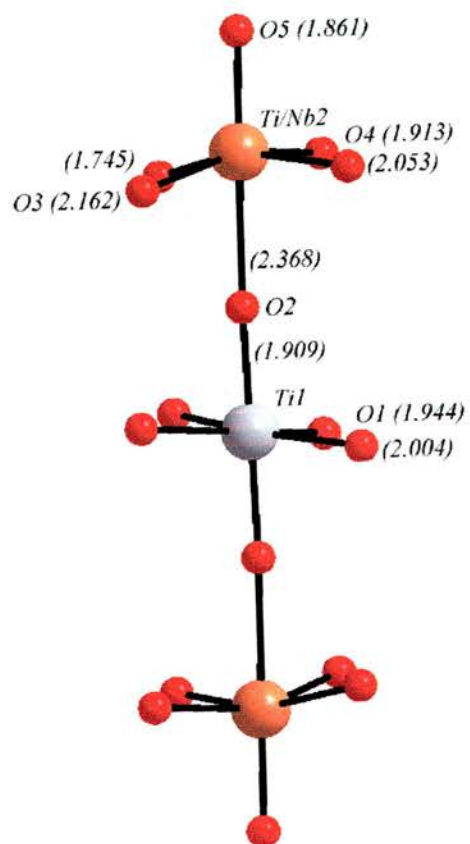


Figure 6.21: Perovskite block of $Ic2m$ model of $CsBi_2Ti_2NbO_{10}$. Ti^{4+} site in grey, Ti^{4+}/Nb^{5+} site in orange, oxygens in red.

Table 6.9: R_{WP} and χ^2 values for primitive orthorhombic refinements of $\text{CsBi}_3\text{Ti}_4\text{O}_{13}$

Space Group	R_{WP}	χ^2	No. Parameters
$P2_1am$	0.0275	19.63	57
$Pbam$	0.0406	42.34	34
$Pmam$	0.0375	36.34	42

this as it would not have been reliable in the presence of an unknown impurity phase.

6.1.3 $\text{CsBi}_3\text{Ti}_4\text{O}_{13}$

The 4-layer phase was previously described as tetragonal[2] with $a = 7.685 \text{ \AA}$, $c = 38.99 \text{ \AA}$. X-ray diffraction patterns indexed with the $a = 2a_T$ supercell are usually found to be weakly distorted orthorhombic systems with $a = \sqrt{2}a_T$. For this reason the compound was analysed using powder neutron diffraction on POLARIS at ISIS.

Examining the experimental X-ray diffraction pattern, one peak is unable to be indexed as part of the main phase, shown in Figure-6.22. This impurity peak can be assigned to $\text{Bi}_4\text{Ti}_3\text{O}_{12}$. This is a logical impurity phase as the 3-layer Aurivillius phase, $\text{Bi}_4\text{Ti}_3\text{O}_{12}$, is highly stable. However, there is only one observable impurity peak in the X-ray diffraction data. Therefore the impurity cannot be uniquely assigned, though it is most likely to be the Aurivillius phase.

The neutron data quite clearly show the peak splitting in several of the more intense peaks, so the main phase is identified as orthorhombic, $a \sim b \sim$

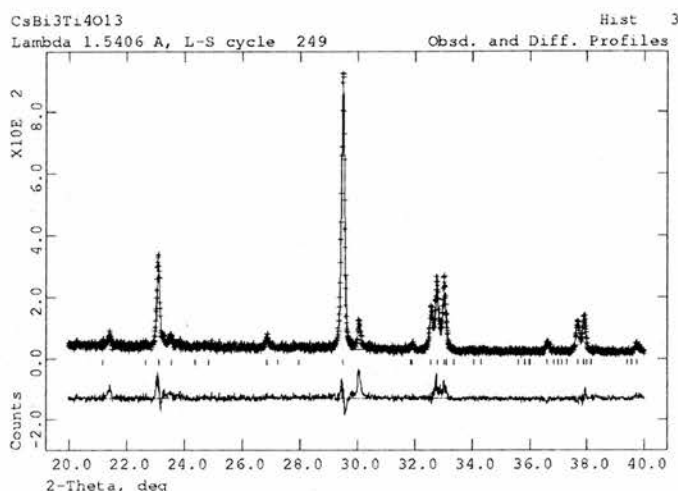


Figure 6.22: X-ray diffraction pattern of CsBi₃Ti₄O₁₃, from 20 to 40 2θ , showing the Bi₄Ti₃O₁₂ impurity peak

$\sqrt{2}a_T$. The presence of the Bi₄Ti₃O₁₂ impurity is also able to be seen in several peaks which cannot be indexed by the main phase. The presence of this impurity phase makes the identification of the correct space group for the main phase difficult. However after careful examination of the data it was decided that the main phase was present in P2₁am, Pbam or Pmam. To confirm which of the three space groups the structure was best described as, refinements were carried out for all three groups. From the fits of the three refinements it is clear that the P2₁am refinement is the most suitable. The χ^2 and R_{WP} values for the refinements are given as Table-6.9.

The P2₁am space group offers the possibility of greater structural distortions over both the Pbam and Pmam space groups. In the Pmam space group the

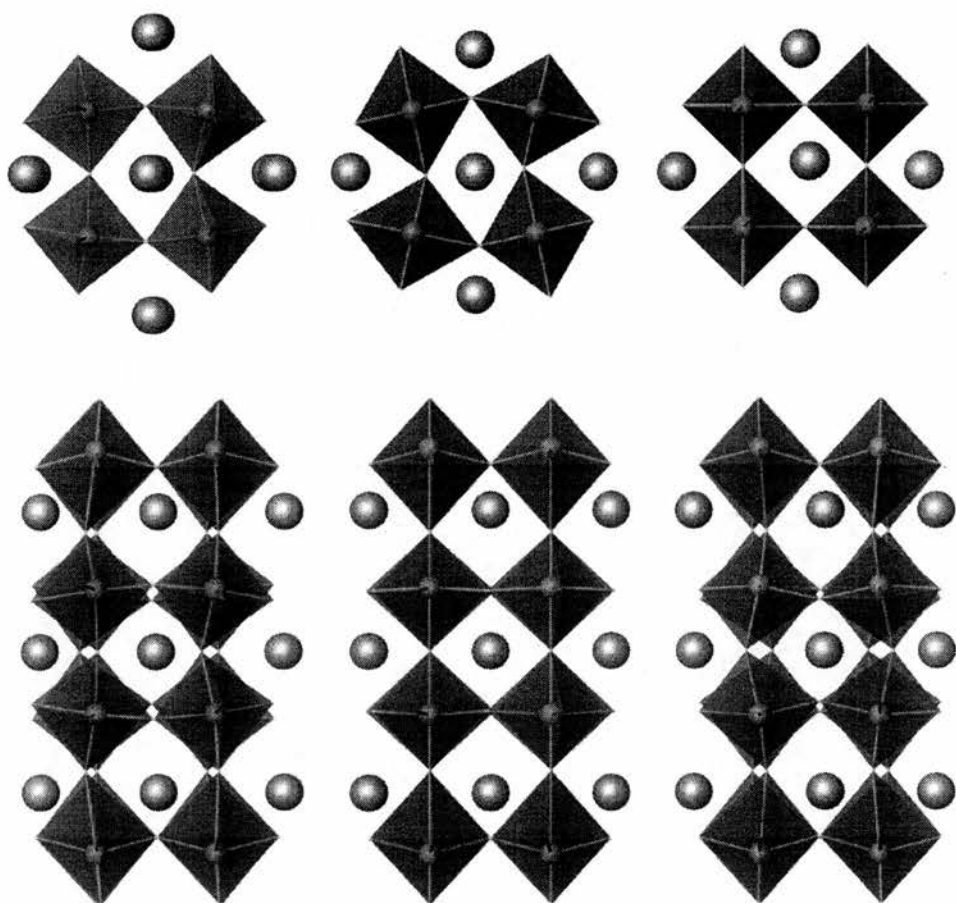


Figure 6.23: $\text{CsBi}_3\text{Ti}_4\text{O}_{13}$, showing (right to left) $P2_1am$, $Pbam$ and $Pmam$ models. Top, $[001]$ view. Bottom, $[110]$ view.

Table 6.10: CsBi₃Ti₄O₁₃ atomic parameters from 25 °C POLARIS data, space group P2₁am, a = 5.4181(2) Å, b = 5.4577(2) Å, c = 19.6117(9) Å. R_{WP} = 0.028, χ^2 = 19.63, for 3664 data points and 5727 contributing reflections, 0.70 < d < 3.1 Å

Atom	Multiplicity	x	y	z	Uiso x 100
Cs	2	0.212(2)	0.236(2)	0.500000	0.3(2)
Bi1	4	0.219(2)	0.267(2)	0.2315(2)	3.2(1)
Bi2	2	0.233(1)	0.273(1)	0.000000	0.8(1)
Ti1	4	0.261(1)	0.758(2)	0.1026(3)	-1.07(6)
Ti2	4	0.256(2)	0.756(2)	0.3311(3)	-0.40(9)
O1	2	0.312(2)	0.824(2)	0.000000	0.4(1)
O2	4	0.289(1)	0.702(1)	0.1970(4)	1.2(1)
O3	4	0.223(1)	0.763(2)	0.4170(2)	0.6(1)
O4	4	0.067(1)	0.038(1)	0.1109(5)	0.8(1)
O5	4	-0.008(1)	0.5460(9)	0.0851(3)	-0.14(8)
O6	4	-0.009(2)	-0.013(2)	0.3048(4)	0.7(1)
O7	4	-0.007(2)	0.499(1)	0.3048(4)	0.4(1)

Table 6.11: CsBi₃Ti₄O₁₃ selected bond lengths

bond	length Å	bond	length Å	bond	length Å
Ti1 O1	2.062(5)	Bi1 O2	3.18(1)	Bi2 O1	2.49(1)
Ti1 O2	1.882(9)	Bi1 O2	2.50(1)	Bi2 O1	3.04(1)
Ti1 O4	1.86(1)	Bi1 O2	2.43(1)	Bi2 O1	2.34(1)
Ti1 O4	2.01(1)	Bi1 O2	3.17(1)	Bi2 O1	3.18(1)
Ti1 O5	1.888(9)	Bi1 O4	2.80(1)	Bi2 O4	2.68(1)
Ti1 O5	2.109(8)	Bi1 O4	3.46(1)	Bi2 O4	3.302(8)
Ti2 O2	2.65(1)	Bi1 O5	3.473(8)	Bi2 O5	2.588(7)
Ti2 O3	1.695(7)	Bi1 O5	3.388(9)	Bi2 O5	2.396(8)
Ti2 O6	1.98(1)	Bi1 O6	2.43(1)	Cs O3	3.05(1) x 2
Ti2 O6	1.96(1)	Bi1 O6	2.48(1)	Cs O3	3.31(1) x 2
Ti2 O7	2.06(1)	Bi1 O7	2.27(1)	Cs O3	3.11(1) x 2
Ti2 O7	1.97(1)	Bi1 O7	2.43(1)	Cs O3	3.21(1) x 2

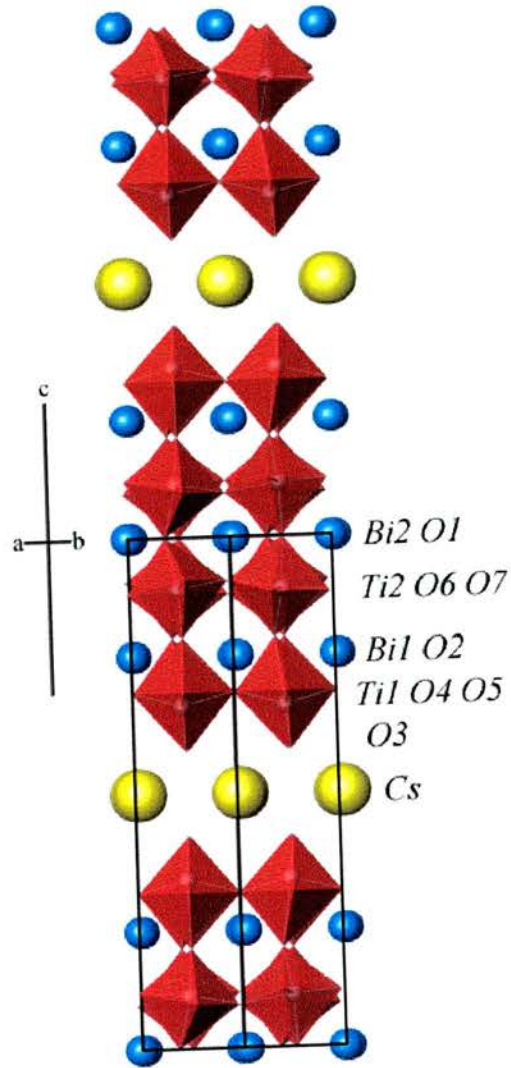


Figure 6.24: $\text{CsBi}_3\text{Ti}_4\text{O}_{13}$ structure, view along $[110]$. Cs atoms in yellow, Bi atoms in blue, TiO_6 octahedra in red.

atomic positions are fixed along a , but not along b . The exception to this are the oxygens in the TiO plane, which are also fixed along b . This results in the view down [001] of the inner octahedra in the structure, as shown in Figure-6.23, appearing regular like the tetragonal parent. The [110] view shows the movement of the oxygens in the perovskite block in the BiO plane. The apparent movement of the oxygens in the TiO plane is not due to any displacement along b . There are two oxygen atom positions in-plane of the Ti cations and they have very slightly different z parameters, giving rise to the apparent distortion. The Pbam model clearly permits movement along both a and b -axes in the TiO plane, shown in Figure-6.23. Looking at the [110] view, the inability of the BiO plane atoms to move along either a , or b is apparent. The P2₁am model movement is permitted both along a and b for all the perovskite atoms. hence, the structure is not regular when viewed along [110] or [001]. Clearly it is this reduction in the symmetry that is required by the structure. The final structural model is given in Table-6.10 and Figure 6.24, with selected bond lengths in Table-6.11.

The distorting effect of the Cs⁺ layer can be examined through the comparison of the octahedron from the CsBiNb₂O₇ 2-layer phase with the octahedra of CsBi₃Ti₄O₁₃. Though the Ti⁴⁺ and the Nb⁵⁺ will have different bonding requirements there will still be some effect from the Cs⁺ layer on the apical oxygen bond length.

As would be expected the outer Ti site in CsBi₃Ti₄O₁₃ has the largest displacement along c , see Figure-6.25, with the Nb site of CsBiNb₂O₇ the next most displaced and the inner Ti site in CsBi₃Ti₄O₁₃ the least affected. The two sites that are next to the Cs⁺ layer are not only larger in their dis-

torted apical bonding, they are very much more distorted. This indicates the strength of the effect of the Cs^+ layer. For the $\text{CsBiNb}_2\text{O}_7$ phase the bond valence calculation gives the oxidation state of the Nb as 5.07, the inner and outer Ti octahedral sites in $\text{CsBi}_3\text{Ti}_4\text{O}_{13}$ are 3.98 and 4.09 respectively, showing that the Cs layer has the effect of creating overbonding in the B-site adjacent.

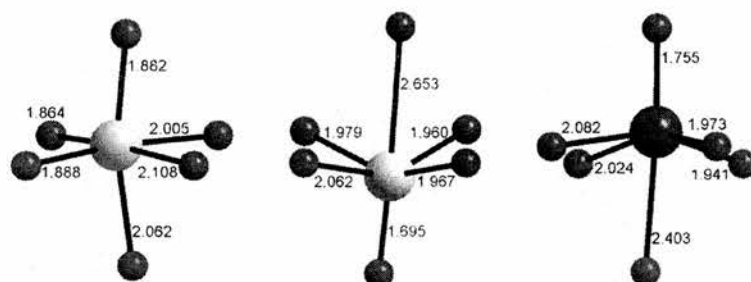


Figure 6.25: Bonding environments for inner Ti site of $\text{CsBi}_3\text{Ti}_4\text{O}_{13}$ (left), outer Ti site of $\text{CsBi}_3\text{Ti}_4\text{O}_{13}$ (middle) and Nb site of $\text{CsBiNb}_2\text{O}_7$ (right).

6.2 Ruddlesden-Popper Phases

The Ruddlesden-Popper phases are characterised as having a double layer of mono or divalent cations separating a perovskite block. These phases can be divided into two different types, those in which the A-site and interlayer atoms are divalent[6, 7] and those in which the interlayer is monovalent and the A-site is trivalent[8]. In this work the focus was on 3-layer mono/trivalent systems, specifically the possibility of doping transition metals into these systems. The $\text{Na}_2\text{La}_2\text{Ti}_3\text{O}_{12}$ phase was characterised by Greaves[9] using

neutron diffraction and was identified as being tetragonal in the I4/mmm space group. The parent phase is centrosymmetric and therefore cannot be a ferroelectric material.

The first dopant that was considered was Ru⁴⁺. As a tetravalent ion it does not require any compensatory oxygen vacancies for charge balancing, when it is substituted in for Ti⁴⁺. Prior work[10] in this area had suggested that doping of up to x=1 is possible for the Na₂La₂Ti_{3-x}Ru_xO₁₂ series, also that the structure remains tetragonal and that there is disorder of the B-site occupancies. It had previously been thought that there may be some opportunity for the B-site to order in a similar way as for the 3-layer Dion-Jacobson phases. This work was a powder X-ray diffraction study, therefore it would be desirable to obtain neutron diffraction data, to identify the degree of disorder, and verify that the material is indeed tetragonal. Neutron diffraction is better for determining accurately the unit cell, due to the increased prominence of superstructure reflections for the oxygen atoms. It is also better for determination of the disorder in the B-site as Ti⁴⁺ has a negative scattering length (-3.438×10^{-15} m) and Ru⁴⁺ has a positive scattering length (7.03×10^{-15} m).

There has been very little work performed on the effect of the lanthanides on the crystal structure of the 3-layer phases. The work to date has tended to be focused on the possibility of ion exchange and of ionic conduction, most of the structural studies being limited to powder X-ray diffraction. The most complete assessment of the structures is of Na₂Ln₂Ti₃O₁₂ (Ln = La, Nd, Sm and Gd)[11], where the structures are all identified as I4/mmm. Looking closely at the details given the trend expected would be for both *a* and *c*

to decrease with decreasing lanthanide size. The a parameter does indeed decrease along the series, however c decreases from La to Nd, increases from Nd to Sm and decreases again from Sm to Gd. This is unusual, and may suggest that the structures are not actually tetragonal, but, that it was simply not possible to discern the orthorhombic distortion using X-ray diffraction. It also may be the case that impurities are present in the sample. The authors detail the attempted synthesis using molten NaNO_3 which resulted in large amounts of impurities, again demonstrating the difficulty in producing phase pure materials.

Previous work on 1st row transition metal doping into the mono/tri-valent Ruddlesden-Popper phases is limited to one report. This details the formation of the three layer $\text{Na}_2\text{Ln}_2\text{Ti}_{3-x}\text{Mn}_x\text{O}_{10}$ series ($\text{Ln} = \text{Sm}, \text{Eu}, \text{Gd}$ and Dy)[12]. In this work the formation of $x = 1$ materials are reported. It was found to be difficult to produce single phase materials, as shown by the need to regrind the samples 6 to 12 times. The materials are all indexed as orthorhombic with a approximately 7.6 \AA , which represents a doubling of the idealised tetragonal a parameter. This doubling of the a length is unusual and is possibly due to the structures being distorted to orthorhombic, though there does exist the possibility of some remaining impurity phase.

6.2.1 $\text{Na}_2\text{La}_2\text{Ti}_{3-x}\text{Ru}_x\text{O}_{10}$

Samples were prepared at $x = 0.5$ and 1 . The $x = 0.5$ phase was analysed using powder X-ray diffraction, the $x = 1$ phase was examined using both powder X-ray and neutron diffraction. Neutron diffraction data having been

collected on POLARIS at ISIS.

Na₂La₂Ti₂RuO₁₀ - Neutron Diffraction

The phase was previously described in the I4/mmm setting, so this model was used as the initial basis for the Rietveld refinement using the neutron data. It was apparent that the neutron data collected were fitted very well by the tetragonal space group. Examining closely the plots of the refinement, Figures-6.26 to 6.29, it is clear that the sample is not completely pure. It is however difficult to identify from the data what the other phase may be due to the weakness of the additional peaks. They are however not superstructure peaks, based on the $a \sim \sqrt{2}a_T$ distortion, so the structure may still have interesting magnetic properties but it will not be a ferroelectric material. Examining the structure for any evidence of ordering reveals that the prediction of the X-ray study was correct. There is present in the structure a degree of disorder over the two octahedral sites, with a slight preference of Ru⁴⁺ for the inner site.

In the final refinement (Table-6.12 and Figure-6.30 with bond lengths in Table-6.2.1) it can be seen that the O1 position has been moved from the special position at $x = 0$. The doubling of the multiplicity of this ion has been compensated for by halving the occupancy of the site. This deviation from the normal I4/mmm model was present in the previous powder X-ray structural refinement. Originally it had been thought that the improvement gained by moving the oxygen away from the special position may be evidence of some structural distortion, possibly an orthorhombic distortion. It appears that, if it is a distortion, however, it is only a local, or short-range, distortion

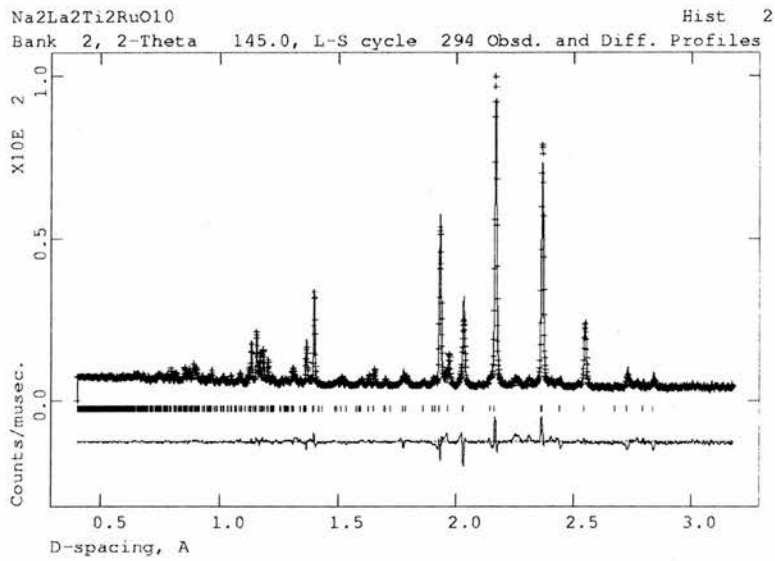


Figure 6.26: Na₂La₂Ti₂RuO₁₀, Rietveld refinement showing I4/mmm reflections, backscattering bank

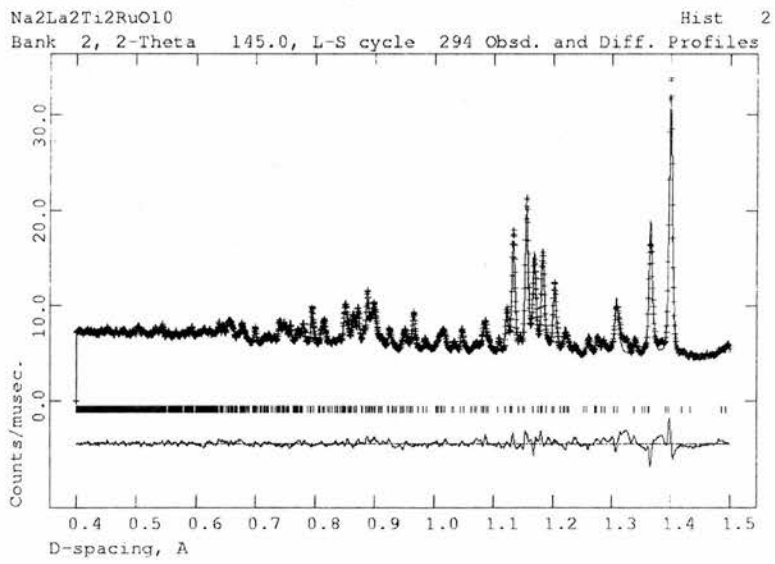


Figure 6.27: Na₂La₂Ti₂RuO₁₀, Rietveld refinement showing I4/mmm reflections, 0.4 to 1.5 Å, backscattering bank

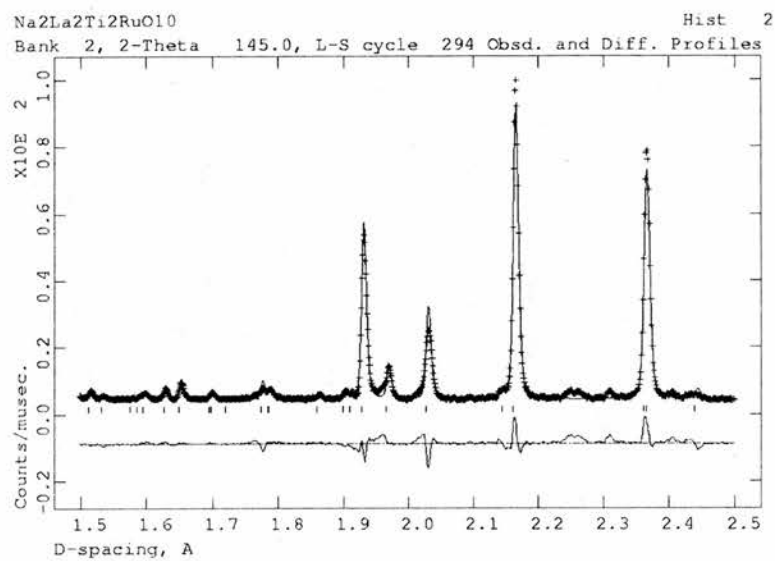


Figure 6.28: Na₂La₂Ti₂RuO₁₀, Rietveld refinement showing I4/mmm reflections, 1.5 to 2.5 Å, backscattering bank

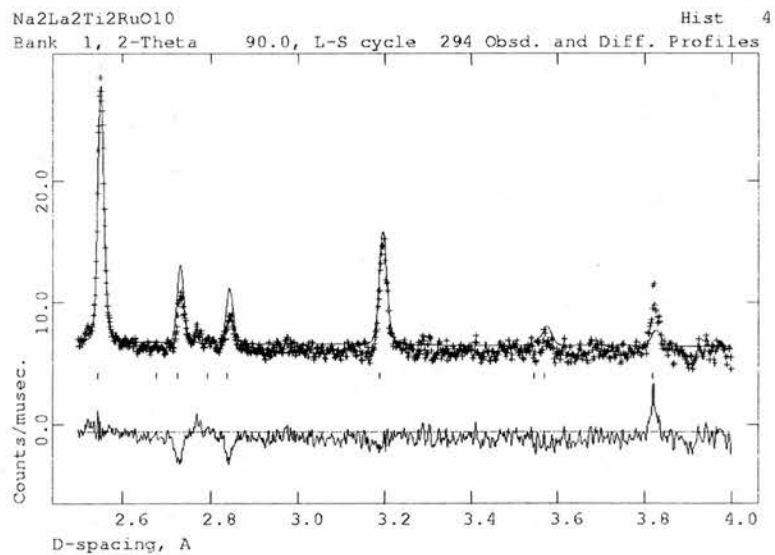


Figure 6.29: Na₂La₂Ti₂RuO₁₀, Rietveld refinement showing I4/mmm reflections, 2.5 to 4 Å, 90 ° data

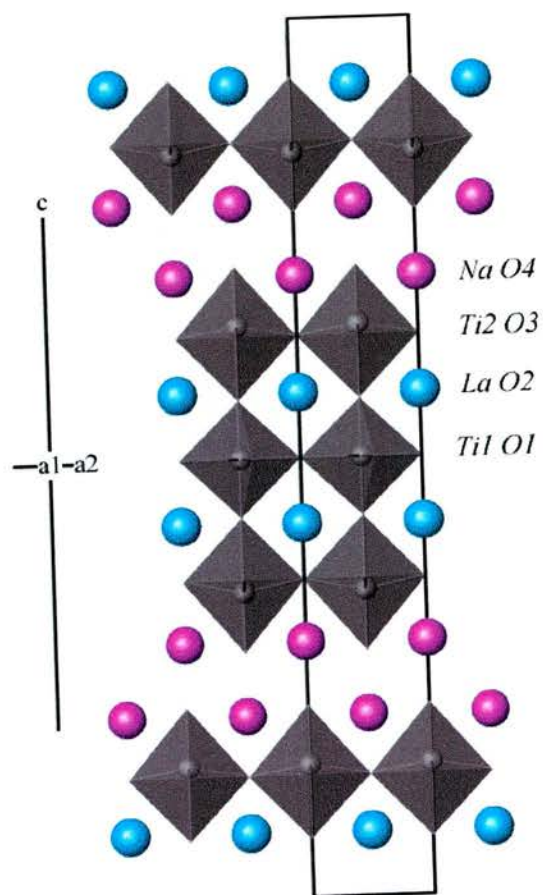


Figure 6.30: $\text{Na}_2\text{La}_2\text{Ti}_2\text{RuO}_{10}$, Na in purple, La in blue, TiO_6 octahedra in grey

Table 6.12: Na₂La₂Ti₂RuO₁₀ atomic parameters from 25 °C POLARIS data, space group I4/mmm, a = 3.85866(6) Å, c = 28.4032(6) Å. R_{WP} = 0.039, χ² = 5.85, for 8660 data points and 1280 contributing reflections, 0.40 < d < 4.1 Å

Atom	Multiplicity	x	y	z	Uiso/Uequiv x 100
Na	4	0.000000	0.000000	0.2923(2)	1.77
La	4	0.000000	0.000000	0.42439(5)	0.54
Ti/Ru1 ¹	2	0.000000	0.000000	0.000000	1.26(7)
Ti/Ru2 ²	4	0.000000	0.000000	0.1509(1)	1.26(7)
O1	8	0.1101(6) ³	0.500000	0.000000	0.63(4)
O2	4	0.000000	0.000000	0.06710(8)	1.16
O3	8	0.000000	0.500000	0.13486(5)	1.15
O4	4	0.000000	0.000000	0.20983(9)	1.52

1 Ti/Ru1 site occupancy is 0.378(5) Ti / 0.622(5) Ru

2 Ti/Ru2 site occupancy is 0.811(2) Ti / 0.189(2) Ru

3 O1 has occupancy 0.5

Atom	U11	U22	U33	U12	U13	U23
Na	1.8(1)	1.8(1)	1.7(2)	0.00	0.00	0.00
La	0.56(4)	0.56(4)	0.49(5)	0.00	0.00	0.00
O2	1.67(6)	1.67(6)	0.14(8)	0.00	0.00	0.00
O3	1.48(7)	0.13(6)	1.8(1)	0.00	0.00	0.00
O4	2.06(7)	2.06(7)	0.44(9)	0.00	0.00	0.00

Table 6.13: Na₂La₂Ti₂RuO₁₀ selected bond lengths

bond	length Å
Na O3	2.829(3) x 4
Na O4	2.729(1) x 4
La O1	2.616(2) x 4
La O1	3.183(2) x 4
La O2	2.739(1) x 4
La O3	2.565(2) x4
Ti1 O1	1.976(1) x 8 ¹
Ti1 O2	1.901(3) x 4
Ti2 O2	2.413(5)
Ti2 O3	1.989(1) x 4
Ti2 O4	1.648(5)

1 O1 has occupancy 0.5

and not long range throughout the structure.

As expected the outer octahedra show an off-centre displacement of Ti⁴⁺ along the *c*-axis. The cation has moved towards the [Na₂] layer to increase the bonding to the apical oxygen ion, as the bonding from the [Na₂] layer is weak. The I4/mmm space group permits only displacement along the *c*-axis, no displacement along *a* or *b*, or any tilting of the octahedra are possible.

6.2.2 Na₂Nd₂Ti_{3-x}Ru_xO₁₀

Synthesis of samples where *x* = 0.5 and 1 were attempted. For the *x* = 0.5 sample, analysis was performed using only powder X-ray diffraction. For the *x* = 1 sample, analysis was performed using both X-ray and neutron powder diffraction data.

Table 6.14: $\text{Na}_2\text{Nd}_2\text{Ti}_{2.5}\text{Ru}_{0.5}\text{O}_{10}$ atomic parameters from 25 °C X-ray data, space group $I4/mmm$, $a = 3.82293(5)$ Å, $c = 28.2829(7)$ Å. $R_{WP} = 0.050$, $\chi^2 = 7.84$, for 4999 data points and 103 contributing reflections, $1 < d < 17.6$ Å

Atom	Multiplicity	x	y	z	Uiso x 100
Na/Nd1 ¹	4	0.000000	0.000000	0.2850(7)	2.50
Na/Nd2 ²	4	0.000000	0.000000	0.4248(1)	2.50
Ti/Ru1 ³	2	0.000000	0.000000	0.000000	2.50
Ti/Ru2 ⁴	4	0.000000	0.000000	0.1492(3)	2.50
O1	4	0.000000	0.500000	0.000000	2.50
O2	4	0.000000	0.000000	0.0617(9)	2.50
O3	8	0.000000	0.500000	0.1319(6)	2.50
O4	4	0.000000	0.000000	0.214(1)	2.50

1 Na/Nd1 site occupancy is 0.960(3) Na / 0.040(3) Nd

2 Na/Nd1 site occupancy is 0.040(3) Na / 0.960(3) Nd

3 Ti/Ru1 site occupancy is 0.780(2) Ti / 0.220(2) Ru

4 Ti/Ru2 site occupancy is 0.860(2) Ti / 0.140(2) Ru

Table 6.15: $\text{Na}_2\text{Nd}_2\text{Ti}_{2.5}\text{Ru}_{0.5}\text{O}_{10}$ selected bond lengths

bond	length Å
Na1 O3	3.03(1) x 4
Na1 O4	2.70(1) x 4
Nd2 O1	2.86(1) x 4
Nd2 O2	2.73(1) x 4
Nd2 O3	2.49(1) x 4
Ti1 O1	1.91(1) x 4
Ti1 O2	1.75(3) x 2
Ti2 O2	2.47(3)
Ti2 O3	1.97(1) x 4
Ti2 O4	1.83(3)

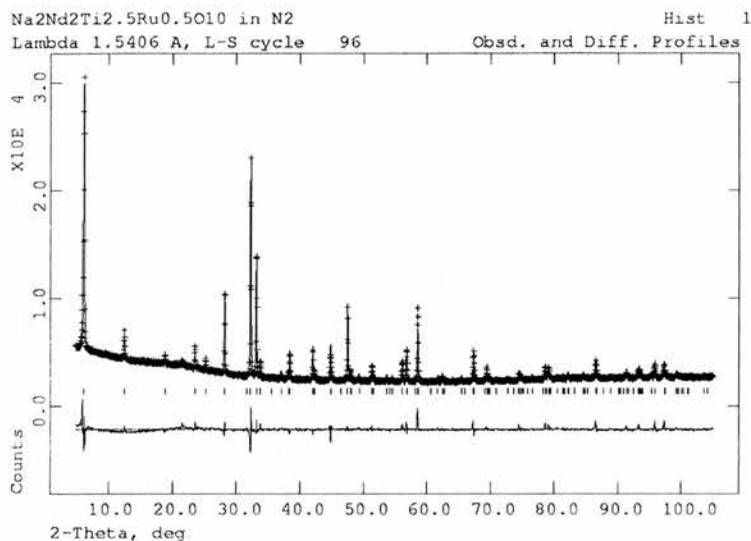


Figure 6.31: Na₂Nd₂Ti_{2.5}Ru_{0.5}O₁₀, X-ray data. Refined as I4/mmm

Na₂Nd₂Ti_{2.5}Ru_{0.5}O₁₀

From the refinement of the X-ray diffraction data, Figure-6.31 it appears that the sample is phase pure. The refinement was performed with the lattice parameters, background parameters, peak profile parameters (GX, GY, GZ, LX) and the atomic thermal parameters and fractional occupancies (except for the oxygen positions) permitted to refine. The sample has been indexed as tetragonal, I4/mmm, the same indexing as for the Na₂La₂Ti₂RuO₁₀ phase. Like the Na₂La₂Ti₂RuO₁₀ refinement there is disorder of the Ti/Ru sites, with Ru⁴⁺ preferring the inner octahedral site, though it is a less drastic difference between the inner and outer octahedral sites in Na₂Nd₂Ti_{2.5}Ru_{0.5}O₁₀. This could be due to the presence of Nd³⁺ as opposed to La³⁺, due to the lower Ru content, or, a combination of both factors. Also found for this sample is a very small amount of disorder in the Na/Nd sites, the amount of

disorder is included in Table-6.14. The level of disorder for these sites shows that the two sites are highly ordered as would be expected. Evident from Table-6.15 is the displacement of the Ti2 site where the Ti is displaced along *c*. Here there is a shorter bond to O4 and a longer bond to O2. This is due to displacement of the Ti cation, to prevent 'underbonding' on the O4 site from occurring due to weak bonding from the Na layer.

$\text{Na}_2\text{Nd}_2\text{Ti}_2\text{RuO}_{10}$

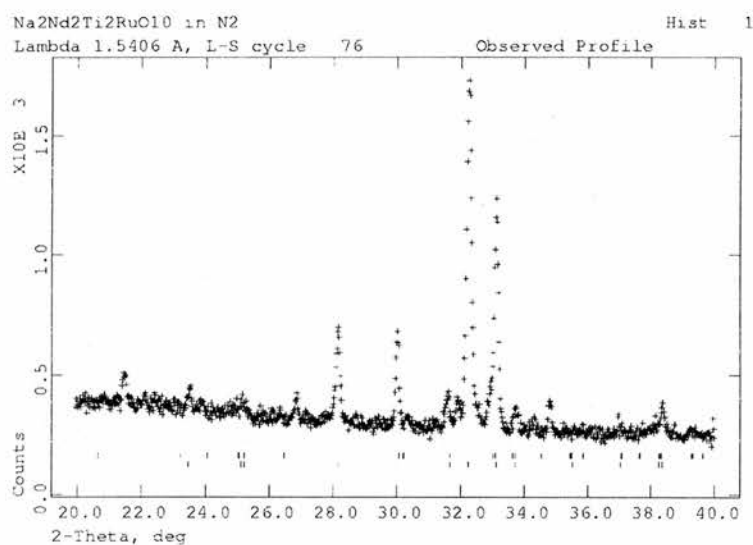


Figure 6.32: $\text{Na}_2\text{Nd}_2\text{Ti}_2\text{RuO}_{10}$, X-ray data from 20 to 40 2θ . Upper tick marks are Pmmm, lower marks are I4/mmm

For the $x = 1$ sample the powder X-ray diffraction data (Figure-6.32) shows an impurity phase. An impurity in these phases is often due to the loss of volatile Na^+ , it follows that any impurity phases would be expected to contain a lower ratio or no Na^+ at all. A thorough search of the PDF database was

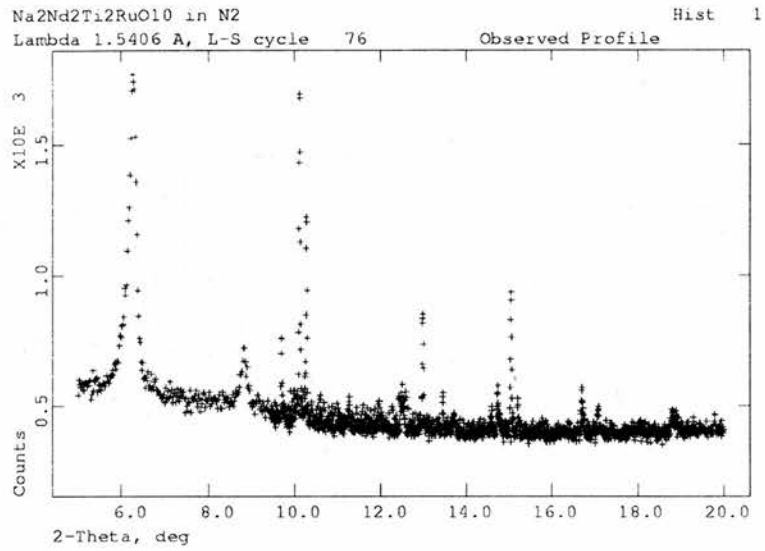


Figure 6.33: Na₂Nd₂Ti₂RuO₁₀, X-ray data from 5 to 20 2θ , showing the additional peak at $2\theta = 8.8$

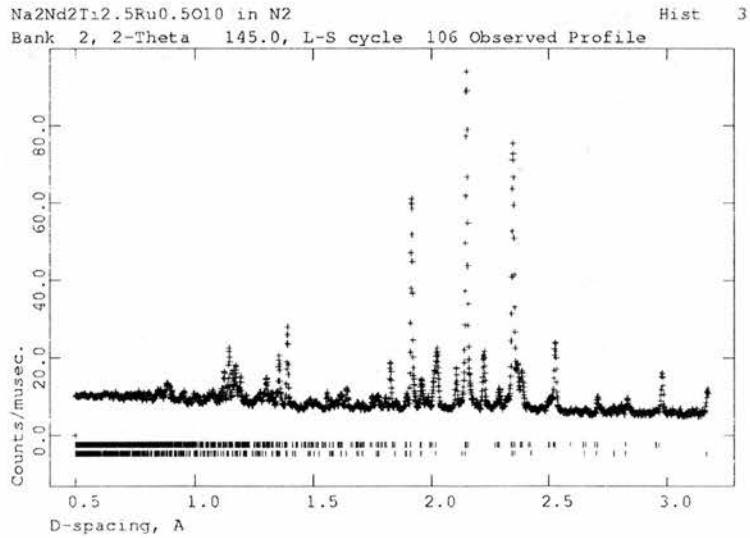


Figure 6.34: Na₂Nd₂Ti₂RuO₁₀, neutron data. Upper tick marks Pmmm, lower marks I4/mmm

performed, from this the impurity peaks could not be indexed as a single phase. The majority of the peaks could be indexed to a pyrochlore phase, of approximate formula $\text{Nd}_2\text{Ti}_2\text{O}_7$. The problem for indexing an impurity was a single peak at $2\theta = 8.8$, shown in Figure-6.33. This peak could not be indexed and the nature of the impurity is still unknown. As a result, indexing of the neutron data has not been possible, a plot of the neutron data is given as Figure-6.34.

6.2.3 $\text{Na}_2\text{Nd}_2\text{Ti}_{2.5}\text{Fe}_{0.5}\text{O}_{9.75}$

As it had been shown that it was possible to substitute an isovalent dopant onto the Ti^{4+} site, the substitution of an aliovalent dopant, Fe^{3+} , was attempted. This requires the creation of charge compensating oxygen vacancies in the perovskite block. The stability of such a phase is unknown. It is clear from examination of the X-ray diffraction data that the reaction did not produce a phase pure material, see Figure-6.35. From this it is clear that the model fits approximately to an $I4/mmm$ tetragonal 3-layer model. However, the peak at $2\theta = 33^\circ$ is clearly not matched and appears to be more than one peak. This impurity intensity may be attributable to a cubic perovskite phase. However, due to the overlapping nature of the two phases it has not been possible to establish the nature of the second phase, or to assign the composition of the main phase.

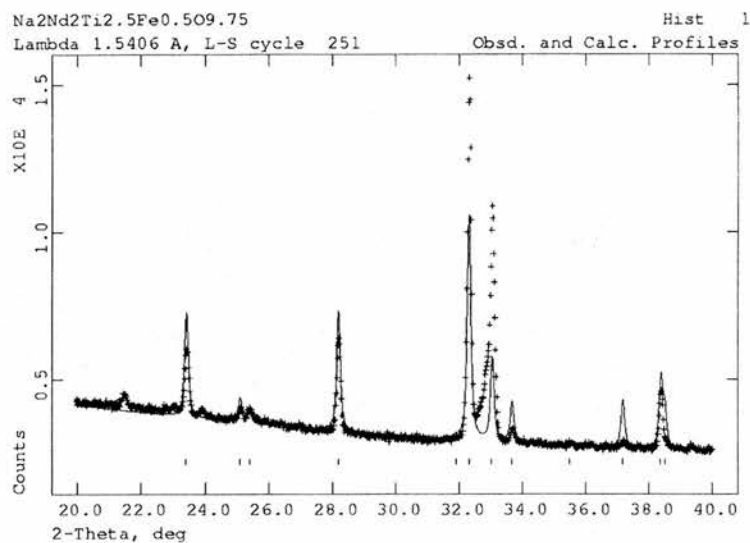


Figure 6.35: $\text{Na}_2\text{Nd}_2\text{Ti}_{2.5}\text{Fe}_{0.5}\text{O}_{9.75}$, X-ray diffraction data, 20 to 40 2θ , showing reflections for $I4/mmm$

6.2.4 $\text{Na}_2\text{Nd}_2\text{Ti}_2\text{MnO}_{10-x}$

One problem with the insertion of manganese into these compounds is that the oxidation state of the manganese present is unclear. Attempted here was the insertion of Mn^{3+} . Examining the X-ray diffraction data (Figure-6.36) it would appear that the sample is phase pure, a single unindexed peak at just over 21° can be attributed to the petroleum jelly used to mount the sample. The neutron diffraction data, however, are not matched by an $I4/mmm$ model. Shown as Figure-6.37 are the neutron data with the orthorhombic, $Pmmm$; $a \sim b \sim \sqrt{2}a_T$, $c \sim c_T$, and tetragonal, $I4/mmm$, permitted reflections indicated. It is clear then neither model correctly fits the data. It would appear that the sample is not phase pure, or possibly a more complex lattice type. If there is an impurity phase present it would

appear to be similar to that for the Ru^{4+} containing phases, and as for the impurities there cannot be identified.

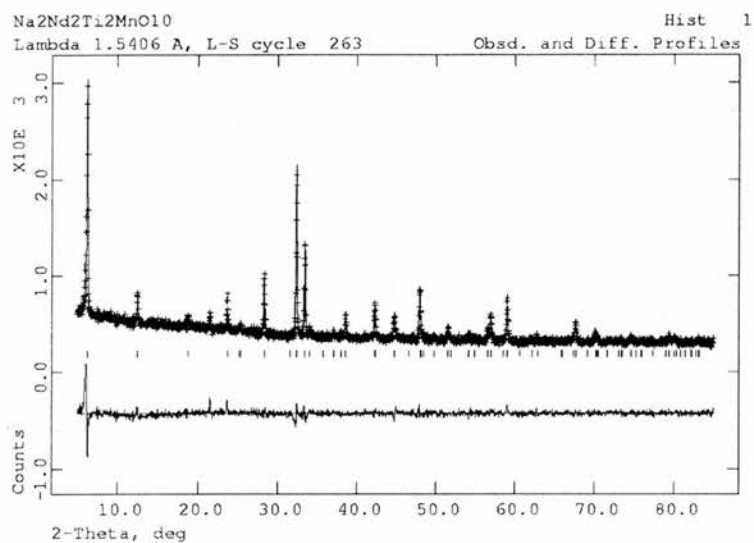


Figure 6.36: $\text{Na}_2\text{Nd}_2\text{Ti}_2\text{MnO}_{10-x}$, X-ray diffraction data, showing reflections for $I4/mmm$

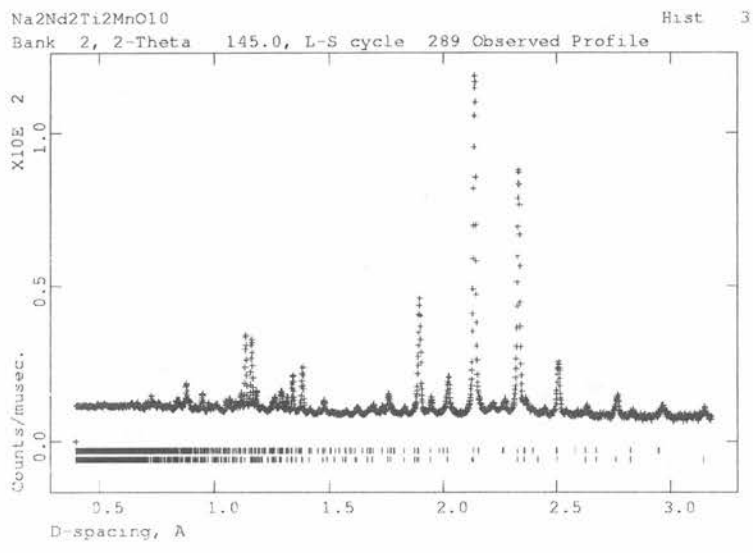


Figure 6.37: Na₂Nd₂Ti₂MnO_{10-x}, neutron diffraction data. Upper tick marks for Pmmm, lower marks for I4/mmm

References

- [1] M. A. Subramanian, J. Gopalakrishnan, and A. W. Sleight, *Mat. Res. Bull.*, 1988, **23**, 837.
- [2] J. Gopalakrishnan, T. Sivakumar, V. Thangadurai, and G. N. Subbanna, *Inorg. Chem.*, 1999, **38**, 2802.
- [3] N. Kumada, N. Kinomura, and A. W. Sleight, *Acta. Cryst. C.*, 1996, **52**, 1063.
- [4] A. R. Armstrong and P. A. Anderson, *Inorg. Chem.*, 1994, **33**, 4366.
- [5] Y.-S. Hong, S.-J. Kim, S.-J. Kim, and J.-H. Choy, *J. Mater. Chem.*, 2000, **10**, 1209.
- [6] S. N. Ruddlesden and P. Popper, *Acta. Cryst.*, 1957, **10**, 538.
- [7] S. N. Ruddlesden and P. Popper, *Acta. Cryst.*, 1958, **11**, 54.
- [8] G. Blasse, *J. Inorg. Chem.*, 1967, **30**, 656.
- [9] A. J. Wright and C. Greaves, *J. Mater. Chem.*, 1996, **6**, 1823.
- [10] J. N. Lalena, A. U. Falster, W. B. Simmons, E. E. Carpenter, J. Wiggins, S. Hariharan, and J. B. Wiley, *Chem. Mater.*, 2000, **12**, 2418.
- [11] K. Park and S.-H. Byeon, *Bull. Korean Chem. Soc.*, 1996, **17**, 168.
- [12] R. E. Schaak, D. Afzal, J. A. Schottenfeld, and T. E. Mallouk, *Chem. Mater.*, 2002, **14**, 442.

Chapter 7

Atomistic Simulations of Aurivillius Phases

7.1 Overview and Prior Work

The Aurivillius phases are structures composed of a perovskite block n -layers thick, formula $[A_{n-1}B_nO_{3n+1}]$ sandwiched between $[Bi_2O_2^{2+}]$ layers [1, 2]. The Aurivillius phases are of continued interest due to their ferroelectric properties, with key pieces of work examining this being carried out in the 1960's [3]. Interest on the systems became renewed when it was noted that the $n=2$ member $SrBi_2Ta_2O_9$ was fatigue free [4] on repeated cycling, and as such could prove useful as an information storage technology.

In this work $n = 3$ and $n = 4$ members are being investigated. The $n = 4$ member is based on the parent $BaBi_4Ti_4O_{15}$ phase [5], a ferroelectric material at room temperature. Previous reports suggested the possibility of substituting group 13 metals such as Ga^{3+} into the B-site for Ti^{4+} , thus creating extrinsic oxygen vacancies [6, 7]. These doped materials were reported as possessing oxide ion conduction properties, however a reappraisal of this work suggests that a Bi_2O_3 phase is present [8], a well-known oxide ion con-

ductor. It is therefore desirable to know if the parent structure is able to facilitate the incorporation of group 13 cations, and oxygen vacancies. Our own experimental work in doping Ga^{3+} into these systems (included in detail in Chapter 3) would suggest that this doping does not occur.

The $n = 3$ phases are doped versions of the $\text{Bi}_4\text{Ti}_3\text{O}_{12}$ structure. Here experimentally the Bi^{3+} is being replaced by La^{3+} to create $\text{Bi}_{4-x}\text{La}_x\text{Ti}_3\text{O}_{12}$ (BLT) for $x = 0$ to 2. These phases have been reported structurally[9] for the $x = 1$ and $x = 2$ phases. A more detailed structural study on this doping at various values of x is given in Chapter 5. There, as in this study, the ability of the interlayer, nominally written as $[\text{Bi}_2\text{O}_2]$, to incorporate Ln^{3+} is of interest, specifically, how does the level of dopant affect the site of doping, which is the preferred site and how does dopant cation size affect the stability? Simulation methods are used here, as in previous work, to investigate the structures at an atomistic level.

7.2 Introduction to Modelling

In this study the structures are simulated utilising the GULP[10] code, by potential fitting, energy minimisation and relaxation. The methods used are based on ionic models with individual atoms assigned charges consistent with their formal oxidation state. Both long range Coulombic interactions and short-range interactions, Van der Waals interactions and Pauli repulsion, are modelled. The short-range potentials are described by the Buckingham potential, Equation-7.1, where A , r and C are empirically derived.

$$V(r) = Ae^{\frac{-r}{\rho}} - \frac{C}{r^6} \quad (7.1)$$

Polarisation of the ions is incorporated using the Dick-Overhauser shell model. The core of the atom and the shell are given charges totalling to the oxidation state, these two charges are connected by a spring constant k . The spring describes the polarisability of ion, this is the ease with which the shell and core are able to move relative to one another during relaxation. This is particularly important when dealing with asymmetric systems with potentially highly polarised ions, such as Bi^{3+} .

To permit the modelling of an accurate defect structure the two region model is employed. In this model the closest region to the defect, region I, is modelled rigorously using an interatomic potential and the local structure is permitted to relax. Within this first region there are approximately 400 ions, enough to give an accurate simulation. Around region I is region IIa, where the structure is not simulated fully using the interatomic potential but is permitted to relax. The outer region is region IIb, in which the structure is modelled only using a continuum model of interactions.

Prior work on using the above methods to investigate the Aurivillius phases includes examining the ionic conduction of the $n=1$ phase Bi_2WO_6 [11], by doping in cations to both A and B sites and introducing extrinsic vacancies. Also, an in depth study of potential fitting to $n=1, 2$ & 3 members of the Aurivillius family, including $\text{Bi}_4\text{Ti}_3\text{O}_{12}$, with an examination of A site cation disorder in the $\text{PbBi}_2\text{Nb}_2\text{O}_9$ structure[12] has been carried out. Before it was possible to perform defect calculations it was necessary to investigate the potentials being used. The starting potentials were those found by Pirovano et al[12]. In that previous study the potentials were used to model to Aurivillius

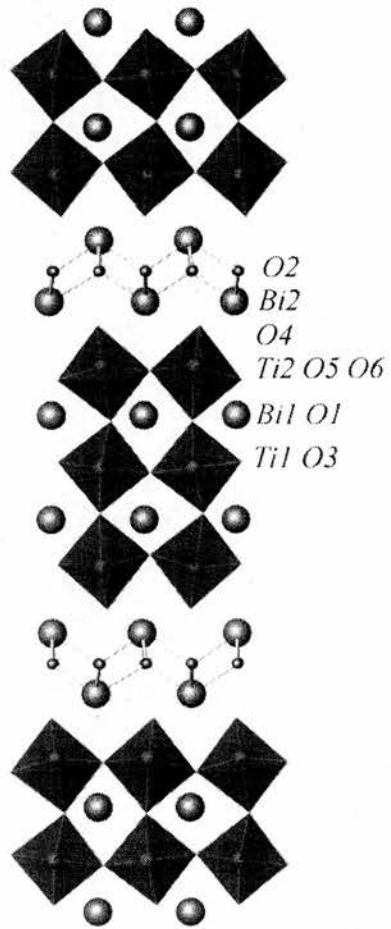


Figure 7.1: $\text{Bi}_4\text{Ti}_3\text{O}_{12}$ structure, view along the $[110]$ direction

phases with $n=1, 2$ and 3 . Here, the fitting of the potentials involved the use of the experimental data for $\text{BaBi}_4\text{Ti}_4\text{O}_{15}$ [5].

A key feature in the structural chemistry of the Aurivillius phases is the observation of severely distorted BO_6 octahedra. Hence, a useful guide to the validity of the modelling is the successful prediction of these octahedral distortions. For this reason it was decided to examine the effect of various Ti-O potentials on the calculated structural model. To determine whether the model produced was a good fit to the experimental data, first the lattice parameters were examined; if these were acceptable the key bond distances were then also examined. In addition to the examination of various established Ti-O potentials, the effect of adjusting the core-shell charge was also investigated. The result of these calculations is the final set of interatomic potentials used in the defect calculations, given in Table-7.1. The match of the final calculated structural model to the experimental model is shown in Table-7.2, which suggests that the structure is being accurately modelled by the chosen potentials.

Table 7.1: Final interatomic potentials used for defect calculations

Bond	A(eV)	r(Å)	C(eV Å ⁶)
Ba-O	4818.416	0.3067	0
Bi-O	49529.35	0.2223	0
Ti-O	2549.4	0.2989	0
O-O	9547.96	0.2192	32

Table 7.2: Calculated and experimental properties of $\text{Bi}_4\text{Ti}_3\text{O}_{12}$

Property	Calculated	Experimental
a	5.447	5.445
b	5.402	5.410
c	33.818	32.856
Bi(1)-O(1)	2.53, 2.86, 3.14, 3.41	2.54, 2.95, 2.96, 3.32
Bi(1)-O(3)	2.32, 2.41, 3.11, 3.23	2.29, 2.43, 3.09, 3.22
Bi(1)-O(5)	2.30, 2.48	2.40, 2.50
Bi(1)-O(6)	2.37, 2.96	2.31, 3.14
Bi(2)-O(2)	2.12, 2.30, 2.31, 2.47	2.19, 2.27, 2.29, 2.46
Bi(2)-O(4)	2.47, 2.57, 3.45, 3.49	2.55, 2.60, 3.21, 3.26
Ti(1)-O(1)	1.88 x 2, 2.03 x 2	1.85 x 2, 2.03 x 2
Ti(1)-O(3)	1.96 x 2	1.98 x 2
Ti(2)-O(3)	2.64	2.32
Ti(2)-O(4)	1.55	1.76
Ti(2)-O(5)	2.04, 2.09	1.94, 2.06
Ti(2)-O(6)	2.00, 2.01	1.89, 2.03
Lattice Energy (eV)	-618.1155	

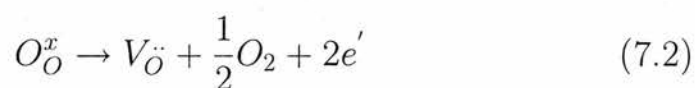
Table 7.3: Calculated isolated vacancy energies (eV)

Vacancy Site	Vacancy Energy (eV)
Bi(1)	44.27
Bi(2)	55.57
Ti(1)	93.16
Ti(2)	96.62
O(1)	24.11
O(2)	15.31
O(3)	22.41
O(4)	18.57
O(5)	18.33
O(6)	18.54

7.2.1 Intrinsic Atomic Defects and Redox Reactions

Calculations were performed on the energies of isolated point defects (vacancies). The resulting energies are given in Table-7.3. Attempts to establish interstitial defect energies were unsuccessful, suggesting that such defects are not feasible. It is clear that the oxygen (O₂) position in the [Bi₂O₂] layer is the lowest energy oxygen vacancy site. This is contrary to the hypothesis put forward previously[13], where the vacancies were proposed to create a brownmillerite structure type, requiring a vacancy in the perovskite block. There is no experimental evidence for the brownmillerite structure, or any oxygen vacancies in Bi₄Ti₃O₁₂.

Many applications result in conditions where materials are expected to be used under a variety of oxygen partial pressures. It is therefore desirable to examine the possibility of certain redox processes. In this system processes involving the reduction of the Ti⁴⁺ to Ti³⁺ have been examined. Lattice oxygen removal may be described as follows:

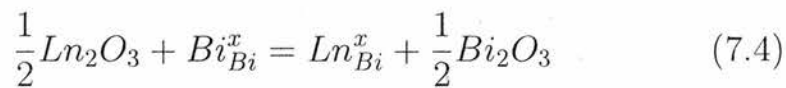
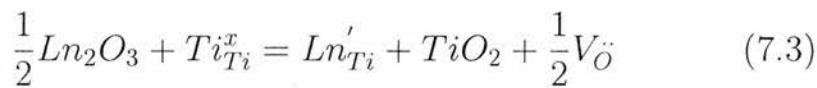


To obtain the e' term the fourth ionisation energy of Ti is subtracted from the defect energy calculated. The possibility of ionisation can then be examined with different compensating oxygen vacancies. Focussing on the most favourable redox process, that for O₂, the energy for the process appears highly favourable, with energies of -1.59 and 1.61 eV/e⁻ for Ti1 and Ti2 respectively. It would be expected that Bi₄Ti₃O₁₂ be easily reducible to a

Ti³⁺ containing phase Bi₄Ti₃O_{12-x}. As far as we are aware no experimental evidence to suggest that such a phenomenon occurs to any significant extent.

7.2.2 Dopant Substitution

It has been demonstrated experimentally that the doping of Ln³⁺ cations for Bi³⁺ in the Bi₄Ti₃O₁₂ decreases the ferroelectric Curie temperature T_C[14]. Classically it was assumed that the lanthanide substitution occurred on the perovskite A-site, Bi1, and not on the [Bi₂O₂] layer site, Bi2. However, recent powder X-ray diffraction studies[9, 15] have stated that this is only an approximation, with La doping on both sites for compositions Bi₃LaTi₃O₁₂ and Bi₂La₂Ti₃O₁₂. Our own findings (Chapter 5) would suggest ordering of the sites at lower La³⁺ content. In this study the approach is to calculate the Ln³⁺ dopant substitution energy for all the Bi³⁺ and Ti⁴⁺ sites, the latter with compensating oxygen vacancies. The substitutions can be represented using Kröger-Vink notation:



The energies of these 'solution' reactions can then be calculated by combining the appropriate defect and lattice energy terms. Using this consistent

approach creates a guide to the relative energies for different dopant ions on the same site, or the same dopant ion on different sites. The solution energies are plotted against dopant ion size in Figure-7.2. Examination of these results reveals several conclusions. The doping of the lanthanide cations into either of the Ti^{4+} sites is indicated as highly unfavourable. This matches with chemical intuition, the Ln^{3+} cations being too large to occupy the octahedral site, and with experimental data. The solution energies obtained for the two Bi^{3+} sites suggest that the $[Bi_2O_2]$ layer site is given slight preference over the perovskite A-site. This is not consistent with experimental observations, where there is normally some disorder, but with a strong preference for the perovskite A-site. The solution energies for the lanthanide cations show no significant trend with cation size, also, there is no change of the difference between the solution energies of the two sites. The difference between these results and those of previous experimental studies can be rationalised by the dopant level. For the simulation only one single dopant ion is inserted, i.e. the calculation takes place at the dilute limit. The simulation result does not suggest that doping will take place only on the $[Bi_2O_2]$ layer site, but that the initial doping will occur on that site. The very small difference in the solution energies for the two Bi^{3+} sites, and the favourable nature of both, would suggest that doping would occur over both sites at higher concentrations. Similar calculations were performed for the smaller trivalent cations, $Me^{3+} = Al, Ga$ and In . For these calculations the $Bi_4Ti_{3-x}Me_xO_{12-x/2}$ series was selected, instead of the more complex $Bi_2Sr_2Nb_2Ti_{1-x}Me_xO_{12-x/2}$ reported experimentally[13]. The results are displayed as a plot of solution energy versus ionic radius (Figure-7.3). Examining the plot, it can be seen that

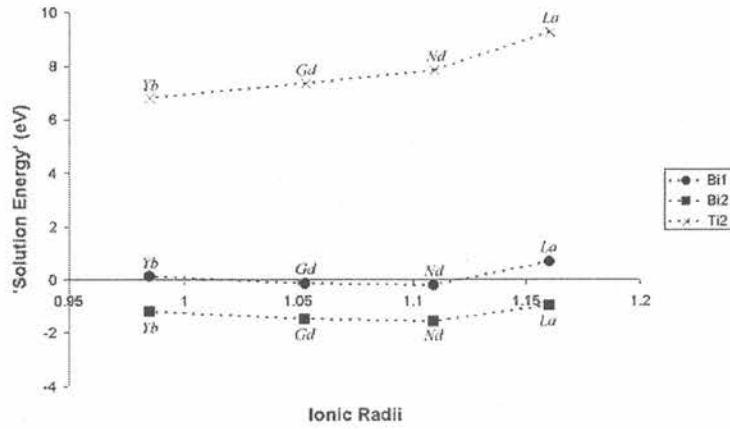


Figure 7.2: Calculated solution energies as a function of ionic radius for Ln^{3+} (Only Ti2 is shown, as it is the lower energy Ti site).

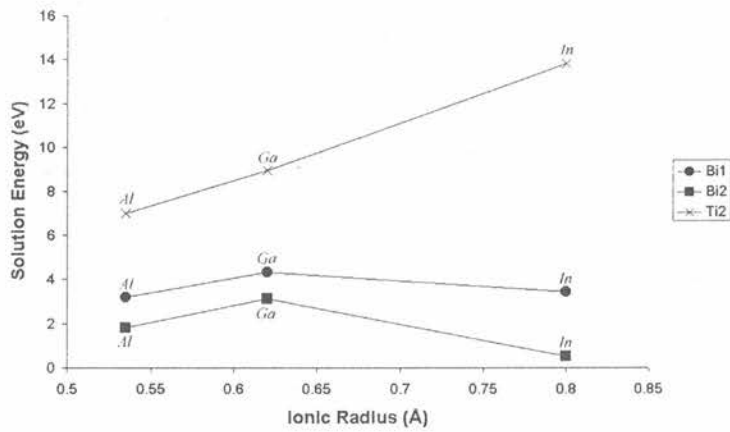


Figure 7.3: Calculated solution energies as a function of ionic radius for Me^{3+} (Only Ti2 is shown, as it is the lower energy site).

both of the Ti^{4+} sites are unsuitable for the insertion of Me^{3+} , which would agree with the most recent experimental study[8]. For the perovskite A-site, Bi1, doping of any of the Me^{3+} cations appears energetically unfavourable. For the $[\text{Bi}_2\text{O}_2]$ layer site, doping of the smaller Ga^{3+} and Al^{3+} cations is not energetically favourable, however, it is suggested that the larger In^{3+} cation may insert into this site. An experimental study of this possibility would be worthwhile.

7.2.3 Vacancy Migration

As the Me^{3+} doped phases were proposed to be oxide ion conductors, via a hopping mechanism, an investigation of the energies of vacancy migration was performed. The procedure for this is to move an oxygen anion linearly between two oxygen vacancy sites, producing an energy profile along the pathway. The difference between the initial energy and the maximum energy gives the activation energy for the migration. Calculations were performed for the $[\text{Bi}_2\text{O}_2]$ oxygen site, O2, and the O1 position in the inner Ti1-O1 plane. It was found that the activation energies for the migrations were 1.6 eV and 2.5 eV, for the O2 and O1 migrations respectively. In a previous study phases based on Bi_2WO_6 were found to have activation energies as low as 0.45 eV. These high energies found for $\text{Bi}_4\text{Ti}_3\text{O}_{12}$ would suggest that it is unlikely that oxygen transport would occur in these phases. This is supported by a lack of confirmed experimental evidence of oxide ion conduction in Aurivillius phases with $n > 1$.

7.3 Conclusions

Simulation techniques have been employed to represent the structure of the 3-layer Aurivillius phase $\text{Bi}_4\text{Ti}_3\text{O}_{12}$. Investigations into the possibility of Ln^{3+} doping have suggested that doping could occur on both of the Bi^{3+} sites, as observed experimentally. However, at the dilute limit a slight preference for the $[\text{Bi}_2\text{O}_2]$ layer site is observed, which maybe unexpected, in the light of recent experimental work. Calculations performed on the doping of smaller Me^{3+} cations have indicated that substitution is unlikely to occur on either the perovskite A or B-sites. Agreeing with our experimental study, detailed in Chapter 3. For the $[\text{Bi}_2\text{O}_2]$ site, however, In^{3+} is suggested as a possible dopant. The possibility of oxygen migration has been examined and appears unlikely. The possibility of reduction of Ti^{4+} to Ti^{3+} in $\text{Bi}_4\text{Ti}_3\text{O}_{12-x}$ is suggested to be possible for both sites.

References

- [1] B. Aurivillius, *Ark. Kemi.*, 1949, **1**, 463.
- [2] B. Aurivillius, *Ark. Kemi.*, 1949, **1**, 499.
- [3] E. C. Subbarao, *J. Phys. Chem. Solids*, 1962, **23**, 665.
- [4] C. A.-P. de Araujo, J. D. Cuchiaro, L. D. McMillan, M. C. Scott, and J. F. Scott, *Nature*, 1995, **374**, 627.
- [5] P. Lightfoot, A. Snedden, S. M. Blake, and K. S. Knight, *Mat. Res. Symp. Proc.*, 2003, **755**, 89.
- [6] K. R. Kendall, J. K. Thomas, and H.-C. zur Loye, *Solid State Ionics*, 1994, **70/71**, 221.
- [7] J. K. Thomas, K. R. Kendall, and H.-C. zur Loye, *Solid State Ionics*, 1994, **70/71**, 225.
- [8] A. Snedden, S. M. Blake, K. S. Knight, and P. Lightfoot, *Solid State Ionics*, 2003, **156**, 439.
- [9] C. H. Hervoches and P. Lightfoot, *J. Solid State Chem.*, 2000, **153**, 66.
- [10] J. D. Gale, *J. Chem. Soc. Faraday Trans.*, 1997, **93**, 629.
- [11] M. S. Islam, S. Lazure, R.-N. Vannier, G. Nowogrocki, and G. Mairesse, *J. Mater. Chem.*, 1998, **8**, 655.
- [12] C. Pirovano, M. S. Islam, R.-N. Vannier, G. Nowogrocki, and G. Mairesse, *Solid State Ionics*, 2001, **140**, 115.
- [13] K. R. Kendall, J. K. Thomas, and H.-C. zur Loye, *Chem. Mater.*, 1995, **7**, 50.
- [14] R. W. Wolfe and R. Newnham, *J. Electrochem. Soc.: Solid State Ionics*, 1969, **116**, 832.
- [15] N. C. Hyatt, J. A. Hriljac, and T. P. Comyn, *Mat. Res. Bull.*, 2003, **38**, 837.

Chapter 8

Concluding Remarks and Further Work

The work contained in this thesis has focused on the structural analysis of layered perovskites, and mainly on the Aurivillius family. From this work several interesting features can be identified. For the $n = 4$ members, $\text{BaBi}_4\text{Ti}_4\text{O}_{15}$ has been confirmed as being described by a unique space group for this family, $F2mm$. For $\text{Bi}_5\text{Ti}_3\text{FeO}_{15}$ it has been shown that there is only one high temperature phase transition, this being an orthorhombic to tetragonal transition which corresponds to the ferroelectric transition, confirmed by a.c. impedance spectroscopy. This behaviour is contrary to that observed for $\text{SrBi}_4\text{Ti}_4\text{O}_{15}$ where an intermediate transition has been identified. Due to the diversity of the behaviour of these compounds an examination of the structure of $\text{BaBi}_4\text{Ti}_4\text{O}_{15}$ at variable temperatures, to examine the nature of the ferroelectric phase change, would be desirable. It would also be of interest to examine lower temperatures to see if any other phase changes take place, possibly to an $A2_1am$ structure.

Investigations into the possibility of doping both $n = 3$ and $n = 4$ Aurivillius

phases with trivalent metal cations has been examined both experimentally and theoretically. This type of doping has previously been suggested to create oxide ion vacancies in the structures, thus permitting the observed oxide ion conduction. The result of attempts to dope $\text{Bi}_2\text{Sr}_2\text{TiNb}_2\text{O}_{12}$ and $\text{BaBi}_4\text{Ti}_4\text{O}_{15}$ with Ga^{3+} ($\text{Bi}_2\text{Sr}_2\text{Ti}_{1-x}\text{Ga}_x\text{Nb}_2\text{O}_{12-x/2}$ and $\text{BaBi}_4\text{Ti}_{4-x}\text{Ga}_x\text{O}_{15-x/2}$) show clearly that even at dopant levels of $x = 0.2$ there is an identifiable impurity phase. The decreasing level of this second phase with decreasing Ga^{3+} level would suggest that the presence of the Ga^{3+} is directly responsible for this impurity. The second phase was identified as being due to Bi_2O_3 , a well known oxide conductor. It would appear from the experimental data that the structure does not accommodate the doping of Ga^{3+} . The molecular-modelling calculations performed agree with the experimental data that insertion of Ga^{3+} is energetically unfavourable, and suggest that the insertion of Al^{3+} and In^{3+} is also unfavourable. Of interest from the calculations is the possibility of In^{3+} doping onto the Bi^{3+} site in the $[\text{Bi}_2\text{O}_2]$ layer, as this is suggested as energetically favourable. There is no previous work documenting such doping and it would be interesting to investigate this area, as this permits the effect of a previously undocumented structural parameter on physical properties to be examined.

Doping of La^{3+} into Aurivillius phases is well documented. However, a systematic study of the insertion of increasing amounts of La^{3+} into Aurivillius phases had not previously been undertaken. Here the series $\text{Bi}_{4-x}\text{La}_x\text{Ti}_3\text{O}_{12}$ and $\text{Bi}_{3-x}\text{La}_x\text{TiNbO}_9$ were investigated. It has been demonstrated that the insertion of high dopant levels is possible whilst still retaining the orthorhombic symmetry. There are orthorhombic superstructure peaks still present in

the series even when the structure is metrically tetragonal. From the experimental data it is not possible to say with certainty on which site the La^{3+} is located. However, it appears that the doping is occurring predominantly at the perovskite A-site, as anticipated. From the atomistic calculations it is suggested that the doping at the dilute limit is occurring at the $[\text{Bi}_2\text{O}_2]$ layer site. Clearly this is contradictory to the experimental data, however, the experimental data at low doping levels are not unambiguous. For these samples an a.c. impedance investigation of the T_C and the ϵ' vs. x would be useful in order to examine the effect symmetry and structural changes have on the physical properties.

For the A1 A2 mixed-layer Aurivillius phases it would appear that the space group previously identified for the A2 A3 $\text{Bi}_7\text{Ti}_4\text{NbO}_{21}$ phase, $I2cm$, can be correctly assigned. Also it appears that to create a sample where defects, such as the stepped defect shown in Chapter 4, requires the intergrowth of two known phases. This may explain why $\text{Bi}_5\text{Nb}_3\text{O}_{15}$ was difficult to characterise while $\text{Bi}_5\text{TiNbWO}_{15}$ appears to be a simpler structure, due to lower amounts of disorder. Indeed, the preservation of the $[\text{WO}_4]$ and $[\text{BiTiNbO}_7]$ perovskite units indicates the need to use compositions which may exist independently. For these phases there has been so little structural characterisation that there is a great deal of work to be done.

For the Dion-Jacobson phases the work here has shown that a great deal of the previous structural characterisation on these materials is not rigorous enough. Here the two $n = 2$ phases have been shown to be described by the previously unreported space group $P2_1am$, with $a \sim b \sim \sqrt{2}a_T$. Also the $n = 4$ phase, $\text{CsBi}_3\text{Ti}_4\text{O}_{13}$ is refined in space group $P2_1am$. A similar

$\sqrt{2}$ distortion is observed for the $n = 3$ phases, with the $\text{CsBi}_2\text{Ti}_2\text{NbO}_{10}$ phase refined in space group $\text{Ic}2\text{m}$. This shows that indexings of X-ray data may often provide incorrect assessments of the unit cell, with many of the orthorhombic superstructure peaks too weak to be observed. The ordering of the B-site cations observed for the $n = 3$ phases is unusual and interesting; it appears that even when the structure is distorted and the octahedra begin to rotate the structure still desires ordering in the B-sites. For this area, structures of higher n may be difficult to prepare, as for all layered series, however, there is still the possibility of Bi^{3+} containing phases with greater numbers of layers. Studies on potential ferroelectric behaviour in these phases would also be advised.

Appendix A

Space Group Assignments

Within the course of the work presented in this thesis many space groups have been used to describe the structures of the synthesised compounds, in this appendix the method of assignment of these space groups is explained. The unit cell of the compound can be searched for using one of the available algorithms. For this work it was found that identification of often subtle orthorhombic distortions was difficult for these programs and manual assignments were performed. The phases that are dealt with here are most normally found with a equal to a of the perovskite or $\sqrt{2}a$ of the perovskite, as discussed in chapter 1. Once the unit cell has been identified a space group may be selected.

Selection of the space group is done using Table 3.2 in the International Tables for Crystallography Volume 1, which gives the specific absences associated with the space groups. By identifying reflections in the diffraction pattern which violate a reflection condition, and gradually discounting those space groups which are no longer valid a set of reflection conditions and a space group are identified.

In many cases a set of reflection conditions will not give a unique space

group assignment. This is particularly valid for $I4/mmm$ and $P4/mmm$, which are both similar to seven other space groups. In these cases convention has been to assign the highest symmetry, $4/mmm$, space group. It is noted that this assigned space group may be incorrect. However, identification from powder data is difficult if not impossible in certain cases.

Appendix B

Synthesis Conditions

Aurivillius Phases



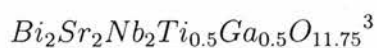
Ba ₂ CO ₃	0.267 g
Bi ₂ O ₃	1.390 g
TiO ₂	0.400 g
Ga ₂ O ₃	0.068 g



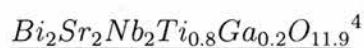
Ba ₂ CO ₃	0.261 g
Bi ₂ O ₃	1.326 g
TiO ₂	0.431 g
Ga ₂ O ₃	0.026 g

¹ Heated for 24 hours at 700 °C, 24 hours at 800 °C and 72 hours at 950 °C in air. Inserted at temperature, air quenched, 5 intermediate grindings, approximately 24 hours apart.

² Heated for 24 hours at 700 °C, 24 hours at 800 °C and 90 hours at 900 °C in air. Inserted at temperature, air quenched, 6 intermediate grindings, approximately 24 hours apart.



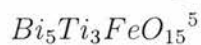
Bi ₂ O ₃	0.910 g
Sr ₂ CO ₃	0.582 g
Nb ₂ O ₅	0.512 g
TiO ₂	0.079 g
Ga ₂ O ₃	0.090 g



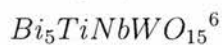
Bi ₂ O ₃	0.913 g
Sr ₂ CO ₃	0.292 g
Nb ₂ O ₅	0.519 g
TiO ₂	0.128 g
Ga ₂ O ₃	0.036 g

³ Heated for 72 hours at 700 °C, 72 hours at 900 °C and 24 hours at 950 °C in air. Inserted at temperature, air quenched with intermediate grindings, approximately 24 hours apart.

⁴ Heated for 24 hours at 700 °C, 72 hours at 800 °C, 24 hours at 900 °C and 90 hours at 950 °C in air. Inserted at temperature, air quenched with intermediate grindings, approximately 24 hours apart.



Bi ₂ O ₃	7.842 g
TiO ₂	1.620 g
Fe ₂ O ₃	0.672 g



Bi ₂ O ₃	8.682 g
TiO ₂	0.595 g
Nb ₂ O ₅	1.006 g
WO ₃	1.753 g

⁵ Heated for 72 hours at 950 °C in air. Inserted at temperature, air quenched with intermediate grindings, approximately 24 hours apart.

⁶ Heated for 24 hours at 800 °C, 24 hours at 900 °C, 72 hours at 1000 °C in air. Inserted at temperature, air quenched with intermediate grindings, approximately 24 hours apart.

<u>$Bi_5Nb_3O_{15}$</u> ⁷		<u>Bi_3TiNbO_9</u> ⁸	
Bi ₂ O ₃	1.496 g	Bi ₂ O ₃	9.199 g
		TiO ₂	1.048 g
Nb ₂ O ₅	0.514 g	Nb ₂ O ₅	1.800 g
<u>$Bi_{2.8}La_{0.2}TiNbO_9$</u> ⁹		<u>$Bi_{2.6}La_{0.4}TiNbO_9$</u> ¹⁰	
Bi ₂ O ₃	8.725 g	Bi ₂ O ₃	8.221 g
La ₂ O ₃	0.439 g	La ₂	0.883 g
TiO ₂	1.067 g	TiO ₂	1.072 g
Nb ₂ O ₅	1.780 g	Nb ₂ O ₅	1.808 g
<u>$Bi_{2.4}La_{0.6}TiNbO_9$</u> ¹¹		<u>$Bi_{2.2}La_{0.8}TiNbO_9$</u> ¹²	
Bi ₂ O ₃	7.720 g	Bi ₂ O ₃	7.186 g
La ₂ O ₃	1.341 g	La ₂	1.830 g
TiO ₂	1.100 g	TiO ₂	1.123 g
Nb ₂ O ₅	1.836 g	Nb ₂ O ₅	1.861 g
<u>$Bi_2LaTiNbO_9$</u> ¹³			
Bi ₂ O ₃	6.640 g		
La ₂ O ₃	2.335 g		
TiO ₂	1.139 g		
Nb ₂ O ₅	1.898 g		

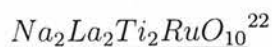
⁷ Heated for 120 hours at 900 °C in air. Inserted at temperature, air quenched with intermediate grindings, approximately 24 hours apart.

⁸⁻¹³ Heated for 24 hours at 800 °C and 48 hours at 1000 °C in air. Inserted at temperature, air quenched with intermediate grindings, approximately 24 hours apart.

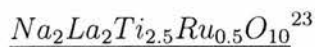
<u>$Bi_{3.9}La_{0.1}Ti_3O_{12}$</u> ¹⁴		<u>$Bi_{3.7}La_{0.3}Ti_3O_{12}$</u> ¹⁵	
Bi ₂ O ₃	9.368 g	Bi ₂ O ₃	8.975 g
La ₂ O ₃	0.170 g	La ₂	0.510 g
TiO ₂	2.470 g	TiO ₂	2.463 g
<u>$Bi_{3.5}La_{0.5}Ti_3O_{12}$</u> ¹⁶		<u>$Bi_{3.3}La_{0.7}Ti_3O_{12}$</u> ¹⁷	
Bi ₂ O ₃	8.614 g	Bi ₂ O ₃	8.225 g
La ₂ O ₃	0.848 g	La ₂	1.218 g
TiO ₂	2.527 g	TiO ₂	2.560 g
<u>$Bi_{3.1}La_{0.9}Ti_3O_{12}$</u> ¹⁸		<u>$Bi_{2.9}La_{1.1}Ti_3O_{12}$</u> ¹⁹	
Bi ₂ O ₃	7.818 g	Bi ₂ O ₃	7.401 g
La ₂ O ₃	1.587 g	La ₂	1.963 g
TiO ₂	2.596 g	TiO ₂	2.628 g
<u>$Bi_{2.7}La_{1.3}Ti_3O_{12}$</u> ²⁰		<u>$Bi_{2.5}La_{1.5}Ti_3O_{12}$</u> ²¹	
Bi ₂ O ₃	6.985 g	Bi ₂ O ₃	6.557 g
La ₂ O ₃	2.355 g	La ₂ O ₃	2.755 g
TiO ₂	2.666 g	TiO ₂	2.699 g

¹⁴⁻²¹ Heated for 24 hours at 900 °C and for 24 hours at 1000 °C in air. Inserted at temperature, air quenched with intermediate grindings, approximately 24 hours apart.

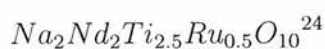
Ruddlesden-Popper Phases



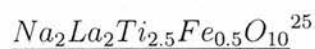
Na ₂ CO ₃	0.416 g
La ₂ O ₃	1.000 g
TiO ₂	0.610 g
RuO ₂	0.200 g



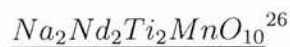
Na ₂ CO ₃	0.416 g
La ₂ O ₃	0.960 g
TiO ₂	0.470 g
RuO ₂	0.390 g



Na ₂ CO ₃	0.42 g
Nd ₂ O ₃	1.01 g
TiO ₂	0.60 g
RuO ₂	0.20 g



Na ₂ CO ₃	0.44 g
Nd ₂ O ₃	1.00 g
TiO ₂	0.49 g
Fe ₂ O ₃	0.25 g



Na ₂ CO ₃	0.44 g
Nd ₂ O ₃	1.04 g
TiO ₂	0.5 g
Mn ₂ O ₃	0.24 g

²²⁻²⁴Heated for 24 hours at 1000 °C in under flowing nitrogen. Heating rate 20 °C/sec, cooling rate 2 °C/sec.

²⁵Heated for 24 hours at 1000 °C in air. Heating rate 20 °C/sec, cooling rate 2 °C/sec.

²⁶Heated for 24 hours at 1000 °C in air on Pt foil. Heating rate 20 °C/sec, cooling rate 2 °C/sec.

Dion-Jacobson Phases

<u>$CsBiNb_2O_7$</u> ²⁷		<u>$CsNdNb_2O_7$</u> ²⁸	
Cs_2CO_3	3.00 g	$CsCO_3$	3.42 g
Bi_2O_3	3.63 g	Nd_2O_3	2.92 g
Nb_2O_5	4.14 g	Nb_2O_5	4.64 g
<u>$CsBi_2Ti_2NbO_{10}$</u> ²⁹		<u>$CsNd_2Ti_2NbO_{10}$</u> ³⁰	
Cs_2CO_3	2.18 g	$CsCO_3$	2.56 g
Bi_2O_3	5.18 g	Nd_2O_3	4.37 g
TiO_2	1.77 g	TiO_2	2.08 g
Nb_2O_5	1.48 g	Nb_2O_5	1.73 g
<u>$CsBi_3Ti_4O_{10}$</u> ³¹			
Cs_2CO_3	2.93 g		
Bi_2O_3	6.29 g		
TiO_2	2.87 g		

^{27,28,30} Heated for 24 hours at 1000 °C in air. Heating rate 20 °C/sec, air quenched from 1000 °C.

²⁹ Heated for 48 hours at 1000 °C in air, with one intermediate grinding. Heating rate 20 °C/sec, air quenched from 1000 °C.

³¹ Heated at 750 °C for 6 hours. Inserted at 750 °C, air quenched from 750 °C.

Appendix C

Ga^{3+} Doping Data

Presented here are the tables of atomic coordinates for the $\text{BaBi}_4\text{Ti}_{4-x}\text{Ga}_x\text{O}_{15-x/2}$ and $\text{Bi}_2\text{Sr}_2\text{Nb}_2\text{Ti}_{1-x}\text{Ga}_x\text{O}_{12-x/2}$ ($x = 0.2, 0.5$ and 1), analysed at ambient temperature using powder X-ray diffraction. These data have been discussed more thoroughly in Chapter 3.

Table C.1: BaBi₄Ti_{3.8}Ga_{0.2}O_{14.9} atomic parameters from 25 °C X-ray data, space group A2₁am, a = 5.4462(4) Å, b = 5.4634(4) Å, c = 41.770(3) Å. Bi₂O₃ space group P $\bar{4}$ 2₁c, a = 7.7630(1) Å, b = A Å, c = 5.6515(1) Å. R_{WP} = 0.172, χ^2 = 5.33, for 3998 data points and 394 contributing reflections, 1.14 < d < 17.6 Å

Atom	Multiplicity	x	y	z	Uiso*100
Ba/Bi1 ¹	4	0.250000	0.260635	0.000000	2.50
Ba/Bi2 ¹	8	0.212274	0.246779	0.105688	2.50
Ba/Bi3 ¹	8	0.236120	0.240095	0.219634	2.50
Ti/Ga1 ²	8	0.281240	0.224440	0.450325	2.50
Ti/Ga2 ²	8	0.264877	0.262909	0.343708	2.50
O1	4	0.324929	0.244131	0.500000	1.97
O2	8	0.559335	0.512968	0.046439	4.00
O3	8	0.297906	0.256588	0.404993	2.04
O4	8	0.540016	0.504334	0.142616	0.95
O5	8	0.273628	0.218394	0.305061	1.20
O6	8	0.532891	0.510057	0.249825	0.57
O7	8	0.004610	-0.023836	0.044976	2.54
O8	8	0.053070	0.009593	0.145635	0.84

¹ Occupancy fixed to 1 Ba / 0 Bi

² Occupancy fixed to 1 Ti / 0 Ga

Atom	Multiplicity	x	y	z	Uiso*100
Bi	8	0.017800	0.253900	0.253200	2.50
O1	8	0.295000	0.307400	0.027000	2.50
O2	4	0.000000	0.500000	0.101000	2.50

Table C.2: BaBi₄Ti_{3.5}Ga_{0.5}O_{14.75} atomic parameters from 25 °C X-ray data, space group A2₁am, a = 5.4701(4) Å, b = 5.4516(4) Å, c = 41.715(3) Å. Bi₂O₃ space group P4̄₂1c, a = 7.763(2) Å, b = A Å, c = 5.652(2) Å. R_{WP} = 0.193, χ² = 4.82, for 3998 data points and 402 contributing reflections, 1.14 < d < 17.6 Å

Atom	Multiplicity	x	y	z	Uiso*100
Ba/Bi1 ¹	4	0.250000	0.238551	0.000000	2.50
Ba/Bi2 ¹	8	0.229401	0.270523	0.105398	2.50
Ba/Bi3 ¹	8	0.236636	0.251805	0.218363	2.50
Ti/Ga1 ²	8	0.296795	0.247752	0.449104	2.50
Ti/Ga2 ²	8	0.267631	0.231728	0.342484	2.50
O1	4	0.324929	0.244131	0.500000	1.97
O2	8	0.559335	0.512968	0.046439	4.00
O3	8	0.297906	0.256588	0.404993	2.04
O4	8	0.540016	0.504334	0.142616	0.95
O5	8	0.273628	0.218394	0.305061	1.20
O6	8	0.532891	0.510057	0.249825	0.57
O7	8	0.004610	-0.023836	0.044976	2.54
O8	8	0.053070	0.009593	0.145635	0.84

¹ Occupancy fixed to 1 Ba / 0 Bi

² Occupancy fixed to 1 Ti / 0 Ga

Atom	Multiplicity	x	y	z	Uiso*100
Bi	8	0.017800	0.253900	0.253200	2.50
O1	8	0.295000	0.307400	0.027000	2.50
O2	4	0.000000	0.500000	0.101000	2.50

Table C.3: BaBi₄Ti₃GaO_{14.5} atomic parameters from 25 °C X-ray data, space group A2₁am, a = 5.470(1) Å, b = 5.453(1) Å, c = 41.744(8) Å. Bi₂O₃ space group P4₂c, a = 7.757(1) Å, b = A Å. c = 5.650(1) Å. R_{WP} = 0.180, χ^2 = 2.99, for 3253 data points and 411 contributing reflections, 1.34 < d < 17.7 Å

Atom	Multiplicity	x	y	z	Uiso*100
Ba/Bi1 ¹	4	0.250000	0.194584	0.000000	2.50
Ba/Bi2 ¹	8	0.201305	0.245946	0.104898	2.50
Ba/Bi3 ¹	8	0.227525	0.260550	0.219131	2.50
Ti/Ga1 ²	8	0.270685	0.250244	0.450744	2.50
Ti/Ga2 ²	8	0.260342	0.228965	0.344499	2.50
O1	4	0.324929	0.244131	0.500000	1.97
O2	8	0.559335	0.512968	0.046439	4.00
O3	8	0.297906	0.256588	0.404993	2.04
O4	8	0.540016	0.504334	0.142616	0.95
O5	8	0.273628	0.218394	0.305061	1.20
O6	8	0.532891	0.510057	0.249825	0.57
O7	8	0.004610	-0.023836	0.044976	2.54
O8	8	0.053070	0.009593	0.145635	0.84

¹ Occupancy fixed to 1 Ba / 0 Bi

² Occupancy fixed to 1 Ti / 0 Ga

Atom	Multiplicity	x	y	z	Uiso*100
Bi	8	0.017800	0.253900	0.253200	2.50
O1	8	0.295000	0.307400	0.027000	2.50
O2	4	0.000000	0.500000	0.101000	2.50

Table C.4: $\text{Bi}_2\text{Sr}_2\text{Nb}_2\text{Ti}_{0.8}\text{Ga}_{0.2}\text{O}_{11.9}$ atomic parameters from 25 °C X-ray data, space group $I4/mmm$, $a = 3.8967(2)$ Å, $b = A$, $c = 33.173(2)$ Å. Bi_2O_3 space group $P\bar{4}2_1c$, $a = 7.7816(1)$ Å, $b = A$ Å, $c = 5.5334(1)$ Å. $R_{WP} = 0.200$, $\chi^2 = 2.83$, for 3749 data points and 171 contributing reflections, $1.20 < d < 17.2$ Å

Atom	Multiplicity	x	y	z	Uiso*100
Bi/Sr1 ¹	4	0.500000	0.500000	0.062207	0.40
Bi/Sr2 ²	4	0.500000	0.500000	0.212971	0.40
Nb/Ti/Ga1 ³	2	0.500000	0.500000	0.500000	2.79
Nb/Ti/Ga2 ³	4	0.500000	0.500000	0.372003	2.79
O1	4	0.500000	0.000000	0.000000	2.50
O2	4	0.500000	0.000000	0.250000	2.50
O3	4	0.500000	0.500000	0.320400	2.50
O4	8	0.500000	0.000000	0.119300	2.50
O5	4	0.500000	0.500000	0.441700	2.50

¹ Occupancy -0.0964 Bi / 1.0964 Sr

² Occupancy 0.5964 Bi / 0.4036 Sr

³ Occupancy fixed to 1 Nb / 0 Ti / 0 Ga

Atom	Multiplicity	x	y	z	Uiso*100
Bi	8	0.017800	0.253900	0.253200	2.50
O1	8	0.295000	0.307400	0.027000	2.50
O2	4	0.000000	0.500000	0.101000	2.50

Table C.5: $\text{Bi}_2\text{Sr}_2\text{Nb}_2\text{Ti}_{0.5}\text{Ga}_{0.5}\text{O}_{11.75}$ atomic parameters from 25 °C X-ray data, space group $I4/mmm$, $a = 3.8990(1) \text{ \AA}$, $b = A$, $c = 33.187(2) \text{ \AA}$. Bi_2O_3 space group $P\bar{4}2_1c$, $a = 7.7816(1) \text{ \AA}$, $b = A \text{ \AA}$, $c = 5.533(1) \text{ \AA}$. $R_{WP} = 0.112$, $\chi^2 = 3.03$, for 3999 data points and 170 contributing reflections, $1.14 < d < 17.5 \text{ \AA}$

Atom	Multiplicity	x	y	z	Uiso*100
Bi/Sr1 ¹	4	0.500000	0.500000	0.061240	1.23
Bi/Sr2 ²	4	0.500000	0.500000	0.213382	1.23
Nb/Ti/Ga1 ³	2	0.500000	0.500000	0.500000	2.85
Nb/Ti/Ga2 ³	4	0.500000	0.500000	0.371879	2.85
O1	4	0.500000	0.000000	0.000000	2.50
O2	4	0.500000	0.000000	0.250000	2.50
O3	4	0.500000	0.500000	0.320400	2.50
O4	8	0.500000	0.000000	0.119300	2.50
O5	4	0.500000	0.500000	0.441700	2.50

¹ Occupancy -0.1314 Bi / 1.1314 Sr

² Occupancy 0.6114 Bi / 0.3686 Sr

³ Occupancy fixed to 1 Nb / 0 Ti / 0 Ga

Atom	Multiplicity	x	y	z	Uiso*100
Bi	8	0.017800	0.253900	0.253200	2.50
O1	8	0.295000	0.307400	0.027000	2.50
O2	4	0.000000	0.500000	0.101000	2.50

Table C.6: $\text{Bi}_2\text{Sr}_2\text{Nb}_2\text{GaO}_{11.5}$ atomic parameters from 25 °C X-ray data, space group $I4/mmm$, $a = 3.9102(1) \text{ \AA}$, $b = A$, $c = 33.270(2) \text{ \AA}$. Bi_2O_3 space group $P\bar{4}2_1c$, $a = 7.789(2) \text{ \AA}$, $b = A \text{ \AA}$, $c = 5.532(2) \text{ \AA}$. $R_{WP} = 0.164$, $\chi^2 = 2.26$, for 4000 data points and 173 contributing reflections, $1.14 < d < 17.6 \text{ \AA}$

Atom	Multiplicity	x	y	z	Uiso*100
Bi/Sr1 ¹	4	0.500000	0.500000	0.060475	2.08
Bi/Sr2 ²	4	0.500000	0.500000	0.214199	2.08
Nb/Ti/Ga1 ³	2	0.500000	0.500000	0.500000	2.13
Nb/Ti/Ga2 ³	4	0.500000	0.500000	0.372207	2.13
O1	4	0.500000	0.000000	0.000000	2.50
O2	4	0.500000	0.000000	0.250000	2.50
O3	4	0.500000	0.500000	0.320400	2.50
O4	8	0.500000	0.000000	0.119300	2.50
O5	4	0.500000	0.500000	0.441700	2.50

¹ Occupancy -0.1599 Bi / 1.1599 Sr

² Occupancy 0.6599 Bi / 0.3401 Sr

³ Occupancy fixed to 1 Nb / 0 Ti / 0 Ga

Atom	Multiplicity	x	y	z	Uiso*100
Bi	8	0.017800	0.253900	0.253200	2.50
O1	8	0.295000	0.307400	0.027000	2.50
O2	4	0.000000	0.500000	0.101000	2.50

Appendix D

Variable Temperature

$\text{Bi}_5\text{Ti}_3\text{FeO}_{15}$ Data

Presented here are the tables of atomic coordinates and some selected bond lengths for $\text{Bi}_5\text{Ti}_3\text{FeO}_{15}$, analysed at various temperatures using powder neutron diffraction. These data have been discussed more thoroughly in Chapter 3.

Table D.1: Bi₅Ti₃FeO₁₅ atomic parameters from 150 °C neutron data, space group A2₁am, a = 5.4703(1) Å, b = 5.4445(1) Å, c = 41.2989(6) Å. R_{WP} = 0.083, $\chi^2 = 2.92$, for 8142 data points and 4620 contributing reflections, 0.43 < d < 4.2 Å

Atom	Multiplicity	x	y	z	Uiso*100
Bi1	4	0.21(2)	0.247(2)	0.000000	2.7(2)
Bi2	8	0.21(2)	0.245(1)	0.1046(1)	1.4(1)
Bi3	8	0.19(2)	0.2688(9)	0.2191(1)	2.0(1)
Ti1 ¹	8	0.250000	0.250000	0.450000	1.00
Ti2 ¹	8	0.250000	0.250000	0.350000	1.00
O1	4	0.29(2)	0.189(3)	0.500000	1.6(3)
O2	8	0.57(2)	0.537(1)	0.0523(2)	1.4(2)
O3	8	0.28(2)	0.309(2)	0.4049(1)	1.2(2)
O4	8	0.49(2)	0.481(2)	0.1392(2)	1.3(2)
O5	8	0.25(2)	0.204(2)	0.3052(1)	1.9(2)
O6	8	0.46(2)	0.491(1)	0.2498(2)	2.1(2)
O7	8	-0.01(2)	-0.031(2)	0.0396(2)	2.0(2)
O8	8	0.04(2)	0.033(2)	0.1474(2)	2.5(3)

¹ Occupancy fixed to 0.75 Ti / 0.25 Fe

Table D.2: Bi₅Ti₃FeO₁₅, 150 °C refinement. Selected bond lengths

bond	length Å	bond	length Å	bond	length Å
Bi1 O1	3.07(2)	Bi2 O2	3.335(8)	Bi3 O5	2.618(9)
Bi1 O1	2.44(2)	Bi2 O2	2.577(8)	Bi3 O5	3.223(9)
Bi1 O1	2.33(1)	Bi2 O3	2.357(9)	Bi3 O5	3.254(9)
Bi1 O1	3.19(1)	Bi2 O3	3.202(9)	Bi3 O5	2.592(9)
Bi1 O2	3.312(9) x 2	Bi2 O3	2.44(1)	Bi3 O6	2.29(1)
Bi1 O2	2.580(8) x 2	Bi2 O3	3.13(1)	Bi3 O6	2.21(1)
Bi1 O7	2.53(1) x 2	Bi2 O4	2.48(1)	Bi3 O6	2.288(9)
Bi1 O7	2.53(1) x 2	Bi2 O4	2.376(9)	Bi3 O6	2.474(9)
		Bi2 O7	3.291(9)		
		Bi2 O7	3.316(7)		
		Bi2 O8	2.30(1)		
		Bi2 O8	2.955(9)		

Table D.3: $\text{Bi}_5\text{Ti}_3\text{FeO}_{15}$ atomic parameters from 250 °C neutron data, space group $A2_1am$, $a = 5.4729(1)$ Å, $b = 5.4484(1)$ Å, $c = 41.3438(5)$ Å. $R_{WP} = 0.066$, $\chi^2 = 1.78$, for 8152 data points and 4600 contributing reflections, $0.43 < d < 4.2$ Å

Atom	Multiplicity	x	y	z	Uiso*100
Bi1	4	0.21(1)	0.244(1)	0.000000	3.0(1)
Bi2	8	0.20(1)	0.2433(8)	0.1046(1)	2.26(9)
Bi3	8	0.19(1)	0.2673(7)	0.2192(1)	2.41(8)
Ti1 ¹	8	0.250000	0.250000	0.450000	1.00
Ti2 ¹	8	0.250000	0.250000	0.350000	1.00
O1	4	0.29(1)	0.191(2)	0.500000	2.1(3)
O2	8	0.56(1)	0.536(1)	0.0525(1)	1.8(2)
O3	8	0.28(1)	0.310(1)	0.4052(1)	1.6(1)
O4	8	0.49(1)	0.480(1)	0.1395(1)	1.4(2)
O5	8	0.25(1)	0.205(1)	0.3054(1)	2.4(2)
O6	8	0.46(1)	0.4909(9)	0.2493(1)	2.1(1)
O7	8	-0.02(1)	-0.032(1)	0.0397(1)	2.7(2)
O8	8	0.03(1)	0.032(2)	0.1475(2)	3.1(2)

¹ Occupancy fixed to 0.75 Ti / 0.25 Fe

Table D.4: $\text{Bi}_5\text{Ti}_3\text{FeO}_{15}$, 250 °C refinement. Selected bond lengths

bond	length Å	bond	length Å	bond	length Å
Bi1 O1	3.04(1)	Bi2 O2	3.335(6)	Bi3 O5	2.646(8)
Bi1 O1	2.47(1)	Bi2 O2	2.579(7)	Bi3 O5	3.202(8)
Bi1 O1	2.35(1)	Bi2 O3	2.364(8)	Bi3 O5	3.243(7)
Bi1 O1	3.17(1)	Bi2 O3	3.201(8)	Bi3 O5	2.606(7)
Bi1 O2	3.311(7) x 2	Bi2 O3	2.435(8)	Bi3 O6	2.286(7)
Bi1 O2	2.606(6) x 2	Bi2 O3	3.140(8)	Bi3 O6	2.206(7)
Bi1 O7	2.543(8) x 2	Bi2 O4	2.498(7)	Bi3 O6	2.293(7)
Bi1 O7	2.509(9) x 2	Bi2 O4	2.384(7)	Bi3 O6	2.482(7)
		Bi2 O7	3.294(7)		
		Bi2 O7	3.311(6)		
		Bi2 O8	2.305(8)		
		Bi2 O8	2.949(7)		

Table D.5: $\text{Bi}_5\text{Ti}_3\text{FeO}_{15}$ atomic parameters from 350 °C neutron data, space group $A2_1am$, $a = 5.4766(1) \text{ \AA}$, $b = 5.4541(1) \text{ \AA}$, $c = 41.4133(4) \text{ \AA}$. $R_{WP} = 0.064$, $\chi^2 = 1.69$, for 8152 data points and 4611 contributing reflections, $0.43 < d < 4.2 \text{ \AA}$

Atom	Multiplicity	x	y	z	Uiso*100
Bi1	4	0.21(1)	0.245(1)	0.000000	3.5(1)
Bi2	8	0.20(1)	0.2450(8)	0.1048(1)	2.43(9)
Bi3	8	0.20(1)	0.2669(8)	0.2192(1)	2.61(9)
Ti1 ¹	8	0.250000	0.250000	0.450000	1.00
Ti2 ¹	8	0.250000	0.250000	0.350000	1.00
O1	4	0.28(1)	0.191(2)	0.500000	2.5(3)
O2	8	0.56(1)	0.535(1)	0.0523(1)	1.7(2)
O3	8	0.28(1)	0.306(1)	0.4049(1)	2.1(2)
O4	8	0.49(1)	0.482(1)	0.1395(1)	2.0(2)
O5	8	0.25(1)	0.206(2)	0.3054(1)	3.0(2)
O6	8	0.47(1)	0.491(1)	0.2496(2)	2.7(2)
O7	8	-0.02(1)	-0.035(1)	0.0400(1)	3.4(2)
O8	8	0.03(1)	0.028(2)	0.1477(2)	3.5(2)

¹ Occupancy fixed to 0.75 Ti / 0.25 Fe

Table D.6: $\text{Bi}_5\text{Ti}_3\text{FeO}_{15}$, 350 °C refinement. Selected bond lengths

bond	length \AA	bond	length \AA	bond	length \AA
Bi1 O1	3.04(1)	Bi2 O2	3.326(6)	Bi3 O5	2.685(9)
Bi1 O1	2.46(2)	Bi2 O2	2.600(7)	Bi3 O5	3.169(9)
Bi1 O1	2.40(1)	Bi2 O3	2.386(9)	Bi3 O5	3.235(7)
Bi1 O1	3.13(1)	Bi2 O3	3.179(9)	Bi3 O5	2.615(7)
Bi1 O2	3.289(8) x 2	Bi2 O3	2.462(9)	Bi3 O6	2.281(8)
Bi1 O2	2.617(7) x 2	Bi2 O3	3.111(9)	Bi3 O6	2.229(8)
Bi1 O7	2.582(9) x 2	Bi2 O4	2.486(8)	Bi3 O6	2.302(8)
Bi1 O7	2.49(1) x 2	Bi2 O4	2.381(7)	Bi3 O6	2.460(8)
		Bi2 O7	3.312(7)		
		Bi2 O7	3.295(7)		
		Bi2 O8	2.337(8)		
		Bi2 O8	2.927(8)		

Table D.7: $\text{Bi}_5\text{Ti}_3\text{FeO}_{15}$ atomic parameters from 450 °C neutron data, space group $A2_1am$, $a = 5.4794(1) \text{ \AA}$, $b = 5.4595(1) \text{ \AA}$, $c = 41.4849(4) \text{ \AA}$. $R_{WP} = 0.063$, $\chi^2 = 1.63$, for 8152 data points and 4599 contributing reflections, $0.43 < d < 4.2 \text{ \AA}$

Atom	Multiplicity	x	y	z	Uiso*100
Bi1	4	0.22(1)	0.245(1)	0.000000	3.9(1)
Bi2	8	0.21(1)	0.2447(9)	0.1048(1)	3.2(1)
Bi3	8	0.21(1)	0.2652(8)	0.2193(1)	3.08(9)
Ti1 ¹	8	0.250000	0.250000	0.450000	1.00
Ti2 ¹	8	0.250000	0.250000	0.350000	1.00
O1	4	0.29(1)	0.192(2)	0.500000	3.3(3)
O2	8	0.56(1)	0.535(1)	0.0523(1)	2.1(2)
O3	8	0.28(1)	0.304(1)	0.4048(1)	2.9(2)
O4	8	0.49(1)	0.485(1)	0.1399(2)	2.2(2)
O5	8	0.25(1)	0.208(2)	0.3055(1)	3.2(2)
O6	8	0.48(1)	0.492(1)	0.2493(2)	3.3(2)
O7	8	-0.01(1)	-0.034(1)	0.0402(2)	4.0(2)
O8	8	0.03(1)	0.027(2)	0.1472(2)	4.2(3)

¹ Occupancy fixed to 0.75 Ti / 0.25 Fe

Table D.8: $\text{Bi}_5\text{Ti}_3\text{FeO}_{15}$, 450 °C refinement. Selected bond lengths

bond	length \AA	bond	length \AA	bond	length \AA
Bi1 O1	3.04(2)	Bi2 O2	3.306(7)	Bi3 O5	2.696(9)
Bi1 O1	2.47(2)	Bi2 O2	2.616(7)	Bi3 O5	3.164(9)
Bi1 O1	2.39(1)	Bi2 O3	2.441(9)	Bi3 O5	3.217(8)
Bi1 O1	3.14(1)	Bi2 O3	3.122(9)	Bi3 O5	2.640(8)
Bi1 O2	3.292(8) x 2	Bi2 O3	2.463(9)	Bi3 O6	2.287(9)
Bi1 O2	2.619(8) x 2	Bi2 O3	3.098(9)	Bi3 O6	2.224(9)
Bi1 O7	2.59(1) x 2	Bi2 O4	2.483(9)	Bi3 O6	2.300(9)
Bi1 O7	2.51(1) x 2	Bi2 O4	2.404(8)	Bi3 O6	2.465(8)
		Bi2 O7	3.322(8)		
		Bi2 O7	3.276(7)		
		Bi2 O8	2.348(9)		
		Bi2 O8	2.883(8)		

Table D.9: $\text{Bi}_5\text{Ti}_3\text{FeO}_{15}$ atomic parameters from 500 °C neutron data, space group $A2_1am$, $a = 5.4812(1) \text{ \AA}$, $b = 5.4637(1) \text{ \AA}$, $c = 41.5412(3) \text{ \AA}$. $R_{WP} = 0.049$, $\chi^2 = 3.17$, for 8356 data points and 4588 contributing reflections, $0.43 < d < 4.2 \text{ \AA}$

Atom	Multiplicity	x	y	z	Uiso*100
Bi1	4	0.22(1)	0.245(1)	0.000000	4.4(1)
Bi2	8	0.22(1)	0.2455(7)	0.1048(1)	3.72(8)
Bi3	8	0.22(1)	0.2651(7)	0.2192(1)	3.25(7)
Ti1 ¹	8	0.250000	0.250000	0.450000	1.00
Ti2 ¹	8	0.250000	0.250000	0.350000	1.00
O1	4	0.28(1)	0.194(2)	0.500000	4.0(3)
O2	8	0.56(1)	0.5351(9)	0.0518(1)	2.1(2)
O3	8	0.28(1)	0.302(1)	0.4046(1)	3.1(1)
O4	8	0.49(1)	0.485(1)	0.1401(1)	2.5(2)
O5	8	0.25(1)	0.211(1)	0.3054(1)	3.7(2)
O6	8	0.48(1)	0.4925(9)	0.2494(1)	3.5(1)
O7	8	-0.01(1)	-0.032(1)	0.0403(1)	4.4(2)
O8	8	0.03(1)	0.022(2)	0.1471(2)	4.6(2)

¹ Occupancy fixed to 0.75 Ti / 0.25 Fe

Table D.10: $\text{Bi}_5\text{Ti}_3\text{FeO}_{15}$, 500 °C refinement. Selected bond lengths

bond	length \AA	bond	length \AA	bond	length \AA
Bi1 O1	3.03(1)	Bi2 O2	3.312(6)	Bi3 O5	2.732(8)
Bi1 O1	2.48(1)	Bi2 O2	2.643(6)	Bi3 O5	3.128(8)
Bi1 O1	2.42(1)	Bi2 O3	2.461(8)	Bi3 O5	3.202(6)
Bi1 O1	3.11(1)	Bi2 O3	3.101(8)	Bi3 O5	2.653(6)
Bi1 O2	3.267(7) x 2	Bi2 O3	2.475(8)	Bi3 O6	2.283(7)
Bi1 O2	2.610(6) x 2	Bi2 O3	3.083(7)	Bi3 O6	2.233(8)
Bi1 O7	2.597(8) x 2	Bi2 O4	2.473(7)	Bi3 O6	2.312(8)
Bi1 O7	2.507(9) x 2	Bi2 O4	2.418(7)	Bi3 O6	2.454(7)
		Bi2 O7	3.327(6)		
		Bi2 O7	3.275(6)		
		Bi2 O8	2.379(8)		
		Bi2 O8	2.851(7)		

Table D.11: $\text{Bi}_5\text{Ti}_3\text{FeO}_{15}$ atomic parameters from 550 °C neutron data, space group $A2_1am$, $a = 5.4826(1) \text{ \AA}$, $b = 5.4667(1) \text{ \AA}$, $c = 41.5866(3) \text{ \AA}$. $R_{WP} = 0.053$, $\chi^2 = 2.28$, for 8356 data points and 4566 contributing reflections, $0.43 < d < 4.2 \text{ \AA}$

Atom	Multiplicity	x	y	z	Uiso*100
Bi1	4	0.22(1)	0.245(1)	0.000000	4.8(1)
Bi2	8	0.22(1)	0.2449(8)	0.1050(1)	4.00(9)
Bi3	8	0.22(1)	0.2650(8)	0.2192(1)	3.51(8)
Ti1 ¹	8	0.250000	0.250000	0.450000	1.00
Ti2 ¹	8	0.250000	0.250000	0.350000	1.00
O1	4	0.28(1)	0.197(2)	0.500000	4.5(3)
O2	8	0.56(1)	0.536(1)	0.0517(1)	2.2(2)
O3	8	0.27(1)	0.299(1)	0.4045(1)	3.8(2)
O4	8	0.49(1)	0.486(1)	0.1401(1)	2.6(2)
O5	8	0.26(1)	0.212(2)	0.3054(1)	4.3(2)
O6	8	0.48(1)	0.494(1)	0.2491(2)	3.8(2)
O7	8	-0.02(1)	-0.033(1)	0.0408(1)	4.8(2)
O8	8	0.02(1)	0.020(2)	0.1470(2)	4.9(3)

¹ Occupancy fixed to 0.75 Ti / 0.25 Fe

Table D.12: $\text{Bi}_5\text{Ti}_3\text{FeO}_{15}$, 550 °C refinement. Selected bond lengths

bond	length \AA	bond	length \AA	bond	length \AA
Bi1 O1	3.01(2)	Bi2 O2	3.308(6)	Bi3 O5	2.75(1)
Bi1 O1	2.49(2)	Bi2 O2	2.664(6)	Bi3 O5	3.11(1)
Bi1 O1	2.44(1)	Bi2 O3	2.49(1)	Bi3 O5	3.200(7)
Bi1 O1	3.08(1)	Bi2 O3	3.071(9)	Bi3 O5	2.655(7)
Bi1 O2	3.256(8) x 2	Bi2 O3	2.487(9)	Bi3 O6	2.280(8)
Bi1 O2	2.616(7) x 2	Bi2 O3	3.068(8)	Bi3 O6	2.226(9)
Bi1 O7	2.624(9) x 2	Bi2 O4	2.468(8)	Bi3 O6	2.326(9)
Bi1 O7	2.51(1) x 2	Bi2 O4	2.423(8)	Bi3 O6	2.457(8)
		Bi2 O7	3.327(7)		
		Bi2 O7	3.253(7)		
		Bi2 O8	2.388(9)		
		Bi2 O8	2.822(9)		

Table D.13: Bi₅Ti₃FeO₁₅ atomic parameters from 600 °C neutron data, space group A2₁am, a = 5.4841(1) Å, b = 5.4701(1) Å, c = 41.6362(2) Å. R_{WP} = 0.044, $\chi^2 = 4.42$, for 8356 data points and 4542 contributing reflections, 0.43 < d < 4.2 Å

Atom	Multiplicity	x	y	z	Uiso*100
Bi1	4	0.23(1)	0.246(1)	0.000000	5.2(1)
Bi2	8	0.23(1)	0.2472(8)	0.1050(1)	4.61(8)
Bi3	8	0.23(1)	0.2635(7)	0.2192(1)	3.75(7)
Ti1 ¹	8	0.250000	0.250000	0.450000	1.00
Ti2 ¹	8	0.250000	0.250000	0.350000	1.00
O1	4	0.28(1)	0.199(2)	0.500000	5.4(3)
O2	8	0.56(1)	0.5353(9)	0.0515(1)	2.4(2)
O3	8	0.27(1)	0.298(1)	0.4044(1)	4.3(1)
O4	8	0.50(1)	0.489(1)	0.1404(1)	3.0(2)
O5	8	0.26(1)	0.214(1)	0.3053(1)	4.3(1)
O6	8	0.49(1)	0.4938(9)	0.2494(1)	4.1(1)
O7	8	-0.01(1)	-0.031(1)	0.0408(1)	5.4(2)
O8	8	0.03(1)	0.015(2)	0.1464(1)	4.9(2)

¹ Occupancy fixed to 0.75 Ti / 0.25 Fe

Table D.14: Bi₅Ti₃FeO₁₅, 600 °C refinement. Selected bond lengths

bond	length Å	bond	length Å	bond	length Å
Bi1 O1	3.00(1)	Bi2 O2	3.295(6)	Bi3 O6	2.758(9)
Bi1 O1	2.50(1)	Bi2 O2	2.681(6)	Bi3 O6	3.098(9)
Bi1 O1	2.47(1)	Bi2 O3	2.540(8)	Bi3 O6	3.178(6)
Bi1 O1	3.05(1)	Bi2 O3	3.022(8)	Bi3 O6	2.672(6)
Bi1 O2	3.235(8) x 2	Bi2 O3	2.501(8)	Bi3 O7	2.285(7)
Bi1 O2	2.618(7) x 2	Bi2 O3	3.047(8)	Bi3 O7	2.249(8)
Bi1 O7	2.634(9) x 2	Bi2 O4	2.467(8)	Bi3 O7	2.326(8)
Bi1 O7	2.503(9) x 2	Bi2 O4	2.423(8)	Bi3 O7	2.438(8)
		Bi2 O7	3.345(6)		
		Bi2 O7	3.252(6)		
		Bi2 O8	2.410(8)		
		Bi2 O8	2.774(8)		

Table D.15: $\text{Bi}_5\text{Ti}_3\text{FeO}_{15}$ atomic parameters from 650 °C neutron data, space group $A2_1am$, $a = 5.4852(1) \text{ \AA}$, $b = 5.4750(1) \text{ \AA}$, $c = 41.6981(3) \text{ \AA}$. $R_{WP} = 0.056$, $\chi^2 = 6.33$, for 8356 data points and 4561 contributing reflections, $0.43 < d < 4.2 \text{ \AA}$

Atom	Multiplicity	x	y	z	Uiso*100
Bi1	4	0.24(2)	0.246(2)	0.000000	5.4(2)
Bi2	8	0.25(2)	0.249(1)	0.1051(1)	5.0(1)
Bi3	8	0.24(2)	0.260(1)	0.2192(1)	4.05(9)
Ti1 ¹	8	0.250000	0.250000	0.450000	1.00
Ti2 ¹	8	0.250000	0.250000	0.350000	1.00
O1	4	0.28(2)	0.205(3)	0.500000	6.2(3)
O2	8	0.57(2)	0.537(1)	0.0516(1)	2.3(2)
O3	8	0.28(2)	0.297(2)	0.4043(1)	4.8(2)
O4	8	0.50(2)	0.490(2)	0.1413(2)	3.0(2)
O5	8	0.27(2)	0.212(2)	0.3052(1)	4.5(2)
O6	8	0.51(2)	0.494(1)	0.2491(2)	4.4(2)
O7	8	-0.00(2)	-0.030(2)	0.0408(2)	5.1(2)
O8	8	0.03(2)	0.010(3)	0.1454(2)	6.3(3)

¹ Occupancy fixed to 0.75 Ti / 0.25 Fe

Table D.16: $\text{Bi}_5\text{Ti}_3\text{FeO}_{15}$, 650 °C refinement. Selected bond lengths

bond	length \AA	bond	length \AA	bond	length \AA
Bi1 O1	2.97(2)	Bi2 O2	3.254(8)	Bi3 O5	2.78(1)
Bi1 O1	2.52(2)	Bi2 O2	2.702(7)	Bi3 O5	3.08(1)
Bi1 O1	2.54(2)	Bi2 O3	2.60(1)	Bi3 O5	3.172(9)
Bi1 O1	2.97(2)	Bi2 O3	2.96(1)	Bi3 O5	2.680(9)
Bi1 O2	3.23(1) x 2	Bi2 O3	2.51(1)	Bi3 O6	2.32(1)
Bi1 O2	2.627(8) x 2	Bi2 O3	3.03(1)	Bi3 O6	2.23(1)
Bi1 O7	2.64(1) x 2	Bi2 O4	2.44(1)	Bi3 O6	2.31(1)
Bi1 O7	2.51(1) x 2	Bi2 O4	2.48(1)	Bi3 O6	2.46(1)
		Bi2 O7	3.377(8)		
		Bi2 O7	3.242(8)		
		Bi2 O8	2.45(1)		
		Bi2 O8	2.68(1)		

Table D.17: $\text{Bi}_5\text{Ti}_3\text{FeO}_{15}$ atomic parameters from 700 °C neutron data, space group $A2_1am$, $a = 5.4835(1) \text{ \AA}$, $b = 5.4801(1) \text{ \AA}$, $c = 41.7600(3) \text{ \AA}$. $R_{WP} = 0.050$, $\chi^2 = 5.00$, for 8356 data points and 4572 contributing reflections, $0.43 < d < 4.2 \text{ \AA}$

Atom	Multiplicity	x	y	z	Uiso*100
Bi1	4	0.24(1)	0.249(2)	0.000000	6.8(2)
Bi2	8	0.24(1)	0.251(2)	0.1055(1)	5.8(1)
Bi3	8	0.23(1)	0.257(1)	0.2191(1)	4.66(9)
Ti1 ¹	8	0.250000	0.250000	0.450000	1.00
Ti2 ¹	8	0.250000	0.250000	0.350000	1.00
O1	4	0.23(1)	0.215(3)	0.500000	8.3(3)
O2	8	0.54(1)	0.543(2)	0.0502(1)	2.8(2)
O3	8	0.25(1)	0.284(2)	0.4041(1)	6.6(2)
O4	8	0.48(1)	0.495(2)	0.1416(2)	3.1(2)
O5	8	0.25(1)	0.228(2)	0.3047(1)	5.4(2)
O6	8	0.50(1)	0.501(1)	0.2492(2)	4.4(2)
O7	8	-0.02(1)	-0.019(2)	0.0418(2)	6.6(3)
O8	8	-0.00(1)	0.012(2)	0.1444(2)	5.9(3)

¹ Occupancy fixed to 0.75 Ti / 0.25 Fe

Table D.18: $\text{Bi}_5\text{Ti}_3\text{FeO}_{15}$, 700 °C refinement. Selected bond lengths

bond	length \AA	bond	length \AA	bond	length \AA
Bi1 O1	2.92(2)	Bi2 O2	3.257(9)	Bi3 O5	2.80(2)
Bi1 O1	2.56(2)	Bi2 O2	2.796(8)	Bi3 O5	3.04(2)
Bi1 O1	2.81(3)	Bi2 O3	2.75(2)	Bi3 O5	3.07(1)
Bi1 O1	2.69(3)	Bi2 O3	2.81(2)	Bi3 O5	2.77(1)
Bi1 O2	3.10(1) x 2	Bi2 O3	2.59(2)	Bi3 O6	2.34(1)
Bi1 O2	2.63(1) x 2	Bi2 O3	2.95(2)	Bi3 O6	2.24(1)
Bi1 O7	2.70(2) x 2	Bi2 O4	2.42(1)	Bi3 O6	2.33(1)
Bi1 O7	2.52(1) x 2	Bi2 O4	2.49(1)	Bi3 O6	2.42(1)
		Bi2 O7	3.357(9)		
		Bi2 O7	3.232(9)		
		Bi2 O8	2.48(1)		
		Bi2 O8	2.59(1)		

Table D.19: $\text{Bi}_5\text{Ti}_3\text{FeO}_{15}$ atomic parameters from 750 °C neutron data, space group $I4/mmm$, $a = 3.8803(1) \text{ \AA}$, $c = 41.8076(4) \text{ \AA}$. $R_{WP} = 0.067$, $\chi^2 = 5.33$, for 4350 data points and 472 contributing reflections, $0.43 < d < 4.2 \text{ \AA}$

Atom	Multiplicity	x	y	z	Uiso*100
Bi1	2	0.000000	0.000000	0.000000	6.9(3)
Bi2	4	0.000000	0.000000	0.1059(1)	5.9(2)
Bi3	4	0.000000	0.000000	0.2188(1)	5.3(1)
Ti1 ¹	4	0.000000	0.000000	0.450900	2.50
Ti2 ¹	4	0.000000	0.000000	0.348100	2.50
O1	2	0.000000	0.000000	0.500000	7.8(5)
O2	8	0.000000	0.500000	0.0470(2)	8.6(2)
O3	4	0.000000	0.000000	0.4040(2)	8.1(3)
O4	8	0.000000	0.500000	0.1428(1)	5.0(2)
O5	4	0.000000	0.000000	0.3040(2)	7.3(3)
O6	4	0.000000	0.500000	0.250000	5.2(3)

¹ Occupancy fixed to 0.75 Ti / 0.25 Fe

Table D.20: $\text{Bi}_5\text{Ti}_3\text{FeO}_{15}$, 750 °C refinement. Selected bond lengths

bond	length \AA	bond	length \AA	bond	length \AA
Bi1 O1	2.7438(1) x 4	Bi2 O2	3.133(6) x 4	Bi3 O5	2.904(4) x 4
Bi1 O2	2.762(5) x 8	Bi2 O3	2.775(2) x 4	Bi3 O6	2.338(3) x 4
		Bi2 O4	2.478(4) x 4		

Table D.21: $\text{Bi}_5\text{Ti}_3\text{FeO}_{15}$ atomic parameters from 800 °C neutron data, space group $I4/mmm$, $a = 3.8833(1) \text{ \AA}$, $c = 41.8431(4) \text{ \AA}$. $R_{WP} = 0.077$, $\chi^2 = 4.27$, for 4350 data points and 472 contributing reflections, $0.43 < d < 4.2 \text{ \AA}$

Atom	Multiplicity	x	y	z	Uiso*100
Bi1	2	0.000000	0.000000	0.000000	6.6(3)
Bi2	4	0.000000	0.000000	0.1058(1)	5.9(2)
Bi3	4	0.000000	0.000000	0.2187(1)	5.3(2)
Ti1 ¹	4	0.000000	0.000000	0.450900	2.50
Ti2 ¹	4	0.000000	0.000000	0.348100	2.50
O1	2	0.000000	0.000000	0.500000	7.2(5)
O2	8	0.000000	0.500000	0.0469(2)	8.7(3)
O3	4	0.000000	0.000000	0.4039(3)	8.0(3)
O4	8	0.000000	0.500000	0.1425(2)	5.9(3)
O5	4	0.000000	0.000000	0.3041(2)	7.0(3)
O6	4	0.000000	0.500000	0.250000	5.4(3)

¹ Occupancy fixed to 0.75 Ti / 0.25 Fe

Table D.22: $\text{Bi}_5\text{Ti}_3\text{FeO}_{15}$, 800 °C refinement. Selected bond lengths

bond	length \AA	bond	length \AA	bond	length \AA
Bi1 O1	2.7459(1) x 4	Bi2 O2	3.138(7) x 4	Bi3 O4	3.732(6) x 4
Bi1 O2	2.761(6) x 8	Bi2 O3	2.776(2) x 4	Bi3 O5	3.573(9) x 4
		Bi2 O4	2.476(6) x 4		

Appendix E

$\text{Bi}_{3-x}\text{La}_x\text{TiNbO}_9$ Structural Data

Data, structural model, selected bond lengths and angles, for the combined X-ray and neutron diffraction refinements of the series $\text{Bi}_{3-x}\text{La}_x\text{TiNbO}_9$, $0 \leq x \leq 1$. Chapter 5 includes a more rigorous investigation of the structures.

Table E.1: $\text{Bi}_{2.8}\text{La}_{0.2}\text{TiNbO}_9$ atomic parameters from 25 °C neutron data, space group $A2_1am$, $a = 5.4446(5)$ Å, $b = 5.4143(5)$ Å, $c = 25.100(3)$ Å. $R_{WP} = 0.117$, $\chi^2 = 100.9$, for 18532 data points and 4877 contributing reflections, $0.43 < d < 4.2$ Å

Atom	Multiplicity	x	y	z	Uiso*100
Bi/La1 ¹	4	0.208(2)	0.7571(6)	0.500000	1.87(5)
Bi/La2 ²	8	0.217(2)	0.7353(4)	0.6986(1)	1.87(5)
Ti/Nb ³	8	0.250000	0.278(2)	0.5878(2)	0.6(2)
O1	4	0.292(2)	0.1784(9)	0.500000	0.7(1)
O2	8	0.265(2)	0.3035(6)	0.6591(1)	0.93(8)
O3	8	0.488(2)	0.5089(5)	0.2498(1)	0.68(7)
O4	8	0.499(2)	0.5256(6)	0.5681(1)	0.23(8)
O5	8	0.566(2)	0.0447(6)	0.5840(1)	0.9(1)

¹ Occupancy 0.60(4) Bi / 0.40(4) La

² Occupancy 1.10(2) Bi / -0.10(2) La

³ Occupancy fixed to 0.5 Nb / 0.5 Ti

Table E.2: $\text{Bi}_{2.8}\text{La}_{0.2}\text{TiNbO}_9$ neutron refinement. Selected bond lengths

bond	length Å	bond	length Å	bond	length Å
Bi/La1 O1	3.167(5)	Bi/La2 O2	2.553(3)	Ti/Nb O1	2.280(7)
Bi/La1 O1	2.327(6)	Bi/La2 O2	3.243(3)	Ti/Nb O2	1.796(7)
Bi/La1 O1	2.291(6)	Bi/La2 O2	2.659(5)	Ti/Nb O4	1.97(1)
Bi/La1 O1	3.200(6)	Bi/La2 O2	3.154(5)	Ti/Nb O4	1.80(1)
Bi/La1 O4	2.647(4) x 2	Bi/La2 O3	2.231(4)	Ti/Nb O5	2.14(1)
Bi/La1 O4	2.561(4) x 2	Bi/La2 O3	2.317(4)	Ti/Nb O5	2.01(1)
Bi/La1 O5	3.266(4) x 2	Bi/La2 O3	2.456(4)		
Bi/La1 O5	2.489(3) x 2	Bi/La2 O3	2.262(4)		

Table E.3: $\text{Bi}_{2.6}\text{La}_{0.4}\text{TiNbO}_9$ atomic parameters from 25 °C neutron data, space group $A2_1am$, $a = 5.4429(6)$ Å, $b = 5.4264(6)$ Å, $c = 25.065(3)$ Å. $R_{WP} = 0.098$, $\chi^2 = 55.77$, for 18529 data points and 4883 contributing reflections, $0.43 < d < 4.2$ Å

Atom	Multiplicity	x	y	z	Uiso*100
Bi/La1 ¹	4	0.219(2)	0.7538(6)	0.500000	2.10(4)
Bi/La2 ²	8	0.221(2)	0.7339(5)	0.6983(1)	2.10(4)
Ti/Nb ³	8	0.250000	0.246(3)	0.5893(2)	0.8(2)
O1	4	0.283(2)	0.1803(8)	0.500000	-0.1(1)
O2	8	0.270(2)	0.2954(6)	0.6587(1)	1.37(8)
O3	8	0.494(2)	0.4997(5)	0.2487(1)	0.71(6)
O4	8	0.493(2)	0.5263(6)	0.5677(1)	1.11(9)
O5	8	0.560(2)	0.0447(6)	0.5840(1)	0.71(9)

¹ Occupancy 0.48(4) Bi / 0.52(4) La

² Occupancy 1.06(2) Bi / -0.06(2) La

³ Occupancy fixed to 0.5 Nb / 0.5 Ti

Table E.4: $\text{Bi}_{2.6}\text{La}_{0.4}\text{TiNbO}_9$ neutron refinement. Selected bond lengths

bond	length Å	bond	length Å	bond	length Å
Bi/La1 O1	3.132(5)	Bi/La2 O2	2.592(3)	Ti/Nb O1	2.273(5)
Bi/La1 O1	2.340(5)	Bi/La2 O2	3.216(3)	Ti/Nb O2	1.765(6)
Bi/La1 O1	2.397(6)	Bi/La2 O2	2.654(4)	Ti/Nb O4	2.09(1)
Bi/La1 O1	3.093(5)	Bi/La2 O2	3.151(4)	Ti/Nb O4	1.95(1)
Bi/La1 O4	2.574(4) x 2	Bi/La2 O3	2.212(4)	Ti/Nb O5	2.01(1)
Bi/La1 O4	2.589(4) x 2	Bi/La2 O3	2.364(4)	Ti/Nb O5	1.89(1)
Bi/La1 O5	3.220(4) x 2	Bi/La2 O3	2.427(4)		
Bi/La1 O5	2.525(3) x 2	Bi/La2 O3	2.283(5)		

Table E.5: $\text{Bi}_{2.4}\text{La}_{0.6}\text{TiNbO}_9$ atomic parameters from 25 °C neutron data, space group $A2_1am$, $a = 5.4446(4)$ Å, $b = 5.4427(4)$ Å, $c = 25.032(2)$ Å. $R_{WP} = 0.080$, $\chi^2 = 39.6$, for 18527 data points and 4731 contributing reflections, $0.43 < d < 4.2$ Å

Atom	Multiplicity	x	y	z	Uiso*100
Bi/La1 ¹	4	0.230(2)	0.7498(4)	0.500000	1.68(3)
Bi/La2 ²	8	0.227(2)	0.7342(3)	0.6990(1)	1.68(3)
Ti/Nb ³	8	0.250000	0.249(2)	0.5870(1)	-0.66(1)
O1	4	0.270(2)	0.1866(7)	0.500000	0.71(9)
O2	8	0.265(2)	0.2988(5)	0.6590(1)	1.58(6)
O3	8	0.488(2)	0.5083(5)	0.2495(1)	0.59(4)
O4	8	0.495(2)	0.5149(6)	0.5683(1)	1.28(7)
O5	8	0.547(2)	0.0351(5)	0.5834(1)	1.48(8)

¹ Occupancy 0.22(3) Bi / 0.78(3) La

² Occupancy 1.06(2) Bi / -0.09(2) La

³ Occupancy fixed to 0.5 Nb / 0.5 Ti

Table E.6: $\text{Bi}_{2.4}\text{La}_{0.6}\text{TiNbO}_9$ neutron refinement. Selected bond lengths

bond	length Å	bond	length Å	bond	length Å
Bi/La1 O1	3.073(4)	Bi/LA2 O2	2.581(2)	Ti1 O1	2.206(4)
Bi/La1 O1	2.387(4)	Bi/La2 O2	3.239(3)	Ti1 O2	1.826(4)
Bi/La1 O1	2.530(6)	Bi/La2 O2	2.712(4)	Ti1 O4	2.022(9)
Bi/La1 O1	2.958(5)	Bi/La2 O2	3.102(4)	Ti1 O4	1.95(1)
Bi/La1 O4	2.575(3) x 2	Bi/La2 O3	2.256(3)	Ti1 O5	1.99(1)
Bi/La1 O4	2.578(3) x 2	Bi/La2 O3	2.280(3)	Ti1 O5	1.90(1)
Bi/La1 O5	3.120(3) x 2	Bi/La2 O3	2.419(3)		
Bi/La1 O5	2.593(2) x 2	Bi/La2 O3	2.292(4)		

Table E.7: $\text{Bi}_{2.2}\text{La}_{0.8}\text{TiNbO}_9$ atomic parameters from 25 °C neutron data, space group I4/mmm, $a = 3.8487(5)$ Å, $c = 25.001(3)$ Å. $R_{WP} = 0.162$, $\chi^2 = 506.6$, for 18537 data points and 4002 contributing reflections, $0.43 < d < 4.2$ Å

Atom	Multiplicity	x	y	z	Uiso*100
Bi/La1 ¹	2	0.500000	0.500000	0.000000	2.66(6)
Bi/La2 ²	4	0.500000	0.500000	0.1992(1)	2.66(6)
Ti/Nb ³	4	0.000000	0.000000	0.0851(2)	-3.5(1)
O1	2	0.500000	0.500000	0.500000	5.5(2)
O2	4	0.000000	0.500000	0.250000	0.73(7)
O3	4	0.000000	0.000000	0.1590(1)	5.8(1)
O4	8	0.000000	0.500000	0.0754(1)	5.09(8)

¹ Occupancy 0.40(7) Bi / 0.60(7) La

² Occupancy 0.90(3) Bi / 0.10(3) La

³ Occupancy fixed to 0.5 Nb / 0.5 Ti

Table E.8: $\text{Bi}_{2.2}\text{La}_{0.8}\text{TiNbO}_9$ neutron refinement. Selected bond lengths

bond	length Å	bond	length Å	bond	length Å
Bi/La1 O1	2.7214(4)	Bi/La2 O2	2.3054(9)	Ti/Nb O1	2.127(4)
Bi/La1 O4	2.693(1)	Bi/La2 O3	2.901(1)	Ti/Nb O3	1.847(6)
				Ti/Nb O4	1.9397(7)

Table E.9: $\text{Bi}_2\text{LaTiNbO}_9$ atomic parameters from 25 °C neutron data, space group I4/mmm, $a = 3.8536(2)$ Å, $c = 24.972(1)$ Å. $R_{WP} = 0.135$, $\chi^2 = 102.3$, for 18487 data points and 4005 contributing reflections, $0.43 < d < 4.2$ Å

Atom	Multiplicity	x	y	z	Uiso*100
Bi/La1 ¹	2	0.500000	0.500000	0.000000	2.34(5)
Bi/La2 ²	4	0.500000	0.500000	0.1992(1)	2.34(5)
Ti/Nb ³	4	0.000000	0.000000	0.0850(2)	-2.7(1)
O1	2	0.500000	0.500000	0.500000	4.1(1)
O2	4	0.000000	0.500000	0.250000	0.70(6)
O3	4	0.000000	0.000000	0.1589(1)	5.36(9)
O4	8	0.000000	0.500000	0.0753(1)	3.84(6)

¹ Occupancy 0.40(7) Bi / 0.60(7) La

² Occupancy 0.90(3) Bi / 0.10(3) La

³ Occupancy fixed to 0.5 Nb / 0.5 Ti

Table E.10: $\text{Bi}_2\text{LaTiNbO}_9$ neutron refinement. Selected bond lengths

bond	length Å	bond	length Å	bond	length Å
Bi/La1 O1	2.7249(1) x 4	Bi/La2 O2	2.3063(8) x 4	Ti/Nb O1	2.122(4)
Bi/La1 O4	2.692(1) x 8	Bi/La2 O3	2.9056(9) x 4	Ti/Nb O3	1.844(5)
				Ti/Nb O4	1.9420(6) x 4

Table E.11: $\text{Bi}_{3-x}\text{La}_x\text{TiNbO}_9$ neutron refinement. Selected TiO_6 octahedral bond angles

x	O-Ti-O Apical	O-Ti-O Equatorial				O-O-O Apical Tilt	O-O-O Equatorial Tilt
0.0	173.17	82.68	91.68	96.12	85.53	160.66	157.42
0.2	168.16	82.64	85.76	96.37	91.36	161.01	159.29
0.4	171.05	81.01	90.16	96.63	85.29	162.04	160.24
0.6	174.53	82.71	89.69	96.32	86.71	162.54	163.88
0.8	180.00	89.10	89.10	89.10	89.10	180.00	180
1.0	180.00	89.11	89.11	89.11	89.11	180.00	180

Appendix F

$\text{Bi}_{4-x}\text{La}_x\text{Ti}_3\text{O}_{12}$ Structural Data

Data, structural model, selected bond lengths and angles, for the combined X-ray and neutron diffraction refinements of the series $\text{Bi}_{4-x}\text{La}_x\text{Ti}_3\text{O}_{12}$, $0 \leq x \leq 2$. Chapter 5 includes a more rigorous investigation of the structures.

Table F.1: $\text{Bi}_{3.9}\text{La}_{0.1}\text{Ti}_3\text{O}_{12}$ atomic parameters from 25°C neutron data, space group B2cb, $a = 5.4460(1) \text{ \AA}$, $b = 5.4118(1) \text{ \AA}$, $c = 32.839(1) \text{ \AA}$. $R_{WP} = 0.051$, $\chi^2 = 21.11$, for 17999 data points and 4513 contributing reflections, $0.43 < d < 4.2 \text{ \AA}$

Atom	Multiplicity x	y	z	Uiso*100	
Bi/La1 ¹	8	-0.0065(3)	-0.0021(2)	0.06663(2)	0.62(2)
Bi/La2 ²	8	-0.0100(3)	0.0167(2)	0.21132(2)	0.62(2)
Ti1	4	0.0268(6)	0.000000	0.500000	-0.28(6)
Ti2	8	0.0423(4)	0.0033(5)	0.37125(4)	0.31(5)
O1	8	0.3133(3)	0.2562(3)	0.00710(5)	2.19(5)
O2	8	0.2611(3)	0.2418(2)	0.24972(5)	0.57(3)
O3	8	0.0759(3)	0.0595(2)	0.44094(3)	0.07(4)
O4	8	0.0470(4)	-0.0530(3)	0.31846(3)	1.03(4)
O5	8	0.2814(3)	0.2256(3)	0.11133(4)	0.26(4)
O6	8	0.3498(3)	0.2951(3)	0.87611(4)	0.83(5)

¹ Occupancy 0.94(1) Bi / 0.06(1) La

² Occupancy 1.01(1) Bi / -0.01(1) La

Table F.2: $\text{Bi}_{3.9}\text{La}_{0.1}\text{Ti}_3\text{O}_{12}$ neutron refinement. Selected bond lengths

bond	length \AA	bond	length \AA	bond	length \AA
Bi1-O1	2.968(2)	Bi2-O2	2.292(2)	Ti1-O1	2.057(3) x 2
Bi1-O1	3.284(2)	Bi2-O2	2.456(2)	Ti1-O1	1.824(2) x 2
Bi1-O1	2.560(2)	Bi2-O2	2.269(2)	Ti1-O3	1.984(1) x 2
Bi1-O1	2.922(2)	Bi2-O2	2.203(2)	Ti2-O3	2.316(2)
Bi1-O3	2.428(1)	Bi2-O4	3.249(2)	Ti2-O4	1.760(2)
Bi1-O3	3.082(1)	Bi2-O4	2.545(2)	Ti2-O5	2.069(3)
Bi1-O3	2.309(1)	Bi2-O4	2.611(2)	Ti2-O5	1.970(3)
Bi1-O3	3.197(1)	Bi2-O4	3.193(2)	Ti2-O6	2.005(3)
Bi1-O5	2.476(2)			Ti2-O6	1.902(3)
Bi1-O5	2.393(2)				
Bi1-O6	3.133(2)				
Bi1-O6	2.314(2)				

Table F.3: $\text{Bi}_{3.7}\text{La}_{0.3}\text{Ti}_3\text{O}_{12}$ atomic parameters from 25 °C neutron data, space group B2cb, $a = 5.4441(2)$ Å, $b = 5.4192(2)$ Å, $c = 32.904(1)$ Å. $R_{WP} = 0.054$, $\chi^2 = 25.45$, for 18027 data points and 4505 contributing reflections, $0.43 < d < 4.2$ Å

Atom	Multiplicity	x	y	z	Uiso*100
Bi/La1 ¹	8	0.0033(2)	-0.0030(2)	0.06672(2)	0.84(2)
Bi/La2 ²	8	-0.002678)	0.0166(2)	0.21147(2)	0.84(2)
Ti1	4	0.0361(6)	0.000000	0.500000	0.23(6)
Ti2	8	0.0453(4)	0.0007(5)	0.37133(4)	0.20(5)
O1	8	0.3207(3)	0.2566(3)	0.00702(5)	2.51(5)
O2	8	0.2632(3)	0.2410(2)	0.24991(5)	0.85(3)
O3	8	0.0788(3)	0.0585(3)	0.44091(3)	0.37(4)
O4	8	0.0501(4)	-0.0511(3)	0.31840(3)	1.00(4)
O5	8	0.2852(3)	0.2258(3)	0.11226(4)	0.03(4)
O6	8	0.3515(3)	0.2943(3)	0.87603(4)	0.47(4)

¹ Occupancy 0.83(1) Bi / 0.17(1) La

² Occupancy 1.02(1) Bi / -0.02(1) La

Table F.4: $\text{Bi}_{3.7}\text{La}_{0.3}\text{Ti}_3\text{O}_{12}$ neutron refinement. Selected bond lengths

bond	length Å	bond	length Å	bond	length Å
Bi1-O1	2.971(2)	Bi2-O2	2.275(2)	Ti1-O1	2.048(3) x 2
Bi1-O1	3.281(2)	Bi2-O2	2.437(2)	Ti1-O1	1.834(3) x 2
Bi1-O1	2.575(2)	Bi2-O2	2.278(2)	Ti1-O3	1.984(1) x 2
Bi1-O1	2.928(2)	Bi2-O2	2.225(2)	Ti2-O3	2.318(2)
Bi1-O3	2.425(2)	Bi2-O4	3.242(2)	Ti2-O4	1.764(2)
Bi1-O3	3.081(2)	Bi2-O4	2.557(2)	Ti2-O5	2.053(3)
Bi1-O3	2.344(2)	Bi2-O4	2.632(2)	Ti2-O5	1.950(3)
Bi1-O3	3.157(1)	Bi2-O4	3.171(2)	Ti2-O6	2.009(3)
Bi1-O5	2.478(2)			Ti2-O6	1.916(3)
Bi1-O5	2.431(2)				
Bi1-O6	3.104(2)				
Bi1-O6	2.331(2)				

Table F.5: $\text{Bi}_{3.5}\text{La}_{0.5}\text{Ti}_3\text{O}_{12}$ atomic parameters from 25 °C neutron data, space group B2cb, $a = 5.4370(3)$ Å, $b = 5.4187(3)$ Å, $c = 32.925(2)$ Å. $R_{WP} = 0.067$, $\chi^2 = 38.53$, for 18033 data points and 4471 contributing reflections, $0.43 < d < 4.2$ Å

Atom	Multiplicity	x	y	z	Uiso*100
Bi/La1 ¹	8	0.0048(3)	-0.0031(2)	0.06688(3)	1.11(2)
Bi/La2 ²	8	-0.0029(3)	0.0150(2)	0.21163(2)	1.11(2)
Ti1	4	0.0353(9)	0.000000	0.500000	0.90(9)
Ti2	8	0.0388(6)	0.0021(6)	0.37135(4)	0.23(6)
O1	8	0.3180(5)	0.2591(4)	0.00671(6)	3.04(7)
O2	8	0.2613(5)	0.2399(3)	0.24971(6)	1.07(4)
O3	8	0.0721(4)	0.0575(3)	0.44077(4)	0.63(5)
O4	8	0.0474(4)	-0.0509(4)	0.31838(4)	0.89(5)
O5	8	0.2809(3)	0.2275(4)	0.11259(5)	0.15(5)
O6	8	0.3429(3)	0.2907(4)	0.87616(5)	0.77(6)

¹ Occupancy 0.76(2) Bi / 0.24(2) La

² Occupancy 0.99(2) Bi / 0.01(2) La

Table F.6: $\text{Bi}_{3.5}\text{La}_{0.5}\text{Ti}_3\text{O}_{12}$ neutron refinement. Selected bond lengths

bond	length Å	bond	length Å	bond	length Å
Bi1-O1	2.974(2)	Bi2-O2	2.263(2)	Ti1-O1	2.029(4) x 2
Bi1-O1	3.270(2)	Bi2-O2	2.431(2)	Ti1-O1	1.848(4) x 2
Bi1-O1	2.589(2)	Bi2-O2	2.274(2)	Ti1-O3	1.985(2) x 2
Bi1-O1	2.926(2)	Bi2-O2	2.231(2)	Ti2-O3	2.312(2)
Bi1-O3	2.422(2)	Bi2-O4	3.233(2)	Ti2-O4	1.768(2)
Bi1-O3	3.070(2)	Bi2-O4	2.566(2)	Ti2-O5	2.056(3)
Bi1-O3	2.385(2)	Bi2-O4	2.644(2)	Ti2-O5	1.948(4)
Bi1-O3	3.108(2)	Bi2-O4	3.157(2)	Ti2-O6	2.005(3)
Bi1-O5	2.466(2)			Ti2-O6	1.898(4)
Bi1-O5	2.445(2)				
Bi1-O6	3.054(2)				
Bi1-O6	2.354(2)				

Table F.7: $\text{Bi}_{3.3}\text{La}_{0.7}\text{Ti}_3\text{O}_{12}$ atomic parameters from 25 °C neutron data, space group B2cb, $a = 5.4315(2)$ Å, $b = 5.4199(2)$ Å, $c = 32.929(1)$ Å. $R_{WP} = 0.076$, $\chi^2 = 36.10$, for 18025 data points and 4472 contributing reflections, $0.43 < d < 4.2$ Å

Atom	Multiplicity	x	y	z	Uiso*100
Bi/La1 ¹	8	0.0224(4)	-0.0029(3)	0.06687(3)	1.00(2)
Bi/La2 ²	8	0.012823	0.0138(3)	0.21155(2)	1.00(2)
Ti1	4	0.048(1)	0.000000	0.500000	0.7(1)
Ti2	8	0.0496(7)	0.0031(7)	0.37113(5)	-0.01(7)
O1	8	0.3277(5)	0.2614(5)	0.00579(8)	3.33(8)
O2	8	0.2759(6)	0.2401(4)	0.24988(7)	0.66(5)
O3	8	0.0795(5)	0.0567(4)	0.44088(5)	0.60(5)
O4	8	0.0603(5)	-0.0509(5)	0.31830(4)	0.40(6)
O5	8	0.2937(5)	0.2293(4)	0.11255(6)	-0.13(6)
O6	8	0.3502(4)	0.2876(4)	0.87655(5)	0.27(7)

¹ Occupancy 0.70(2) Bi / 0.30(2) La

² Occupancy 0.95(2) Bi / 0.05(2) La

Table F.8: $\text{Bi}_{3.3}\text{La}_{0.7}\text{Ti}_3\text{O}_{12}$ neutron refinement. Selected bond lengths

bond	length Å	bond	length Å	bond	length Å
Bi1-O1	2.974(3)	Bi2-O2	2.267(3)	Ti1-O1	2.005(5) x 2
Bi1-O1	3.230(3)	Bi2-O2	2.420(3)	Ti1-O1	1.864(4) x 2
Bi1-O1	2.623(3)	Bi2-O2	2.272(3)	Ti1-O3	1.978(2) x 2
Bi1-O1	2.911(3)	Bi2-O2	2.242(3)	Ti2-O3	2.321(2)
Bi1-O3	2.421(3)	Bi2-O4	3.225(3)	Ti2-O4	1.765(2)
Bi1-O3	3.059(3)	Bi2-O4	2.569(3)	Ti2-O5	2.062(4)
Bi1-O3	2.437(3)	Bi2-O4	2.655(3)	Ti2-O5	1.951(4)
Bi1-O3	3.050(3)	Bi2-O4	3.138(3)	Ti2-O6	1.996(4)
Bi1-O5	2.453(3)			Ti2-O6	1.893(4)
Bi1-O5	2.451(2)				
Bi1-O6	3.004(2)				
Bi1-O6	2.374(2)				

Table F.9: $\text{Bi}_{3.1}\text{La}_{0.9}\text{Ti}_3\text{O}_{12}$ atomic parameters from 25 °C neutron data, space group B2cb, $a = 5.4244(3)$ Å, $b = 5.4189(3)$ Å, $c = 32.938(2)$ Å. $R_{WP} = 0.097$, $\chi^2 = 61.15$, for 18030 data points and 4501 contributing reflections, $0.43 < d < 4.2$ Å

Atom	Multiplicity	x	y	z	Uiso*100
Bi/La1 ¹	8	0.0043(7)	-0.0038(3)	0.06687(4)	1.28(3)
Bi/La2 ²	8	-0.007759	0.0108(4)	0.21162(3)	1.28(3)
Ti1	4	0.029(2)	0.000000	0.500000	0.9(1)
Ti2	8	0.022(1)	0.0047(9)	0.37104(6)	0.27(9)
O1	8	0.2988(9)	0.2685(8)	0.0048(1)	4.1(1)
O2	8	0.254(1)	0.2401(6)	0.2497(1)	1.12(7)
O3	8	0.0435(8)	0.0574(6)	0.44078(6)	0.92(7)
O4	8	0.0325(8)	-0.0508(7)	0.31829(5)	0.84(8)
O5	8	0.2665(7)	0.2335(7)	0.11279(8)	0.28(8)
O6	8	0.3155(6)	0.2830(6)	0.87695(7)	0.6(1)

¹ Occupancy 0.58(2) Bi / 0.42(2) La

² Occupancy 0.97(2) Bi / 0.03(2) La

Table F.10: $\text{Bi}_{3.1}\text{La}_{0.9}\text{Ti}_3\text{O}_{12}$ neutron refinement. Selected bond lengths

bond	length Å	bond	length Å	bond	length Å
Bi1-O1	2.984(4)	Bi2-O2	2.267(4)	Ti1-O1	1.935(8) x 2
Bi1-O1	3.192(4)	Bi2-O2	2.408(4)	Ti1-O1	1.923(7) x 2
Bi1-O1	2.654(4)	Bi2-O2	2.267(4)	Ti1-O3	1.977(2) x 2
Bi1-O1	2.889(4)	Bi2-O2	2.249(4)	Ti2-O3	2.318(3)
Bi1-O3	2.401(4)	Bi2-O4	3.206(4)	Ti2-O4	1.764(3)
Bi1-O3	3.059(4)	Bi2-O4	2.581(4)	Ti2-O5	2.049(6)
Bi1-O3	2.529(5)	Bi2-O4	2.690(4)	Ti2-O5	1.968(6)
Bi1-O3	2.950(5)	Bi2-O4	3.099(4)	Ti2-O6	1.973(6)
Bi1-O5	2.442(4)			Ti2-O6	1.889(6)
Bi1-O5	2.469(3)				
Bi1-O6	2.926(3)				
Bi1-O6	2.410(3)				

Table F.11: $\text{Bi}_{2.9}\text{La}_{1.1}\text{Ti}_3\text{O}_{12}$ atomic parameters from 25 °C neutron data, space group B2cb, $a = 5.4182(3)$ Å, $b = 5.4182(3)$ Å, $c = 32.944(2)$ Å. $R_{WP} = 0.076$, $\chi^2 = 69.16$, for 18034 data points and 4534 contributing reflections, $0.43 < d < 4.2$ Å

Atom	Multiplicity	x	y	z	Uiso*100
Bi/La1 ¹	8	0.0134(8)	-0.0013(3)	0.06656(3)	1.73(3)
Bi/La2 ²	8	0.0105(8)	0.0082(3)	0.21159(2)	1.73(3)
Ti1	4	0.004(2)	0.000000	0.500000	1.7(1)
Ti2	8	0.011(2)	0.0043(7)	0.37104(5)	0.93(6)
O1	8	0.306(1)	0.2869(8)	0.00439(8)	2.54(7)
O2	8	0.264(1)	0.2437(8)	0.24949(8)	0.68(4)
O3	8	0.0222(9)	0.0514(5)	0.44128(4)	1.22(6)
O4	8	0.022(1)	-0.0507(5)	0.31779(4)	1.63(7)
O5	8	0.2588(5)	0.2433(7)	0.11358(6)	0.40(6)
O6	8	0.294341	0.2831(8)	0.87822(7)	2.25(9)

¹ Occupancy 0.49(2) Bi / 0.51(2) La

² Occupancy 0.97(2) Bi / 0.03(2) La

Table F.12: $\text{Bi}_{2.9}\text{La}_{1.1}\text{Ti}_3\text{O}_{12}$ neutron refinement. Selected bond lengths

bond	length Å	bond	length Å	bond	length Å
Bi1-O1	3.024(3)	Bi2-O2	2.251(4)	Ti1-O1	2.01(1) x 2
Bi1-O1	3.220(3)	Bi2-O2	2.362(4)	Ti1-O1	1.895(8) x 2
Bi1-O1	2.610(3)	Bi2-O2	2.301(5)	Ti1-O3	1.957(2) x 2
Bi1-O1	2.836(3)	Bi2-O2	2.271(4)	Ti2-O3	2.329(2)
Bi1-O3	2.438(3)	Bi2-O4	3.180(3)	Ti2-O4	1.780(2)
Bi1-O3	3.007(3)	Bi2-O4	2.579(3)	Ti2-O5	2.014(6)
Bi1-O3	2.687(6)	Bi2-O4	2.827(6)	Ti2-O5	1.981(7)
Bi1-O3	2.782(6)	Bi2-O4	2.945(6)	Ti2-O6	1.933(8)
Bi1-O5	2.434(3)			Ti2-O6	1.928(7)
Bi1-O5	2.501(4)				
Bi1-O6	2.821(3)				
Bi1-O6	2.466(3)				

Table F.13: $\text{Bi}_{2.7}\text{La}_{1.3}\text{Ti}_3\text{O}_{12}$ atomic parameters from 25 °C neutron data, space group B2cb, $a = 5.4176(5)$ Å, $b = 5.4176(5)$ Å, $c = 32.948(3)$ Å. $R_{WP} = 0.108$, $\chi^2 = 120.60$, for 18532 data points and 4546 contributing reflections, $0.43 < d < 4.2$ Å

Atom	Multiplicity	x	y	z	Uiso*100
Bi/La1 ¹	8	0.015(1)	-0.0046(5)	0.06668(4)	1.57(4)
Bi/La2 ²	8	0.014(1)	0.0112(5)	0.21149(4)	1.57(4)
Ti1	4	-0.001(3)	0.000000	0.500000	1.5(2)
Ti2	8	0.015(2)	-0.002(1)	0.37097(7)	0.39(9)
O1	8	0.307987	0.289(1)	0.0039(1)	2.5(1)
O2	8	0.265(1)	0.248(1)	0.2495(1)	0.72(7)
O3	8	0.025(1)	0.0483(8)	0.44115(6)	1.06(9)
O4	8	0.025(1)	-0.0454(9)	0.31769(6)	1.5(1)
O5	8	0.260(2)	0.2408(9)	0.11367(9)	0.3(1)
O6	8	0.292(2)	0.280(1)	0.87827(9)	1.5(1)

¹ Occupancy 0.68(4) Bi / 0.32(4) La

² Occupancy 0.67(4) Bi / 0.34(4) La

Table F.14: $\text{Bi}_{2.7}\text{La}_{1.3}\text{Ti}_3\text{O}_{12}$ neutron refinement. Selected bond lengths

bond	length Å	bond	length Å	bond	length Å
Bi1-O1	3.053(5)	Bi2-O2	2.251(6)	Ti1-O1	2.03(2) x 2
Bi1-O1	3.210(5)	Bi2-O2	2.355(6)	Ti1-O1	1.88(1) x 2
Bi1-O1	2.626(5)	Bi2-O2	2.330(7)	Ti1-O3	1.961(2) x 2
Bi1-O1	2.815(5)	Bi2-O2	2.257(6)	Ti2-O3	2.329(3)
Bi1-O3	2.437(5)	Bi2-O4	3.165(5)	Ti2-O4	1.772(3)
Bi1-O3	3.007(5)	Bi2-O4	2.588(5)	Ti2-O5	1.99(1)
Bi1-O3	2.677(9)	Bi2-O4	2.825(9)	Ti2-O5	1.96(1)
Bi1-O3	2.785(9)	Bi2-O4	2.936(9)	Ti2-O6	1.94(1)
Bi1-O5	2.435(5)			Ti2-O6	1.96(1)
Bi1-O5	2.519(5)				
Bi1-O6	2.788(5)				
Bi1-O6	2.471(4)				

Table F.15: $\text{Bi}_{2.5}\text{La}_{1.5}\text{Ti}_3\text{O}_{12}$ atomic parameters from 25 °C neutron data, space group B2cb, $a = 5.4143(2)$ Å, $b = 5.4143(2)$ Å, $c = 32.946(1)$ Å. $R_{WP} = 0.037$, $\chi^2 = 6.00$, for 13588 data points and 4517 contributing reflections, $0.43 < d < 3.08$ Å

Atom	Multiplicity	x	y	z	Uiso*100
Bi/La1 ¹	8	0.0144(6)	-0.0003(4)	0.06648(3)	1.22(1)
Bi/La2 ²	8	0.0183(6)	0.0103(4)	0.21156(3)	1.22(1)
Ti1	4	0.005(2)	0.000000	0.500000	0.35(6)
Ti2	8	-0.0029(8)	-0.0136(4)	0.37073(4)	-0.829(9)
O1	8	0.3139(8)	0.2954(7)	0.00488(8)	1.06(4)
O2	8	0.2683(6)	0.246(1)	0.24912(7)	0.41(2)
O3	8	0.020(1)	0.0384(5)	0.44134(5)	1.03(4)
O4	8	0.025(1)	-0.0391(6)	0.31789(6)	1.85(6)
O5	8	0.2727(8)	0.2557(6)	0.11372(6)	0.31(2)
O6	8	0.261(1)	0.2525(9)	0.87899(7)	1.31(5)

¹ Occupancy 0.36(5) Bi / 0.64(5) La

² Occupancy 0.89(5) Bi / 0.11(5) La

Table F.16: $\text{Bi}_{2.5}\text{La}_{1.5}\text{Ti}_3\text{O}_{12}$ neutron refinement. Selected bond lengths

bond	length Å	bond	length Å	bond	length Å
Bi1-O1	3.052(3)	Bi2-O2	2.233(5)	Ti1-O1	2.012(8) x 2
Bi1-O1	3.273(3)	Bi2-O2	2.359(4)	Ti1-O1	1.912(6) x 2
Bi1-O1	2.555(3)	Bi2-O2	2.330(4)	Ti1-O3	1.945(2) x 2
Bi1-O1	2.816(3)	Bi2-O2	2.260(5)	Ti2-O3	2.346(2)
Bi1-O3	2.511(3)	Bi2-O4	3.513(2)	Ti2-O4	1.753(3)
Bi1-O3	2.928(3)	Bi2-O4	3.129(4)	Ti2-O5	2.012(4)
Bi1-O3	2.697(6)	Bi2-O4	2.626(3)	Ti2-O5	1.859(4)
Bi1-O3	2.757(6)	Bi2-O4	2.848(6)	Ti2-O6	2.029(6)
Bi1-O5	2.510(4)			Ti2-O6	1.944(5)
Bi1-O5	2.427(3)				
Bi1-O6	2.622(5)				
Bi1-O6	2.627(5)				

Table F.17: $\text{Bi}_2\text{La}_2\text{Ti}_3\text{O}_{12}$ atomic parameters from 25 °C neutron data, space group I4/mmm, $a = 3.8330(3)$ Å, $c = 33.040(3)$ Å. $R_{WP} = 0.064$, $\chi^2 = 25.54$, for 14448 data points and 5233 contributing reflections, $0.43 < d < 3.08$ Å

Atom	Multiplicity	x	y	z	Uiso*100
Bi/La1 ¹	4	0.500000	0.500000	0.06627(8)	0.66(3)
Bi/La2 ²	4	0.500000	0.500000	0.21233(8)	0.66(3)
Ti1	2	0.500000	0.500000	0.500000	1.9(2)
Ti2	4	0.500000	0.500000	0.3690(1)	-0.05(5)
O1	4	0.500000	0.000000	0.000000	10.8(4)
O2	4	0.500000	0.000000	0.250000	1.03(6)
O3	4	0.500000	0.500000	0.4393(1)	1.60(7)
O4	4	0.500000	0.500000	0.3184(2)	3.6(1)
O5	8	0.500000	0.000000	0.11829(8)	1.04(4)

¹ Occupancy 0.26(2) Bi / 0.75(2) La

² Occupancy 0.75(2) Bi / 0.26(2) La

Table F.18: $\text{Bi}_2\text{La}_2\text{Ti}_3\text{O}_{12}$ neutron refinement. Selected bond lengths

bond	length Å	bond	length Å
Bi1-O1	2.910(2)	Ti1-O1	1.9165(2) x 2
Bi1-O3	2.7166(4)	Ti1-O3	2.005(4)
Bi1-O5	2.574(2)	Ti2-O3	2.325(6)
Bi2-O2	2.285(1)	Ti2-O4	1.671(8)
Bi2-O4	2.894(2)	Ti2-O5	1.962(1)
Bi2-O5	3.651(4)		

Appendix G

Publications From This Work

1. Structural behavior of the four-layer Aurivillius-phase ferroelectrics

SrBi₄Ti₄O₁₅ and Bi₅Ti₃FeO₁₅, C. H. Hervoches, A. Snedden, R. Riggs, S. H. Kilcoyne, P. Manuel, P. Lightfoot, *J. Solid State Chem.* 2002, **164**, 280.

2. Oxide ion conductivity in Ga-doped Aurivillius phases - a reappraisal, A. Snedden, S. M. Blake, K. S. Knight, P. Lightfoot, *Solid State Ionics* 2003, **156**, 439

3. Ferroelectric phase transitions in SrBi₂Nb₂O₉ and Bi₅Ti₃FeO₁₅ - a powder neutron diffraction study, A. Snedden, C. H. Hervoches, P. Lightfoot, *Phys. Rev. B.* 2003, **67**, 092102

4. Structural distortions in the layered perovskites CsANb₂O₇ (A = Nd, Bi), A. Snedden, K. S. Knight, P. Lightfoot, *J. Solid State Chem.* 2003, **173**, 309

5. Contrasting structural behaviour in the Aurivillius phase ferroelectrics Bi₄Ti₃O₁₂, BaBi₄Ti₄O₁₅ and Ba₂Bi₄Ti₅O₁₈, P. Lightfoot, A. Snedden, S. M. Blake, K. S. Knight, *Mater. Res. Symp. Proc.* In press

6. Orientation Dependence of Ferroelectric Properties of Pulsed Laser Ablated Bi_{4-x}Nd_xTi₃O₁₂ Films, A. Garg, Z. H. Barber, M. Dawber, J. F. Scott, A. Snedden, and P. Lightfoot, *Appl. Phys. Lett* 2003, **83**, 2414